Energy transfer dynamics in molecular layers of porphyrin derivatives

Energy transfer dynamics in molecular layers of porphyrin derivatives

proefschrift

ter verkrijging van de graad van doctor
aan de Technische Universiteit Delft,
op gezag van de Rector Magnificus prof. dr. ir. J.T. Fokkema,
voorzitter van het College voor Promoties,
in het openbaar te verdedigen op dinsdag 25 maart 2008 om 12:30 uur

door

Jannetje Maria HUIJSER

scheikundig ingenieur
geboren te Sint Philipsland

Dit proefschrift is goedgekeurd door de promotor:
Prof. dr. L.D.A. Siebbeles

Samenstelling promotiecommissie:

Rector Magnificus,	voorzitter
Prof. dr. L.D.A. Siebbeles,	Technische Universiteit Delft, promotor
Prof. dr. habil. T.S. Balaban,	Universiteit Karlsruhe
Prof. dr. R.J.M. Klein Gebbink,	Universiteit Utrecht
Prof. dr. H. van Amerongen,	Universiteit Wageningen
Prof. dr. J. Schoonman,	Technische Universiteit Delft
Prof. dr. S.J. Picken,	Technische Universiteit Delft
Dr. ir. T.J. Savenije,	Technische Universiteit Delft

Dr. ir. T.J. Savenije heeft als begeleider in belangrijke mate aan de totstandkoming van het proefschrift bijgedragen.

The research described in this thesis was performed within the DelftChemTech department of the Faculty of Applied Sciences of Delft University of Technology. This research was embedded in the Delft Research Centre "Sustainable Energy: Extraction, Conversion and Use", which is one of the thirteen multidisciplinary focus research themes or Delft Research Centres (DRCs) TU Delft has identified.

Printed by: Ponsen & Looijen B.V.
ISBN 978-90-6464-229-6

CONTENTS

CHAPTER 1

Effect of molecular organization on energy transfer dynamics in natural and biomimetic light-harvesting systems

1.1. Introduction

Life on earth would not be possible without the supply of solar energy. The sun provides energy to our planet with an average rate of about 100 000 TW, which exceeds the world's present rate of energy consumption of approximately 14 TW by 7000 times. In other words, the energy involved in only 1 hour of sunlight falling on our planet equals the total amount of energy used by the whole world population annually. The nowadays global energy demand is however mainly fulfilled by burning fossil fuels, leading to several problems and threats such as declining reserves, political instability and gaseous emission causing global environmental changes. An eminent example of utilizing sunlight is illustrated by photosynthesis. This process is utilized in plants and green algae to convert CO_2 and H_2O into carbohydrates. Photosynthesis leads to the production of more than 100 billion tons of dry mass globally per year, equivalent to a mean rate of energy storage of 100 TW.[1]

The first crucial step in photosynthesis involves the capture of solar light. To absorb sunlight efficiently, photosynthetic organisms are equipped with light-harvesting systems. These light-harvesting systems are in general based on chlorophyll or bacteriochlorophyll molecules embedded in a protein matrix. The chromophore molecules absorb the incident sunlight, while the presence of proteins is essential for the specific three-dimensional structure of the light-harvesting complex. An exception to protein-chromophore complexes is the chlorosome; i.e. the light-harvesting complex of green sulfur bacteria. In contrast to the above complexes, the three-dimensional structure of a chlorosome is solely based on chromophore-chromophore interactions as described in more detail in section 3.1. Absorption of an incident photon results in the promotion of an electron from the ground state to a higher energetic state. Relaxation of the excited state leads to the formation of a strongly bound neutral electron-hole pair, also referred to as an exciton. Excitons are transported by diffusion through one or more light-harvesting complexes towards a reaction center, where exciton dissociation into a positive and negative charge carrier pair takes place. The charged intermediates formed are used to produce highly energetic compounds; e.g. adenosine triphosphate (ATP), which drive the metabolism of the photosynthetic organism.[2-9]

Natural light-harvesting complexes are found in various molecular configurations. This configuration affects the energy transfer dynamics between adjacent chromophore molecules. The impact of the configuration is illustrated by the two different values for the energy transfer rate (k_{ET}) observed for different substructures of the bacterial light-

harvesting complex II (LHII) (see Figure 1.1). The LHII complex is based on two rings of protein subunits both enclosing bacteriochlorophyll (BChl) molecules, as depicted in Figure 1.1. One ring is based on 16 or 18 BChl molecules with the molecular plane oriented parallel to the central axis.[2] Energy transfer between two neighboring BChl molecules within this ring occurs on a time scale of 100-300 fs.[10,11] The other ring consists of 8 or 9 BChl molecules with all molecular planes aligned perpendicular to the central axis.[6,12] Energy transfer within this ring occurs slower with typical time scales ranging from 0.5 - 1 ps.[2] The clear difference in energy transfer dynamics between these two rings illustrates the influence of the intermolecular distance and orientation on the actual energy transfer dynamics.

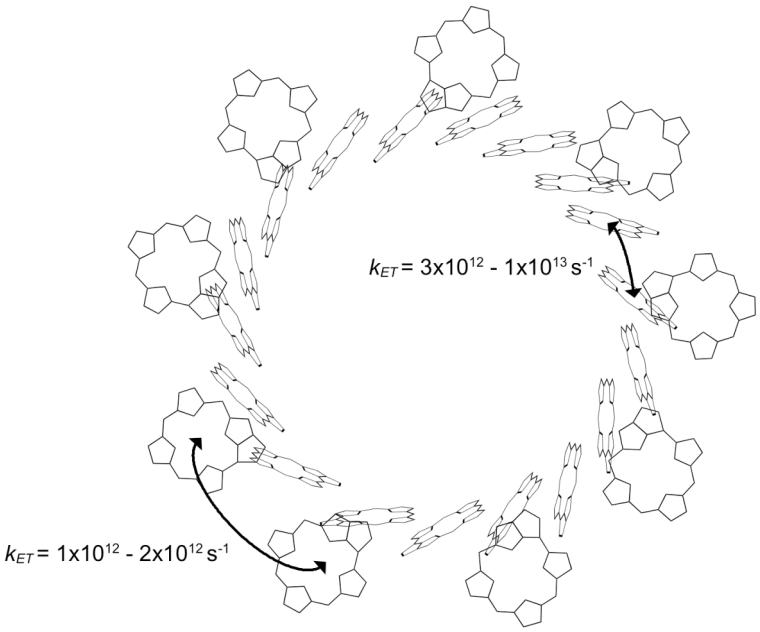

Figure 1.1. Chromophore arrangement in LHII of the purple bacterium *Rhodopseudomonas acidophila*.[6] The energy transfer rate depends on the relative orientation of the chromophores.

The concept of a well-organized light-harvesting structure capable of light absorption and energy migration, combined with a reaction center where exciton dissociation occurs, could be applied in a solar cell. Such a cell could be realized by applying a light absorbing chromophore (dye) layer on top of an electron-accepting material such as a transparent wide bandgap n-type semiconductor (see Figure 1.2A). Exposure to sunlight leads to the formation of excitons in the dye layer. Excitons that reach the interface with the electron-accepting semiconductor can undergo dissociation into free charge carriers by electron injection into the conduction band of the semiconductor.[13] In this concept the

organic dye layer has the combined function of light absorption and electron donor. This type of cell is commonly denoted as a dye-sensitized solar cell (DSSC). The in general short distance an exciton is able to diffuse,[14-16] originating from either a poor exciton diffusion coefficient or a short exciton lifetime, has led to the development of the Grätzel-cell (see Figure 1.2B). This cell is based on a three-dimensional continuous network of semiconductor nanoparticles coated with a monolayer of dye molecules.[17] In such cell the prerequisite of an efficient energy transfer pathway through the dye layer towards the interface with the electron-accepting semiconductor is avoided. However, a drawback of a nanostructured network involves the more elaborate cell design required to compensate for the complicated charge transport. The efficiently functioning photosynthetic light-harvesting complexes, on the other hand, demonstrate that efficient energy transfer over long distances can be realized by optimizing the relative orientation of the molecules. This offers promising possibilities for the realization of solar cells based on a light-absorbing dye and an electron-accepting material in a bilayer configuration, which is favorable for charge transport.

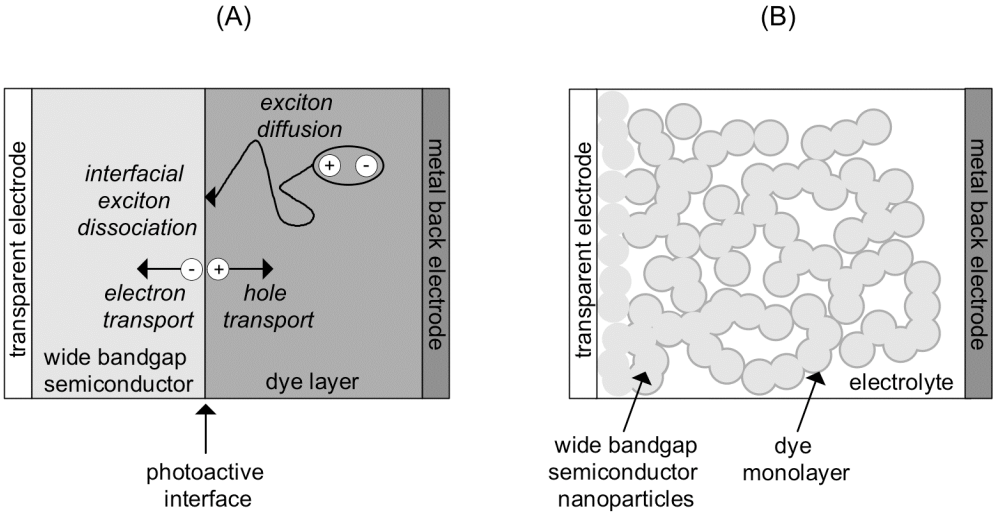

Figure 1.2. A dye-sensitized solar cell (DSSC) based on a wide bandgap semiconductor and chromophore in a bilayer (A) and a nanostructured configuration (B).

This review focuses on the impact of the molecular organization of natural and artificial chromophore molecules on the dynamics of energy transfer. Artificial molecules considered involve porphyrin and phthalocyanine derivatives. Both natural BChl molecules (Figure 1.5A) and porphyrin derivatives (Table 1.1) are based on four pyrrole rings cyclically interconnected at the alpha position by a *meso* carbon atom. In case of

phthalocyanine derivatives the *meso* carbon atoms are replaced by nitrogen atoms (see Table 1.4). These materials exhibits a characteristic S_0-S_2 optical transition, denoted as the Soret absorption band, and S_0-S_1 transitions referred to as the Q-bands.[18] The magnitude of the transition dipole moment of the S_0-S_1 transition is relatively small for porphyrin derivatives and increases on going to BChl and phthalocyanine derivatives.[19-23]

The theoretical background for the relationship between the molecular organization and the energy transfer dynamics is presented in section 1.2. Section 1.3 summarizes experimental findings on the energy transfer dynamics between BChl molecules in the natural chlorosome (1.3.1), porphyrin derivatives (1.3.2) and phthalocyanine derivatives (1.3.3) and relates the observed energy transfer rates to the organization of the chromophore molecules.

1.2. Theory

1.2.1. The incoherent energy transfer rate for hopping motion of excitons

Energy transfer is in general considered to occur via a through-space mechanism. In order to describe the intermolecular energy transfer rate in an array of chromophore molecules, two limiting cases for energy transfer can be distinguished.[24] Parameters that determine these extremes include the rate involved in adapting thermal equilibrium after an electronic transition took place (k_{relax}) and the actual energy transfer rate (k_{ET}) from an initial energy donor site (D^*) towards a final acceptor site (A), see Figure 1.3. In case $k_{relax} << k_{ET}$, an exciton will move much faster between molecular sites as compared to relaxation of the nuclear configuration, leading to delocalization of the excitation energy over several chromophore molecules. This type of motion is commonly denoted as coherent transport. In the other limiting case; i.e. $k_{relax} >> k_{ET}$, relaxation occurs prior to energy transfer, resulting in localization of the excitation energy on one chromophore molecule. In this regime, motion of excitons can be considered as an incoherent diffusive hopping process between single molecules. Only the incoherent regime will be considered below.

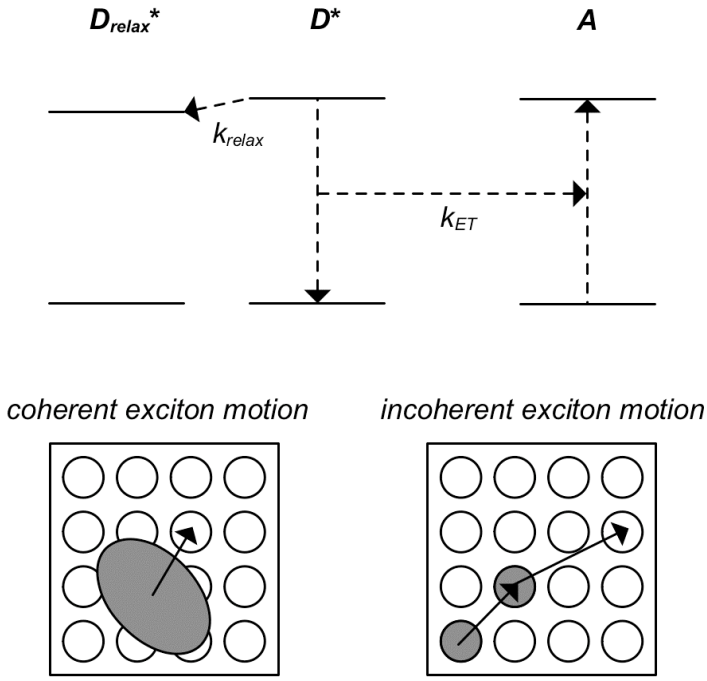

Figure 1.3. Energy transfer between donor *D* and acceptor *A* occurring with rate k_{ET} and intramolecular relaxation to thermal equilibrium with rate k_{relax}. Depending on the ratio of these two parameters, an exciton could either be delocalized over several chromophore molecules or be localized on a single molecule.

The average intermolecular hopping rate for singlet excitons can be derived from Fermi's golden rule:[24]

$$k_{ET} = \frac{2\pi}{\hbar} \sum_{\{m,n\}} \sum_{\{s,t\}} f\left(E_{D*}^{m}\right) f\left(E_{A}^{n}\right) \left| \left\langle \Psi_{D*}^{m} \Psi_{A}^{n} \middle| J_{COUL} \middle| \Psi_{D}^{s} \Psi_{A*}^{t} \right\rangle \right|^{2} \delta\left(E_{D*}^{m} + E_{A}^{n} - E_{D}^{s} - E_{A*}^{t}\right) \qquad (1.1)$$

The weight factors $f\left(E_{D*}^{m}\right)$ and $f\left(E_{A}^{n}\right)$ describe the population of the vibrational states associated to the donor excited state and acceptor ground state. The wave function of the initial quantum state *m* of the donor in the excited state is denoted by Ψ_{D*}^{m}. The other wave functions are denoted analogously. The operator J_{COUL} describes the Coulombic interaction between the electron on the donor and the electron on the acceptor. The Dirac-delta function $\delta\left(E_{D*}^{m} + E_{A}^{n} - E_{D}^{s} - E_{A*}^{t}\right)$ ensures energy conservation. The double sum runs over the initial vibrational quantum states *m* of the donor and *n* of the acceptor and their final states *s* and *t*. According to the Born-Oppenheimer approximation, a total wave function is the product of an electronic wave function and a vibrational wave function. In the Condon approximation; i.e. the electronic part of the coupling factor does not depend

on the nuclear arrangement, the matrix element of the Coulomb operator reduces to an excitonic coupling weighted by the Franck-Condon overlaps between the initial and final vibrational states:

$$\left\langle \Psi_{D*}^{m}\Psi_{A}^{n}\left|J_{COUL}\right|\Psi_{D}^{s}\Psi_{A*}^{t}\right\rangle = \left\langle \psi_{D*}\left(\vec{r}_1\right)\psi_{A}\left(\vec{r}_2\right)\left|J_{COUL}\right|\psi_{D}\left(\vec{r}_1\right)\psi_{A*}\left(\vec{r}_2\right)\right\rangle \left\langle \chi_{D*}^{m}\left|\chi_{D}^{s}\right.\right\rangle \left\langle \chi_{A}^{n}\left|\chi_{A*}^{t}\right.\right\rangle \tag{1.2}$$

The factor χ_{D*}^{m} represents the vibrational wave function of the donor in the excited state, whereas $\psi_{D*}\left(\vec{r}_1\right)$ denotes the electronic wave function with $\vec{r}_1$ the position vector of the excited electron. The other wave functions are defined analogously.

The energy transfer rate can be expressed in terms of the donor emission and the acceptor absorption spectra. Such expression can be obtained by recasting the Dirac-delta function in equation 1.1 into two parts:

$$\delta\left(E_{D*}^{m}+E_{A}^{n}-E_{D}^{s}-E_{A*}^{t}\right)=\int\delta\left(E_{D*}^{m}-E_{D}^{s}-E\right)\delta\left(E_{A}^{n}-E_{A*}^{t}+E\right)dE \tag{1.3}$$

Introduction of the donor emission line shape $F_D(E)$ and acceptor absorption line shape $A_A(E)$, given by

$$F_D(E)=\sum_{\{m,s\}} f\left(E_{D*}^{m}\right)\left\langle \chi_{D*}^{m}\left|\chi_{D}^{s}\right.\right\rangle^2 \delta\left(E_{D*}^{m}-E_{D}^{s}-E\right) \tag{1.4}$$

and

$$A_A(E)=\sum_{\{n,t\}} f\left(E_{A}^{n}\right)\left\langle \chi_{A}^{n}\left|\chi_{A*}^{t}\right.\right\rangle^2 \delta\left(E_{A}^{n}-E_{A*}^{t}+E\right) \tag{1.5}$$

leads to the following expression for the energy transfer rate:[24, 25]

$$k_{ET}=\frac{2\pi}{\hbar}\left|V_{DA}\right|^2\int F_D(E)A_A(E)dE \tag{1.6}$$

The factor V_{DA} denotes the excitonic coupling between donor and acceptor and is given by:

$$V_{DA}=\left\langle \psi_{D*}\left(\vec{r}_1\right)\psi_{A}\left(\vec{r}_2\right)\left|J_{COUL}\right|\psi_{D}\left(\vec{r}_1\right)\psi_{A*}\left(\vec{r}_2\right)\right\rangle \tag{1.7}$$

The integral in equation 1.6 can be considered as the overlap between the normalized donor emission and acceptor absorption, as schematically depicted in Figure 1.4. The donor emission and acceptor absorption line shapes are defined as

$$F_D(E) = \frac{E^{-3} I_D(E)}{\int E^{-3} I_D(E) dE} \tag{1.8}$$

$$A_A(E) = \frac{E^{-1} \alpha_A(E)}{\int E^{-1} \alpha_A(E) dE} \tag{1.9}$$

with $I_D(E)$ the donor fluorescence spectrum and $\alpha_A(E)$ the optical absorption spectrum of the acceptor.[24-26] It should be noted that the limits of integration are determined by the optical transitions relevant for energy transfer.

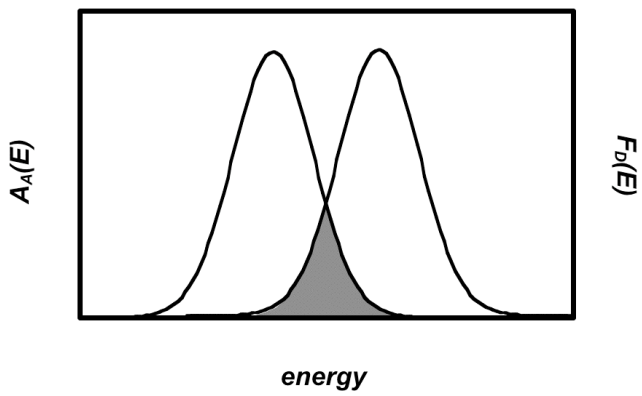

Figure 1.4. Spectral overlap between the donor emission and the acceptor absorption line shapes.

1.2.2. The Förster model

The Förster model for energy transfer[27, 28] is based on a through-space energy transfer process and is only valid for a donor-acceptor distance that exceeds the spatial extent of the exciton state. This energy transfer mechanism does not require spatial overlap of orbitals of the donor and acceptor. Förster energy transfer can be considered as the simultaneous emission of the excitation energy by the donor and absorption by the acceptor via the exchange of a virtual photon. Note, that the donor and acceptor can be identical molecules. The Förster model is based on a point-dipole approximation of the excitonic coupling.[25,29] According to this approximation, the excitonic coupling in equation 1.7 is given by

$$|V_{DA}| = \frac{|\kappa|}{4\pi\varepsilon_0} \frac{|\vec{\mu}_D||\vec{\mu}_A|}{R_{DA}^3} \tag{1.10}$$

with $\left|\vec{\mu}_D\right|$ and $\left|\vec{\mu}_A\right|$ denoting the absolute values of the transition dipole moments of the donor and acceptor involved and R_{DA} the center-to-center distance between the donor and acceptor. The orientation factor κ is defined as

$$\kappa = \vec{e}_D \cdot \vec{e}_A - 3\left(\vec{e}_D \cdot \vec{r}_{DA}\right)\left(\vec{e}_A \cdot \vec{r}_{DA}\right) \tag{1.11}$$

where $\vec{e}_D$ and $\vec{e}_A$ represent the unit vectors along the transition dipole moments of donor and acceptor and $\vec{r}_{DA}$ is the unit vector along the direction connecting the centers of donor and acceptor. The value of $|\kappa|$ is always in the interval [0-2]. Combination of equations 1.6 and 1.10 gives the following expression for the Förster energy transfer rate:

$$k_{ET} = \frac{|\kappa|^2}{8\hbar\pi\varepsilon_0^2}\frac{\left|\vec{\mu}_D\right|^2\left|\vec{\mu}_A\right|^2}{R_{DA}^6}\int F_D(E)A_A(E)dE \tag{1.12}$$

The value for the exciton diffusion coefficient (D_E) is given by:

$$D_E = k_{ET}R_{DA}^2 \tag{1.13}$$

The average distance an exciton is able to travel by diffusion before decay to the ground state occurs is represented by the exciton root-mean-square displacement (Λ_D). In case of one-dimensional exciton diffusion, Λ_D is defined by:

$$\Lambda_D = \sqrt{2D_E\tau_E} \tag{1.14}$$

The extent of exciton diffusion is usually characterized by the exciton diffusion length (Λ_E):

$$\Lambda_E = \sqrt{D_E\tau_E} \tag{1.15}$$

Note, that observed values for exciton diffusion lengths might be affected by structural defects. Combination of equations 1.12, 1.13 and 1.15 results in:

$$\Lambda_E = \frac{|\kappa|\left|\vec{\mu}_D\right|\left|\vec{\mu}_A\right|}{\varepsilon_0 R_{DA}^2}\sqrt{\frac{\tau_E}{8\hbar\pi}}\sqrt{\int F_D(E)A_A(E)dE} \tag{1.16}$$

Equation 1.16 shows that energy transfer is facilitated by a large orientation factor, exciton lifetime and spectral overlap, while the distance between donor and acceptor must be kept as short as possible.

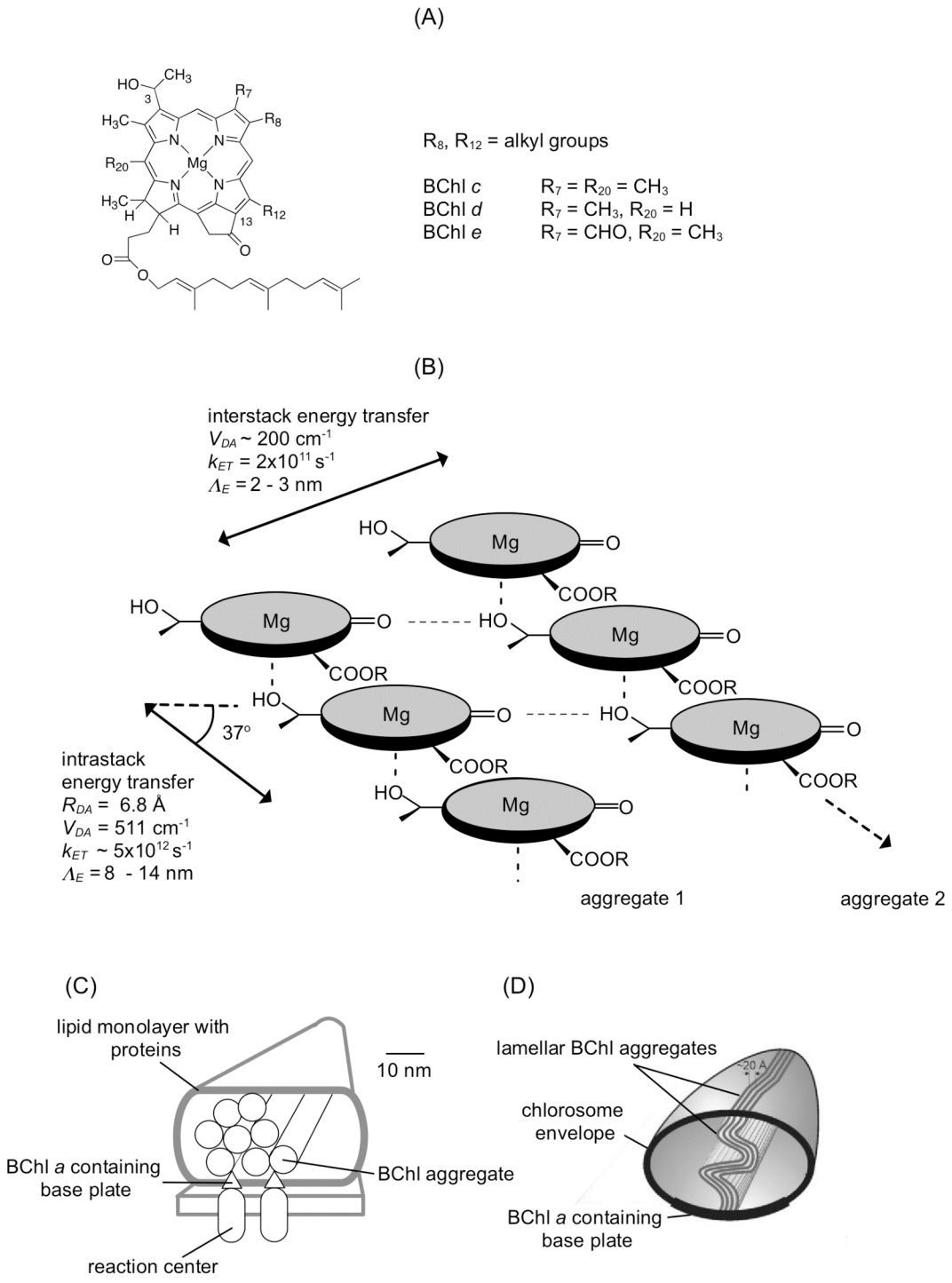

Figure 1.5. Chemical structures of bacteriochlorophyll *c*, *d* and *e* (A) and a model for the self-assembly of BChl molecules together with the singlet energy transfer dynamics between and within self-assembled stacks (B). Figures C and D show two different models proposed for the supramolecular nanostructure of self-assembled BChl molecules inside the chlorosome: rod-shaped components (C) and a lamellar organization of the aggregates (D). Figure D is taken from ref. 30.

1.3. Structure and energy transfer dynamics in linear light-harvesting systems

1.3.1. The chlorosome in green sulfur bacteria

From all known photosynthetic organisms, the green sulfur bacteria are able to survive under the lowest illumination conditions. They are even able to live at depths of 100 m in the Black see, where the light intensity is nearly 10^6 times lower than near the surface.[31,32] The fact that these bacteria are able to survive under such extremely low illumination conditions is in part attributed to a highly efficient functioning antenna system.[30, 32-34] Green sulfur bacteria are equipped with a unique photosynthetic antenna complex, the chlorosome, an ellipsoidal shaped organelle with a typical size of 15 nm × 30 nm × 100 nm.[35] A chlorosome is based on self-assembled BChl *c, d* and *e* molecules (see Figure 1.5A for the chemical structure) organized by BChl-BChl rather than by BChl-protein interactions. Such interaction is in sharp contrast to other photosynthetic antenna complexes where the chromophore molecules are embedded in a protein matrix.

Self-assembly of the chlorosomal BChl molecules is induced by the formation of a coordinative bond between the central Mg atom and the 3-hydroxy group of an adjacent molecule, as shown in Figure 1.5B. Additional interactions involve the hydrogen bonding between the activated 3-hydroxy group and a 13-keto group of a third BChl molecule and π-π interactions between adjacent BChl macrocycles.[36] The supramolecular nanostructure of self-assembled BChl molecules inside a chlorosome is still under debate. Staehelin et al. have suggested the presence of rod-shaped components with a diameter of about 10 nm as depicted in Figure 1.5C.[35] Alternatively, Psencik et al. have recently proposed a lamellar organization of the self-assembled BChl aggregates (stacks), as shown in Figure 1.5D.[30] In each of the proposed structures, the chlorosomal BChl aggregates are connected via the BChl *a* containing base plate to the reaction center and surrounded by a lipid monolayer to form the photosynthetic apparatus.[2] Whether apart from intrastack energy transfer also interstack energy transfer is required to transport excitons via the base plate towards the reaction center depends on the actual supramolecular nanostructure of BChl aggregates within a chlorosome.

The excitonic coupling V_{DA} between adjacent BChl molecules within a BChl aggregate has been calculated on basis of the point-dipole approximation (see section 1.2.2) to be as high as 511 cm^{-1}.[34] The excitonic coupling between molecules situated in adjacent self-assembled aggregates amounts to 200 cm^{-1}.[34] Energy transfer between

adjacent self-assembled BChl aggregates takes place on a typical time scale of 5 ps. Within one aggregate energy transfer occurs extremely fast, typically on a time scale of a few hundreds of femtoseconds, corresponding to an energy transfer rate in the order of 5×10^{12} s^{-1}.[34, 37, 38] Since this value is comparable to those observed for the circular systems described in section 1, the value for k_{ET} within chlorosomal BChl stacks most likely does not solely account for the ability of chlorosome containing bacteria to live under such extreme conditions.

The energy transfer rate of 5×10^{12} s^{-1} between BChl molecules separated by 6.8 Å[39] corresponds to an exciton diffusion coefficient in the order of 2×10^{-6} m^2/s, see equation 1.13. During its lifetime of 30 ps - 80 ps[34] an exciton can on average make 150 - 400 hops before decay to the ground state occurs. The value for Λ_E follows from equation 1.15 to be in the order of 8 nm - 14 nm. The one-dimensional exciton root-means-square displacement Λ_D within one BChl aggregate follows from equation 1.14 to amount to 12 nm - 19 nm. The fast energy transfer occurring within a BChl aggregate induced by molecular self-assembly has inspired many researchers synthesizing artificial close mimics of self-assembling BChls, characterizing their structural properties and studying the energy transfer dynamics in these complexes. In particular the groups of Tamiaki in Japan and Balaban and Würthner in Germany have followed a biomimetic approach for the syntheses of artificial chromophores self-assembling in a similar way as the chlorosomal BChls.[40-49] Sections 3.2 and 3.3 give an overview of studies on the impact of the molecular organization on energy transfer dynamics in various self-assembling mimics of natural BChls.

1.3.2. Porphyrin derivatives

1.3.2.1. Non-covalently organized porphyrin derivatives

In this section exciton diffusion in the materials presented in Table 1.1 is discussed. Table 1.2 provides the structural information and parameters relevant for energy transfer for these materials. The earliest reports on the synthesis, morphological characterization and exciton diffusion in non-covalently self-organizing porphyrin derivatives date from almost 20 years ago. Gregg et al.[50,51] have synthesized and characterized several porphyrin derivatives, of which zinc octakis (β-octyloxyethyl)porphyrin (ZnOOEP) (see

Table 1.1 for the chemical structure) has been studied most intensively. This porphyrin derivative exhibits a highly ordered columnar stacking in the solid crystalline phase and a slightly less ordered columnar stacking in the liquid-crystalline phase.[50,51] From phase-dependent photovoltaic features of a device based on ZnOOEP, a decrease in Λ_E on going from the solid to the liquid-crystalline phase has been found.[52]

Table 1.1. Chemical structures of the porphyrin derivatives discussed in section 1.3.2.1.

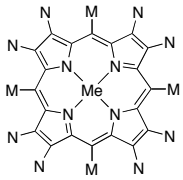

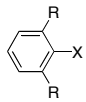

Acronym	Me	M	N	X	R
ZnOOEP	Zn	H	$(CH_2)_2O(CH_2)_7CH_3$		
H_2TPP	H_2		H	H	H
H_2TEPP	H_2		H	C_2H_5	H
H_2TnBuPP	H_2		H	n-C_4H_9	H
H_2TOPP	H_2		H	n-C_8H_{17}	H
ZnTOPP	Zn		H	n-C_8H_{17}	H
ZnBuP	Zn		H	H	$C(CH_3)_3$
ZnOP	Zn		H	H	CH_2OCH_3

Hydrophobic interactions between aliphatic subunits, introduced by alkyl substituents at the *para* position (*X* in Table 1.1) of the phenyl groups of tetraphenylporphyrin derivatives, have been widely used to introduce liquid-crystalline behavior. In this way the molecular organization and consequently the energy transfer dynamics can be affected. For singlet excitons Λ_E in layers of unsubstituted *meso*-tetraphenylporphyrin (H_2TPP, see Table 1.1 for the chemical structure) has been determined using the time-resolved microwave conductivity (TRMC) technique[16,53] to amount to only 0.7 nm.[54] This low value has been attributed to the presence of exciton trapping face-to-face dimers or larger H-aggregate like structures embedded within disordered H_2TPP monomer domains. Formation of H-aggregates leads to a forbidden transition between the lowest excited state and the ground state, which prevents fluorescence from the lowest excited state. According to the Förster theory the energy transfer rate then becomes zero, so that H-aggregates act as exciton traps. This negatively affects the exciton diffusion length. It was found that introduction of ethyl substituents reduces the extent of H-aggregation, leading to an enhancement of Λ_E to 7.5 nm.[54]

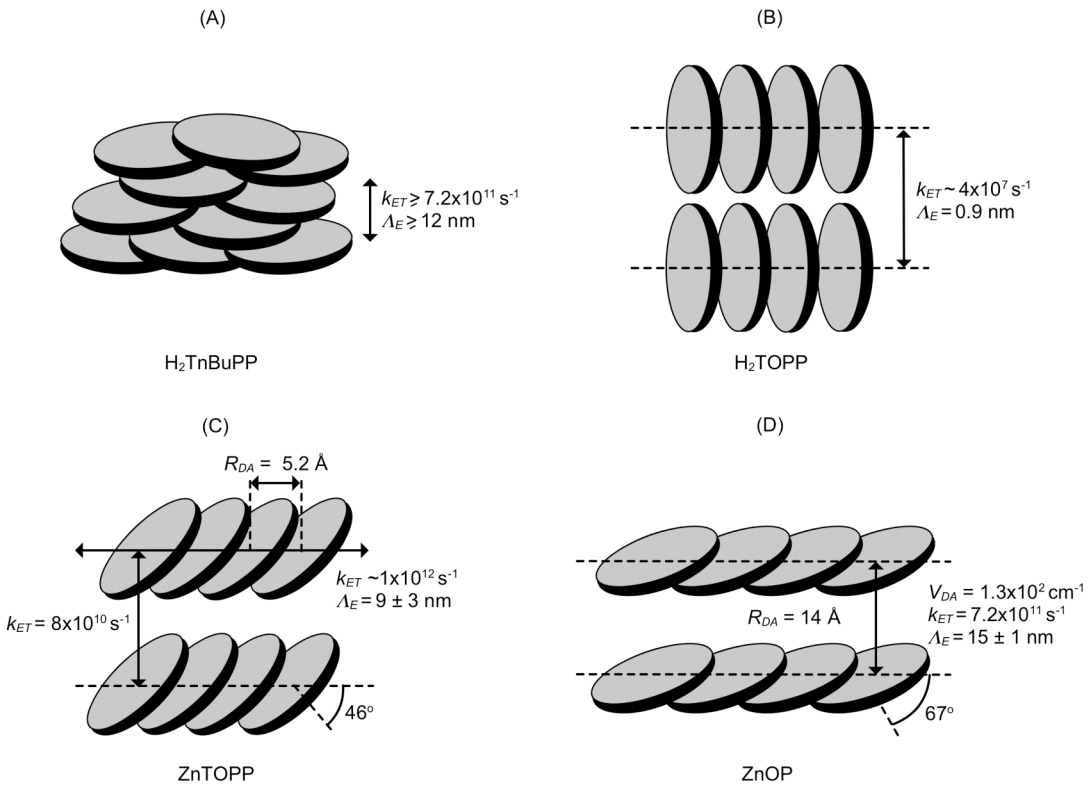

Figure 1.6. Molecular organization and singlet energy transfer parameter values for H_2TnBuPP, H_2TOPP, ZnTOPP and ZnOP layers.

The presence of n-butyl substituents in H_2TnBuPP molecules results in the spontaneous formation of a nematically structured layer as shown schematically in Figure 1.6A on spincoating from $CHCl_3$. The molecules in this layer are aligned homeotropically with respect to the exciton dissociating interface with TiO_2.[55] H_2TnBuPP exhibits similar absorption and emission spectra as H_2TEPP.[54,55] However, the mutual parallel arrangement of the H_2TnBuPP molecules in the homeotropic nematic layer results in a higher value for the orientation factor $|\kappa|$ as compared to the disordered H_2TEPP layer[56, 57], which enhances k_{ET} (see equation 1.12). As a result, the value for Λ_E in the H_2TnBuPP layer in the direction perpendicular to the interface with TiO_2 is reaching a value exceeding 12 nm, as deduced from TRMC experiments.[55]

Free-base homologues with n-hexyl or longer n-alkyl substituents have been observed to show a liquid-crystalline behavior.[58] The singlet exciton lifetime generally increases with the length of the n-alkyl side chain[54, 55, 59, 60], which in turn enhances the intersystem-crossing yield to triplet states. Singlet exciton diffusion in disordered H_2TOPP layers has

been observed to hardly occur. However, for triplet excitons Λ_E amounts to 9.6 nm.[61] Heating the disordered H_2TOPP layer above the crystalline to liquid-crystalline transition temperature and cooling down has been suggested to result in the formation of columnar stacks, as shown in Figure 1.6B, aligned with their long axis parallel to the TiO_2 substrate. No triplet exciton diffusion between these stacks has been observed. The singlet exciton diffusion length between H_2TOPP stacks, in the direction perpendicular to the TiO_2 substrate, has been determined to be only 0.9 nm.[61]

The zinc analogue of H_2TOPP; i.e. ZnTOPP, has been reported to form tilted columnar stacks as depicted in Figure 1.6C. The value of Λ_E within a stack has been deduced from fluorescence decay experiments in the presence of intentionally added exciton quenchers to be as long as 9±3 nm, corresponding to a singlet intrastack energy transfer rate of 10^{12} s^{-1}.[62] In contrast, interstack exciton diffusion has been found to be considerably less efficient with an energy transfer rate that amounts to only 8×10^{10} s^{-1}.[15, 62-64] The tendency of molecular stacks to align parallel to a substrate[61, 65] is therefore expected to result in a short Λ_E in the direction towards an exciton dissociating interface.

Apart from self-organization by the utilization of hydrophobic interactions, molecular organization can also be realized by the formation of coordinative bonds between electron-donating and -accepting groups, analogous to the structure of a chlorosomal BChl aggregate shown in Figure 1.5B. Numerous reports deal with the synthesis and structural characterization of self-assembling mimics of BChl molecules such as porphyrin and chlorin derivatives.[40,42, 66-70] Although such mimics have been shown to be applicable for the photosensitization of (nanostructured) wide bandgap semiconductors[71, 72], so far no efficient energy transfer through a stack in the direction towards an exciton dissociating interface has been realized. This is most likely due to a (partial) coverage of the electron-accepting semiconductor surface by non-assembled monomers. On energetic grounds energy transfer from an aggregate towards a monomer is likely to be inefficient. In addition, the alignment of stacks that are in direct contact with the semiconductor is most likely unfavorable for electron injection into the semiconductor. In case stacks are aligned parallel to a semiconductor surface, the presence of bulky substituents leads to a large distance between the porphyrin core and the semiconductor, which might in turn decrease the electron injection rate.[73] Realizing a proper contact between stacks and the semiconductor surface is a promising way towards application of such mimics in molecular devices.

Table 1.2. Structural properties and energy transfer dynamics of the porphyrin derivatives discussed in section 1.3.2.1.

Acronym	Structure	R_{DA} (Å)	k_{ET} (s^{-1})	D_E (m^2/s)	τ_E (s)	Λ_E (nm)	Refs.
H_2TPP	disordered with H-aggregates			2×10^{-9}	2.6×10^{-10}	0.7	54
H_2TEPP	disordered			7×10^{-8}	8.0×10^{-10}	7.5	54
$H_2TnBuPP$	Figure 1.6A	4.5	$\geq7.1\times10^{11}$	$\geq1.4\times10^{-7}$	1.0×10^{-9}	≥12	55
H_2TOPP	disordered					9*	61
	Figure 1.6B	~20	$\sim4\times10^{7}$	1.5×10^{-10}	6.0×10^{-9}	0.9	61
ZnTOPP	Figure 1.6C	5.0	$\sim1\times10^{12}$	2.5×10^{-7}		9±3	15, 62-64
ZnBuP	disordered	15	4×10^{10}	1×10^{-7}	7.4×10^{-11}	3±1	74
ZnOP	Figure 1.6D	14	7.2×10^{11}	1.4×10^{-6}	1.6×10^{-10}	15±1	74

* triplet excitons

Recently it has been demonstrated that a zinc porphyrin derivative denoted as ZnOP, containing electron-donating methoxymethyl substituents (see Table 1.1 for the chemical structure) self-organizes into large ordered domains by the formation of coordinative bonds between the central Zn atom and the methoxymethyl substituents.[75] Remarkably, energy transfer between self-assembled ZnOP stacks occurs rather efficient. The exciton diffusion length found from TRMC experiments is as long as 15±1 nm. The large value for Λ_E might originate from the strong tilt of the molecules as depicted in Figure 1.6D, leading to a relatively short interstack distance and consequently to a strong interstack excitonic coupling as follows from equation 1.10. The value for Λ_E in non-assembling disordered ZnBuP (see Table 1.1 for the chemical structure) is found to equal only 3±1 nm. The longer Λ_E observed for ZnOP mainly originates from a stronger excitonic coupling V_{DA}, which amounts to 130 cm^{-1} between ZnOP molecules in adjacent stacks and only 36 cm^{-1} between disordered ZnBuP molecules.[74] The strong excitonic coupling and large Λ_E found for ZnOP as compared to ZnBuP illustrate the effect of molecular self-assembly on the energy transfer dynamics.[74]

Table 1.3. Intramolecular energy transfer rate between identical (k_{ET}) or non-isoenergetic ($k_{ET,d}$) porphyrin subunits (*Pmon*) linked at the *meso* positions by selected spacers.

Spacer	R_{DA} (Å)	k_{ET} (s^{-1})	$k_{ET,D}$ (s^{-1})	Refs.
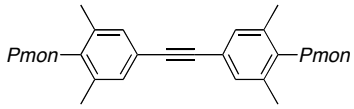			1×10^{10}	76
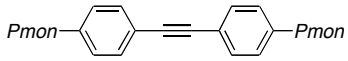	19.6	2×10^{10}	4×10^{10}	76, 77
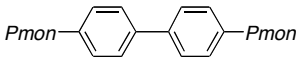	17.0		9×10^{10}	78
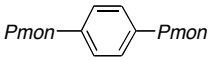	12.7	1×10^{11}	3×10^{11}	77, 79
Pmon−*Pmon*	8.4		2×10^{12}	78

1.3.2.2. Covalently linked porphyrin derivatives

Intramolecular energy transfer dynamics in porphyrin-based oligomers depend on the nature of the individual porphyrin subunits and the spacer linking the porphyrin monomers at the *meso* positions (position *M* of the porphyrin molecular structure shown in Table 1.1). The energy transfer rate between non-isoenergetic subunits ($k_{ET,d}$), e.g. from a zinc porphyrin to a free-base porphyrin, is in general in the same order of magnitude as the value for identical porphyrin subunits (k_{ET}).[76,77,79] Table 1.3 summarizes literature values for the intramolecular energy transfer rates between porphyrin subunits linked by spacers as indicated. Energy transfer is expected to occur both via the Förster and a through-bond[80] mechanism, since the observed values are too high to be attributed solely to a Förster mechanism.[76] The degree to which extent both mechanisms contribute to the intramolecular energy transfer is expected to depend on the nature of the spacer. Addition of groups that hinder the linker and the porphyrin subunits to adopt a geometry tending towards coplanarity slows down the energy transfer rate. This is explained by a reduced through-bond excitonic coupling between the porphyrin subunits on decreasing the coplanarity.[76] Replacing a diphenylethyne spacer by a diphenyl spacer enhances k_{ET}

significantly. This effect proceeds for a p-phenylene spacer and is pronounced for a single bond spacer. In case of the latter an energy transfer rate as high as 2×10^{12} s^{-1} has been found.[78] The enhancement of k_{ET} is attributed to an increase in excitonic coupling between the porphyrin subunits across the linker on reducing the length of the linking spacer.[77,78]

1.3.3. Phthalocyanine derivatives

The essential difference in molecular structure between the porphyrins discussed in previous section and phthalocyanines involves the nature of the bridge connecting the four pyrrole rings. In case of the first, the pyrrole rings are connected via carbon atoms, while phthalocyanines are based on four pyrrole rings connected via nitrogen atoms (see Table 1.4). This difference leads to more intense Q-bands in case of phthalocyanine derivatives, originating from a factor of two larger transition dipole moments.[21,22] A number of publications deal with the determination of Λ_E from the photovoltaic response of photovoltaic devices based on vacuum evaporated phthalocyanine films on top of an electron-accepting layer. The value for Λ_E in vacuum evaporated zinc phthalocyanine (ZnPc, see Table 1.4 for the chemical structure) has been reported to equal 30±10 nm[15], while for vacuum evaporated copper phthalocyanine (CuPc) layers Λ_E values range from 10±3 nm[81] to 68±20 nm[82].

Free-base and metal phthalocyanine derivatives having aliphatic substituents *R* (see Table 1.4 for the chemical structures) are well-known to possess liquid-crystalline behavior.[83-86] In the solid crystalline phase, molecules generally tend to form stacks in which the molecular planes are tilted with respect to the columnar axis as depicted in Figure 1.7A. The tilt angle might reduce to zero on going from the solid crystalline phase towards the liquid-crystalline phase, depending on the nature of the substituents.[84] In case a tilt is absent in the liquid-crystalline phase, phthalocyanine molecules typically arrange in a pattern of hexagonally packed columns, as shown in Figure 1.7C.[84, 85, 87, 88] Because of the steric hindrance between the aliphatic substituents of adjacent molecules, a staggered conformation of molecules with a 45° twist angle around the central columnar axis is the most likely intracolumnar molecular arrangement.[84]

Table 1.4. Chemical structures of the phthalocyanine derivatives discussed in section 1.3.3.

Acronym	Me	R
ZnPc	Zn	H
CuPc	Cu	H
$H_2(CH_2OC_{12})_8Pc$	H_2	$CH_2O(CH_2)_{11}CH_3$
$H_2(CH_2OC_{18})_8Pc$	H_2	$CH_2O(CH_2)_{17}CH_3$
$Zn(CH_2OC_{12})_8Pc$	Zn	$CH_2O(CH_2)_{11}CH_3$

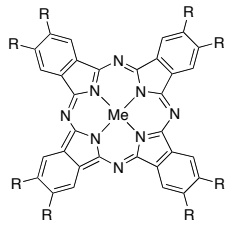

ZnPcIm$_4$-PDI$_4$

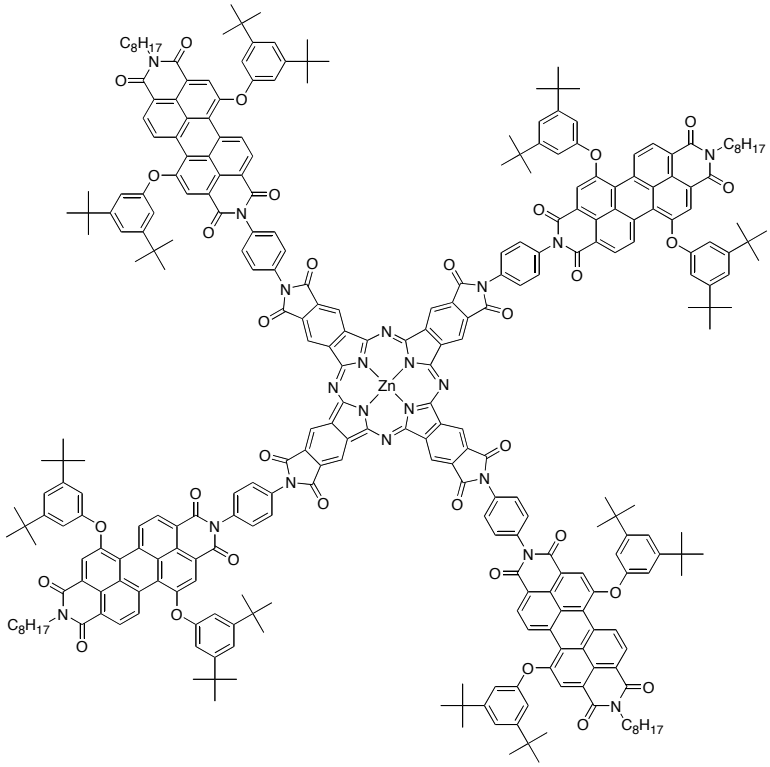

A number of publications involve experimental studies on singlet exciton motion in phthalocyanine derivatives. Blanzat et al.[89] have studied exciton diffusion in $H_2(CH_2OC_{12})_8Pc$ (see Table 1.4 for the chemical structure). In the solid crystalline phase, $H_2(CH_2OC_{12})_8Pc$ molecules form a columnar structure with a tilt angle of 24°, as shown in Figure 1.7A. [89] The intracolumnar center-to-center distance R_{DA} amounts to 4.3 Å.[85] For singlet excitons the intracolumnar Λ_D has been observed to be 10-20 nm,[89] yielding Λ_E = 7-14 nm. Remarkably, the zinc phthalocyanine perylenediimide derivative ZnPcIm$_4$-PDI$_4$ (see Table 1.4 for the chemical structure) has been observed to form a non-tilted

crystalline columnar structure, as shown in Figure 1.7B, with the molecular transition dipole moments most likely aligned parallel to each other. The intracolumnar k_{ET} is as high as 6.25×10^{12} s^{-1}.[90] Combining this with an exciton lifetime of 260 ps[90] and estimating R_{DA} to equal 3.5 Å[84] results in Λ_E = 14 nm.

Table 1.5. Structural properties and energy transfer dynamics of the phthalocyanine derivatives discussed in section 1.3.3.

Acronym	Structure	R_{DA} (Å)	k_{ET} (s^{-1})	D_E (m^2/s)	τ_E (s)	Λ_E (nm)	Refs.
ZnPc						30±10	15
CuPc						10±3	81
						68±20	82
$H_2(CH_2OC_{12})_8Pc$	Figure 1.7A	4.3				7-14	85, 89
$ZnPcIm_4$-PDI_4	Figure 1.7B	3.5	6.25×10^{12}	7.7×10^{-7}	2.6×10^{-10}	14	84, 90
$H_2(CH_2OC_{18})_8Pc$	crystalline	4.5	3×10^{9}	6.2×10^{-10}		45*	91
	liquid-crystalline	4.5	5×10^{9}	1×10^{-9}		47*	91
$Zn(CH_2OC_{12})_8Pc$	crystalline	3.6	7×10^{7}	9×10^{-12}	3×10^{-5}	16*	92
	Figure 1.7C	3.6	7×10^{8}	9.4×10^{-11}	1.1×10^{-6}	10*	92

* triplet excitons

The motion of triplet excitons has also been studied for a variety of phthalocyanine derivatives. As compared to singlet excitons, the energy transfer rate for triplet excitons is several orders of magnitude lower. However the considerably longer lifetime of triplet states yields Λ_E values of several tens of nanometers; i.e. comparable to that for singlet excitons. For two different phthalocyanine derivatives, $H_2(CH_2OC_{18})_8Pc$[45] and $Zn(CH_2OC_{12})_8Pc$[46], the value of D_E for triplet excitons increases on going from the solid crystalline towards the liquid-crystalline phase, which has tentatively been attributed to an improvement of the column continuity.[91,92] Table 1.5 summarizes the structural properties and photophysical parameters for the phthalocyanine derivatives discussed in this section.

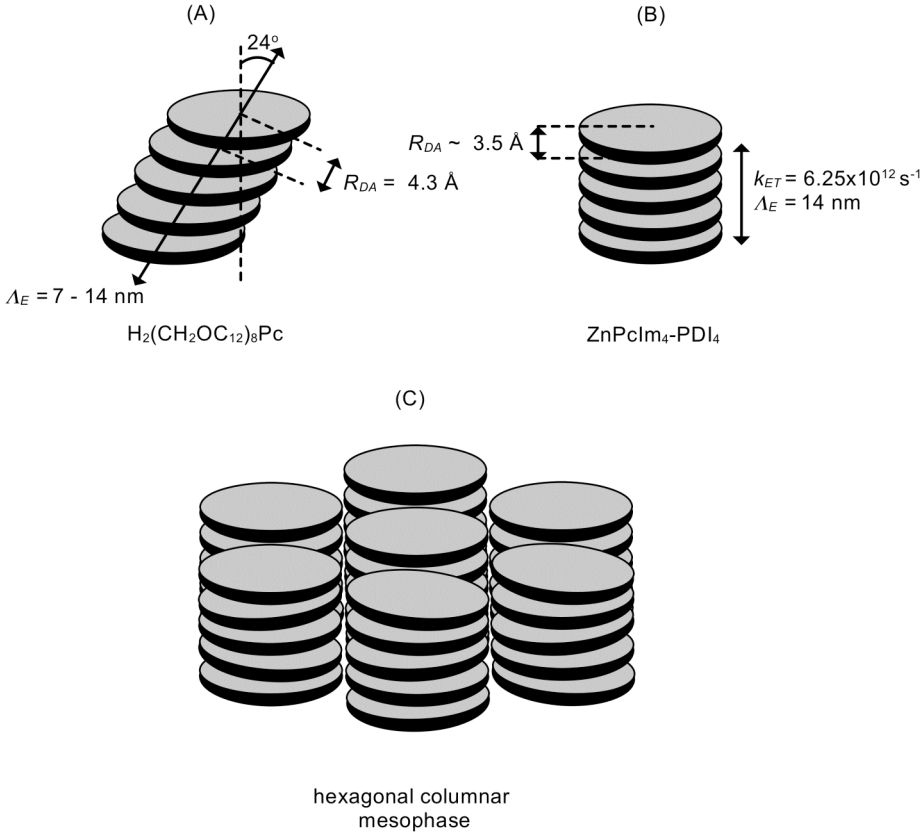

Figure 1.7. Molecular organization and singlet energy transfer parameter values for $H_2(CH_2OC_{12})_8Pc$ (A), $ZnPcIm_4$-PDI_4 (B) and the structure of a hexagonal columnar mesophase (C).

1.4. Aim of this thesis

The aim of this thesis is to provide a fundamental understanding of the influence of the molecular organization of artificial biomimetic chromophore molecules on the energy transfer dynamics. A more comprehensive understanding of this impact shows promising prospects for the realization of longer exciton diffusion lengths. Chromophore molecules involved in this thesis include several porphyrin derivatives with self-organizing features. Before the start of this project, only a few studies on the energy transfer dynamics in porphyrin derivatives have been reported in the literature. However, these publications often lack detailed information about the specific molecular organization and do not allow a quantitative analysis of the impact of the molecular organization on the energy transfer dynamics. The singlet exciton diffusion lengths in porphyrin derivatives realized so far are all below 10 nm and often even in the order of only 1 nm, which is too short to

realize efficient photovoltaic devices of such materials in a bilayer configuration with an n-type semiconductor.

The energy transfer dynamics in various structured porphyrin layers on an electron-accepting semiconductor were studied using the time-resolved microwave conductivity (TRMC) method.[16,53] This technique is based on probing the charge carriers formed on exciton dissociation at the interface of porphyrin and an electron-accepting semiconductor. Exciton diffusion lengths have been deduced from the number of charge carriers formed. Methods used to study the molecular organization include (polarized) optical absorption and fluorescence techniques, polarized optical microscopy and X-ray diffraction. This research has led to an improvement of the exciton diffusion length from a few nanometers to several tens of nanometers; i.e. comparable to the exciton diffusion length in natural light-harvesting systems. The impact of the molecular organization on the exciton diffusion length is discussed in terms of the Förster theory. To make these materials attractive for application in a photovoltaic device based on a dye and a semiconductor in a bilayer configuration, the long exciton diffusion lengths obtained should be enhanced further by a factor of 3-4 to values comparable to the optical penetration depth.

1.5. Outline of this thesis

Chapter 2: Effect of the structure of substituents on charge separation in meso-tetraphenylporphyrin/TiO_2 bilayers

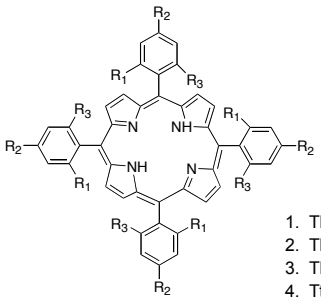

1. TPP $R_1 = R_2 = R_3 = H$
2. TMePP $R_1 = R_3 = H$, $R_2 = CH_3$
3. TEPP $R_1 = R_3 = H$, $R_2 = C_2H_5$
4. TtBuPP $R_1 = R_3 = H$, R_2 = tert-butyl
5. TtriMePP $R_1 = R_2 = R_3 = CH_3$

Bilayers of these porphyrin derivatives on TiO_2 show significant differences in charge separation efficiency. The observed values are discussed in terms of the exciton diffusion length and the interfacial electron injection yield.

Chapter 3: Exciton diffusion and interfacial charge separation in meso-tetraphenylporphyrin/TiO_2 bilayers: effect of ethyl substituents

The exciton diffusion length in ethyl substituted TEPP layers significantly exceeds the value observed for unsubstituted TPP. The difference is attributed to the presence of exciton trapping H-aggregates in case of the latter.

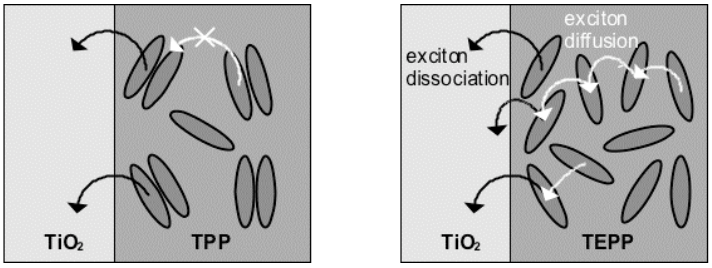

Chapter 4: Efficient light-harvesting layers of homeotropically aligned porphyrin derivatives

The introduction of n-butyl side chains results in a nematic layer structure in which the molecules are homeotropically aligned. The long exciton diffusion length observed of ≥12 nm is related to this specific molecular organization.

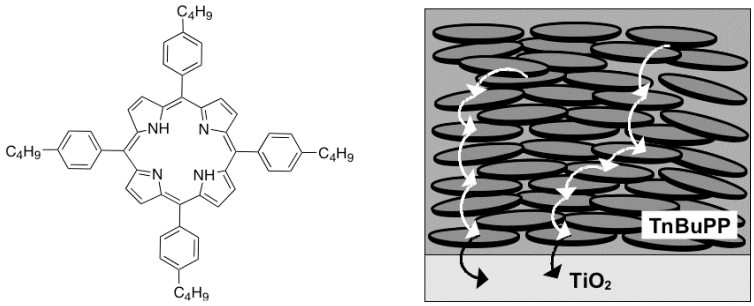

Chapter 5: Thermally deactivated exciton diffusion in a nematic layer of homeotropically aligned tetraphenylporphyrin derivatives

To gain insight into the exciton transfer mechanism in a TnBuPP layer, the energy transfer dynamics have been determined at various temperatures. The exciton diffusion length decreases from ≥20 nm at 90 K to ≥12 nm at 300 K. Combining these values with an increase in exciton lifetime from 0.52 ns at 90 K to 1.95 ns at 300 K and an intermolecular distance of 4.5 Å gives a decrease of the energy transfer rate from $\geq 3.8\times10^{12}$ s^{-1} at 90 K to $\geq 3.7\times10^{11}$ s^{-1} at 300 K. This decrease is attributed to larger fluctuations in exciton site energies and excitonic couplings at higher temperatures. Exciton motion in a TnBuPP layer hence occurs via a band like mechanism, rather than by thermally activated Förster-like hopping.

Chapter 6: Photosensitization of TiO_2 and SnO_2 by artificial self-assembling mimics of the natural chlorosomal bacteriochlorophylls

Layers are observed to consist of both self-assembled stacks and monomers. The formation of charge-separated states mainly originates from the latter. The low contribution of self-assembled stacks is most likely due to an unfavorable interaction with the semiconductor substrate.

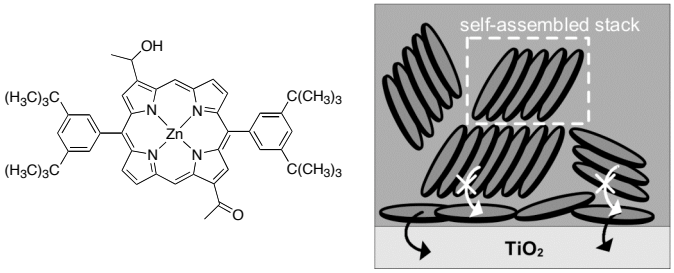

Chapter 7: Efficient exciton transport in layers of self-assembled porphyrin derivatives

Energy transfer between self-assembled stacks is observed to occur highly efficient. This is attributed to a strong excitonic coupling between adjacent stacks.

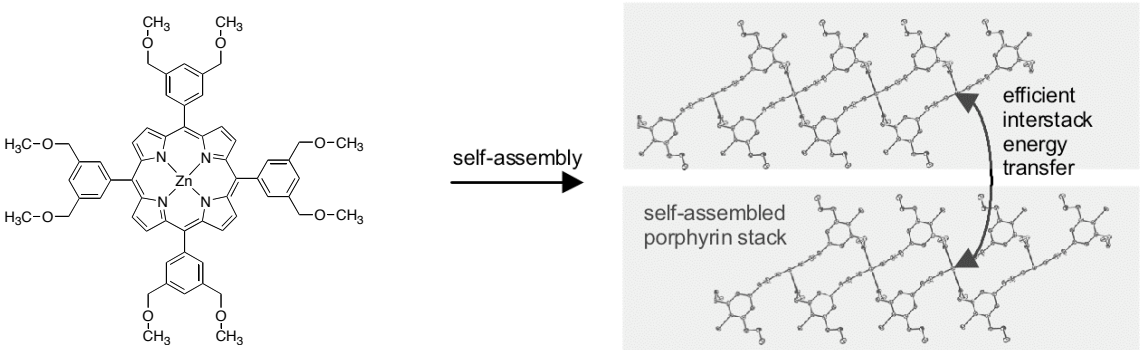

Chapter 8: An experimental study on the molecular organization and exciton diffusion in a bilayer of a porphyrin and poly(3-hexylthiophene)

The exciton diffusion length in P3HT deposited onto H_2TMPyP exceeds the value reported for P3HT on TiO_2 by almost a factor of three. This is attributed to a high degree of order for the first, enhancing the excitonic coupling between the P3HT chains and consequently the energy transfer rate.

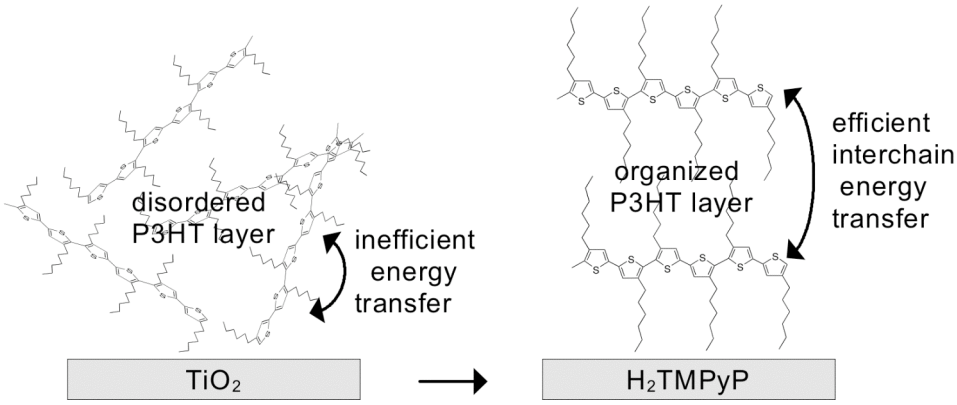

References

(1) Barber, J., *Philosophical Transactions of the Royal Society A-Mathematical Physical and Engineering Sciences* **2007,** 365, (1853), 1007-1023.

(2) Amerongen, H. v.; Valkunas, L.; Grondelle, R. v., *Photosynthetic excitons*. World Scientific: Singapore, 2000.

(3) Kühlbrandt, W.; Wang, D. N., *Nature* **1991,** 350, 130-134.

(4) Krauss, N.; Hinrichs, W.; Witt, I.; Fromme, P.; Pritzkow, W.; Dauter, Z.; Betzel, C.; Wilson, K. S.; Witt, H. T.; Saenger, W., *Nature* **1993,** 361, (6410), 326-331.

(5) Kühlbrandt, W.; Neng Wang, D.; Fujiyoshi, Y., *Nature* **1994,** 367, 614-621.

(6) McDermott, G.; Prince, S. M.; Freer, A. A.; Hawthornthwaitelawless, A.M.; Papiz, M. Z.; Cogdell, R. J.; Isaacs, N. W., *Nature* **1995,** 374, 517-521.

(7) Oijen, A. M. v.; Ketelaars, M.; Köhler, J.; Aartsma, T. J.; Schmidt, J., *Science* **1999,** 285, 400-402.

(8) Roszak, A. W.; Howard, T. D.; Southall, J.; Gardiner, A. T.; Law, C. J.; Isaacs, N. W.; Cogdell, R. W., *Science* **2003,** 302, 1969-1972.

(9) Liu, Z.; Yan, H.; Wang, K.; Kuang, T.; Zhang, J.; Gui, L.; An, X.; Chang, W., *Nature* **2004,** 428, 287-292.

(10) Grondelle, R. v.; Dekker, J. P.; Gillbro, T.; Sundstrom, V., *Biochimica et Biophysica Acta-Bioenergetics* **1994,** 1187, (1), 1-65.

(11) Jimenez, R.; Dikshit, S. N.; Bradforth, S. E.; Fleming, G. R., *Journal of Physical Chemistry* **1996,** 100, (16), 6825-6834.

(12) Koepke, J.; Hu, X. C.; Muenke, C.; Schulten, K.; Michel, H., *Structure* **1996,** 4, (5), 581-597.

(13) Gregg, B. A., *Journal of Physical Chemistry B* **2003,** 107, (20), 4688-4698.

(14) Wohrle, D.; Tennigkeit, B.; Elbe, J.; Kreienhoop, L.; Schnurpfeil, G., *Molecular Crystals and Liquid Crystals* **1993,** 230, 221-226.

(15) Kerp, H. R.; Donker, H.; Koehorst, R. B. M.; Schaafsma, T. J.; Faassen, E. E. v., *Chemical Physics Letters* **1998,** 298, (4-6), 302-308.

(16) Kroeze, J. E.; Savenije, T. J.; Warman, J. M., *Journal of Photochemistry and Photobiology A-Chemistry* **2002,** 148, 49-55.

(17) O'Regan, B.; Grätzel, M., *Nature* **1991,** 353, (6346), 737-740.

(18) Gouterman, M., *The Porphyrins; Volume III*. Academic Press: New York, 1978; Vol. 3.

(19) Hasegawa, J.; Ohkawa, K.; Nakatsuji, H., *Journal of Physical Chemistry B* **1998,** 102, (50), 10410-10419.
(20) Leupold, D.; Stiel, H.; Teuchner, K.; Nowak, F.; Sandner, W.; Ucker, B.; Scheer, H., *Physical Review Letters* **1996,** 77, (22), 4675-4678.
(21) Wong, K. F.; Bagchi, B.; Rossky, P. J., *Journal of Physical Chemistry A* **2004,** 108, (27), 5752-5763.
(22) Toyota, K.; Hasegawa, J.; Nakatsuji, H., *Journal of Physical Chemistry A* **1997,** 101, (4), 446-451.
(23) Hilborn, R. C., *American Journal of Physics* **1982,** 50, (11), 982-986.
(24) May, V.; Kühn, O., *Charge and Energy Transfer Dynamics in Molecular Systems. A Theoretical Introduction*. Wiley-VCH: Berlin, 2000.
(25) Hennebicq, E.; Pourtois, G.; Scholes, G. D.; Herz, L. M.; Russell, D. M.; Silva, C.; Setayesh, S.; Grimsdale, A. C.; Mullen, K.; Bredas, J. L.; Beljonne, D., *Journal of the American Chemical Society* **2005,** 127, (13), 4744-4762.
(26) Pope, M.; Svenberg, C. E., *Electronic Processes in Organic Crystals and Polymers*. second ed.; Oxford Science Publications: New York, 1999.
(27) Förster, T. H., *Discuss. Faraday Soc.* **1959**, (27), 7.
(28) Förster, T. H., *Fluoreszenz Organischer Verbindungen*. Göttingen, 1951.
(29) Scholes, G. D., *Annual Review of Physical Chemistry* **2003,** 54, 57-87.
(30) Psencik, J.; Ikonen, T. P.; Laurinmaki, P.; Merckel, M. C.; Butcher, S. J.; Serimaa, R. E.; Tuma, R., *Biophysical Journal* **2004,** 87, (2), 1165-1172.
(31) Overmann, J.; Cypionka, H.; Pfennig, N., *Limnology and Oceanography* **1992,** 37, 150-155.
(32) Frigaard, N. U.; Chew, A. G. M.; Li, H.; Maresca, J. A.; Bryant, D. A., *Photosynthesis Research* **2003,** 78, (2), 93-117.
(33) Frigaard, N. U.; Bryant, D. A., *Archives of Microbiology* **2004,** 182, 265-276.
(34) Prokhorenko, V. I.; Steensgaard, D. B.; Holzwarth, A. F., *Biophysical Journal* **2000,** 79, (4), 2105-2120.
(35) Staehelin, L. A.; Golecki, J. R.; Fuller, R. C.; Drews, G., *Archives of Microbiology* **1978,** 119, (3), 269-277.
(36) Balaban, T. S.; Tamiaki, H.; Holzwarth, A. R., Chlorins Programmed for Self-Assembly. In *Topics in Current Chemistry*, Heidelberg, 2005; Vol. 258, pp 1-38.
(37) Psencik, J.; Polivka, T.; Nemec, P.; Dian, J.; Kudrna, J.; Maly, P.; Hala, J., *Journal of Physical Chemistry A* **1998,** 102, (23), 4392-4398.
(38) Savikhin, S.; Zhu, Y. W.; Lin, S.; Blankenship, R. E.; Struve, W. S., *Journal of Physical Chemistry* **1994,** 98, (40), 10322-10334.
(39) Holzwarth, A. R.; Schaffner, K., *Photosynthetic Research* **1994,** 41, 225-233.
(40) Jesorka, A.; Balaban, T. S.; Holzwarth, A. R.; Schaffner, K., *Angewandte Chemie - International Edition* **1996,** 23-24, 2861-2863.
(41) Kureishi, Y.; Tamiaki, H., *Journal of Porphyrins and Phthalocyanines* **1998,** 2, (2), 159-169.
(42) Miyatake, T.; Tamiaki, H.; Holzwarth, A. R.; Schaffner, K., *Helvetica Chimica Acta* **1999,** 82, (6), 797-810.
(43) Kureishi, Y.; Shiraishi, H.; Tamiaki, H., *Journal of Electroanalytical Chemistry* **2001,** 496, (1-2), 13-20.
(44) Balaban, T. S.; Linke-Schaetzel, M.; Bhise, A. D.; Vanthuyne, N.; Roussel, C., *European Journal of Organic Chemistry* **2004**, (18), 3919-3930.
(45) Balaban, T. S.; Linke-Schaetzel, M.; Bhise, A. D.; Vanthuyne, N.; Roussel, C.; Anson, C. E.; Buth, G.; Eichhofer, A.; Foster, K.; Garab, G.; Gliemann, H.;

Goddard, R.; Javorfi, T.; Powell, A. K.; Rosner, H.; Schimmel, T., *Chemistry-A European Journal* **2005,** 11, (8), 2267-2275.
(46) Kunieda, M.; Tamiaki, H., *European Journal of Organic Chemistry* **2006**, (10), 2352-2361.
(47) Huber, V.; Lysetska, M.; Wurthner, F., *Small* **2007,** 3, (6), 1007-1014.
(48) Roger, C.; Muller, M. G.; Lysetska, M.; Miloslavina, Y.; Holzwarth, A. R.; Wurthner, F., *Journal of the American Chemical Society* **2006,** 128, (20), 6542-6543.
(49) Huber, V.; Katterle, M.; Lysetska, M.; Wurthner, F., *Angewandte Chemie-International Edition* **2005,** 44, (20), 3147-3151.
(50) Gregg, B. A.; Fox, M. A.; Bard, A. J., *Journal of the American Chemical Society* **1989,** 111, (8), 3024-3029.
(51) Yuan, Y.; Gregg, B. A.; Lawrence, M. F., *Journal of Materials Research* **2000,** 15, (11), 2494-2498.
(52) Gregg, B. A., *Molecular Crystals and Liquid Crystals Science and Technology Section a-Molecular Crystals and Liquid Crystals* **1994,** 257, 219.
(53) Haas, M. P. de; Warman, J. M., *Chemical Physics* **1982,** 73, 35-53.
(54) Huijser, A.; Savenije, T. J.; Kroeze, J. E.; Siebbeles, L. D. A., *Journal of Physical Chemistry B* **2005,** 109, 20166-20173.
(55) Huijser, A.; Savenije, T. J.; Kotlewski, A.; Picken, S. J.; Siebbeles, L. D. A., *Advanced Materials* **2006,** 18, 2234-2239.
(56) Visser, H. M.; Kleima, F. J.; Stokkum, I. H. M. v.; Grondelle, R. v.; Amerongen, H. v., *Chemical Physics* **1996,** 210, 297-312.
(57) Yang, J.; Winnik, M. A., *Journal of Physical Chemistry B* **2005,** 109, 18408-18417.
(58) Shimizu, Y.; Miya, M.; Nagata, A.; Ohta, K.; Yamamoto, I.; Kusabayashi, S., *Liquid Crystals* **1993,** 14, (3), 795-805.
(59) Yatskou, M. M.; Donker, H.; Koehorst, R. B. M.; van Hoek, A.; Schaafsma, T. J., *Chemical Physics Letters* **2001,** 345, (1-2), 141-150.
(60) Huijser, A.; Savenije, T. J.; Siebbeles, L. D. A., *Thin Solid Films* **2006,** 511-512, 208-213.
(61) Kroeze, J. E.; Koehorst, R. B. M.; Savenije, T. J., *Advanced Functional Materials* **2004,** 14, (10), 992-998.
(62) Yatskou, M. M.; Donker, H.; Novikov, E. G.; Koehorst, R. B. M.; van Hoek, A.; Apanasovich, V. V.; Schaafsma, T. J., *Journal of Physical Chemistry A* **2001,** 105, (41), 9498-9508.
(63) Donker, H.; van Hoek, A.; van Schaik, W.; Koehorst, R. B. M.; Yatskou, M. M.; Schaafsma, T. J., *Journal of Physical Chemistry B* **2005,** 109, (36), 17038-17046.
(64) Donker, H.; Koehorst, R. B. M.; Schaafsma, T. J., *Journal of Physical Chemistry B* **2005,** 109, 17031-17037.
(65) Piris, J.; Debije, M. G.; Stutzmann, N.; van de Craats, A. M.; Watson, M. D.; Mullen, K.; Warman, J. M., *Advanced Materials* **2003,** 15, (20), 1736-1740.
(66) Tamiaki, H., *Coordination Chemistry Reviews* **1996,** 148, 183-197.
(67) Balaban, T. S.; Goddard, R.; Linke-Schaetzel, M.; Lehn, J. M., *Journal of the American Chemical Society* **2003,** 125, (14), 4233-4239.
(68) Balaban, T. S., *Accounts of Chemical Research* **2005,** 38, (8), 612-623.
(69) Kunieda, M.; Tamiaki, H., *Journal of Organic Chemistry* **2005**, (70), 820-828.
(70) Kunieda, M.; Tamiaki, H., *European Journal of Organic Chemistry* **2006,** 10, 2352-2361.
(71) Kay, A.; Grätzel, M., *Journal of Physical Chemistry* **1993,** 97, (23), 6272-6277.

(72) Kay, A.; Humphrybaker, R.; Grätzel, M., *Journal of Physical Chemistry* **1994,** 98, (3), 952-959.
(73) Huijser, A.; Marek, P.; Savenije, T. J.; Siebbeles, L. D. A.; Scherer, T.; Hauschild, R.; Szmytkowski, J.; Kalt, H.; Hahn, H.; Balaban, T. S., *Journal of Physical Chemistry C* **2007,** 111, 11726-11733.
(74) Huijser, A.; Suijkerbuijk, B. M. J. M.; Klein Gebbink, R. J. M.; Savenije, T. J.; Siebbeles, L. D. A., *Journal of the American Chemical Society* **2007,** accepted.
(75) Suijkerbuijk, B. M. J. M.; Tooke, D. M.; Lutz, M.; Spek, A. L.; Koten, G. v.; Klein Gebbink, R. J. M., *Chem. Asian J.* **2007,** 2, 889-903.
(76) Hsiao, J. S.; Krueger, B. P.; Wagner, R. W.; Johnson, T. E.; Delaney, J. K.; Mauzerall, D. C.; Fleming, G. R.; Lindsey, J. S.; Bocian, D. F.; Donohoe, R. J., *Journal of the American Chemical Society* **1996,** 118, (45), 11181-11193.
(77) Yang, S. I.; Lammi, R. K.; Seth, J.; Riggs, J. A.; Arai, T.; Kim, D. H.; Bocian, D. F.; Holten, D.; Lindsey, J. S., *Journal of Physical Chemistry B* **1998,** 102, (47), 9426-9436.
(78) Cho, H. S.; Jeong, D. H.; Yoon, M. C.; Kim, Y. H.; Kim, Y. R.; Kim, D.; Jeoung, S. C.; Kim, S. K.; Aratani, N.; Shinmori, H.; Osuka, A., *Journal of Physical Chemistry A* **2001,** 105, (17), 4200-4210.
(79) Sessler, J. L.; Capuano, V. L.; Harriman, A., *Journal of the American Chemical Society* **1993,** 115, (11), 4618-4628.
(80) Scholes, G. D.; Ghiggino, K. P.; Oliver, A. M.; Paddonrow, M. N., *Journal of Physical Chemistry* **1993,** 97, (46), 11871-11876.
(81) Peumans, P.; Yakimov, A.; Forrest, S. R., *Journal of Applied Physics* **2003,** 93, (7), 3693-3723.
(82) Stubinger, T.; Brutting, W., *Journal of Applied Physics* **2001,** 90, (7), 3632-3641.
(83) Piechocki, C.; Simon, J.; Skoulios, A.; Guillon, D.; Weber, P., *Journal of the American Chemical Society* **1982,** 104, (19), 5245-5247.
(84) Weber, P.; Guillon, D.; Skoulios, A., *Liquid Crystals* **1991,** 9, (3), 369-382.
(85) Ohta, K.; Jacquemin, L.; Sirlin, C.; Bosio, L.; Simon, J., *New Journal of Chemistry* **1988,** 12, (8-9), 751-754.
(86) Eichhorn, H., *Journal of Porphyrins and Phthalocyanines* **2000,** 4, (1), 88-102.
(87) Guillon, D.; Weber, P.; Skoulios, A.; Piechocki, C.; Simon, J., *Molecular Crystals and Liquid Crystals* **1985,** 130, 223.
(88) Van der Pol, J. F.; Neeleman, E.; Zwikker, J. W.; Nolte, R. J. M.; Drenth, W.; Aerts, J.; Visser, R.; Picken, S. J., *Liquid Crystals* **2006,** 33, (11-12), 1378-1387.
(89) Blanzat, B.; Barthou, C.; Tercier, N.; Andre, J. J.; Simon, J., *Journal of the American Chemical Society* **1987,** 109, (20), 6193-6194.
(90) Li, X. Y.; Sinks, L. E.; Rybtchinski, B.; Wasielewski, M. R., *Journal of the American Chemical Society* **2004,** 126, (35), 10810-10811.
(91) Markovitsi, D.; Tranthi, T. H.; Briois, V.; Simon, J.; Ohta, K., *Journal of the American Chemical Society* **1988,** 110, (6), 2001-2002.
(92) Markovitsi, D.; Lecuyer, I., *Chemical Physics Letters* **1988,** 149, (3), 330-333.
(93) Peumans, P.; Forrest, S. R., *Applied Physics Letters* **2001,** 79, (1), 126-128.
(94) Peumans, P.; Uchida, S.; Forrest, S. R., *Nature* **2003,** 425, (6954), 158-162.
(95) Satake, A.; Kobuke, Y., *Organic & Biomolecular Chemistry* **2007,** 5, (11), 1679-1691.
(96) Fuchs, H.; Zimmermann, J.; Roder, B., *Optics Communications* **2003,** 220, (1-3), 119-127.

CHAPTER 2

Effect of the structure of substituents on charge separation in *meso*-tetraphenylporphyrin/TiO_2 bilayers*

The efficiency of photo-induced charge separation in smooth *meso*-tetra(alkylphenyl)porphyrin/TiO_2 bilayers has been investigated using the time-resolved microwave conductivity (TRMC) technique. Particular attention has been paid to the effect of the structure of the substituents on the charge separation efficiency. The chemical structure of the substituents is found to affect the charge separation efficiency significantly. Ethyl-substituted *meso*-tetraphenylporphyrin/TiO_2 bilayers exhibit a charge separation efficiency of 6.2 % at the absorption maximum, which is considerably higher than the efficiencies near 1 % or even lower found for the other porphyrin derivatives. The low charge separation efficiencies of these porphyrin/TiO_2 bilayers are discussed in terms of a short exciton diffusion length and/or a low interfacial electron injection yield (ϕ_{inj}). The short exciton diffusion lengths are related to a short lifetime of the singlet state and a low energy transfer rate between porphyrin molecules due to a low fluorescence rate constant. The results suggest that the value of ϕ_{inj} is affected by the presence of alkyl substituents on the phenyl groups.

---

* This chapter is based on: Annemarie Huijser, Tom J. Savenije and Laurens D.A. Siebbeles, *Thin Solid Films* **2006**, *511-512*, 208-213.

2.1. Introduction

Dye-sensitized solar cells, based on an electron accepting inorganic semiconductor coated with a light absorbing dye, exhibit advantages over silicon-based solar cells such as cheap processing, chromatic flexibility and a practically infinite variety of materials.[1] The wide bandgap inorganic semiconductor such as TiO_2 does not absorb visible light, but is photosensitized by the dye layer. Absorption of a photon by the dye results in the formation of a strongly bound electron-hole pair, also referred to as an exciton. The exciton may migrate to the interface with the semiconductor, where charge separation can occur by injection of an electron from the dye into the conduction band of the semiconductor. The separated electron and hole formed at the interface can either recombine or escape from each other. Application of such a bilayer in a sandwich configuration yields a photovoltaic device in which the charge carriers can be collected by the electrodes.

A major problem in using organic dye layers is the small distance an exciton is able to travel by diffusion. The penetration depth of visible light in organic dye layers is typically 100 nm, while the exciton diffusion length (Λ_E) is usually found to be only a few nanometers.[2,3] The exciton diffusion length depends on the exciton diffusion coefficient (D_E) and the exciton lifetime (τ_E) according to:

$$\Lambda_E = \sqrt{D_E \tau_E} \tag{2.1}$$

Because of this short exciton diffusion length, the photoactive part of the dye layer is restricted to a few monolayers near the interface with the semiconductor. Excitons formed further away from the interface decay before reaching the interface by radiationless processes or under emission of a photon. The short exciton diffusion length results in a low charge separation efficiency and hence in a low cell performance.

One way to overcome this problem is the use of nanocrystalline semiconductor films, thus reducing the mean distance excitons need to diffuse to reach the interface.[1,4,5] A performance over 10 % has been achieved for a cell based on an interpenetrating network of dye-coated nanocrystalline TiO_2 particles and a hole transporting electrolyte.[4] However, due to complications involved in the use of a liquid electrolyte,[6] there is currently a great interest in the development of total solid-state organic/inorganic solar cells, for which a maximum performance of 3-4 % has been realized so far.[7-9] Another approach to enhance the charge separation efficiency involves an increase of the exciton

diffusion length. According to equation 2.1 this can be achieved by a longer exciton lifetime and/or a larger exciton diffusion coefficient.

Porphyrin-based dyes have attracted considerable attention to be applied in solar cells because of their very strong light absorption in the visible part of the solar emission spectrum. Combined with TiO_2 as an electron acceptor, efficient charge separation has been observed.[10-14] Current research on porphyrin/TiO_2 combinations is focused on improvement of the exciton diffusion length,[2,3,15,16] enhancement of the interfacial electron injection yield[16,17] and improvement of the charge transport properties.[18-20] Previous studies have shown that changes in the chemical structure of *meso*-tetraphenylporphyrins strongly affect the charge separation efficiency of these porphyrins in a bilayer with TiO_2. The introduction of a Pd atom[21] or an octyl substituent at the para-positions of the phenyl groups[15] results in an almost 10 times increased charge separation efficiency since the exciton transport in these dye films occurs via the triplet level. Exciton transport via the triplet route, however, is less attractive as compared to transport via the singlet route because of unwanted chemical degradation of the dye.[22,23]

The aim of the present work is to provide information about the influence of substituents on the photo-induced charge separation efficiency. Figure 2.1 shows the chemical structures of the porphyrins investigated. Differences in charge separation efficiency will be discussed in terms of the exciton diffusion length and the interfacial electron injection yield.

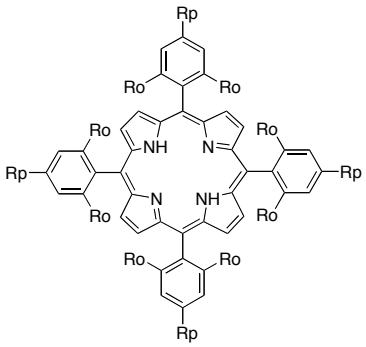

1	TPP	Ro = Rp = H
2	TMePP	Ro = H, Rp = CH_3
3	TEtPP	Ro = H, Rp = C_2H_5
4	TtBuPP	Ro = H, Rp = tert-butyl
5	TtriMePP	Ro = Rp = CH_3

Figure 2.1. Chemical structures of the porphyrins investigated.

2.2. Experimental methods

Sample preparation: Thin smooth TiO_2 films with a thickness of ca. 100 nm, prepared by chemical vapor deposition onto 1x12x25 mm^3 quartz substrates, were purchased from Everest Coatings, Delft, The Netherlands. *Meso*-tetraphenylporphyrin (TPP) was purchased from Porphyrin Systems, Lübeck, Germany. *Meso*-tetra(4-methylphenyl)porphyrin (TMePP), *meso*-tetra(4-ethylphenyl)porphyrin (TEtPP), *meso*-tetra(4-tert-butylphenyl)porphyrin (TtBuPP) and *meso*-tetra(2,4,6-trimethylphenyl)porphyrin (TtriMePP) were purchased from Frontier Scientific, Logan, USA. The chemical structures of these porphyrins are shown in Figure 2.1. Porphyrin films with a thickness in the order of 30 nm were prepared by spin-coating from the corresponding solution in $CHCl_3$ (Anhydrous, 99+%, Aldrich) at 2500 rpm under N_2 atmosphere onto either a quartz or a TiO_2 substrate. The thickness of the porphyrin films was determined using a Veeco Dektak 8 Stylus Profiler.

Optical characterization: Optical transmission and reflection spectra were recorded with a Perkin Elmer Lambda 900 UV/VIS/NIR spectrometer. From the transmission and reflection spectra, the optical density (OD) and the fraction of absorbed light (F_A) were calculated according to equations 2.2 and 2.3, with I_T the intensity of the transmitted light, I_0 the incident light intensity and I_R the intensity of the reflected light:[14]

$$OD = -\log\left(\frac{I_T}{I_0 - I_R}\right) \tag{2.2}$$

$$F_A = 1 - \left(\frac{I_T + I_R}{I_0}\right) \tag{2.3}$$

The wavelength dependences of the OD and F_A are denoted the "absorption spectrum" and the "attenuation spectrum", respectively. Steady-state and time-resolved fluorescence spectra were recorded with a Lifespec – ps setup using a 405 nm excitation source (Edinburgh Instruments) and related to the optical attenuation.

TRMC measurements: The time-resolved microwave conductivity (TRMC) technique and experimental setup have been described previously.[3,24] The porphyrin/TiO_2 bilayers were mounted in an X-band microwave cavity at a position of maximum electric field strength. The microwave frequency used in these experiments was ca. 8.45 GHz. Samples were illuminated through the quartz substrate with a nanosecond laser pulse, resulting in a

change in conductivity due to an excess of mobile electrons in the TiO_2. The incident intensity (I_0) was varied between 10^{11} - 10^{13} photons/cm^2 per pulse.

The data analysis has been described in detail earlier. Briefly, the formation of mobile charge carriers leads to an increase of the photoconductance (ΔG), followed by an eventual decrease resulting from decay of charge carriers. The change in photoconductance is related to the normalized change in reflected microwave power ($\Delta P/P$) by:

$$\frac{\Delta P}{P} = -K\Delta G \tag{2.4}$$

The sensitivity factor K was determined as described in ref. 25 and amounts to 7×10^4 S^{-1}. The mobility of electrons varied for different TiO_2 layers. To take this into account, the photoconductance obtained on pulsed illumination with visible light was divided by the maximum photoconductance obtained on selective excitation of TiO_2 at 300 nm.[3] From the maximum of the photoconductance (ΔG_{max}), the incident photon to charge separation efficiency (IPCSE) at wavelength λ was calculated according to:

$$IPCSE(\lambda) = \frac{\Delta G_{\max}(\lambda)}{\Delta G_{\max}(\lambda = 300\ nm)} \frac{I_0(\lambda = 300\ nm)}{I_0(\lambda)} F_A(\lambda = 300\ nm)\ 100\% \tag{2.5}$$

This efficiency denotes the ratio of the number of electrons injected into the TiO_2 to the number of incident photons and may be compared with the incident photon to current efficiency (IPCE).

2.3. Results and discussion

2.3.1. Optical characterization

Figure 2.2 shows the normalized optical density spectra and the steady-state fluorescence spectra of the porphyrins spin-coated on quartz. The strong absorption between 400 nm and 450 nm (the 'Soret band') results from the S_0-S_2 transition. Transitions from S_0 to two energetically slightly different S_1 levels and their higher vibrational modes cause the less intense Q-bands between 500 nm and 700 nm.[26] The OD spectrum of TtriMePP shows a broadening of the Soret band and slightly blue-shifted Q-bands as compared to the almost similar OD spectra of the other porphyrins. All

porphyrin films exhibit an intense fluorescence band at 660 nm and a second fluorescence band at 720 nm. Large variations in fluorescence quantum yield (ϕ_F) are observed. The unsubstituted TPP exhibits the lowest fluorescence quantum yield, while a 30 times higher fluorescence quantum yield is found for the TriMePP film.

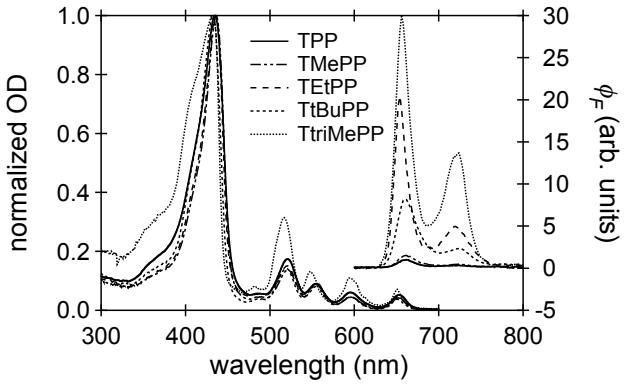

Figure 2.2. Normalized optical density and fluorescence spectra of 30±5 nm thick porphyrin films on quartz.

Figure 2.3 shows the fluorescence decays of the porphyrin films. Fitting a mono-exponential decay to the experimental data (included in Figure 2.3) yielded exciton lifetimes ranging between 260 ps to 4.44 ns for TPP films and TtriMePP films, respectively. The exciton lifetimes obtained from the fits are shown in Table 2.1. The exciton lifetime is related to the fluorescence quantum yield and the fluorescence rate constant (k_F) according to:[27]

$$\phi_F = k_F \tau_E \tag{2.6}$$

The difference in fluorescence quantum yields is caused both by a difference in exciton lifetime and/or a difference in fluorescence rate constant. The relative fluorescence rate constants for the different porphyrins are obtained from the exciton lifetimes and the relative fluorescence quantum yields using equation 2.6. The results are presented in Table 2.1. Note that the relative fluorescence rate constants do not resemble the trend in the exciton lifetimes. This must be due to a variation of the radiationless decay rates for the different porphyrins. The fluorescence rate constants found for the TMePP film and the TtriMePP film are only slightly higher than the fluorescence rate constant found for the TPP film. However, the fluorescence rate constants of the TtBuPP and especially the TEtPP film are significantly higher as compared to the TPP film. Since the fluorescence

lifetimes and quantum yields of these porphyrins in solution are found to be similar, the different fluorescence quantum yields and lifetimes observed for the various porphyrin films are expected to be caused by differences in intermolecular interactions. These differences may affect exciton transport and consequently the charge separation efficiency in porphyrin/TiO_2 bilayers.

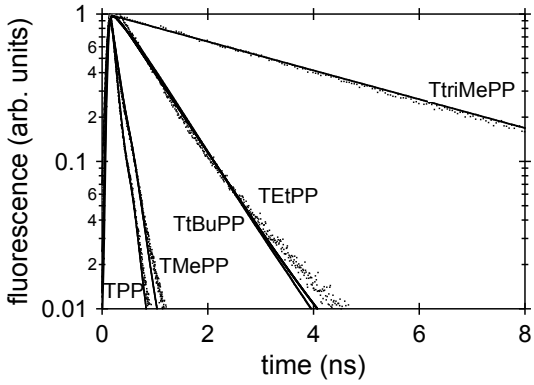

Figure 2.3. Fluorescence decays of 30±5 nm thick porphyrin films on quartz together with the corresponding mono-exponential fits. Between brackets the exciton lifetimes resulting from these fits.

2.3.2. Photoconductivity measurements

Figure 2.4 shows the photoconductance transients on pulsed illumination at 430 nm of the porphyrin/TiO_2 bilayers, divided by ΔG_{max} obtained on pulsed illumination of the sample at 300 nm. The initial rise of the transients is due to the 18 ns instrument response time of the system. Equal amounts of positive and negative charge carriers are formed on pulsed illumination. These charge carriers both contribute to the photoconductance. However, the change in photoconductance is mainly due to the mobile electrons in the TiO_2, since the mobility of holes in porphyrins is substantially lower.[28,29] The TEtPP/TiO_2 bilayer exhibits a significantly higher photoconductance than the other bilayers. The TPP/TiO_2 and the TMePP/TiO_2 bilayers exhibit similar photoconductance transients. The photoconductance transients of the TtBuPP/TiO_2 and the TtriMePP/TiO_2 bilayers are also similar and are even lower than those of the TPP/TiO_2 and the TMePP/TiO_2 bilayers. The charge-separated state persists into the microsecond domain. Since the current experiments were carried out in the absence of charge collecting electrodes, decay of the photoconductance is not due to extraction of charge carriers

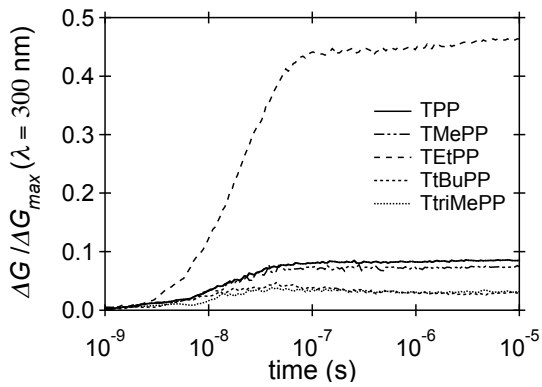

Figure 2.4. Photoconductance transients of the porphyrin/TiO_2 bilayers on pulsed illumination at 430 nm with 1×10^{12} photons/cm^2/pulse, divided by ΔG_{max} obtained on pulsed illumination at 300 nm of the corresponding bare TiO_2 films with 1.5×10^{11} photons/cm^2/pulse. The porphyrin films have a thickness of 40±5 nm.

From the maximum of the transients shown in Figure 2.4, the IPCSE at 430 nm can be calculated using equation 2.5. The results are presented in Table 2.1. The IPCSE values of the TPP/TiO_2 and the TMePP/TiO_2 bilayers amount to 1.2 % and 1.0 %, respectively. The higher photoconductance of the TEtPP/TiO_2 bilayer results in a significantly larger IPCSE of 6.2 %. The relatively low photoconductance of the TtBuPP/TiO_2 and the TtriMePP/TiO_2 bilayers result in an IPCSE of only 0.5 % for both bilayers.

Figure 2.5 shows the IPCSE as function of wavelength ('photoaction spectrum') for the TMePP/TiO_2, TEtPP/TiO_2 and the TtriMePP/TiO_2 bilayers, as well as their optical attenuation spectra. It is obvious that these photoaction spectra follow the corresponding optical attenuation spectra, which demonstrates photosensitization of the TiO_2 by the porphyrin layer. The photoaction spectra obtained for the TPP/TiO_2 and the TtBuPP/TiO_2 bilayers were similar to those observed for the TMePP/TiO_2 and the TtriMePP/TiO_2 bilayers, respectively. The small deviation of the photoaction spectra from the optical attenuation spectra may be attributed to sub-bandgap excitation of electronic states within the optical bandgap of TiO_2.[3]

The IPCSE depends on the fraction of incident photons that is reflected by the bilayer (F_R), the number of excitons that reaches the porphyrin/TiO_2 interface normalized to the number of incident photons (S) and the interfacial injection yield relative to all modes of interfacial exciton deactivation (ϕ_{inj}):[30]

$$IPCSE = (1 - F_R)\phi_{inj} S(\alpha, L, \Lambda_E)\ 100\% \tag{2.7}$$

S depends on the exponential optical absorption coefficient (a), the porphyrin film thickness (L) and the exciton diffusion length (Λ_E). Since F_R, α and L do not vary significantly for the various porphyrin/TiO_2 bilayers, the differences in IPCSE must be due to a difference in ϕ_{inj} and/or Λ_E.

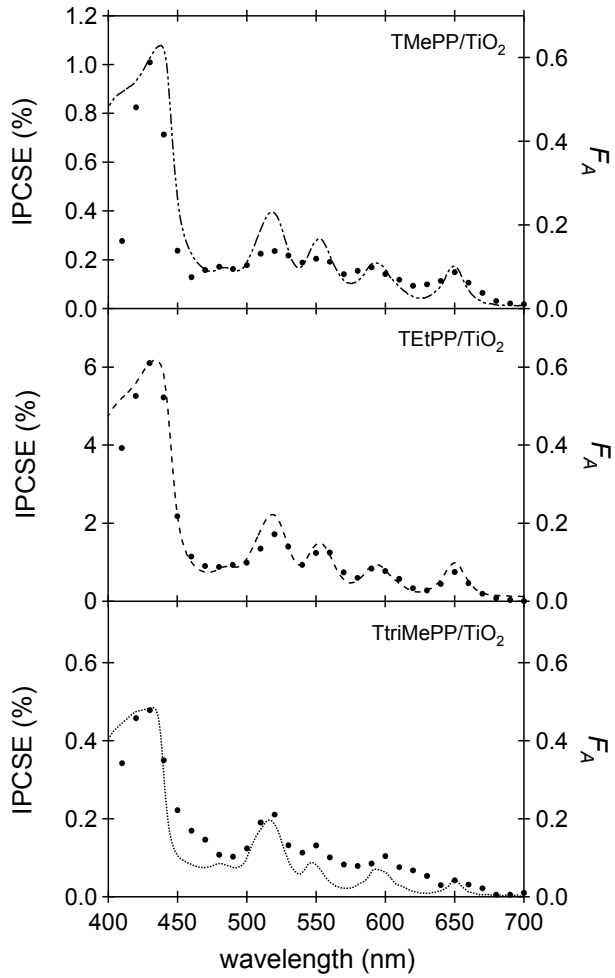

Figure 2.5. F_A (lines) and the experimental IPCSE values (dots) of TMePP/TiO_2, TEtPP/TiO_2 and TtriMePP/TiO_2 bilayers as function of wavelength. The porphyrin films have a thickness of 40±5 nm. Note the different scales along the vertical axes.

Exciton diffusion in the porphyrin films is expected to occur via the Förster mechanism. Förster energy transfer, with exciton hopping rate k_{ET}, occurs by the exchange of a virtual photon between donor and acceptor and is only possible if there is a non-zero overlap of the emission and absorption spectra. The spectra presented in Figure 2.2 show that the latter condition is fulfilled. The exciton diffusion coefficient D_E is

proportional to the fluorescence rate constant (k_F) and the distance between donor and acceptor (R_{DA}) according to: [31, 32]

$$D_E \propto k_{ET} R_{DA}^2 \propto \frac{k_F}{R_{DA}^4} \tag{2.8}$$

As can be seen in Table 2.1, the exciton lifetime, fluorescence rate constant and IPCSE are similar for TPP and TMePP. This implies that Λ_E and ϕ_{inj} must also be comparable.

The data in Table 2.1 show that the exciton lifetime for a TEtPP film is approximately 3 times higher than for a TPP film, while the fluorescence rate constant is 6.5 times higher. The higher fluorescence rate constant k_F results in a higher exciton diffusion coefficient as follows from equation 2.8. Together with the longer exciton lifetime this results in an increase of the exciton diffusion length for TEtPP as follows from equation 2.1, which explains the higher IPCSE of TEtPP/TiO_2 bilayers as compared to TPP/TiO_2 bilayers. A more detailed study on the structure of TPP and TEtPP layers is presented in chapter 3.

When comparing the exciton lifetime and the fluorescence rate constant of TtBuPP films with those of TPP and TEtPP films, one would expect an IPCSE higher than only 0.5 %. The very low IPCSE could be due to poor interfacial electron injection, caused by the tert-butyl side chains on the para-positions of the phenyl groups, preventing electronic coupling with the semiconductor. Another possible reason for the low IPCSE is a large distance between exciton donating and accepting species due to the presence of bulky tert-butyl substituents. According to equation 2.8 this results in a small D_E and consequently a short Λ_E.

On basis of the long exciton lifetime observed for a TtriMePP film (4.44 ns), one would expect a high IPCSE according to equations. 2.1 and 2.7. However, the IPCSE at the absorption maximum is only 0.5 %, which is most likely due to a low ϕ_{inj}. In *meso*-tetraphenylporphyrin molecules the angle between the porphyrin plane and the phenyl groups depends on the energy involved in steric hindrance and π-π electronic interaction between the porphyrin plane and the phenyl groups. In *meso*-tetraphenylporphyrins with substituents only on the para-positions of the phenyl groups, the optimum angle between the porphyrin plane and the phenyl groups is 63°.[33] In TtriMePP molecules, however, the presence of methyl groups at the ortho-positions of the phenyl groups are expected to increase the steric hindrance, hence increasing the angle between the porphyrin plane and

the phenyl groups. This larger angle together with the presence of the methyl groups at the ortho-positions may hamper the electronic interaction with the TiO_2, thus resulting in a low ϕ_{inj}. In addition, the methyl groups at the ortho-positions may affect the redox potential of TtriMePP in such a way that ϕ_{inj} becomes smaller. Enhancement of ϕ_{inj} offers the opportunity to increase the charge separation efficiency of TtriMePP/TiO_2 bilayers significantly.

Table 2.1. Exciton properties and charge separation efficiencies of the porphyrins investigated.

Porphyrin	relative ϕ_F	τ_E (ns)	relative k_F	$IPCSE_{430\ nm}$ (%)
TPP	1	0.26	3.8	1.2
TMePP	1.5	0.30	5.0	1.0
TEtPP	20	0.80	25	6.2
TtBuPP	8.0	0.70	11	0.5
TtriMePP	30	4.44	6.8	0.5

2.4. Conclusions

Although the chemical structures of the porphyrins investigated only differ slightly, the presence of substituents is found to affect the charge separation efficiency significantly. TEtPP/TiO_2 bilayers exhibit a maximum charge separation efficiency of 6.2 %, which is considerably higher than the charge separation efficiencies near 1 % or even lower found for the other porphyrin derivatives. The low charge separation efficiencies of these porphyrin/TiO_2 bilayers are discussed in terms of a short exciton diffusion length and a low interfacial electron injection yield. The short exciton diffusion lengths are related to a short lifetime of the singlet state and a low energy transfer rate between porphyrin molecules due to a low fluorescence rate constant. The results suggest that the value of ϕ_{inj} is affected by the presence of alkyl substituents on the phenyl groups.

Acknowledgment

The authors thank Dr. J.E. Kroeze for fruitful discussions. The research was supported financially by the Delft Research Centre for Sustainable Energy.

References

(1) Grätzel, M., *Nature* **2001,** 414, 338-344.
(2) Kerp, H. R.; Donker, H.; Koehorst, R. B. M.; Schaafsma, T. J.; Faassen, E. E. v., *Chemical Physics Letters* **1998,** 298, (4-6), 302-308.
(3) Kroeze, J. E.; Savenije, T. J.; Warman, J. M., *Journal of Photochemistry and Photobiology A-Chemistry* **2002,** 148, 49-55.
(4) O'Regan, B.; Grätzel, M., *Nature* **1991,** 353, (6346), 737-740.
(5) Bach, U.; Lupo, D.; Comte, P.; Moser, J. E.; Weissortel, F.; Salbeck, J.; Spreitzer, H.; Grätzel, M., *Nature* **1998,** 395, (6702), 583-585.
(6) Sommeling, P. M.; Spath, M.; Smit, H. J. P.; Bakker, N. J.; Kroon, J. M., *Journal of Photochemistry and Photobiology A-Chemistry* **2004,** 164, (1-3), 137-144.
(7) Kruger, J.; Plass, R.; Grätzel, M., *Applied Physics Letters* **2002,** 81, (2), 367-369.
(8) Schmidt-Mende, L.; Zakeeruddin, S. M.; Grätzel, M., *Applied Physics Letters* **2005,** 86, (1), 013504.
(9) Beek, W. J. E.; Wienk, M. M.; Janssen, R. A. J., *Advanced Materials* **2004,** 16, (12), 1009.
(10) Kay, A.; Humphrybaker, R.; Grätzel, M., *Journal of Physical Chemistry* **1994,** 98, (3), 952-959.
(11) Boschloo, G. K.; Goossens, A., *Journal of Physical Chemistry* **1996,** 100, (50), 19489-19494.
(12) Koehorst, R. B. M.; Boschloo, G. K.; Savenije, T. J.; Goossens, A.; Schaafsma, T. J., *Journal of Physical Chemistry B* **2000,** 104, (10), 2371-2377.
(13) Tachibana, Y.; Haque, S. A.; Mercer, I. P.; Durrant, J. R.; Klug, D. R., *Journal of Physical Chemistry B* **2000,** 104, (6), 1198-1205.
(14) Kroeze, J. E.; Savenije, T. J.; Warman, J. M., *Journal of the American Chemical Society* **2004,** 126, 7608.
(15) Kroeze, J. E.; Koehorst, R. B. M.; Savenije, T. J., *Advanced Functional Materials* **2004,** 14, (10), 992-998.
(16) Gregg, B. A., *Molecular Crystals and Liquid Crystals Science and Technology Section a-Molecular Crystals and Liquid Crystals* **1994,** 257, 219.
(17) Ma, T. L.; Inoue, K.; Yao, K.; Noma, H.; Shuji, T.; Abe, E.; Yu, J. H.; Wang, X. S.; Zhang, B. W., *Journal of Electroanalytical Chemistry* **2002,** 537, (1-2), 31-38.
(18) Savenije, T. J.; Koehorst, R. B. M.; Schaafsma, T. J., *Journal of Physical Chemistry B* **1997,** 101, (5), 720-725.
(19) Savenije, T. J.; Goossens, A., *Physical Review B* **2001,** 6411, (11).
(20) Wamser, C. C.; Kim, H. S.; Lee, J. K., *Optical Materials* **2003,** 21, (1-3), 221-224.
(21) Kroeze, J. E.; Savenije, T. J.; Warman, J. M., *Advanced Materials* **2002,** 14, (23), 1760-1763.
(22) Scurlock, R. D.; Wang, B.; Ogilby, P. R.; Sheats, J. R.; Clough, R. L., *Journal of the American Chemical Society* **1995,** 117, 10194-10202.
(23) Granzhan, A.; Penzkofer, A.; Hauska, G., *Journal of Photochemistry and Photobiology A-Chemistry* **2004,** 165, 75-89.
(24) Haas, M. P. de; Warman, J. M., *Chemical Physics* **1982,** 73, 35-53.
(25) Savenije, T. J.; Haas, M. P. de.; Warman, J. M., *Zeitschrift fur Physikalische Chemie-International Journal of Research in Physical Chemistry & Chemical Physics* **1999,** 212, 201-206.
(26) Gouterman, M., *The Porphyrins; Volume III.* Academic Press: New York, 1978; Vol. 3.

(27) Turro, N. J., *Modern Molecular Photochemistry*. The Benjamin/Cummings Publishing Company, Inc, Menlo Park, CA: 1978.
(28) Schouten, P. G.; Warman, J. M.; Haas, M.P. de; Fox, M. A.; Pan, H. L., *Nature* **1991,** 353, (6346), 736-737.
(29) Bak, T.; Nowotny, J.; Rekas, M.; Sorrell, C. C., *Journal of Physics and Chemistry of Solids* **2003,** 64, (7), 1069-1087.
(30) Kroeze, J. E.; Savenije, T. J.; Vermeulen, M. J. W.; Warman, J. M., *Journal of Physical Chemistry B* **2003,** 107, (31), 7696-7705.
(31) Förster, T. H., *Discuss. Faraday Soc.* **1959,** 27, 7-17.
(32) Sariciftci, N. S., *Progress in Quantum Electronics* **1995,** 19, (2), 131-159.
(33) Hofstra, U.; Koehorst, R. B. M.; Schaafsma, T., *Magnetic Resonance in Chemistry* **1988,** 26, 167.

CHAPTER 3

Exciton diffusion and interfacial charge separation in *meso*-tetraphenylporphyrin/TiO_2 bilayers: effect of ethyl substituents*

The photo-induced charge separation efficiency in porphyrin/TiO_2 bilayers has been determined using the time-resolved microwave conductivity (TRMC) technique. Porphyrins investigated are unsubstituted *meso*-tetraphenylporphyrin (TPP) and *meso*-tetra(4-ethylphenyl)porphyrin (TEPP). TEPP/TiO_2 bilayers exhibit a charge separation efficiency per incident photon at the Soret band maximum of 6.2 %, which is considerably higher than the efficiency of 1.2 % found for TPP/TiO_2 bilayers. Exciton diffusion lengths of 7 Å for TPP and 75 Å for TEPP are obtained from fitting a model for the charge separation efficiency to the experimental data. Optical measurements on the porphyrin derivatives on quartz yield a 20 times higher fluorescence quantum yield and a 7 times higher fluorescence rate constant for TEPP layers as compared to TPP layers. The exciton lifetime of 800 ps found for TEPP layers is considerably longer than the lifetime of 260 ps in TPP layers. The exciton diffusion coefficients, determined from the exciton diffusion length and the exciton lifetime, are found to be 2×10^{-9} m^2/s for TPP and 7×10^{-8} m^2/s for TEPP. The difference is discussed in terms of the presence of face-to-face dimers or larger aggregates in TPP layers.

---

* This chapter is based on: Annemarie Huijser, Tom J. Savenije, Jessica E. Kroeze and Laurens D.A. Siebbeles, *Journal of Physical Chemistry B* **2005**, *109,* 20166-20173.

3.1. Introduction

Solar cells consisting of a light absorbing organic dye and an electron accepting inorganic semiconductor exhibit advantages over silicon-based solar cells, including opportunities of cheap processing, chromatic flexibility and a practically unlimited choice of materials.[1] The working principle of a dye-sensitized solar cell is based on the photophysical processes that are schematically depicted in Figure 3.1. The wide bandgap semiconductor such as TiO_2 and SnO_2 does not absorb visible light, but is photosensitized by the dye layer. This dye layer absorbs photons from the visible part of the solar spectrum, thereby promoting an electron from the ground state to a higher energetic level (Figure 3.1, process 1). The resulting strongly bound electron-hole pair, which consists of the excited electron and a positively charged electron vacancy, is referred to as an exciton. These excitons may migrate to the interface with the semiconductor (3), where charge separation (*CS*) can occur by electron injection from the S_1 level of the dye layer into the conduction band of the semiconductor (7). Other competing processes are intersystem crossing to the triplet level (4), and decay to the ground state by radiationless decay (5) or under emission of a photon (6). The electrons and holes formed at the interface by charge separation can either recombine (8) or escape from each other. In a photovoltaic device charges are collected by electrodes on top of the semiconductor film and the dye layer and can perform work in an external circuit.

The performance of flat organic/inorganic bilayer solar cells is typically much less than 1 %.[2, 3] The low performance is to a large extent due to the fact that the exciton diffusion length is small compared to the optical absorption length. For organic dyes the light absorption length is typically 100 nm. However, the exciton diffusion length

$$\Lambda_E = \sqrt{D_E \tau_E} \tag{3.1}$$

with D_E the exciton diffusion coefficient and τ_E the exciton lifetime, is often found to be only a few nanometers.[4, 5] Due to this short exciton diffusion length, the photoactive part of the dye layer is restricted to a few monolayers near the interface. Excitons formed further away from the interface decay by non-radiative (5) or radiative (6) processes before reaching the interface and do not contribute to the photocurrent.

One way to overcome this problem is the use of nanocrystalline semiconductor films.[1,6,7] This results in a much larger interfacial area between the light absorbing molecules and the semiconductor, thus reducing the mean distance excitons have to diffuse to reach the interface. A performance of more than 10 % has been achieved for a

cell based on an interpenetrating network of dye-coated nanocrystalline TiO_2 particles and a hole transporting electrolyte.[6] However, due to complications involved in the use of a liquid electrolyte[8], there is currently a great interest in the development of total solid-state organic/inorganic solar cells. For all solid-state nanocrystalline organic/inorganic solar cells a maximum performance of 3-4 % has been realized so far.[9-11] An alternative approach to overcome the limited exciton diffusion length in organic dye layers involves enhancement of the exciton diffusion length within the dye layer. As follows from equation 3.1, this can be realized by enhancing the natural exciton lifetime and/or the exciton diffusion coefficient.

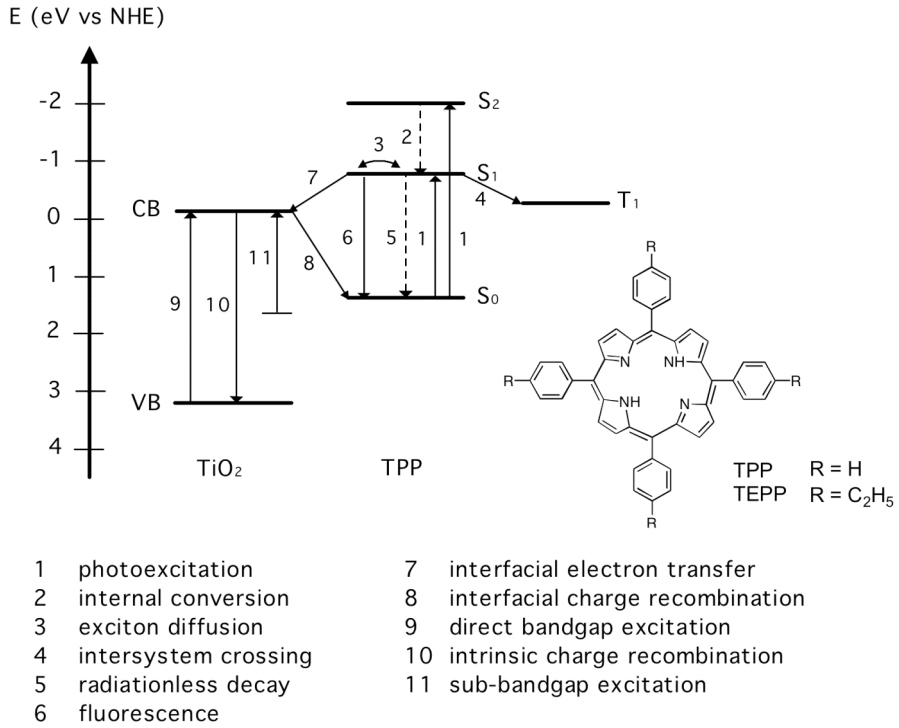

Figure 3.1. The energy levels of *meso*-tetraphenylporphyrin (TPP) in solution, the conduction (*CB*) and valence band (*VB*) positions of anatase TiO_2, and the processes occurring on optical excitation. The inset shows the chemical structure of the porphyrins investigated.

Porphyrin-based dyes have attracted considerable attention to be applied as sensitizers because of the overlap of their optical absorption spectrum with the solar emission spectrum. Combined with TiO_2 or SnO_2 as an electron acceptor, efficient charge separation has been observed.[12-18] Current research is focused on improvement of the interfacial electron injection yield by the use of binding groups and linkers[19-22], on enhancement of the exciton diffusion length[4,5,23-26] and improvement of the charge

transport properties.[21, 27, 28] It is well known that derivatives of tetraphenylporphyrins can form dimers or larger aggregates, in solution[29-31] and in thin films.[30, 32] Previous studies have shown that aggregation affects the exciton natural lifetime[31,33,34] and the quantum yield for interfacial electron injection (ϕ_{inj}).[35]

Recently, we have studied charge separation in *meso*-tetra(4-n-octylphenyl)porphyrin/TiO_2 bilayers.[23] The incident photon to charge separation efficiency (IPCSE) at the absorption maximum was found to be 10 %. After heating above the crystalline-lamellar discotic phase transition temperature of the porphyrin the IPCSE decreases to 1 %. The change of the IPCSE has been attributed to a change of the porphyrin layer structure from isotropic before heating to an anisotropic layer consisting of columnar aggregates oriented with their long axis parallel to the TiO_2 substrate after heating. This negative temperature effect on the IPCSE is of course undesirable for practical use of porphyrin dyes in photovoltaic devices.

Also the introduction of a Pd atom in *meso*-tetra(4-carboxyphenyl)porphyrin molecules has been found to increase the IPCSE at the absorption maximum from 1 % to 12 %.[36,37] Exciton transport in these porphyrin films occurs via the triplet level. The exciton diffusion length in these layers equals 28 nm, resulting from an exciton lifetime of 10 μs and an exciton diffusion coefficient of 8×10^{-11} m^2/s. Exciton transport via the triplet route, however, is less attractive as compared to transport via the singlet route because of unwanted chemical degradation of the dye.[38,39]

The aim of the present work is to provide information on the exciton diffusion length and the efficiency of photo-induced charge separation in bilayers of the porphyrin derivatives *meso*-tetraphenylporphyrin (TPP) and *meso*-tetra(4-ethylphenyl)porphyrin (TEPP) with TiO_2. These porphyrins differ by an ethyl group at the para-phenyl positions (see inset of Figure 3.1). Steady-state optical absorption and fluorescence spectroscopy as well as fluorescence lifetime measurements on films spin-coated on quartz substrates were used to characterize the porphyrin layer. Charge separation efficiencies in porphyrin/TiO_2 bilayers were determined with the time-resolved microwave conductivity (TRMC) method. Excitons were created in the dye layer by illumination with a nanosecond laser pulse, which results in a change in conductivity due to electron injection into the TiO_2 film. Charge separation efficiencies were determined as a function of intensity, wavelength and porphyrin layer thickness. Values for the exciton diffusion length and the interfacial injection yield were obtained by fitting an analytical model for exciton diffusion to the experimental data. Together with the measured fluorescence

lifetimes, these values were used to derive the exciton diffusion coefficients in the porphyrin layers. The knowledge about the factors determining the exciton diffusion length is useful for the development of more efficient solar cells based on porphyrins.

3.2. Experimental methods

Sample preparation: Thin smooth TiO_2 films were purchased from Everest Coatings, Delft, The Netherlands. They were prepared by chemical vapor deposition onto 1x12x25 mm^3 quartz substrates, followed by annealing in air at 450 °C for 1 h in order to obtain anatase TiO_2.[40] The TiO_2 film thickness was ca. 100 nm. *Meso*-tetraphenylporphyrin (TPP) and *meso*-tetra(4-ethylphenyl)porphyrin (TEPP) were purchased from Porphyrin Systems and Frontier Scientific, respectively, and were used without further purification. Thin porphyrin films were prepared by spin-coating from a solution in $CHCl_3$ (Anhydrous, 99+%, Aldrich) at 2500 rpm under N_2 atmosphere onto either a quartz or a TiO_2 substrate. Prior to film deposition, these substrates were dried at 450 °C for 1 h in order to remove H_2O from the surface. Film thicknesses of porphyrin layers were determined by a Veeco Dektak 8 Stylus Profiler. The S_0 levels of TPP and TEPP were determined by cyclic voltammetry, using an Ag/AgCl reference electrode and a 0.5 M tetrabutylammonium perchlorate solution in acetonitrile. The position of the S_0 level was found to be equal to 1.3 eV vs. NHE for both compounds.

Optical characterization: Optical transmission spectra of dilute solutions of the porphyrin molecules in $CHCl_3$ were recorded with a Perkin Elmer Lambda 40 UV/VIS spectrometer. Optical transmission and reflection spectra of thin films were recorded with a Perkin Elmer Lambda 900 UV/VIS/NIR spectrometer, using an integrating sphere. From the transmission and reflection spectra, the fraction of absorbed light (F_A) and the optical density (*OD*) were calculated.[17] Steady-state fluorescence spectra were recorded with a Photon Technology International Photoluminescence setup. Fluorescence lifetime measurements on dilute solutions were performed by illumination with a pulsed Megaplus N_2 laser (337 nm, pulse width < 1 ns) and detecting the fluorescence at 660 nm. Transient fluorescence data of thin films were collected using an IBH NanoLED-07 pulsed laser diode excitation source (404 nm, pulse width < 100 ps). The emission was detected through a 650 nm band pass filter by a Hamamatsu microchannel plate photomultiplier. The total instrument response time was 100 ps. The resulting decay curves were analyzed using IBH DAS6 analysis software.

TRMC measurements: The TRMC technique has been fully described previously.[5, 41] The porphyrin/TiO_2 bilayers were mounted in an X-band microwave cavity at a position of maximum electric field. To exclude any O_2-induced degradation effects of the organic layer, sample preparation and experiments were performed under N_2 atmosphere. The microwave frequency used in these experiments was ca. 8.45 GHz.

Pulses in a wavelength range of 410 nm to 700 nm (pulse width 3 ns) were obtained by pumping an OPO with the third harmonic of a Q-switched Nd:YAG laser (Infinity, Coherent). In order to obtain pulses with a wavelength in the UV part of the spectrum, visible laser pulses were frequency doubled by a SHG yielding pulses with a width of 2.5 ns. The sample was illuminated either through the quartz substrate ('backside', (BS)) or through the porphyrin layer ('front-side', (FS)). The incident intensity was varied between 10^{11}-10^{13} photons/cm^2 per pulse, using metallic neutral density filters.

The formation of mobile charge carriers due to pulsed illumination leads to an increase of the conductance (ΔG), which is followed by an eventual decrease resulting from decay of charge carriers. The change in microwave power reflected by the microwave measuring cell on pulsed illumination (ΔP) was monitored using microwave circuitry and detection equipment which has been described previously.[41] The temporal change in reflected microwave power is related to ΔG by:

$$\frac{\Delta P(t)}{P} = -K\Delta G(t) \tag{3.2}$$

The sensitivity factor K was determined as described previously[42] and had a value of 7×10^4 S^{-1} for the current cell design and materials. The change in conductance is related to the product of the average concentrations (N_i) and mobilities (μ_i) of charge carriers by:

$$\Delta G(t) = e\beta L \sum N_i(t)\mu_i \tag{3.3}$$

In equation 3.3, β is the ratio between the broad and narrow inner dimensions of the waveguide (2.08 for the X-band waveguide used), L is the thickness of the TiO_2 layer and e the elementary charge. From the maximum of the photoconductance during time (ΔG_{max}), the parameter $\eta\Sigma\mu$ is calculated according to:

$$\eta\sum\mu = \frac{\Delta G_{\max}}{e\beta I_0} \tag{3.4}$$

where I_0 is the integrated incident light intensity (photons/cm^2/pulse) , $\Sigma\mu$ is the sum of the hole and electron mobilities and η is the number of charge carrier pairs produced per incident photon at the time where the photoconductance is maximal.

For a bilayer system, the incident photon to charge separation efficiency (IPCSE) was derived in the following way. Since the electron mobility (μ_e) in anatase TiO_2 is much higher than the hole mobility, $\Sigma\mu$ is close to equal to the electron mobility.[43] The electron mobility in TiO_2 was obtained on direct bandgap excitation (Figure 3.1, process 9) using UV (300 nm) radiation. At 300 nm photons absorbed by the semiconductor lead to formation of free electrons in the conduction band, hence

$$\sum \mu \approx \mu_e \approx \frac{\left[\eta \sum \mu\right]_{300\ nm}}{\phi F_{A,300\ nm}} \tag{3.5}$$

where ϕ is the quantum yield for charge carrier formation, which is assumed to be equal to one.[44] In a porphyrin/TiO_2 bilayer, the mobility of holes in the porphyrin layer is much lower than the electron mobility in TiO_2,[43,45] therefore only the production of mobile electrons in TiO_2 results in a measurable change of the microwave conductivity. From μ_e and $\eta\Sigma\mu$ obtained on pulsed illumination of a bilayer system with visible light, the IPCSE can thus be calculated using equation 3.6:

$$IPCSE = \frac{\left[\eta \sum \mu\right]}{\mu_e} \cdot 100\ \% \tag{3.6}$$

3.3. Results

3.3.1. Optical characterization

Effects of chemical structure and intermolecular interactions on the photophysical properties of the materials were studied by absorption and fluorescence measurements on solutions and thin films. Figure 3.2A shows the normalized optical density spectra of dilute solutions of TPP and TEPP in $CHCl_3$, together with their steady-state fluorescence spectra. For both solutions identical absorption and fluorescence spectra and fluorescence quantum yields were found. The S_0-S_2 transition results in a strong absorption band between 400 nm and 450 nm (the 'Soret' band) with an absorption maximum at 420 nm. Transitions from S_0 to two energetically slightly different S_1 levels and their higher vibrational modes cause the less intense Q bands between 500 nm and 700 nm.[46] From the observation that excitation at 430 nm and at 520 nm yield identical fluorescence spectra, it is concluded that electrons excited to the S_2 or a higher level decay rapidly to the S_1 level by internal conversion (Figure 3.1, process 2). The most intense fluorescence

was recorded at 654 nm, which is due to the S_1-S_0 transition. The second fluorescence band at 716 nm is caused by a transition to a vibrationally excited state of the S_0 level.

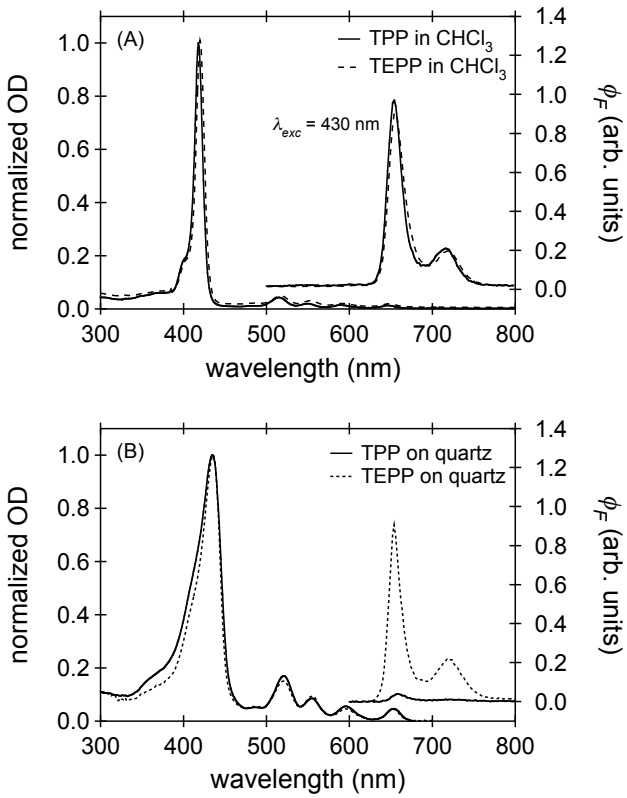

Figure 3.2. Normalized optical density spectra and relative fluorescence quantum yields as a function of wavelength for TPP (solid lines) and TEPP (dashed lines) in solution (A) and as spin-coated films (30 ± 5 nm) on quartz (B).

Figure 3.2B shows the normalized optical density and fluorescence spectra of TPP and TEPP films on quartz. The absorption spectra of both films show a red-shift and a broadening of the Soret band as compared to the spectra in solution. Both films exhibit a maximum absorption at 435 nm. In comparison to TEPP, the TPP film exhibits a small broadening of at most 20 nm at the blue-side of the Soret band. Much larger differences between TPP and TEPP layers were found in the fluorescence spectra. The location of the fluorescence maxima of the films are similar to those of the solutions, but in contrast to the equal fluorescence quantum yields in solution, films of TEPP exhibit an approximately 20 times higher fluorescence quantum yield than TPP films. The fluorescence quantum yields of both films were found to be independent of the intensity of the excitation light. Hence, bimolecular exciton-exciton annihilation does not play a significant role at the intensities applied.

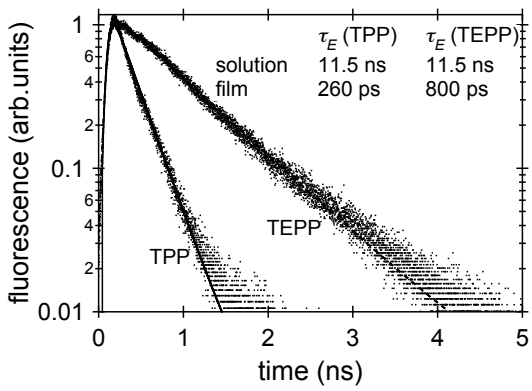

Figure 3.3. Fluorescence decay of 30±5 nm thick TPP (solid line) and TEPP (dashed line) films on quartz together with the corresponding mono-exponential fits. The exciton lifetimes in solution and in the films are given in the inset.

The solutions of TPP and TEPP were found to exhibit an identical fluorescence lifetime of 11.5 ns, which is comparable to literature values for TPP.[47, 48] In contrast, the time-resolved fluorescence decays in Figure 3.3 show that excitons in TEPP films decay more slowly than those in TPP films. Fitting of a mono-exponential decay convoluted over the excitation pulse duration and the time-response of detection yields singlet exciton lifetimes equal to τ_E = 260 ps and τ_E = 800 ps for TPP and TEPP films, respectively. The exciton lifetime of 310 ps found by Hall and co-workers[49] for TPP films is comparable to the result from the current work.

The differences in fluorescence quantum yield and singlet exciton lifetime are caused by different rate constants for the exciton decay processes (Figure 3.1, processes 4-7). Since the porphyrin films are deposited on quartz, interfacial electron transfer can be ruled out. The possible decay pathways are intersystem crossing, radiationless decay and fluorescence. The exciton lifetime is related to the rate constants for fluorescence (k_F), radiationless decay (k_{NR}) and intersystem crossing (k_{ISC}) by:[50]

$$\tau_E = \frac{1}{k_F + k_{NR} + k_{ISC}} \tag{3.7}$$

The fluorescence quantum yield (ϕ_F) is given by:[50]

$$\phi_F = \frac{k_F}{k_F + k_{NR} + k_{ISC}} = k_F \cdot \tau_E \tag{3.8}$$

Using the experimental exciton lifetimes and the ratio of the fluorescence quantum yields in TPP and TEPP films, it is found from equations 3.7 and 3.8 that the fluorescence rate constant in TEPP is approximately 7 times higher than in TPP. For metal-free porphyrins the timescale for intersystem crossing is of the order of 10 nanoseconds.[48] Since the

exciton lifetimes are much shorter, the contribution of intersystem crossing (k_{ISC}) can be neglected in equations 3.7 and 3.8. Hence, the combination of a longer τ_E and a higher k_F for TEPP films is only possible if k_{NR} is smaller than in TPP films. From the results described above it can be deduced that k_{NR} for TEPP films is at least 3 times smaller than for TPP films, see Appendix A.

3.3.2. Photoconductivity measurements

Microwave conductivity transients: Figure 3.4 shows the TRMC signals obtained on pulsed illumination at 430 nm of a bare TPP film on quartz, a TPP/TiO_2 bilayer and a TEPP/TiO_2 bilayer. The samples were illuminated through the quartz substrate ('backside'), yielding a high initial exciton concentration near the porphyrin/TiO_2 interface for the bilayer systems. Since the mobility of holes in porphyrins is much lower than the mobility of electrons in TiO_2,[43, 51] the observed change in photoconductance is due to the production of mobile electrons in the TiO_2 film. The initial rise of the TRMC signals is due to the 18 ns instrument response time of the system.

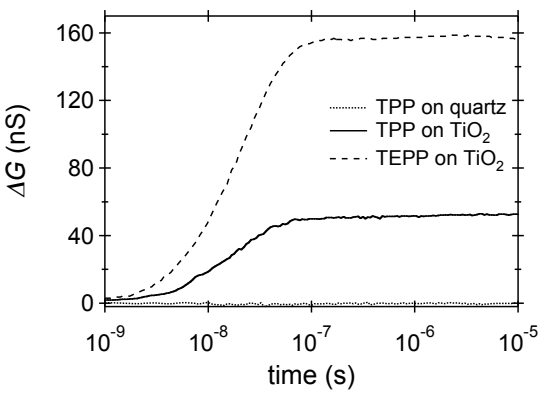

Figure 3.4. TRMC signals obtained on backside pulsed excitation at 430 nm (5×10^{12} photons/cm^2/pulse) of a bare TPP film (dotted line), a 42±5 nm TPP/TiO_2 bilayer (solid line) and a 37±5 nm TEPP/TiO_2 bilayer (dashed line).

As can be seen in Figure 3.4, illumination of a TPP film on quartz did not result in any detectable TRMC signal. The same was found for a TEPP film on quartz. Excitation of bare TiO_2 layers with visible light was found to result in a small short-lived signal, which is ascribed to sub-bandgap excitation (Figure 3.1, process 11) of electronic states within the optical bandgap.[5] Hence, the large and long-lived photoconductance observed for the bilayer systems demonstrates the photosensitization of the anatase TiO_2 by the

porphyrin layer. The charge-separated state persists to the microsecond domain. The eventual decay of the photoconductance is due to interfacial electron-hole recombination and/or electron trapping. Since the current experiments were carried out in the absence of charge collecting electrodes, the decay of the photoconductance is not due to extraction of charge carriers. For the TEPP/TiO_2 bilayer a significantly higher TRMC signal was found than for the TPP/TiO_2 bilayer, which can be attributed to more efficient charge separation in the TEPP/TiO_2 bilayer, as will be discussed below.

Charge separation efficiencies: The IPCSE can be calculated from the TRMC signal obtained on UV excitation of bare TiO_2 and the TRMC signal observed on pulsed illumination of a bilayer with visible light, using equation 3.6. Figure 3.5 shows the IPCSE values determined on 430 nm excitation of the TPP/TiO_2 and TEPP/TiO_2 bilayers as a function of the incident light intensity. At intensities below 10^{12} photons/cm^2/pulse the IPCSE values were found to be independent of the light intensity. Hence, exciton-exciton annihilation and bimolecular charge recombination processes can be neglected at these low intensities. At these intensities, the IPCSE of the TPP/TiO_2 bilayer amounts to 1.2 %, in agreement with earlier studies,[52] and to 6.2 % for the TEPP/TiO_2 bilayer.

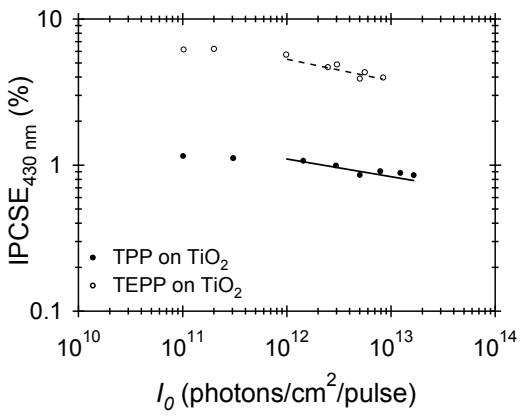

Figure 3.5. Intensity dependence of the IPCSE on 430 nm backside pulsed illumination of a 42±5 nm TPP/TiO_2 bilayer (solid dots) and a 37±5 nm TEPP/TiO_2 bilayer (open dots).

For intensities larger than 10^{12} photons/cm^2 per pulse the IPCSE was found to decrease with I_0 according to:

$$IPCSE \propto I_0^{\delta-1} \tag{3.9}$$

The exponents were found to be δ = 0.91 and δ = 0.83 for the TPP/TiO_2 and the TEPP/TiO_2 bilayers, respectively. Note that equation 3.9 corresponds to a power law dependence of the photoconductance on the intensity ($\Delta G \propto I_0^{\delta-1}$).

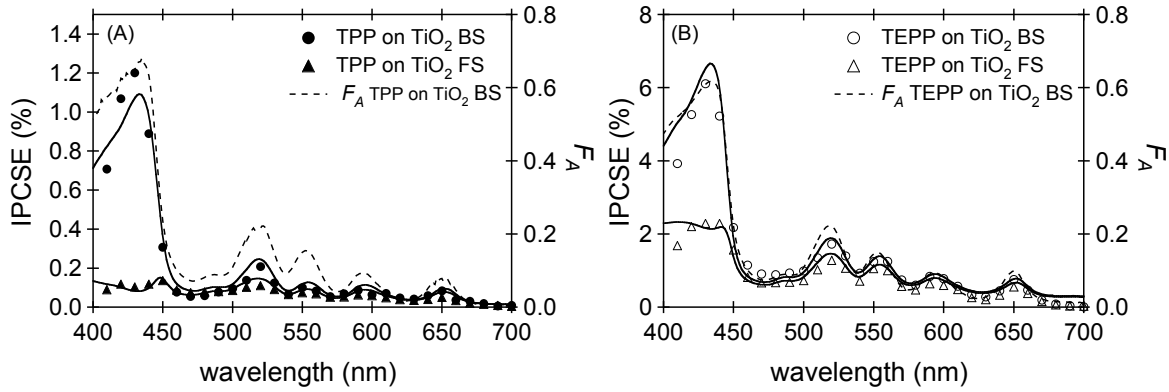

Figure 3.6. The fraction of absorbed light F_A (dashed line) and the experimental IPCSE values of a 42±5 nm TPP/TiO_2 bilayer as a function of wavelength on backside (dots) and front-side (triangles) illumination and the wavelength dependence of the IPCSE calculated using equation 3.10 with ϕ_{inj} = 0.37 and Λ_E = 7 Å (A) (solid lines). The results for a 37±5 nm TEPP/TiO_2 bilayer are shown in (B), with ϕ_{inj} = 0.37 and Λ_E = 75 Å.

Figure 3.6 shows the IPCSE as function of wavelength ('photoaction spectrum') for both bilayers determined on backside and front-side illumination as well as their optical attenuation spectra. The average illumination intensity was equal to 6×10^{12} photons/cm^2/pulse. To correct for bimolecular effects due to variations in illumination intensity over this wavelength range, the measured IPCSE values were extrapolated to an illumination intensity of 1×10^{11} photons/cm^2/pulse using equation 3.9. It is obvious that the photoaction spectra for backside illumination of both TPP/TiO_2 and TEPP/TiO_2 closely follow the corresponding optical attenuation spectra, which again demonstrates the photosensitization of TiO_2 by the porphyrin layers. In case of backside illumination, excitons are mainly created near the porphyrin/TiO_2 interface. In contrast, front-side illumination leads mainly to formation of excitons near the porphyrin/gas interface and especially in case of a short optical absorption length only few excitons near the porphyrin/TiO_2 interface. Since the thickness of the porphyrin layer is expected to largely exceed the exciton diffusion length, only excitons created near the porphyrin/TiO_2 interface result in charge separated states. Hence, front-side illumination results in lower IPCSE values than backside illumination.

Parameters affecting the IPCSE: The exciton diffusion length and the interfacial electron injection yield can be obtained using the theoretical model for the IPCSE described previously.[53] The IPCSE depends on the fraction of incident photons that is reflected by the bilayer (F_R), the number of excitons that reaches the porphyrin/TiO_2 interface normalized to the number of incident photons (S) and the interfacial injection yield relative to all modes of interfacial exciton deactivation (ϕ_{inj}):

$$IPCSE = \left(1 - F_R\right) \cdot S(\alpha, L, \Lambda_E) \cdot \phi_{inj} \cdot 100\% \qquad (3.10)$$

S depends on the exponential optical absorption coefficient (α), the porphyrin layer thickness (L) and the exciton diffusion length (Λ_E). Analytical expressions for S on backside (S_{BQ}) and front-side illumination (S_{FQ}) have been derived by solving the classical diffusion equation for steady-state conditions and are given in Appendix B.[53-55] Accurate values for ϕ_{inj} and Λ_E can be obtained by varying the thickness of the porphyrin layer. If the thickness of the porphyrin layer is much larger than the exciton diffusion length, a large difference in IPCSE between backside and front-side illumination can be expected. In that case the IPCSE does not vary much with layer thickness for backside illumination. This is due to the fact that mainly those excitons created within a distance Λ_E from the interface can undergo interfacial charge separation. In contrast, for front-side illumination increasing L leads to a smaller concentration of excitons near the porphyrin/TiO_2 interface. As a consequence the IPCSE decreases with increasing L and eventually becomes zero. If the thickness of the porphyrin layer is smaller than the exciton diffusion length, the difference in IPCSE between backside and front-side illumination disappears, since in this case all excitons are able to reach the porphyrin/TiO_2 interface. Increasing L will then lead to an increase of the IPCSE since more light is absorbed as the layer becomes thicker.

Figures 3.7A and 3.7B show the dependence of the IPCSE on the porphyrin layer thickness on backside and front-side illumination for TPP/TiO_2 and TEPP/TiO_2 bilayers, respectively. Since F_R varied between different samples, the ratio of IPCSE to (1-F_R) is shown. The data presented in Figure 3.7A exhibit a dependence of the IPCSE on L that does not agree with the expectations as discussed in the previous paragraph. This is most likely due to variation of porphyrin layer structure, and consequently the exciton diffusion length, with the layer thickness, as will be discussed in the next section. The data in Figure 3.7B can be excellently described by equation 3.10 and equations B1 and B2 (See Appendix B). Fits of these equations to the experimental data yield an exciton diffusion

length of 75 Å and an interfacial electron injection yield ϕ_{inj} = 0.37 for a TEPP/TiO_2 bilayer. With these parameters and the known wavelength dependence of α, also the front-side and backside photoaction spectra for the TEPP/TiO_2 bilayer were calculated, see Figure 3.6B. The calculated action spectra agree very well with the experimental results.

Although the thickness dependence of the IPCSE for the TPP/TiO_2 bilayers in Figure 3.7A cannot be described by equation 3.10 and equations B1 and B2, the photoaction spectrum for a particular porphyrin layer thickness could be described by these equations, see the fits in Figure 3.6A. The photoaction spectrum in Figure 3.6A was obtained for a sample for which $L >> \Lambda_E$. In this case the IPCSE is mainly determined by the product of ϕ_{inj} and Λ_E. Therefore it is not possible to determine accurate values of these parameters independently. Taking the interfacial electron injection yield in TPP/TiO_2 bilayers equal to those found for TEPP/TiO_2 layers yields an exciton diffusion length of 7 Å, which is more than 10 times smaller than Λ_E in TEPP layers.

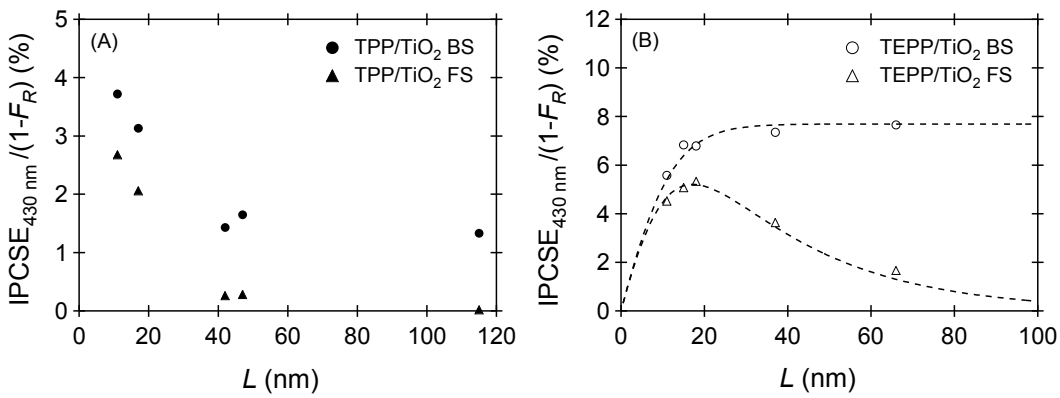

Figure 3.7. IPCSE/(1-F_R) as a function of the porphyrin layer thickness for TPP/TiO_2 (A) and TEPP/TiO_2 (B) bilayers, obtained on excitation at 430 nm with 5×10^{12} photons/cm^2/pulse. Dots represent backside illumination, triangles front-side illumination.

3.4. Discussion

The exciton diffusion lengths and lifetimes can be used to determine the singlet exciton diffusion coefficient using equation 3.1. This yields a value of 2×10^{-9} m^2/s for a TPP layer and a much higher value of 7×10^{-8} m^2/s for a TEPP layer. Both values are much larger than the triplet exciton diffusion coefficient observed in Pd substituted

porphyrin layers (8×10^{-11} m^2/s).[36, 37] For the porphyrin molecules considered here, exciton diffusion is expected to occur via the Förster mechanism.[56,57] Förster energy transfer occurs by the exchange of a virtual photon, with hopping rate k_{ET}, and can only occur if there is a non-zero overlap of the emission and the absorption spectra. The data in Figure 3.2B show that the latter condition is fulfilled. The exciton diffusion constant is linearly proportional to the fluorescence rate constant according to: [56, 58]

$$D_E = k_{ET} \cdot R_{DA}^2 = \frac{9000(\ln 10)\kappa^2 J_F k_F}{128\pi^5 n^4 N_A R_{DA}^4} \tag{3.11}$$

In equation 3.11, κ^2 is a factor describing the relative orientation of the transition dipoles of donor and acceptor species, J_F an integral taking into account the overlap of the absorption and emission spectra, n the refractive index, N_A Avogadro's number and R_{DA} the distance between donor and acceptor species. According to equation 3.11 the larger k_F found for TEPP layers leads to a higher exciton diffusion coefficient. The value of k_F for TEPP is 7 times higher than for TPP, while the exciton diffusion coefficient is a factor 35 higher. This could be due to the fact that also κ^2 and/or R_{DA} are different for TPP and TEPP layers.

The lower fluorescence rate constant found for TPP films could be caused by the presence of face-to-face molecular dimers or larger aggregates. In such aggregates electronic coupling between the molecular orbitals on the individual molecules leads to a splitting of the electronic levels, as shown in Figure 3.8 for a dimer. In porphyrin molecules the transition dipole moments for the S_0-S_2 and S_0-S_1 transitions are parallel to the plane of the molecule.[46] Hence face-to-face molecular stacking leads to formation of H-aggregates.[59] For H-dimers the in-phase interaction of the two transition dipole moments leads to the higher lying E" level and the out-of-phase interaction yields the lower lying E' level, as discussed by Kasha.[60] The optical transition between the E' exciton state and the ground state is forbidden. Analogously, in larger H-aggregates the optical transition between the lowest exciton state and the ground state is forbidden. Hence fluorescence from the lowest excited state is prevented by formation of H-aggregates. In that case, exciton diffusion between different H-aggregates via the Förster mechanism is impossible. The low fluorescence rate constant and the small exciton diffusion coefficient in TPP layers could thus be due to the presence of H-aggregates. The ethyl groups in TEPP seem to reduce the extent to which H-aggregates are present in the film. The stronger tendency of TPP molecules to form H-aggregates may be caused by

the lower solubility in $CHCl_3$ due to the absence of alkyl side chains. The average distance or the relative orientation between individual molecules in non-aggregated domains in a film may differ from the mutual arrangement of different H-aggregates. These differences in R_{DA} or κ^2 may also lower D_E as follows from equation 3.11, explaining that the exciton diffusion coefficient in TEPP layers is 35 times larger than in TPP layers while the value of k_F is only a factor 7 higher.

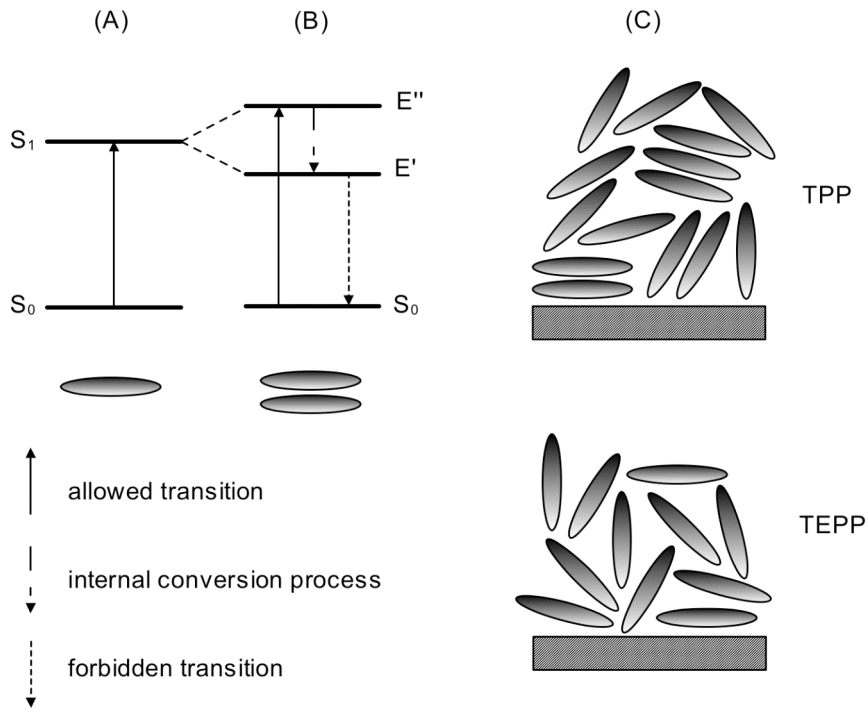

Figure 3.8. Representation of the energy levels of a porphyrin monomer (a) and a dimeric H-aggregate (b). In (c) a schematic view of the structure of TPP and TEPP layers is shown.

The tendency of TPP molecules to form H-aggregates can also explain the unexpected thickness dependence of the IPCSE for TPP/TiO_2 bilayers, shown in Figure 3.7A. Thicker TPP layers were prepared by spin-coating from a more concentrated solution, in which formation of H-aggregates is expected to occur to a larger extent. If this is the case, the exciton diffusion length decreases for thicker TPP layers. This would in turn lead to a decrease of the IPCSE with increasing porphyrin layer thickness, as indeed observed for TPP, see Figure 3.7A. Since the shapes of the fluorescence spectra of the TPP and TEPP layers (Figure 3.2B) are very similar, it is likely that the remaining fluorescence of the TPP layer is due to non-aggregated porphyrin molecules. This indicates the presence of both H-aggregates and single molecules in TPP layers.

Note, that formation of H-aggregates in a film does not necessarily lead to a blue-shift of the absorption spectrum as compared to the solution spectrum. This can be due to the fact that the change in dielectric environment on going from a solution to a film may result in a red-shift, which can dominate over the blue-shift due to formation of H-aggregates. The identical onset of the Soret band at the red side observed for TPP and TEPP films indicates that in both films non-aggregated molecules are present. The tail at the blue side of the Soret band observed for TPP films is attributed to a minor amount of H-aggregates.

Since the energy of an exciton on an H-aggregate will be lower than on an individual molecule in a less ordered domain in the film, H-aggregates may act as exciton traps. Exciton diffusion between H-aggregates is hampered due to the negligible Förster transfer rate, as a result of the forbidden fluorescence transition. However, excitons may well be delocalized over an entire H-aggregate.[61] Hence, in case the dye layer consists of H-aggregates oriented perpendicularly to the TiO_2 substrate and in contact with the latter, the exciton diffusion length corresponds to the length of the H-aggregate. In case long H-aggregates can be arranged in this manner, a high charge separation efficiency may be achieved. Our work, however, indicates that a relatively long exciton diffusion length and consequently a high charge separation efficiency can also be realized in a layer in which energy transfer occurs between randomly oriented single molecules.

The value of ϕ_{inj} = 0.37 found for the interfacial electron injection yield in a TEPP/TiO_2 bilayer is significantly smaller than the electron injection yield close to unity reported earlier for *meso*-tetra(4-carboxyphenyl)porphyrin on nanocrystalline TiO_2.[62] Note that ϕ_{inj} is defined as the fractional yield of free electrons due to dissociation of excitons that have reached the interface between the porphyrin layer and the TiO_2. Hence, the interfacial injection yield is not affected by the exciton diffusion length and therefore the present value of ϕ_{inj} can be directly compared with the results for the system studied in ref. 62 in which each porphyrin molecule is directly attached to TiO_2. The fact that the electron injection yield found in the present work differs from that in ref. 62 could be due to the fact that the measurements described in ref. 62 were carried out in the presence of an external electric field, which prevents geminate recombination. Alternatively, it could be argued that the absence of an anchoring group reduces the electronic interaction between the porphyrin molecule and TiO_2, thus leading to a lower electron injection

yield.[63] Enhancement of the relatively low injection yield offers the opportunity of a further improvement of the charge separation efficiency in TEPP/TiO_2 bilayer systems.

3.5. Conclusions

The charge separation efficiency per incident photon in TEPP/TiO_2 bilayers is 6.2 % for excitation at the Soret band maximum, which is considerably higher than the efficiency of 1.2 % found for TPP/TiO_2 bilayers. This difference is attributed to a larger exciton diffusion length in TEPP. The exciton diffusion length in TEPP is found to be 75 Å, while this is only 7 Å in TPP layers. The larger exciton diffusion length in TEPP layers in mainly due to a higher exciton diffusion coefficient, which is equal to 7×10^{-8} m^2/s for TEPP and only 2×10^{-9} m^2/s for TPP. The larger exciton diffusion length is also caused by a longer exciton lifetime, which is found to be 800 ps for TEPP and only 260 ps for TPP. The lower exciton diffusion constant in TPP layers is explained in terms of the presence of H-aggregates.

Acknowledgment

The authors thank Dr. F.C. Grozema, Dr. H. Donker and Dr. J.M. Warman for fruitful discussions. The research was supported financially by the Delft Research Centre for Sustainable Energy.

Supporting Information

Appendix A

The lower limit of the ratio of the rate constants for radiationless decay of excitons in TPP and TEPP layers can be derived from equations 3.7 and 3.8 and the experimental exciton lifetimes and fluorescence quantum yields. Rewriting equations 3.7 and 3.8 and neglecting k_{ISC} gives equations A1 and A2:

$$k_F + k_{NR} = \frac{1}{\tau_E} \tag{A1}$$

$$k_F = \frac{\phi_F}{\tau_E} \tag{A2}$$

Equation A2 gives the ratio of the fluorescence rate constants:

$$\frac{k_{F,TEPP}}{k_{F,TPP}} = \frac{\phi_{F,TEPP}}{\phi_{F,TPP}} \frac{\tau_{E,TPP}}{\tau_{E,TEPP}} \ (\approx 7) \tag{A3}$$

Equation A1 gives for TPP and TEPP:

$$k_{F,TPP} + k_{NR,TPP} = \frac{1}{\tau_{E,TPP}} \tag{A4}$$

$$k_{F,TEPP} + k_{NR,TEPP} = \frac{1}{\tau_{E,TEPP}} \tag{A5}$$

Since all rate constants have to be positive, equation A5 gives for the rate constants for fluorescence and radiationless decay in TEPP films:

$$k_{F,TEPP} \leq \frac{1}{\tau_{E,TEPP}} \tag{A6}$$

$$k_{NR,TEPP} \leq \frac{1}{\tau_{E,TEPP}} \tag{A7}$$

Combination of equations A3 and A6 yields:

$$k_{F,TPP} \leq \frac{\phi_{F,TPP}}{\phi_{F,TEPP}} \frac{1}{\tau_{E,TPP}} \tag{A8}$$

Combination of A4 and A8 gives:

$$k_{NR,TPP} \geq \frac{1}{\tau_{E,TPP}} - \frac{\phi_{F,TPP}}{\phi_{F,TEPP}} \frac{1}{\tau_{E,TPP}} \tag{A9}$$

From equations A7 and A9, the ratio of the rate constants for radiationless decay is obtained:

$$\frac{k_{NR,TPP}}{k_{NR,TEPP}} \geq \left(\frac{1}{\tau_{E,TPP}} - \frac{\phi_{F,TPP}}{\phi_{F,TEPP}} \frac{1}{\tau_{E,TPP}} \right) \cdot \tau_{E,TEPP} \tag{A10}$$

Substitution of the measured exciton lifetimes and the ratio of the fluorescence quantum yields gives:

$$\frac{k_{NR,TPP}}{k_{NR,TEPP}} \geq 3 \tag{A11}$$

Appendix B

The factor S represents the number of excitons that reaches the porphyrin/TiO_2 interface normalized to the number of incident photons. In case of exciton quenching at the porphyrin/gas interface, S on backside illumination (S_{BQ}) depends on the exponential optical absorption coefficient (α), the porphyrin layer thickness (L) and the exciton diffusion length (Λ_E) according to:

$$S_{BQ} = \left(\frac{\alpha^2 \Lambda_E^2}{\alpha^2 \Lambda_E^2 - 1} \right) \left(1 + \frac{e^{-\alpha L} \csc h\left(\frac{L}{\Lambda_E} \right) - \coth\left(\frac{L}{\Lambda_E} \right)}{\alpha \Lambda_E} \right) \tag{B1}$$

The value for S on front-side illumination (S_{FQ}) follows from:

$$S_{FQ} = \left(\frac{\alpha^2 \Lambda_E^2}{\alpha^2 \Lambda_E^2 - 1} \right) \left(\frac{\csc h\left(\frac{L}{\Lambda_E} \right) - e^{-\alpha L} \coth\left(\frac{L}{\Lambda_E} \right)}{\alpha \Lambda_E} - e^{-\alpha L} \right) \tag{B2}$$

References

(1) Grätzel, M., *Nature* **2001,** 414, 338-344.

(2) Savenije, T. J.; Warman, J. M.; Goossens, A., *Chemical Physics Letters* **1998,** 287, (1-2), 148-153.

(3) Breeze, A. J.; Schlesinger, Z.; Carter, S. A.; Brock, P. J., *Phys. Rev. B.* **2001,** 6412, (12), 125205.

(4) Kerp, H. R.; Donker, H.; Koehorst, R. B. M.; Schaafsma, T. J.; Faassen, E. E. v., *Chemical Physics Letters* **1998,** 298, (4-6), 302-308.

(5) Kroeze, J. E.; Savenije, T. J.; Warman, J. M., *Journal of Photochemistry and Photobiology A-Chemistry* **2002,** 148, 49-55.

(6) O'Regan, B.; Grätzel, M., *Nature* **1991,** 353, (6346), 737-740.

(7) Bach, U.; Lupo, D.; Comte, P.; Moser, J. E.; Weissortel, F.; Salbeck, J.; Spreitzer, H.; Grätzel, M., *Nature* **1998,** 395, (6702), 583-585.

(8) Sommeling, P. M.; Spath, M.; Smit, H. J. P.; Bakker, N. J.; Kroon, J. M., *Journal of Photochemistry and Photobiology A-Chemistry* **2004,** 164, (1-3), 137-144.

(9) Kruger, J.; Plass, R.; Grätzel, M., *Applied Physics Letters* **2002,** 81, (2), 367-369.

(10) Schmidt-Mende, L.; Zakeeruddin, S. M.; Grätzel, M., *Applied Physics Letters* **2005,** 86, (1), 013504.

(11) Beek, W. J. E.; Wienk, M. M.; Janssen, R. A. J., *Advanced Materials* **2004,** 16, (12), 1009.

(12) Kay, A.; Humphrybaker, R.; Grätzel, M., *Journal of Physical Chemistry* **1994,** 98, (3), 952-959.

(13) Fessenden, R. W.; Kamat, P. V., *Journal of Physical Chemistry* **1995,** 99, (34), 12902-12906.

(14) Boschloo, G. K.; Goossens, A., *Journal of Physical Chemistry* **1996,** 100, (50), 19489-19494.

(15) Koehorst, R. B. M.; Boschloo, G. K.; Savenije, T. J.; Goossens, A.; Schaafsma, T. J., *Journal of Physical Chemistry B* **2000,** 104, (10), 2371-2377.

(16) Tachibana, Y.; Haque, S. A.; Mercer, I. P.; Durrant, J. R.; Klug, D. R., *Journal of Physical Chemistry B* **2000,** 104, (6), 1198-1205.

(17) Kroeze, J. E.; Savenije, T. J.; Warman, J. M., *Journal of the American Chemical Society* **2004,** 126, 7608.

(18) Hasobe, T.; Kashiwagi, Y.; Absalom, M. A.; Sly, J.; Hosomizu, K.; Crossley, M. J.; Imahori, H.; Kamat, P. V.; Fukuzumi, S., *Advanced Materials* **2004,** 16, (12), 975-979.

(19) Odobel, F.; Blart, E.; Lagree, M.; Villieras, M.; Boujtita, H.; El Murr, N.; Caramori, S.; Bignozzi, C. A., *Journal of Materials Chemistry* **2003,** 13, (3), 502-510.
(20) Clifford, J. N.; Yahioglu, G.; Milgrom, L. R.; Durrant, J. R., *Chemical Communications* **2002**, (12), 1260-1261.
(21) Wamser, C. C.; Kim, H. S.; Lee, J. K., *Optical Materials* **2003,** 21, (1-3), 221-224.
(22) Campbell, W. M.; Burrell, A. K.; Officer, D. L.; Jolley, K. W., *Coordination Chemistry Reviews* **2004,** 248, 1363-1379.
(23) Kroeze, J. E.; Koehorst, R. B. M.; Savenije, T. J., *Advanced Functional Materials* **2004,** 14, (10), 992-998.
(24) Gregg, B. A., *Molecular Crystals and Liquid Crystals Science and Technology Section a-Molecular Crystals and Liquid Crystals* **1994,** 257, 219.
(25) Balaban, T. S.; Bhise, A. D.; Fischer, M.; Linke-Schaetzel, M.; Roussel, C.; Vanthuyne, N., *Angewandte Chemie-International Edition* **2003,** 42, (19), 2140-2144.
(26) Balaban, T. S.; Linke-Schaetzel, M.; Bhise, A. D.; Vanthuyne, N.; Roussel, C.; Anson, C. E.; Buth, G.; Eichhofer, A.; Foster, K.; Garab, G.; Gliemann, H.; Hoddard, R.; Javorfi, T.; Powell, A. K.; Rosner, H.; Schimmel, T., *Chemistry-a European Journal* **2005,** 11, (8), 2268-2275.
(27) Savenije, T. J.; Koehorst, R. B. M.; Schaafsma, T. J., *Journal of Physical Chemistry B* **1997,** 101, (5), 720-725.
(28) Savenije, T. J.; Goossens, A., *Physical Review B* **2001,** 6411, (11).
(29) Kroon, J. M.; Koehorst, R. B. M.; vanDijk, M.; Sanders, G. M.; Sudholter, E. J. R., *Journal of Materials Chemistry* **1997,** 7, (4), 615-624.
(30) Maiti, N. C.; Mazumdar, S.; Periasamy, N., *Journal of Porphyrins and Phthalocyanines* **1998,** 2, (4-5), 369-376.
(31) Khairutdinov, R. F.; Serpone, N., *Journal of Physical Chemistry B* **1999,** 103, (5), 761-769.
(32) Yatskou, N. N.; Apanasovich, V. V., *Journal of Applied Spectroscopy* **2002,** 69, (1), 82-88.
(33) Leray, I.; Vernieres, M. C.; Pansu, R.; BiedCharreton, C.; Faure, J., *Thin Solid Films* **1997,** 303, (1-2), 295-301.
(34) Yatskou, N. N.; Apanasovich, V. V.; Koehorst, R. B. M.; Hoek, A. v.; Schaafsma, T., *Journal of Applied Spectroscopy* **2003,** 70, 372.
(35) Anderson, N. A.; Ai, X.; Lian, T. Q., *Journal of Physical Chemistry B* **2003,** 107, (51), 14414-14421.
(36) Kroeze, J. E.; Savenije, T. J.; Warman, J. M., *Advanced Materials* **2002,** 14, (23), 1760-1763.
(37) Kroeze, J. E.; Savenije, T. J.; Candeias, L. P.; Warman, J. M.; Siebbeles, L. D. A., *Solar Energy Materials and Solar Cells* **2005,** 85, (2), 189-203.
(38) Scurlock, R. D.; Wang, B.; Ogilby, P. R.; Sheats, J. R.; Clough, R. L., *Journal of the American Chemical Society* **1995,** 117, 10194-10202.
(39) Granzhan, A.; Penzkofer, A.; Hauska, G., *Journal of Photochemistry and Photobiology A-Chemistry* **2004,** 165, 75-89.
(40) Van de Krol, R.; Goossens, A.; Schoonman, J., *Journal of the Electrochemical Society* **1998,** 145, (10), 3697-3697.
(41) Haas, M. P. de; Warman, J. M., *Chemical Physics* **1982,** 73, 35-53.

(42) Savenije, T. J.; Haas, M. P. de; Warman, J. M., *Zeitschrift fur Physikalische Chemie-International Journal of Research in Physical Chemistry & Chemical Physics* **1999,** 212, 201-206.
(43) Bak, T.; Nowotny, J.; Rekas, M.; Sorrell, C. C., *Journal of Physics and Chemistry of Solids* **2003,** 64, (7), 1069-1087.
(44) Shiga, A.; Tsujiko, A.; Yae, S.; Nakato, Y., *Bulletin of the Chemical Society of Japan* **1998,** 71, (9), 2119-2125.
(45) Schouten, P. G.; Warman, J. M.; Haas, M. P. de; Fox, M. A.; Pan, H. L., *Nature* **1991,** 353, (6346), 736-737.
(46) Gouterman, M., *The Porphyrins; Volume III*. Academic Press: New York, 1978; Vol. 3.
(47) Levanon, H.; Vega, S., *Journal of Chemical Physics* **1974,** 61, (6), 2265-2274.
(48) Kalyanasundaram, K.; Neumann-Spallart, M., *Journal of Physical Chemistry* **1982,** 86, (26), 5163-5169.
(49) Hall, R. S.; Oh, Y. S.; Johnson, C. S., *Journal of Physical Chemistry* **1980,** 84, (7), 756-767.
(50) Turro, N. J., *Modern Molecular Photochemistry*. The Benjamin/Cummings Publishing Company, Inc, Menlo Park, CA: 1978.
(51) Checcoli, P.; Conte, G.; Salvatori, S.; Paolesse, R.; Bolognesi, A.; Berliocchi, A.; Brunetti, F.; D'Amico, A.; Di Carlo, A.; Lugli, P., *Synthetic Metals* **2003,** 138, (1-2), 261-266.
(52) Kroeze, J. E.; Savenije, T. J.; Warman, J. M., *Proceedings of the SPIE* **2003,** 4801, 67-79.
(53) Kroeze, J. E.; Savenije, T. J.; Vermeulen, M. J. W.; Warman, J. M., *Journal of Physical Chemistry B* **2003,** 107, (31), 7696-7705.
(54) Simpson, O., *Proc. R. Soc. London Ser. A* **1957,** 238, 402-411.
(55) Sodergren, S.; Hagfeldt, A.; Olsson, J.; Lindquist, S. E., *Journal of Physical Chemistry* **1994,** 98, (21), 5552-5556.
(56) Förster, T. H., *Discuss. Faraday Soc.* **1959,** 27, 7-17.
(57) Faure, S.; Stern, C.; Guilard, R.; Harvey, P. D., *Journal of the American Chemical Society* **2004,** 126, (4), 1253-1261.
(58) Sariciftci, N. S., *Progress in Quantum Electronics* **1995,** 19, (2), 131-159.
(59) May, V.; Kühn, O., *Charge and Energy Transfer Dynamics in Molecular Systems. A Theoretical Introduction*. Wiley-VCH: Berlin, 2000.
(60) Kasha, M.; Rawls, H. R.; Ashraf Et.-Bayoumi, M., *Pure and Applied Chemistry* **1965,** 11, 371-392.
(61) Markovitsi, D.; Gallos, L. K.; Lemaistre, J. P.; Argyrakis, P., *Chemical Physics* **2001,** 269, (1-3), 147-158.
(62) Cherian, S.; Wamser, C. C., *Journal of Physical Chemistry B* **2000,** 104, (15), 3624-3629.
(63) Ma, T. L.; Inoue, K.; Noma, H.; Yao, K.; Abe, E., *Journal of Photochemistry and Photobiology A-Chemistry* **2002,** 152, (1-3), 207-212.

CHAPTER 4

Efficient light-harvesting layers of homeotropically aligned porphyrin derivatives*

Nowadays dye-sensitized solar cells are based on a nanostructured interpenetrating network of dye and semiconductor, which overcomes the prerequisite of a long exciton diffusion length, however also hampers charge carrier transport. This work demonstrates that efficient light-induced charge separation is not necessarily only obtained in case of a nanostructured network, but can also be achieved in a bilayer configuration. The efficient exciton transport present in this bilayer is attributed to a homeotropical nematic alignment of the porphyrin dye molecules.

* This chapter is based on: Annemarie Huijser, Tom J. Savenije, Arkadiusz Kotlewski, Stephen J. Picken and Laurens D.A. Siebbeles, *Advanced Materials* **2006**, *18,* 2234-2239.

4.1. Introduction

The dye-sensitized solar cell, based on a wide bandgap semiconductor photosensitized with an organic dye, is an attractive low-cost alternative to conventional silicon-based solar cells.[1] Absorption of a photon by the dye results in the formation of a strongly bound electron-hole pair, also referred to as an exciton. A key feature of the dye-sensitized solar cell is that efficient exciton decay into separate charge carriers can only occur at the interface between the dye and the semiconductor, leading to injection of an electron into the conduction band of the semiconductor.[2] Since Grätzel and co-workers reported an efficiency over 10 % for a cell based on an interpenetrating network of dye-coated nanocrystalline TiO_2 particles and a liquid electrolyte containing a iodide/triiodide redox mediator[3], the use of nanostructured films in photovoltaic devices has been studied extensively. Due to complications involved in the use of a liquid electrolyte,[4] there is presently a great interest in the development of all solid-state organic/inorganic solar cells. For these cells a maximum performance of 4 % has been realized so far.[5] The use of nanostructured networks avoids the necessity of long-range exciton diffusion through the dye layer. However, in such systems electron transport is hampered by trapping at surface defects.[6] The difficulties involved in electron transport can be avoided by using a bilayer configuration consisting of a bulk semiconductor and a relatively thick dye layer. In order to realize efficient charge separation in such a bilayer configuration, the distance excitons are able to cover by diffusion (exciton diffusion length) needs to be equal to or larger than the light penetration depth, which has a typical value of 50-100 nm. The exciton diffusion length in molecular organic dye layers is usually in the order of only a few nm[7-10], although nature shows that it is possible to transport excitation energy efficiently over considerably longer distances. An example is found in the photosynthetic apparatus of purple bacteria, which consists of reaction centers and two types of light-harvesting complexes: LHI and LHII. The light-harvesting complexes consist of chlorophyll and carotenoid molecules, kept in place by proteins.[11-13] The presence of chlorophyll molecules leads to a strong light absorption. In addition, the structure of the light-harvesting complexes provides a highly efficient pathway for exciton transport; 80 % - 90 % of the excitons formed on light absorption are transferred to the reaction center, where charge separation occurs.[14] For a few molecular dye systems only, exciton diffusion lengths considerably longer than a few nm have been realized in vacuum thermal deposited layers.[15, 16] However, the expensive elaborate deposition technique makes these layers commercially less attractive and could only be applied for a few dye materials.

Chlorophylls and their analogues are attractive candidates for application in dye-sensitized solar cells[17, 18], since these molecules strongly absorb light and they have the potential to provide pathways for long-range exciton transport. Porphyrin derivatives are of particular interest because of their improved stability as compared to chlorophylls. Of crucial importance is the realization of low-cost dye layers in which photons are efficiently harvested. Recent studies have shown that the lifetime of the excited states[19] and the mutual arrangement of porphyrin dye molecules[20, 21] play a key factor in realizing efficient light-harvesting layers. In this paper we present the results of a study on the molecular arrangement and exciton diffusion in thin spin-coated *meso*-tetra(4-n-butylphenyl)porphyrin (TnBuPP) films. It is shown that a bilayer of TnBuPP and TiO_2 yields a light-induced charge separation efficiency that largely exceeds previous findings.

Steady-state optical absorption and fluorescence spectroscopy, polarized optical microscopy, and X-ray diffraction (XRD) are used to elucidate the arrangement of TnBuPP molecules. The light-induced charge separation efficiency in 35±5 nm thick TnBuPP films spin-coated on top of a smooth TiO_2 layer is determined using the time-resolved microwave conductivity (TRMC) technique.[22] This technique is based on probing the formation of mobile charge carriers formed on pulsed illumination by a change in microwave power transmitted through the sample. The light-induced charge separation efficiency is represented by the incident photon to charge separation efficiency (IPCSE). The IPCSE denotes the ratio of the number of electrons injected into TiO_2 to the number of incident photons. Application of an analytical model for exciton diffusion to the experimental data gives the exciton diffusion length.[22]

4.2. Experimental methods

Sample preparation: Meso-tetra(4-n-butylphenyl)porphyrin (TnBuPP) (see inset Figure 4.1(II) for the chemical structure) was custom-made by Frontier Scientific, Logan, USA. Thin smooth anatase TiO_2 films with a thickness of ca. 100 nm, prepared by chemical vapor deposition onto 1x12x25 mm^3 quartz substrates, were purchased from Everest Coatings, Delft, The Netherlands. TnBuPP films with a thickness of 35±5 nm were prepared by spin-coating from a solution in $CHCl_3$ (Anhydrous, 99+%, Aldrich, c = 3 mg/ml) at 2500 rpm under N_2 atmosphere onto either a quartz (I) or a TiO_2 (II) substrate. The thickness of the TnBuPP layers was determined using a Veeco Dektak 8 Stylus Profiler.

Optical characterization: Optical transmission and reflection spectra were recorded using a Perkin Elmer Lambda 900 UV/VIS/NIR spectrometer. The fraction of absorbed light (F_A) and the optical density (OD) were calculated as described in ref. 23. The wavelength dependent OD and F_A are denoted as the "absorption spectrum" and the "optical attenuation spectrum", respectively. Steady state and time-resolved fluorescence spectra were recorded with a Lifespec – ps setup using a 405 nm excitation source (Edinburgh Instruments). Optical micrographs of the films were recorded between crossed polarizers using a Nikon Eclipse E600 Polarizing Optical Microscope.

X-Ray Diffraction Analysis: X-ray diffraction (XRD) measurements were performed in the reflection mode on a Bruker-AXS D5005 theta-theta diffractometer equipped with a diffracted-beam graphite monochromator using a Cu anode ($\lambda_{K\alpha}$= 1.5408 Å) operated at 45 kV and 40 mA.

Photoconductivity Measurements: The TRMC technique and experimental setup has been described previously.[9,24] The TnBuPP/TiO_2 bilayers were mounted in an X-band microwave cavity at a position of maximum electric field strength. The sample was illuminated through the TiO_2 substrate with an incident intensity (I_0) of 1×10^{11} photons/cm^2 per pulse.

The data analysis has been described in detail earlier.[23] Formation of mobile charge carriers due to pulsed illumination leads to an increase of the photoconductance (ΔG), followed by an eventual decrease resulting from decay of charge carriers. The increase in photoconductance is related to the normalized change in reflected microwave power ($\Delta P/P$) by:

$$\frac{\Delta P(t)}{P} = -K\Delta G(t) \tag{4.1}$$

The sensitivity factor K was determined as described in ref. 25 and equals 7×10^4 S^{-1}. From the maximum of ΔG, the incident photon to charge separation efficiency (IPCSE) was calculated as described in ref. 21.

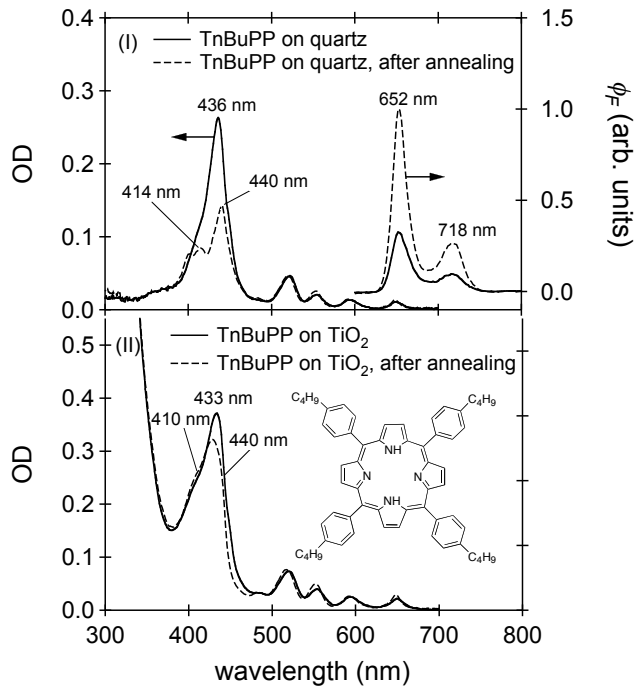

Figure 4.1. Optical density and fluorescence spectra of TnBuPP on quartz (I) and on TiO_2 (II) as spin-coated (solid) and after annealing (dashed). The chemical structure of TnBuPP is given in the inset of (II).

4.3. Results and discussion

Figure 4.1(I) shows the optical density (OD) and fluorescence spectra of 35±5 nm thick TnBuPP films spin-coated on quartz. Although TnBuPP does not exhibit a phase transition between room temperature and 300 °C[26], the OD and fluorescence spectra considerably change after annealing the film at 150 °C for 15 minutes. Annealing causes the Soret band at 436 nm to split up into a red-shifted and a blue-shifted absorption band. As compared to the Soret band, the Q-bands above 500 nm only show minor changes due to annealing, as will be explained below. The fluorescence quantum yield becomes 3 times higher due to annealing. The OD spectrum of 35±5 nm thick TnBuPP on TiO_2 is presented in Figure 4.1(II). As compared to TnBuPP on quartz, the effect of annealing on the OD is less pronounced, as will be discussed below. Fluorescence in the TnBuPP/TiO_2 bilayer is almost completely quenched, which is attributed to exciton dissociation into separate charge carriers at the interface between TnBuPP and TiO_2.

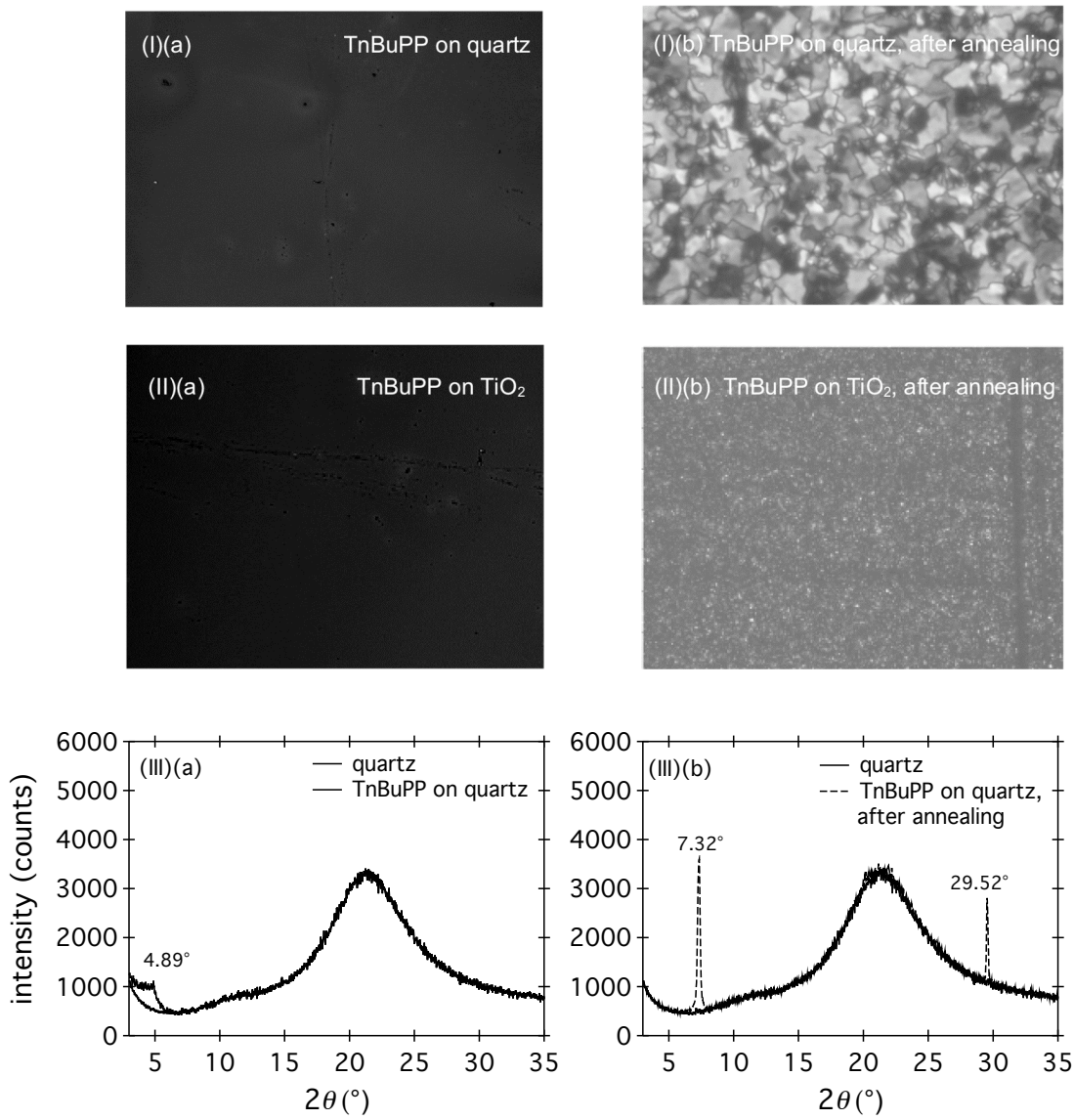

Figure 4.2. Optical micrograph of TnBuPP on quartz (I) and TiO_2 (II) as spin-coated (a) and after annealing (b) obtained between crossed polarizers with 50x magnification. Figure (III) shows the XRD patterns of quartz, TnBuPP on quartz as spin-coated (a) and after annealing (b).

Figures 4.2(I) and 4.2(II) show polarizing optical microscopy images of TnBuPP on quartz (I) and TiO_2 (II) as spin-coated (a) and after annealing (b). Both on quartz and on TiO_2 the spin-coated TnBuPP film appears dark between crossed polarizers. In addition, the colour does not change on rotation of the sample. These findings are either due to an isotropic film structure or due to a homeotropic molecular alignment (molecular planes aligned parallel to the TiO_2 substrate). Interestingly, after annealing the TnBuPP film exhibits birefrigerent domains between crossed polarizers, indicating the presence of crystalline regions. The effect of annealing on the OD spectrum and the microstructure is

less pronounced for TnBuPP on TiO_2 than TnBuPP on quartz, indicating a lower tendency for TnBuPP to form crystalline regions on a TiO_2 substrate. This could be attributed to the greater roughness of the TiO_2 substrate, as observed by Atomic Force Microscopy.

Figure 4.2(III) presents the X-ray diffraction (XRD) patterns of quartz, TnBuPP on quartz as spin-coated (a) and after annealing (b). Note that only periodic interatomic distances which are directed perpendicular to the substrate are detected.[27] The XRD pattern of TnBuPP on TiO_2 is found to be similar to that of the bare TiO_2 substrate, which could be attributed to the slight roughness of the TiO_2 substrate as compared to quartz. The presence of a broad peak in the XRD pattern of TnBuPP on quartz around $2\theta = 4.89°$ indicates the presence of molecular order in the film as spin-coated, which excludes an isotropic structure. The presence of two sharp peaks upon annealing indicates an enhancement of the degree of structural order.

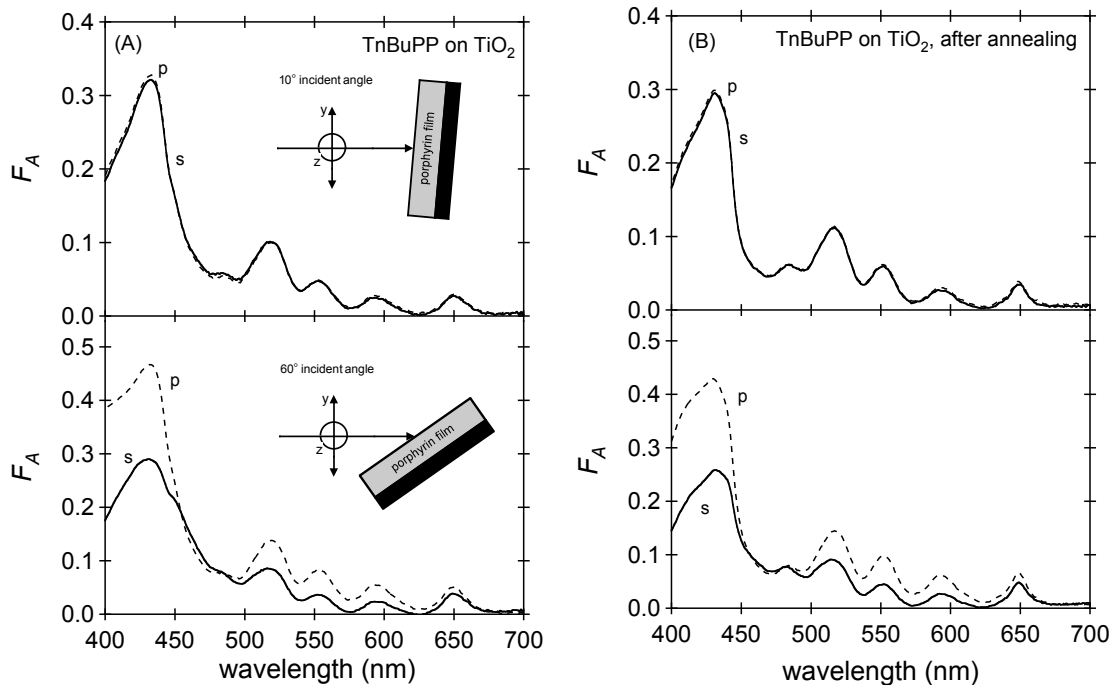

Figure 4.3. Optical attenuation spectra of TnBuPP on TiO_2 as spin-coated (A) and after annealing (B) using p- and s-polarized light and incident angles of 10° and 60°.

In order to elucidate the molecular alignment with respect to the substrate, the influence of the direction of the electric field vector of the incident light on the absorption strength has been investigated. The transition dipole moment vectors of the S_0-S_2 and the S_0-S_1 transitions are directed parallel to the plane of the molecule.[28] Maximum light

absorption is therefore achieved in case the electric field vector of the light is parallel to the molecular plane. Figure 4.3A shows the fraction of absorbed light (F_A) polarized along either the p- or the s-axis recorded at angles between incident beam and surface normal vector of 10° and 60° for TnBuPP on TiO_2 as spin-coated. Similar results were obtained for TnBuPP on quartz. At 10° the value of F_A is almost insensitive to the polarization direction of the incident light, whereas at 60° the value of F_A is considerably lower for s-polarized light. This unambiguously demonstrates that TnBuPP molecules are homeotropically aligned. Figure 4.3B shows that the annealed film exhibits similar characteristics, which implies that the homeotropic molecular alignment is preserved, However, the mutual arrangement of TnBuPP molecules changes as follows from Figures 4.1 and 4.2.

Combining the results presented in Figures 4.1-4.3 allows elucidating the structure of the film as spin-coated and after annealing. The data in Figure 4.3 are indicative for a homeotropic molecular alignment with respect to the substrate. The presence of only a broad peak and the absence of any sharp peak in the XRD pattern of the spin-coated film rules out the presence of a well-developed periodic structure directed perpendicular to the substrate. Hence, the film does not consist of columns oriented perpendicular to the substrate. Secondly, the dark appearance of the film between crossed polarizers excludes the presence of domains in which the molecular columns are tilted with respect to the substrate. We therefore conclude that the film has a frozen nematic structure[29] in which the molecules exhibit a preferential homeotropic alignment with respect to the substrate (see inset Figure 4.4A). To the knowledge of the authors, homeotropic alignment of porphyrin derivatives has been reported in one previous study only.[30] However, in the work of ref. 30 the homeotropic alignment was not uniformly present over the entire layer and was not achieved spontaneously upon film deposition. The present study is the first to show a spontaneous uniform homeotropic molecular alignment for a porphyrin derivative. The homeotropic alignment is preserved upon annealing. However, the degree of structural order considerably increases during annealing as follows from the appearance of sharp peaks in the XRD pattern. The blue- and red-shift of the Soret absorption band indicate the simultaneous presence of H- and J-aggregates. This could be due to an edge-to-edge molecular arrangement as described in refs. 31 to 33 (see inset Figure 4.4B). As compared to the Soret band, the Q-bands above 500 nm only show minor changes due to

annealing. This is attributed to the smaller transition dipole moments for the Q-bands, resulting in a smaller exciton splitting.[31]

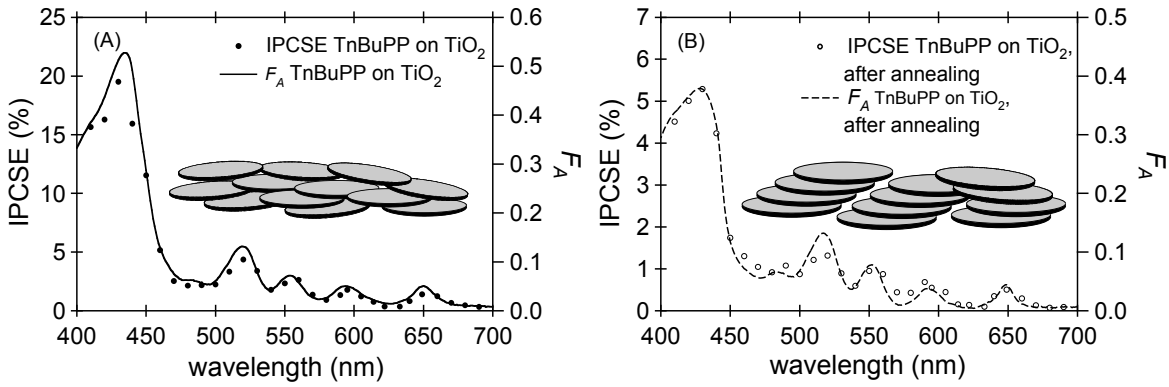

Figure 4.4. Optical attenuation and IPCSE spectra of TnBuPP on TiO_2 as spin-coated (A) and after annealing (B). The inset of (A) shows the structure of the film as spin-coated and the inset of (B) the film structure after annealing.

Figure 4.4A shows the IPCSE as function of wavelength for TnBuPP on TiO_2 as spin-coated. The IPCSE spectrum closely follows the optical attenuation spectrum included in Figure 4.4A, which demonstrates photosensitization of TiO_2 by TnBuPP. The IPCSE at the absorption maximum equals 20 %. To our knowledge, this is the most efficient charge separation for porphyrin films on smooth TiO_2 realized so far. It was found from the kinetics of the TRMC signal that electrons are injected into TiO_2 on a timescale much shorter than the 18 ns instrumental response time.[20] Hence, the contribution from long-lived triplet excitons is insignificant and charge separated states only result from singlet excited states. The presence of singlet excited states does not lead to chemical degradation, in contrast to triplet excited states.[34,35] This is an important advantage of TnBuPP/TiO_2 bilayers as compared to the bilayer described in ref. 19, for which a maximum IPCSE equal to 10 % resulting from triplet excited states was found.

The exciton diffusion length (Λ_E) was obtained from fitting a model for the charge separation efficiency to the experimental data, analogous to the work described in ref. 22

$$IPCSE = (1 - F_R)\phi_{inj} S(\alpha, \Lambda_E, L)100\% \qquad (4.2)$$

with F_R the fraction of incident photons reflected by the bilayer, ϕ_{inj} the interfacial electron injection yield relative to all modes of interfacial exciton decay and S the number of excitons that reaches the TnBuPP/TiO_2 interface normalized to the number of incident

photons. The factor S depends on the exponential optical absorption coefficient (α), the TnBuPP layer thickness (L) and Λ_E. The exciton diffusion length is related to the exciton diffusion coefficient (D_E) and the exciton lifetime (τ_E) according to:[36, 37]

$$\Lambda_E = \sqrt{D_E \tau_E} \tag{4.3}$$

At the TnBuPP/gas interface excitons could either be quenched or reflected. Analytical expressions for S in case of quenching (S_{BQ}) and reflection (S_{BR}) are given in the Supporting Information.

Taking the experimental values IPCSE = 20 %, $\alpha = 2.7\times10^7$ m^{-1}, $F_R = 0.17$ at 430 nm, L = 35 nm and the upper limit of the interfacial electron injection yield $\phi_{inj} = 1$ gives the lower limit for Λ_E. In case excitons are quenched at the TnBuPP/gas interface the lower limit of Λ_E equals 13 nm, while a lower limit equal to 12 nm is obtained in case of exciton reflection. This value exceeds previous findings on singlet exciton diffusion lengths in spin-coated porphyrin layers significantly. The lower limit of Λ_E equal to 12 nm and the exciton lifetime τ_E found to be equal to 1 ns give a lower limit for D_E of 1.4×10^{-7} m^2/s. This value is a factor of two higher than D_E observed earlier for an isotropic *meso*-tetra(4-ethylphenyl)porphyrin film.[21] In case of incoherent exciton hopping between molecules, D_E depends on the exciton transfer rate (k_{ET}) and the distance between adjacent molecules (R_{DA}) according to:[13]

$$D_E = k_{ET} R_{DA}^2 \tag{4.4}$$

Assuming a value for R_{DA} of 4.5 Å gives a lower limit for k_{ET} equal to 7.1×10^{11} s^{-1}. This value is in the same order of magnitude as the k_{ET} in natural light-harvesting complexes, which has a typical value of 10^{12} s^{-1}.[13] Note that most likely not all excitons that have reached the interface with TiO_2 decay effectively into separate charge carriers.[21, 38] This corresponds to a ϕ_{inj} smaller than unity and consequently an even longer Λ_E and higher k_{ET}. The lower limit for ϕ_{inj} is obtained from assuming an infinitely long Λ_E (in practice more than two times the TnBuPP layer thickness). In case of exciton quenching at the TnBuPP/gas interface, a lower limit for ϕ_{inj} equal to 0.63 is obtained, while in case of exciton reflection this lower limit equals 0.36. The latter value is similar to the value for ϕ_{inj} obtained for isotropic *meso*-tetra(4-ethylphenyl)porphyrin films on TiO_2[21], which is not surprising considering the minor differences in chemical structure between this porphyrin derivative and TnBuPP.

Comparison of Figures 4.4A and 4.4B shows that annealing leads to a decrease of the IPCSE by a factor four. Taking the experimental values IPCSE = 5 %, $\alpha = 2.1\times10^7$ m^{-1}, $F_R = 0.24$ at 430 nm, $L = 35$ nm and $\phi_{inj} = 1$ gives a lower limit for Λ_E of 4 nm and 3 nm in case of exciton quenching and reflection at the TnBuPP/gas interface, respectively. Most likely ϕ_{inj} is smaller than unity, leading to a longer Λ_E. The lower limit for ϕ_{inj} equals 0.23 in case of exciton quenching at the TnBuPP/gas interface, while in case of exciton reflection the lower limit equals 0.13.

The diffusion of an exciton involves the transfer of excitation energy between adjacent molecules. The mechanism of singlet exciton transfer can range from exciton delocalization[13, 39] to incoherent exciton diffusion via the Förster[40] mechanism, depending on the degree of exciton coupling between adjacent molecules.[13,14,39,41] The energy transfer rate k_{ET} is proportional to the factor κ^2, which depends on the mutual orientation of adjacent molecules according to

$$\kappa = \vec{\mu}_1 \cdot \vec{\mu}_2 - 3(\vec{\mu}_1 \cdot \vec{r})(\vec{\mu}_2 \cdot \vec{r}) \qquad (4.5)$$

where $\vec{\mu}_1$ and $\vec{\mu}_2$ represent the transition dipole moments and $\vec{r}$ the vector connecting the centers of the molecules, all normalized to unit length.

The long Λ_E found for the TnBuPP film as spin-coated originates from an efficient exciton transfer pathway through the homeotropic nematic layer to the interface with TiO_2. In a recent study the relatively long Λ_E of 7 nm, found for an isotropic *meso*-tetra(4-ethylphenyl)porphyrin (TEPP) film, has been ascribed to a relatively high fluorescence rate constant.[21] The fluorescence rate constant of the TnBuPP film is found to be comparable to that of the TEPP film. However, the mutual parallel arrangement of the molecules in the homeotropic nematic layer yields a higher value of κ^2 as compared to an isotropic layer[41,42], which enhances the energy transfer rate k_{ET}. In addition, in a homeotropic nematic layer k_{ET} in the direction perpendicular to the interface is considerably higher than k_{ET} in other directions as discussed in refs. 43 and 44. The efficient exciton transfer in the direction perpendicular to the TnBuPP/TiO_2 interface makes these bilayers promising candidates for photovoltaic applications.

4.4. Conclusions

This study shows that an efficient light-harvesting layer is realized by homeotropic nematic molecular arrangement. The incident photon to charge separation efficiency equal to 20 % at the absorption maximum is the most efficient light-induced charge

separation in porphyrin based bilayers realized so far.[15,16] Due to the long exciton diffusion length and the applied low-cost deposition technique, TnBuPP is a promising candidate for application in photovoltaic devices. In conclusion, this work demonstrates that efficient light-induced charge separation is not necessarily only obtained in case of dye-sensitized solar cells based on a nanostructured network, but can also be achieved in a bilayer configuration.

Acknowledgment

N.M. van der Pers of the Department of Materials Science and Engineering, Delft University of Technology, is acknowledged for the XRD analysis. The research was supported financially by the Delft Research Centre for Sustainable Energy.

Supporting Information

The factor S represents the number of excitons that reaches the TnBuPP/TiO_2 interface normalized to the number of incident photons. In case of exciton quenching at the porphyrin/gas interface, S depends on the exponential optical absorption coefficient (α), the TnBuPP layer thickness (L) and the exciton diffusion length (Λ_E) according to

$$S_{BQ} = \left(\frac{\alpha^2\Lambda_E^2}{\alpha^2\Lambda_E^2 - 1}\right)\left(1 + \frac{e^{-\alpha L}\csc h\left(\frac{L}{\Lambda_E}\right) - \coth\left(\frac{L}{\Lambda_E}\right)}{\alpha\Lambda_E}\right) \quad \text{(S1)}$$

while in case of exciton reflection at the porphyrin/gas interface, S is given by:

$$S_{BR} = \left(\frac{\alpha^2\Lambda_E^2}{\alpha^2\Lambda_E^2 - 1}\right)\left(1 - e^{-\alpha L}\sec h\left(\frac{L}{\Lambda_E}\right) - \frac{\tanh\left(\frac{L}{\Lambda_E}\right)}{\alpha\Lambda_E}\right) \quad \text{(S2)}$$

References

(1) Grätzel, M., *Nature* **2001,** 414, 338-344.
(2) Gregg, B. A., *Journal of Physical Chemistry B* **2003,** 107, (20), 4688-4698.
(3) O'Regan, B.; Grätzel, M., *Nature* **1991,** 353, (6346), 737-740.
(4) Sommeling, P. M.; Spath, M.; Smit, H. J. P.; Bakker, N. J.; Kroon, J. M., *Journal of Photochemistry and Photobiology A-Chemistry* **2004,** 164, (1-3), 137-144.
(5) Schmidt-Mende, L.; Zakeeruddin, S. M.; Grätzel, M., *Applied Physics Letters* **2005,** 86, (1), 013504.

(6) Nelson, J.; Chandler, R. E., *Coordination Chemistry Reviews* **2004,** 248, (13-14), 1181-1194.
(7) Wohrle, D.; Tennigkeit, B.; Elbe, J.; Kreienhoop, L.; Schnurpfeil, G., *Molecular Crystals and Liquid Crystals* **1993,** 230, 221-226.
(8) Kerp, H. R.; Donker, H.; Koehorst, R. B. M.; Schaafsma, T. J.; Faassen, E. E. v., *Chemical Physics Letters* **1998,** 298, (4-6), 302-308.
(9) Kroeze, J. E.; Savenije, T. J.; Warman, J. M., *Journal of Photochemistry and Photobiology A-Chemistry* **2002,** 148, 49-55.
(10) Peumans, P.; Yakimov, A.; Forrest, S. R., *Journal of Applied Physics* **2003,** 93, (7), 3693-3723.
(11) Kühlbrandt, W.; Wang, D. N., *Nature* **1991,** 350, 130-134.
(12) Savage, H.; Cyrklaff, M.; Montoya, G.; W., K.; Sinning, I., *Structure* **1996,** 4, (3), 243-252.
(13) Amerongen, H. v.; Valkunas, L.; Grondelle, R. v., *Photosynthetic excitons*. World Scientific: Singapore, 2000.
(14) Ritz, T.; Park, S.; Schulten, K., *Journal of Physical Chemistry B* **2001,** 105, 8259-8267.
(15) Peumans, P.; Uchida, S.; Forrest, S. R., *Nature* **2003,** 425, (6954), 158-162.
(16) Peumans, P.; Forrest, S. R., *Applied Physics Letters* **2001,** 79, (1), 126-128.
(17) Kay, A.; Humphrybaker, R.; Grätzel, M., *Journal of Physical Chemistry* **1994,** 98, (3), 952-959.
(18) Boschloo, G. K.; Goossens, A., *Journal of Physical Chemistry* **1996,** 100, (50), 19489-19494.
(19) Kroeze, J. E.; Savenije, T. J.; Warman, J. M., *Advanced Materials* **2002,** 14, (23), 1760-1763.
(20) Kroeze, J. E.; Koehorst, R. B. M.; Savenije, T. J., *Advanced Functional Materials* **2004,** 14, (10), 992-998.
(21) Huijser, A.; Savenije, T. J.; Kroeze, J. E.; Siebbeles, L. D. A., *Journal of Physical Chemistry B* **2005,** 109, 20166-20173.
(22) Kroeze, J. E.; Savenije, T. J.; Vermeulen, M. J. W.; Warman, J. M., *Journal of Physical Chemistry B* **2003,** 107, (31), 7696-7705.
(23) Kroeze, J. E.; Savenije, T. J.; Warman, J. M., *Journal of the American Chemical Society* **2004,** 126, 7608.
(24) Haas, M. P. de; Warman, J. M., *Chemical Physics* **1982,** 73, 35-53.
(25) Savenije, T. J.; Haas, M. P. de; Warman, J. M., *Zeitschrift fur Physikalische Chemie-International Journal of Research in Physical Chemistry & Chemical Physics* **1999,** 212, 201-206.
(26) Shimizu, Y.; Miya, M.; Nagata, A.; Ohta, K.; Yamamoto, I.; Kusabayashi, S., *Liquid Crystals* **1993,** 14, (3), 795-805.
(27) Cullity, B. D.; Stock, S. R. t., *Elements of X-ray diffraction*. 3 ed.; Prentice Hall: New Yersey, 2001.
(28) Gouterman, M., *The Porphyrins; Volume III*. Academic Press: New York, 1978; Vol. 3.
(29) Eichhorn, H., *Journal of Porphyrins and Phthalocyanines* **2000,** 4, (1), 88-102.
(30) Eichhorn, S. H.; Bruce, D. W.; Guillon, D.; Gallani, J. L.; Fischer, T.; Stumpe, J.; Geue, T., *Journal of Materials Chemistry* **2001,** 11, 1576-1584.
(31) Kasha, M.; Rawls, H. R.; Ashraf Et.-Bayoumi, M., *Pure and Applied Chemistry* **1965,** 11, 371-392.
(32) Schick, G. A.; Schreiman, I. C.; Wagner, R. W.; Lindsey, J. S.; Bocian, D. F., *Journal of the American Chemical Society* **1989,** 111, (4), 1344-1350.

(33) Kroon, J. M.; Koehorst, R. B. M.; vanDijk, M.; Sanders, G. M.; Sudholter, E. J. R., *Journal of Materials Chemistry* **1997,** 7, (4), 615-624.
(34) Scurlock, R. D.; Wang, B.; Ogilby, P. R.; Sheats, J. R.; Clough, R. L., *Journal of the American Chemical Society* **1995,** 117, 10194-10202.
(35) Granzhan, A.; Penzkofer, A.; Hauska, G., *Journal of Photochemistry and Photobiology A-Chemistry* **2004,** 165, 75-89.
(36) Turro, N. J., *Modern Molecular Photochemistry*. The Benjamin/Cummings Publishing Company, Inc, Menlo Park, CA: 1978.
(37) Södergren, S.; Hagfeldt, A.; Olsson, J.; Lindquist, S. E., *Journal of Physical Chemistry* **1994,** 98, (21), 5552-5556.
(38) Kroeze, J. E.; Savenije, T. J.; Candeias, L. P.; Warman, J. M.; Siebbeles, L. D. A., *Solar Energy Materials and Solar Cells* **2005,** 85, (2), 189-203.
(39) May, V.; Kühn, O., *Charge and Energy Transfer Dynamics in Molecular Systems. A Theoretical Introduction*. Wiley-VCH: Berlin, 2000.
(40) Förster, T. H., *Discuss. Faraday Soc.* **1959**, (27), 7.
(41) Visser, H. M.; Kleima, F. J.; Stokkum, I. H. M. v.; Grondelle, R. v.; Amerongen, H. v., *Chemical Physics* **1996,** 210, 297-312.
(42) Yang, J.; Winnik, M. A., *Journal of Physical Chemistry B* **2005,** 109, 18408-18417.
(43) Bacchiocchi, C.; Zannoni, C., *Phys. Rev. E.* **1998,** 58, (3), 3237.
(44) Bacchiocchi, C.; Zannoni, C., *Chemical Physics Letters* **1997,** 268, 541-548.

CHAPTER 5

Thermally deactivated exciton diffusion in a nematic layer of homeotropically aligned tetraphenylporphyrin derivatives*

The energy transfer dynamics in a nematic layer of homeotropically aligned *meso*-tetra(4-n-butylphenyl)porphyrin (TnBuPP) molecules have been determined at different temperatures using the time-resolved microwave conductivity technique. The lower limit of the exciton diffusion length decreases from 20 nm at 90 K to 12 nm at 300 K. Combining these values with an increase in exciton lifetime from 0.52 ns at 90 K to 1.95 ns at 300 K and an intermolecular distance of 4.5 Å gives a decrease of the energy transfer rate from $\geq 3.8\times10^{12}$ s^{-1} at 90 K to $\geq 3.7\times10^{11}$ s^{-1} at 300 K. This decrease is attributed to larger fluctuations in exciton site energies and excitonic couplings at higher temperatures. Exciton motion in a TnBuPP layer hence occurs via a band like mechanism, rather than by thermally activated Förster-like hopping.

* This chapter is based on: Annemarie Huijser, Tom J. Savenije, Stefan C.J. Meskers, Martien J.W. Vermeulen and Laurens D.A. Siebbeles, *Physical Review Letters,* to be submitted.

5.1. Introduction

Energy transfer is a key process not only in photosynthetic light-harvesting complexes, but also in photocatalytic and photovoltaic molecular devices.[1,2] The main function of the dye molecules present in these systems involves the absorption of sunlight, resulting in the promotion of electrons from the ground state to a higher energetic state. Relaxation of the excited state results in the formation of a strongly bound electron-hole pair, also referred to as an exciton. Excitons are transferred by diffusion via several dye molecules towards a reactive interface, where exciton dissociation into charged intermediates occurs. Recently, we reported on energy transfer in a nematic layer of homeotropically aligned *meso*-tetra(4-n-butylphenyl)porphyrin (TnBuPP) molecules (see the inset of Figure 5.1A for the chemical structure of TnBuPP and Figure 5.2B for the molecular organization).[3] We found that the exciton diffusion length (Λ_E) in TnBuPP is at least 12 nm, which is considerably longer than values commonly found for amorphous molecular dye layers.[4-6] Only for a few molecular dye systems, values for Λ_E in the order of tens of nanometers have been realized.[3,7-13] In order to further enhance Λ_E in a TnBuPP layer to a value comparable to the optical penetration depth, more insight into the exciton motion mechanism is required.

Depending on the magnitude of the exciton-phonon coupling, two limiting cases for the energy transfer mechanism can be distinguished. In case of strong exciton-phonon coupling, the exciton-induced lattice deformation leads to thermally activated incoherent exciton hopping between localized states.[14,15] This approximation forms the basis of the Förster model,[16,17] which is commonly used to describe energy transfer between organic dye molecules.[18-23] The energy transfer rate (k_{ET}) from B800 to B850 in the bacterial light-harvesting complex II has been observed to increase from 8.3×10^{11} s^{-1} at 77 K to 1.4×10^{12} s^{-1} at 300 K.[24,25] Also within a porphyrin-chlorin dimer k_{ET} from the porphyrin subunit towards the chlorin subunit increases from 6.8×10^{10} s^{-1} at 77 K to 1.4×10^{11} s^{-1} at 300 K.[26] On the contrary, in case of weak exciton-phonon coupling energy transfer can be considered as a band like mechanism, with a thermally deactivated k_{ET} due to larger fluctuations in exciton site energies and excitonic couplings at higher temperatures. This limit forms the basis of e.g. the Haken-Strobl-Reineker model.[27] Thermally deactivated energy transfer has been observed for naphthalene and anthracene crystals, for which k_{ET} (~5×10^{6} s^{-1} at 125 K) typically decreases by a factor of 3-5 on increasing the temperature

to 300 K.[28-31] The temperature dependence of k_{ET} can thus provide information about the specific energy transfer mechanism in a TnBuPP layer.

5.2. Experimental methods

Exciton motion was studied for a layer of TnBuPP deposited onto TiO_2, which bilayer was prepared as described previously.[3] Optical transmission and fluorescence spectra and fluorescence decays at 90 K and 300 K were recorded with the equipment described in ref. 32 using an Oxford Optistat bath cryostat. Optical reflection spectra were measured at 300 K as described in ref. 3 and assumed to be temperature independent. The optical absorption coefficient (α) and fraction of absorbed light (F_A) were determined from the optical transmission and reflection as described in ref. 33. Exciton diffusion through the TnBuPP layer towards the interface with TiO_2 was studied at 90 K and 300 K using the time-resolved microwave conductivity (TRMC) method[3,6,34] using a temperature controlled X-band microwave cavity under N_2 atmosphere. Excitons in the TnBuPP layer formed on pulsed laser excitation that reach the interface with TiO_2 can undergo interfacial dissociation into separate charge carriers by electron injection into TiO_2 with an efficiency ϕ_{gen}. The formation of highly mobile conduction band electrons in TiO_2 results in a change of the photoconductance ($\Delta G(t)$), followed by an eventual decrease due to decay of charge carriers. Within the intensity range of 10^{10} - 10^{12} photons/cm^2 per pulse, $\Delta G(t)$ linearly increases with the illumination intensity (I_0) and closely follows the optical absorption spectrum of TnBuPP, in agreement with previous results.[3] The incident photon to charge separation efficiency (IPCSE) was determined from $\Delta G(t)$ on visible excitation and the maximum value of the transient photoconductance obtained on selective excitation of TiO_2 at 300 nm ($\Delta G_{max,\lambda=300\ nm}$) as described in ref. 35. The IPCSE denotes the ratio of the number of electrons injected into the TiO_2 to the number of incident photons and increases with the value of Λ_E as explained below.

5.3. Results and discussion

Figure 5.1A shows α and the fluorescence quantum yield (ϕ_F) of TnBuPP on quartz as function of wavelength at 90 K (dashed) and 300 K (solid). The so-called Soret absorption band that peaks at 436 nm originates from the S_0-S_2 transition.[36] The full width at half maximum (FWHM) of the Soret band increases to a small extent with temperature from 25 nm at 90 K to 29 nm at 300 K, coinciding with a slight decrease of

α. The broadening of the absorption band at higher temperature can be attributed to an increase of the width of the energy distribution of the electronic states involved in the optical transition. This might either be due to an enhanced population of higher vibrational levels of the electronic ground state and/or a less regular molecular organization. The transitions from the S_0 state to two energetically slightly different S_1 levels and their higher vibrational modes lead to the four less intense Q-bands between 500 nm and 700 nm.[36] The transition from the lowest S_1 level towards the lowest vibrational mode of the ground state gives rise to the most intense fluorescence band. The second fluorescence band is due to the transition to a higher vibrational mode of the ground state.[36] Increasing the temperature results in a blue shift of the fluorescence bands and an enhancement of the intensity of the second fluorescence band. The blue shift in fluorescence might originate from a lower extent of spectral diffusion at 300 K due to the shorter distance excitons are able to travel as derived below. In addition, release from an exciton trap is more likely at 300 K, which also can contribute to a blue shift in fluorescence.

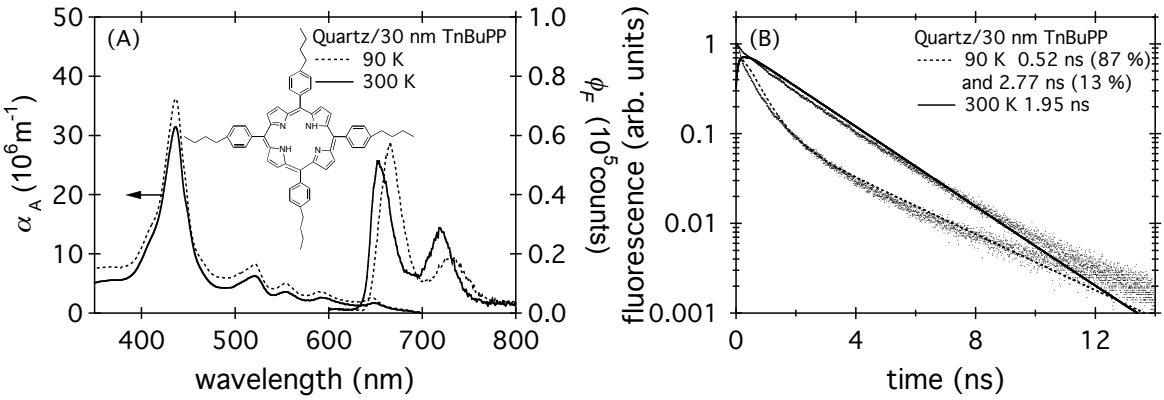

Figure 5.1. Optical absorption coefficient and fluorescence quantum yield as function of wavelength of TnBuPP on quartz at 90 K (dashed) and 300 K (solid) (A). The inset shows the chemical structure of TnBuPP. Figure B shows the fluorescence decays of TnBuPP on quartz at 90 K and 300 K recorded on excitation at 405 nm, detected at maximum fluorescence. Fits of a bi-exponential (90 K) or mono-exponential (300 K) function convoluted with the instrumental response function to the fluorescence decays and the lifetimes are included.

Figure 5.1B shows the fluorescence decays of TnBuPP on quartz at 90 K and 300 K. The decay at 90 K clearly exhibits two different slopes. Fitting a bi-exponential function convoluted with the instrumental response function to this decay yields lifetimes of 0.52 ns and 2.7 ns, with the first component contributing the major part (87 %) to the signal.

At 300 K the fluorescence decay is slower than at 90 K and exhibits only one slope. Fitting a mono-exponential function convoluted with the instrumental response function to this decay yields an exciton lifetime of 1.95 ns.[37] The enhancement of the exciton lifetime might either be due to a slight change in layer morphology on increasing the temperature or attributed to the shorter distance excitons are able to travel as derived below and consequently less quenching at defects.

Figure 5.2 shows the photophysical processes occurring on visible excitation of a bilayer of TnBuPP and TiO_2. Absorption of photons by the TnBuPP layer leads to the formation of excitons (1). Those excitons that are able to reach the interface with TiO_2 by diffusion (2) could undergo interfacial charge separation by electron injection into TiO_2 (3). Electrons injected into TiO_2 are measured by a change in reflected microwave power, from which the IPCSE can be determined as described in ref. 35. The value of the IPCSE depends on the efficiency of processes 1-3 according to[38]

$$IPCSE = (1 - F_R)\phi_{gen} S(\alpha, \Lambda_E, L) \cdot 100 \ \% \qquad (5.1)$$

with F_R denoting the fraction of photons reflected at the sample surface and ϕ_{gen} the interfacial charge generation yield relative to all modes of interfacial exciton deactivation. The factor S represents the number of excitons that reaches the interface between TnBuPP and TiO_2 normalized to $I_0(1-F_R)$, i.e. the number of photons entering the sample. The value of S depends on the optical absorption coefficient (α), the value of Λ_E and the thickness of the TnBuPP layer (L). Analytical expressions for S in case of exciton quenching (S_{BQ}) and exciton reflection (S_{BR}) at the interface of TnBuPP and N_2 are given in Appendix A of the Supporting Information. The effect of the temperature on ϕ_{gen} and S is investigated by determining the IPCSE values of both a thin monolayer like film of TnBuPP on TiO_2 (bilayer A) and a thick film of TnBuPP on TiO_2 (bilayer B). The value of ϕ_{gen} is assumed to be independent of the TnBuPP layer thickness, in agreement with previous experiments.[39]

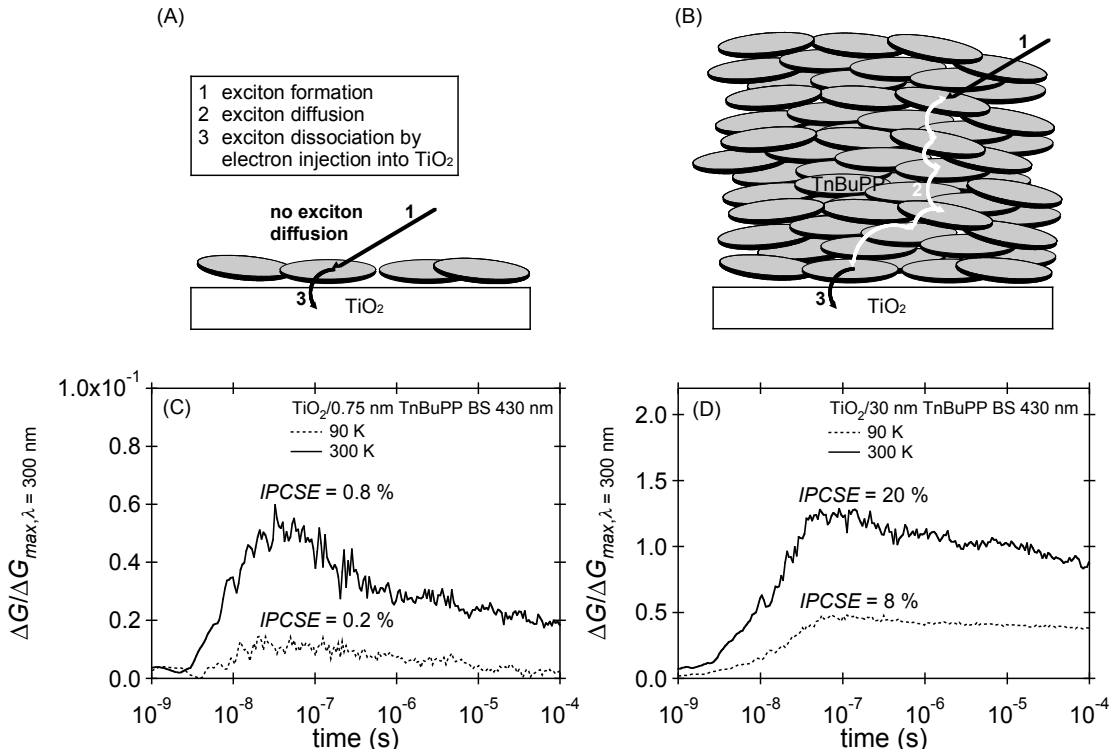

Figure 5.2. Processes occurring on visible excitation of 0.75 nm TnBuPP on TiO_2 (A) and 30 nm TnBuPP on TiO_2 (B). Panels C and D show the photoconductance transients at 90 K (dashed) and 300 K (solid) of these bilayers on pulsed excitation at 430 nm with 2×10^{11} photons/cm^2 per pulse, divided by ΔG_{max} obtained on pulsed illumination at 300 nm with 5×10^{10} photons/cm^2 per pulse.

Figures 5.2C and 5.2D show the photoconductance transients at 90 K (dashed) and 300 K (solid) obtained on pulsed illumination at 430 nm (close to the maximum of the Soret absorption band of TnBuPP) of bilayer A and B, respectively, divided by ΔG_{max} obtained on pulsed illumination at 300 nm. The initial rise of the transients is due to the 18 ns instrument response time of the system. The maximum value of $\Delta G/\Delta G_{max,\lambda = 300\ nm}$ at 300 K significantly exceeds that at 90 K. Using the methodology described in ref. 35, the IPCSE value for bilayer A is determined to be 0.2 % at 90 K and 0.8 % at 300 K. Since in bilayer A all TnBuPP molecules are supposed to be in direct contact with the TiO_2, diffusion of excitons does not play a role. The number of excitons formed in the TnBuPP monolayer at 90 K will be almost identical to that at 300 K since the optical absorption is hardly temperature dependent. The enhancement of the IPCSE on increasing the temperature must thus be due to a four-fold increase of ϕ_{gen} from ≤0.25 at 90 K to ≤1 at 300 K[3], see equation 5.1. The thermally activated ϕ_{gen} likely originates from a lower

extent of interfacial charge recombination at higher temperatures. Alternatively, in case the geometry of the TnBuPP cation and the neutral TnBuPP molecule in the excited state are significantly different, the thermal activation could be explained in terms of the Marcus theory for electron transfer.[40]

The IPCSE for bilayer B at 90 K amounts to 8 %. Increasing the temperature to 300 K enhances the IPCSE to 20 %, in agreement with previous experiments.[3] From the observation that this enhancement is less than the four-fold increase of ϕ_{inj}, it is concluded that the factor S decreases on increasing the temperature, see equation 5.1. This could either originate from a decrease of α or from a reduced Λ_E. The only weak temperature dependence of α (see Figure 5.1A) excludes the first option and leads to the conclusion that the value of Λ_E has to decrease on increasing the temperature. The high IPCSE value of 8 % at 90 K can only be explained on basis of equation 5.1 and a value for $\phi_{gen} \leq 0.25$ in case at the interface of TnBuPP and N_2 excitons are assumed to be reflected. The occurrence of exciton quenching at this interface would deactivate too many excitons to lead to an IPCSE value as high as 8 %. The experimental values for the IPCSE and ϕ_{gen}, $\alpha = 3.1\times10^7$ m^{-1}, $F_R = 0.17$ and $L = 30$ nm, and using equations 5.1 and A2, give a lower limit for Λ_E at 90 K equal to 20 nm. Analogous, the IPCSE value of 20 % and $\phi_{gen} \leq 1$ at 300 K, combined with $\alpha = 2.7\times10^7$ m^{-1}, $F_R = 0.17$ and $L = 30$ nm, leads to a lower limit for Λ_E equal to 12 nm. Hence, the exciton diffusion length decreases from ≥20 nm at 90 K to ≥12 nm at 300 K.[41]

The exciton diffusion length depends on the exciton diffusion coefficient (D_E) and exciton lifetime (τ_E) according to:

$$\Lambda_E = \sqrt{D_E \tau_E} \tag{5.2}$$

The value of D_E is determined by the energy transfer rate (k_{ET}) and center-to-center distance between adjacent dye molecules (R_{DA}):

$$D_E = k_{ET} R_{DA}^2 \tag{5.3}$$

Combining the reduction of Λ_E on increasing the temperature with the increase in τ_E from 0.52 ns at 90 K to 1.95 ns at 300 K and using equation 5.2 gives $D_E \geq 7.7\times10^{-7}$ m^2/s at 90 K and $D_E \geq 7.4\times10^{-8}$ m^2/s at 300 K. Application of equation 5.3 with $R_{DA} = 4.5$ Å^3 leads to values for k_{ET} of $\geq 3.8\times10^{12}$ s^{-1} at 90 K and $\geq 3.7\times10^{11}$ s^{-1} at 300 K. The decrease of k_{ET} on increasing the temperature can be attributed to a broadening of the distribution in site

energies due to a less regular layer structure and due to a stronger extent of lattice vibrations. This explanation is in agreement with the changes in optical absorption spectrum on increasing the temperature as shown in Figure 5.1A and discussed above. The observation of thermally deactivated exciton diffusion shows that exciton motion in a TnBuPP layer, occurring over distances of several tens of nanometers, can be described by a band like mechanism, rather than by the Förster hopping model commonly used to describe exciton motion in molecular dye layers.

5.4 Conclusions

The energy transfer dynamics in a nematic layer of homeotropically aligned *meso*-tetra(4-n-butylphenyl)porphyrin (TnBuPP) molecules have been determined at different temperatures using the time-resolved microwave conductivity technique. The exciton diffusion length decreases from ≥20 nm at 90 K to ≥12 nm at 300 K. Combining these values with an increase in exciton lifetime from 0.52 ns at 90 K to 1.95 ns at 300 K and an intermolecular distance of 4.5 Å gives a decrease of the energy transfer rate from $\geq 3.8\times10^{12}$ s^{-1} at 90 K to $\geq 3.7\times10^{11}$ s^{-1} at 300 K. The decrease is attributed to larger fluctuations in exciton site energies and excitonic couplings at higher temperatures. Exciton motion in a TnBuPP layer hence occurs via a band like mechanism, rather than by thermally activated Förster-like hopping.

Acknowledgment

The research is supported financially by the Delft Research Centre for Sustainable Energy.

Supporting Information

Appendix A

The factor S represents the number of excitons that reaches the TnBuPP/TiO_2 interface normalized to the number of incident photons. In case of exciton quenching at the interface of TnBuPP and N_2, S depends on the exponential optical absorption coefficient (α), the TnBuPP layer thickness (L) and the exciton diffusion length (Λ_E) according to:

$$S_{BQ} = \left(\frac{\alpha^2\Lambda_E^2}{\alpha^2\Lambda_E^2 - 1}\right)\left(1 + \frac{e^{-\alpha L}\csc h\left(\frac{L}{\Lambda_E}\right) - \coth\left(\frac{L}{\Lambda_E}\right)}{\alpha\Lambda_E}\right) \quad \text{(A1)}$$

In case of exciton reflection at interface of TnBuPP and N_2, the factor S is equal to:[38]

$$S_{BR} = \left(\frac{\alpha^2\Lambda_E^2}{\alpha^2\Lambda_E^2 - 1}\right)\left(1 - e^{-\alpha L}\sec h\left(\frac{L}{\Lambda_E}\right) - \frac{\tanh\left(\frac{L}{\Lambda_E}\right)}{\alpha\Lambda_E}\right) \quad \text{(A2)}$$

References

(1) Amerongen, H. v.; Valkunas, L.; Grondelle, R. v., *Photosynthetic excitons*. World Scientific: Singapore, 2000.
(2) Kamat, P. V., *Journal of Physical Chemistry C* **2007,** 111, (7), 2834-2860.
(3) Huijser, A.; Savenije, T. J.; Kotlewski, A.; Picken, S. J.; Siebbeles, L. D. A., *Advanced Materials* **2006,** 18, 2234-2239.
(4) Wohrle, D.; Tennigkeit, B.; Elbe, J.; Kreienhoop, L.; Schnurpfeil, G., *Molecular Crystals and Liquid Crystals* **1993,** 230, 221-226.
(5) Kerp, H. R.; Donker, H.; Koehorst, R. B. M.; Schaafsma, T. J.; Faassen, E. E. v., *Chemical Physics Letters* **1998,** 298, (4-6), 302-308.
(6) Kroeze, J. E.; Savenije, T. J.; Warman, J. M., *Journal of Photochemistry and Photobiology A-Chemistry* **2002,** 148, 49-55.
(7) Peumans, P.; Uchida, S.; Forrest, S. R., *Nature* **2003,** 425, (6954), 158-162.
(8) Peumans, P.; Forrest, S. R., *Applied Physics Letters* **2001,** 79, (1), 126-128.
(9) Peumans, P.; Yakimov, A.; Forrest, S. R., *Journal of Applied Physics* **2003,** 93, (7), 3693-3723.
(10) Stubinger, T.; Brutting, W., *Journal of Applied Physics* **2001,** 90, (7), 3632-3641.
(11) Kroeze, J. E.; Savenije, T. J.; Warman, J. M., *Advanced Materials* **2002,** 14, (23), 1760-1763.
(12) Donker, H.; van Hoek, A.; van Schaik, W.; Koehorst, R. B. M.; Yatskou, M. M.; Schaafsma, T. J., *Journal of Physical Chemistry B* **2005,** 109, (36), 17038-17046.
(13) Huijser, A.; Suijkerbuijk, B. M. J. M.; Klein Gebbink, R. J. M.; Savenije, T. J.; Siebbeles, L. D. A., *Journal of the American Chemical Society* **2007,** accepted.
(14) Markvart, T.; Greef, R., *Journal of Chemical Physics* **2004,** 121, (13), 6401-6405.
(15) May, V.; Kühn, O., *Charge and Energy Transfer Dynamics in Molecular Systems. A Theoretical Introduction, second, revised and enlarged edition*. Wiley-VCH: Berlin, 2004.
(16) Förster, T. H., *Discuss. Faraday Soc.* **1959**, (27), 7.
(17) Förster, T. H., *Fluoreszenz organischer Verbindungen*. Göttingen, 1951.
(18) Jang, S.; Newton, M. D.; Silbey, R. J., *Journal of Physical Chemistry B* **2007,** 111, (24), 6807-6814.
(19) Minkowski, C.; Calzaferri, G., *Angewandte Chemie-International Edition* **2005,** 44, (33), 5325-5329.

(20) Faure, S.; Stern, C.; Guilard, R.; Harvey, P. D., *Journal of the American Chemical Society* **2004,** 126, (4), 1253-1261.
(21) Scholes, G. D.; Jordanides, X. J.; Fleming, G. R., *Journal of Physical Chemistry B* **2001,** 105, (8), 1640-1651.
(22) Cinque, G.; Croce, R.; Holzwarth, A.; Bassi, R., *Biophysical Journal* **2000,** 79, (4), 1706-1717.
(23) Causgrove, T. P.; Brune, D. C.; Blankenship, R. E., *Journal of Photochemistry and Photobiology B-Biology* **1992,** 15, (1-2), 171-179.
(24) Pullerits, T.; Hess, S.; Herek, J. L.; Sundstrom, V., *Journal of Physical Chemistry B* **1997,** 101, 10560-10567.
(25) Wu, H. M.; Savikhin, S.; Reddy, N. R. S.; Jankowiak, R.; Cogdell, R. J.; Struve, W. S.; Small, G. J., *Journal of Physical Chemistry* **1996,** 100, (29), 12022-12033.
(26) Zenkevich, E. I.; Knyukshto, V. N.; Shulga, A. M.; Kuzmitsky, V. A.; Gael, V. I.; Levinson, E. G.; Mironov, A. F., *Journal of Luminescence* **1997,** 75, (3), 229-244.
(27) Haken, H.; Reineker, P., *Zeitschrift fur Physik* **1972,** 249, (3), 253-268.
(28) Powell, R. C., *Journal of Chemical Physics* **1973,** 58, (3), 920-925.
(29) Powell, R. C.; Soos, Z. G., *Physical Review B* **1972,** 5, (4), 1547-1556.
(30) Powell, R. C., *Physical Review B* **1970,** 2, (6), 2090-2097.
(31) Bose, H. N.; Bhaumik, M. L., *Journal of Chemical Physics* **1957,** 26, (6), 1757-1758.
(32) Gomez, R.; Veldman, D.; Blanco, R.; Seoane, C.; Segura, J. L.; Janssen, R. A. J., *Macromolecules* **2007,** 40, (8), 2760-2772.
(33) Kroeze, J. E.; Savenije, T. J.; Warman, J. M., *Journal of the American Chemical Society* **2004,** 126, 7608.
(34) Haas, M. P. de; Warman, J. M., *Chemical Physics* **1982,** 73, 35-53.
(35) Huijser, A.; Savenije, T. J.; Siebbeles, L. D. A., *Thin Solid Films* **2006,** 511-512, 208-213.
(36) Gouterman, M., *The Porphyrins; Volume III*. Academic Press: New York, 1978; Vol. 3.
(37) This value exceeds the exciton lifetime of 1 ns reported in ref. 3. The difference originates from the fact that the experiment in ref. 3 involves a freshly prepared sample for which the exciton lifetime has not reached the steady-state value of 2 ns, while the current lifetime has been determined for a sample for which the exciton lifetime has stabilized to 1.95 ns at 300 K.
(38) Kroeze, J. E.; Savenije, T. J.; Vermeulen, M. J. W.; Warman, J. M., *Journal of Physical Chemistry B* **2003,** 107, (31), 7696-7705.
(39) Huijser, A.; Savenije, T. J.; Kroeze, J. E.; Siebbeles, L. D. A., *Journal of Physical Chemistry B* **2005,** 109, 20166-20173.
(40) Marcus, R. A., *Reviews of Modern Physics* **1993,** 65, (3), 599-610.
(41) Note, that the values for ϕ_{gen} of 0.25 at 90 K and 1 at 300 K are upper limits. The lower limit for ϕ_{gen} at 90 K is obtained from equations 7.1 and A2 in case Λ_E is assumed to strongly exceed L, resulting in $\phi_{gen} \geq 0.16$. Since the value for ϕ_{gen} is enhanced by a factor of four on increasing the temperature from 90 K to 300 K, this leads to $\phi_{gen} \geq 0.64$ at 300 K. The lower limit of $\phi_{gen} = 0.64$ and the *IPCSE* value of 20 % give $\Lambda_E \leq 22$ nm at 300 K. Depending on the magnitude of ϕ_{gen}, Λ_E hence decreases by at least a factor of 1.7 on increasing the temperature from 90 K to 300 K.

CHAPTER 6

Photosensitization of TiO_2 and SnO_2 by artificial self-assembling mimics of the natural chlorosomal bacteriochlorophylls*

The fact that from all known photosynthetic organisms the green sulfur bacteria are able to survive under the lowest illumination conditions illustrates the highly efficient exciton transport through their chlorosomes, resulting from self-assembly of the bacteriochlorophyll *c* molecules. A challenging task is to mimic the principle of self-assembling chromophores in artificial light-harvesting devices. We have studied exciton transport and dissociation in a bilayer of an electron-accepting semiconductor and an artificial self-assembling zinc porphyrin that mimics natural chlorosomal bacteriochlorophylls using the time-resolved microwave conductivity (TRMC) method. Scanning electron microscopy reveals the presence of large domains with dimensions up to several micrometers that consist of self-assembled stacks. In addition to these large self-assembled stacks, optical characterization also reveals the presence of non-assembled monomers. Predominantly those photons that are absorbed by the monomers lead to the formation of charge-separated states. The low contribution of self-assembled stacks to the formation of charge-separated states most likely results from their interaction with the semiconductor, combined with the presence of monomers at the semiconductor surface and the energetically unfavorable exciton transfer from a stack to a monomer. Realizing an ordered structure of stacks with an appropriate contact with the electron-accepting semiconductor possibly improves their contribution to the formation of charge-separated states.

---

* This chapter is based on: Annemarie Huijser, Peter L. Marek, Tom J. Savenije, Laurens D.A. Siebbeles, Torsten Scherer, Robert Hauschild, Jedrzej Szmytkowski, Heinz Kalt, Horst Hahn and Teodor Silviu Balaban, *Journal of Physical Chemistry C* **2007**, *111*, 11726-11733.

6.1. Introduction

The high efficiency of photosynthetic processes originates in part from the specific orientation of the chromophore molecules that are present in light-harvesting systems. In general, light-harvesting systems are based on chromophore-protein complexes, in which the proteins determine the orientation of the chromophore molecules. This specific orientation ensures an efficient transport of the excitation energy towards the reaction center. An exception to chromophore-protein based light-harvesting systems is the chlorosome, present in green sulfur bacteria. In a chlorosome the bacteriochlorophyll (BChl) *c* molecules self-assemble without the aid of proteins.[1, 2] The chemical structure of BChl *c* is shown in Figure 6.1A. Essential for self-assembly are i) the ligation of the central magnesium atom by the hydroxy group of the next molecule and ii) the π-π interactions between the macrocycles. Self-assembly affects the optical properties of the bacteriochlorophyll *c* molecules and results in an efficient exciton pathway through the chlorosome to the reaction center. The fact that from all known photosynthetic organisms the green sulfur bacteria are able to survive under the lowest illumination conditions illustrates the light-harvesting effectiveness of their chlorosomes.[3-5]

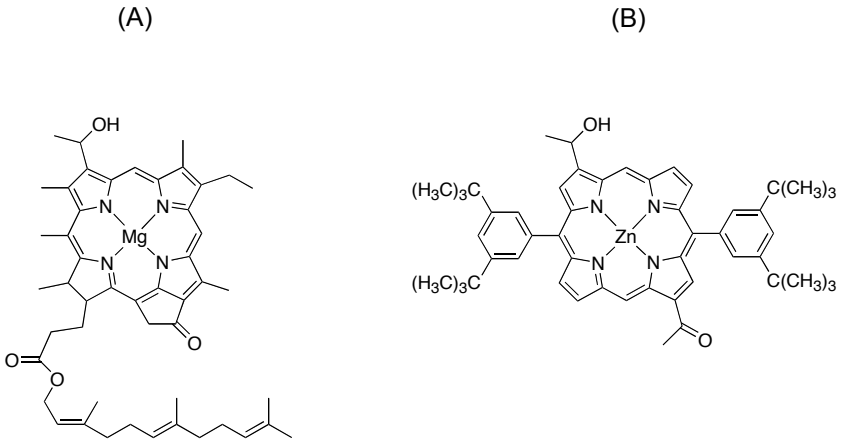

Figure 6.1. Chemical structures of bacteriochlorophyll *c* (A) and *3,13-ZnPor* (B).

A challenging task is to mimic the principle of self-assembling chromophores in an artificial light-harvesting device. The concept of exciton dissociation into charge-separated states in the reaction center of light-harvesting complexes shows considerable similarities with the dye-sensitized solar cell.[6,7] The key feature of the dye-sensitized solar cell is the efficient exciton dissociation at the interface of dye and electron-accepting semiconductor, leading to the injection of an electron into the conduction band

of the semiconductor. Since O'Regan and Grätzel reported an efficiency over 10 % for a cell based on an interpenetrating network of dye-coated nanocrystalline TiO_2 particles and a liquid electrolyte[8], such nanostructured systems have been studied extensively. Because of complications involved in the use of a liquid electrolyte, current research is focused on the development of all solid-state solar cells, for which a maximum performance of 4 % has been realized so far.[9] Application of nanostructured systems avoids the necessity of efficient long-range exciton transport through the dye layer. However, in such systems electron transport is hindered due to trapping at surface defect states.[10] The difficulties involved in electron transport can be avoided by application of dye and electron-accepting semiconductor in a bilayer configuration. A prerequisite for an efficient bilayer-based solar cell is the presence of an exciton transport pathway through the dye layer to the interface with the electron-accepting semiconductor. This may be realized by the application of self-assembling chromophore molecules that mimic the chlorosome structure.

In the present work we have studied exciton transport and dissociation in a bilayer of an electron-accepting semiconductor and an artificial self-assembling zinc porphyrin (see Figure 6.1B) that mimics natural chlorosomal BChls.[11,12] The presence of self-assembled stacks has been verified using scanning electron microscopy (SEM) and optical absorption. Exciton transport and dissociation, resulting in the formation of charge-separated states, has been studied using the time-resolved microwave conductivity (TRMC) technique.[13,14]

6.2. Experimental methods

Sample preparation: Thin smooth TiO_2 films with a thickness of ca. 100 nm, prepared by chemical vapor deposition onto 1x12x25 mm^3 quartz substrates, were purchased from Everest Coatings, Delft, The Netherlands. Thin smooth SnO_2 films with a thickness of ca. 200 nm, prepared by reactive magnetron sputtering, are a generous gift of the Fraunhofer Institut Elektronenstrahl- und Plasmatechnik, Dresden, Germany. Racemic 3-(1-hydroxyethyl)-13-acetyl-10,20-bis-(3,5-di-*tert*-butylphenyl)-porphinato zinc (*3,13-ZnPor*) was synthesized as described in the literature.[5] The chemical structure of *3,13-ZnPor* is shown in Figure 6.1B. Since anhydrous conditions are essential for self-assembly, solvents were dried in advance. Dichloromethane was distilled from calcium hydride and n-heptane was distilled from sodium metal, both under nitrogen atmosphere. Porphyrin film deposition was performed by spin-coating from a solution in

dichloromethane at 2500 rpm. Annealing treatments were performed at a temperature of 200 °C for a period of 15 minutes. Both film deposition and annealing treatments were performed under N_2 atmosphere, with H_2O and O_2 concentrations below 10 ppm. Porphyrin film thicknesses were determined using a Veeco Dektak 8 Stylus Profiler and found to be 150±5 nm, 90±5 nm and 140±5 nm for *3,13-ZnPor* spin-coated on TiO_2, SnO_2 and quartz substrates, respectively.

Scanning electron microscopy: Scanning electron micrographs were recorded using a Leo 1530 Gemini Scanning Electron Microscope (SEM), operated at an accelerating voltage of 20 kV. Samples were sputtered with a ca. 6 nm thin Pt film prior to SEM investigation.

Optical characterization: Optical transmission spectra of *3,13-ZnPor* solutions were recorded using a Perkin-Elmer Lambda 40 UV-VIS spectrophotometer. Optical transmission and reflection spectra of thin films were recorded with a Perkin-Elmer Lambda 900 UV/VIS/NIR spectrophotometer, using an integrating sphere. From the transmission and reflection spectra, the optical density (OD) and the fraction of absorbed light (F_A) were determined using equations 6.1 and 6.2, with I_T the intensity of the transmitted light, I_0 the incident light intensity and I_R the intensity of the reflected light:

$$OD = -\log\left(\frac{I_T}{I_0 - I_R}\right) \tag{6.1}$$

$$F_A = 1 - \left(\frac{I_T + I_R}{I_0}\right) \tag{6.2}$$

The wavelength dependences of the OD and the F_A are referred to as the OD spectrum and the attenuation spectrum, respectively.

Photoconductivity measurements: The TRMC technique and experimental setup have been described previously.[13,14] Samples were mounted in an X-band microwave cavity at a position of maximum electric field. Experiments were performed under N_2 atmosphere. Samples were illuminated through the quartz substrate, resulting in a high initial exciton concentration near the exciton-dissociating interface between the *3,13-ZnPor* layer and TiO_2 or SnO_2. The incident intensity was varied between 10^{10} - 10^{14} photons/cm^2 per pulse. The laser pulse has a full width at half maximum equal to 3 ns.

The data analysis has been described earlier.[15] Briefly, the formation of mobile charge carriers due to pulsed illumination leads to an increase of the photoconductance (ΔG),

followed by an eventual decrease caused by the decay of charge carriers. From the maximum of the photoconductance (ΔG_{max}), the incident photon to charge separation efficiency (IPCSE) was determined as described in the literature.[16]

6.3. Results and discussion

Figure 6.2 shows the OD spectrum of a dilute solution of *3,13-ZnPor* in a strong solvent, i.e. CH_2Cl_2. The strong Soret band at 434 nm and the two less intense Q-bands at 565 nm and 610 nm are characteristic absorption bands for a zinc porphyrin monomer.[17] The addition of nonpolar solvents such as n-heptane or n-hexane induces self-assembly.[5] Self-assembly of *3,13-ZnPor* has been realized by the addition of a major amount of n-heptane to a concentrated solution of *3,13-ZnPor* in CH_2Cl_2, corresponding to a ratio of CH_2Cl_2 to n-heptane of 1:20. The OD spectrum of this solution is included in Figure 6.2. The broad absorption bands at 507 nm, 587 nm and 642 nm originate from self-assembling *3,13-ZnPor* stacks.[12] The absorption band at 422 nm results from a residual amount of *3,13-ZnPor* monomers.[18] Addition of a minute amount of a solvent that competes for the metal ligation, in this case pyridine, to this solution disrupts the self-assembly and results in the presence of predominantly *3,13-ZnPor* monomers. The OD spectrum of this solution is identical to that observed for *3,13-ZnPor* in CH_2Cl_2.

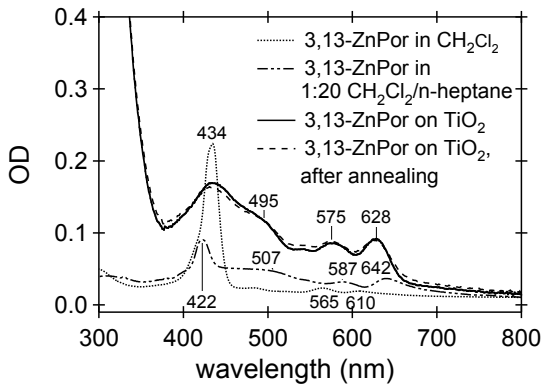

Figure 6.2. OD spectra of *3,13-ZnPor* in CH_2Cl_2 (dotted), in 1:20 CH_2Cl_2/n-heptane (alternating dotted and dashed), *3,13-ZnPor* (from CH_2Cl_2) on TiO_2 as spincoated (solid) and after annealing (dashed).

Figure 6.2 also shows the OD spectrum of *3,13-ZnPor* spin-coated from a solution in CH_2Cl_2 on TiO_2. The absorption band below 350 nm originates from TiO_2. In analogy with the OD spectra discussed in the previous section, the broad absorption bands at 495

nm, 575 nm and 628 nm originate from self-assembled *3,13-ZnPor* stacks. The absorption band at 434 nm indicates the presence of *3,13-ZnPor* monomers. Annealing at 200°C for 15 minutes slightly lowers the monomer absorption band. Since untreated *3,13-ZnPor* and annealed *3,13-ZnPor* dissolved in CH_2Cl_2 exhibit identical OD spectra, the occurrence of chemical degradation upon annealing is ruled out.

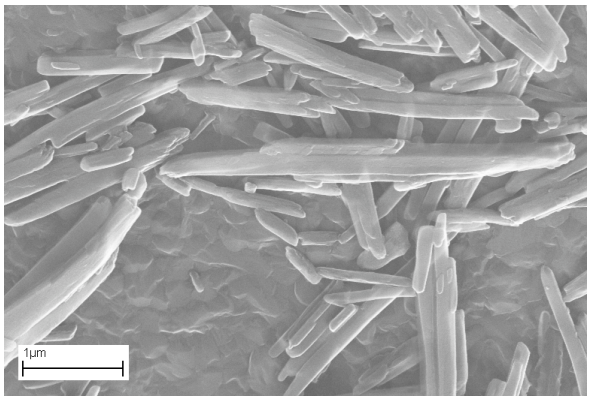

Figure 6.3. Scanning electron micrograph of a *3,13-ZnPor* film on TiO_2, after annealing at 200ºC for 15 minutes.

Figure 6.3 shows the scanning electron micrograph of the annealed *3,13-ZnPor* film on TiO_2. This micrograph reveals the presence of large domains with dimensions up to several micrometers that consist of self-assembled *3,13-ZnPor* stacks. The relative arrangement of *3,13-ZnPor* stacks and monomers could not be deduced from this micrograph.

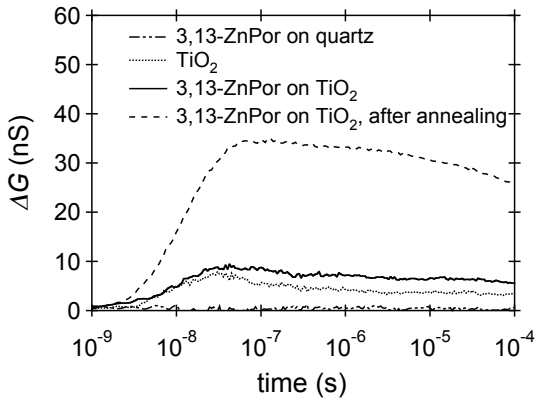

Figure 6.4. Photoconductance transients obtained on pulsed excitation at 430 nm ($1 \cdot 10^{13}$ photons/cm^2/pulse) of *3,13-ZnPor* on quartz (alternating dotted and dashed), bare TiO_2 (dotted), and *3,13-ZnPor* on TiO_2 as spincoated (solid) and after annealing (dashed).

Figure 6.4 shows the photoconductance transients obtained on pulsed illumination at 430 nm of a bare spin-coated *3,13-ZnPor* film on quartz, a bare TiO_2 film and a bilayer of *3,13-ZnPor* on TiO_2 as spin-coated and after annealing. Since the electron mobility in TiO_2 largely exceeds the hole mobility in porphyrins[19,20], an observed change in photoconductance predominantly results from an excess of mobile electrons present in the TiO_2 film. The initial rise of the photoconductance transients is due to the 18 ns instrumental response time.

Excitation of a *3,13-ZnPor* film on quartz does not result in a detectable change in photoconductance. Pulsed illumination of bare TiO_2 results in a short-lived signal, which could be attributed to sub-bandgap excitation of electronic states present within the optical bandgap.[21] In contrast, illumination of in particular the annealed *3,13-ZnPor*/TiO_2 bilayer results in a larger and longer-lived change in photoconductance, which demonstrates photosensitization of TiO_2 by the *3,13-ZnPor* film. Note, that this photosensitization effect is considerably less pronounced for the non-annealed bilayer.

As discussed above, the OD spectrum of the *3,13-ZnPor*/TiO_2 bilayer reveals the presence of both self-assembled *3,13-ZnPor* stacks and non-assembled *3,13-ZnPor* monomers. In order to elucidate to which extent these two morphologically different features contribute to the formation of charge-separated states, the light-induced charge separation efficiency has been determined as function of excitation wavelength. Figure 6.5A shows the incident photon to charge separation efficiency (IPCSE) spectrum of *3,13-ZnPor* on TiO_2 as spin-coated and after annealing. Note, that the shape of the IPCSE spectrum, in particular of the non-annealed bilayer, might be affected by a contribution originating from sub-bandgap excitation of TiO_2. Annealing causes the maximum IPCSE to increase from 0.6 % to 2.2 %, however it hardly affects the shape of the IPCSE spectrum.

The enhanced light-induced charge separation efficiency realized upon annealing is either caused by an enlargement of the exciton diffusion length or an enhancement of the interfacial electron injection yield relative to all modes of interfacial exciton decay (ϕ_{inj}).[16] The only minor changes in the OD spectrum indicate that annealing hardly affects the local molecular organization. The enhanced light-induced charge separation efficiency obtained on annealing is therefore most likely caused by more efficient electron injection rather than by a longer exciton diffusion length. From comparison of the IPCSE spectrum of the annealed *3,13-ZnPor*/TiO_2 bilayer with the attenuation spectrum, also included in Figure 6.5A, it follows that the feature near 434 nm in the

IPCSE spectrum due to absorption by *3,13-ZnPor* monomers is significantly more pronounced than the features at 495 nm, 575 nm and 628 nm caused by the self-assembled *3,13-ZnPor* stacks. We therefore conclude that photons absorbed by the *3,13-ZnPor* monomers are most effective to produce charge-separated states. Formation of charge-separated states is less efficient for self-assembled *3,13-ZnPor* stacks.

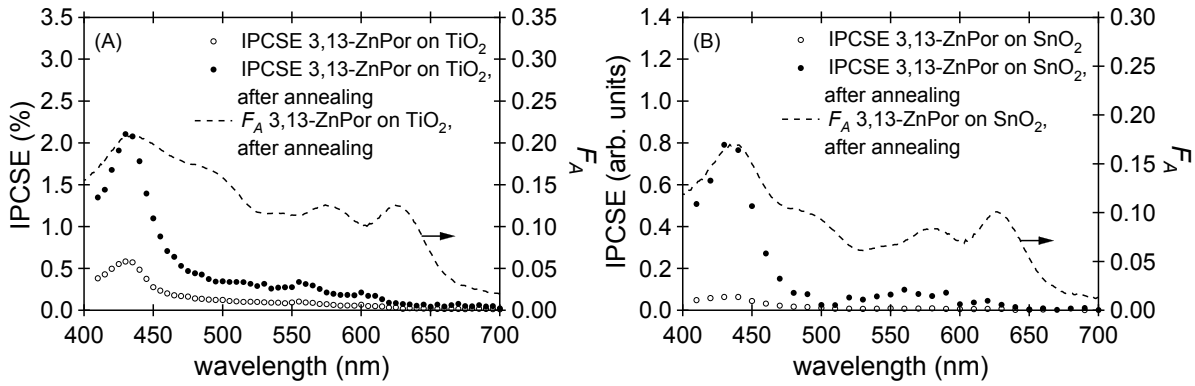

Figure 6.5. The experimental IPCSE values of *3,13-ZnPor* on TiO_2 as spincoated (open dots) and after annealing (solid dots) and the fraction of absorbed light F_A (solid) of the annealed bilayer (A). Figure (B) shows analogous characteristics for *3,13-ZnPor* on SnO_2.

A possible reason for the low contribution of *3,13-ZnPor* stacks involves the energy of the exciton state, which might be too low for efficient electron injection into the conduction band of TiO_2. In order to elucidate whether this is the case, similar experiments have been performed using SnO_2 as the electron-accepting semiconductor. SnO_2 has a 0.6 eV higher electron affinity as compared to TiO_2.[6] Figure 6.5B shows the IPCSE spectrum of *3,13-ZnPor* on smooth SnO_2 as spin-coated and after annealing. Also included is the attenuation spectrum of the bilayer, which again shows the presence of both monomers and self-assembled *3,13-ZnPor* stacks. As also observed for TiO_2-based bilayers, the IPCSE of the *3,13-ZnPor*/SnO_2 bilayer increases significantly upon annealing. The shape of the IPCSE spectrum, both before and after annealing, is similar to those of the *3,13-ZnPor*/TiO_2 bilayer. This indicates that the inefficient conversion of excited states on self-assembled *3,13-ZnPor* stacks into charge-separated states is most likely not due to the energy level of the exciton state.

Another plausible explanation for a low contribution of self-assembled *3,13-ZnPor* stacks to the formation of charge-separated states involves the exciton transfer between stacks and monomers and the interaction of stacks with the semiconductor surface. As

shown in Figure 6.2, self-assembled stacks exhibit a smaller bandgap as compared to monomers. Consequently, only exciton transfer from a monomer to a stack is energetically favorable, in contrast to the reverse energy transfer process. A stack could thus act as exciton trap. The observed IPCSE values in the order of 1-2 % are typical for exciton diffusion over distances in the order of 1 nm[16], corresponding to a few monolayers of molecules. The major contribution from non-assembled *3,13-ZnPor* monomers to the formation of charge-separated states may originate from their presence at the surface of the electron-accepting semiconductor. Efficient conversion of excitons present on the self-assembled *3,13-ZnPor* stacks into charge-separated states requires an ordered structure of stacks that are in direct contact with the electron-accepting semiconductor. In addition, the interaction between the self-assembled stack and the semiconductor surface has to be appropriate for efficient electron injection. Methods to realize this are currently under investigation.

6.4. Conclusions

We have studied photosensitization of smooth TiO_2 and SnO_2 by an artificial self-assembling zinc porphyrin that mimics natural chlorosomal bacteriochlorophyll*s*. Self-assembly of these zinc porphyrin molecules results in the formation of large domains with dimensions up to several micrometers. In addition to these self-assembled stacks, the porphyrin layer also contains non-assembled zinc porphyrin monomers. Predominantly those photons absorbed by the monomers leads to the formation of charge-separated states. The low contribution of self-assembled stacks to the formation of charge-separated states most likely originates from the interaction with the semiconductor, combined with the presence of non-assembled monomers at the semiconductor surface and the energetically unfavorable exciton transfer from a stack to a monomer. Realizing an ordered structure of stacks with appropriate contact with the electron-accepting semiconductor possibly enhances their contribution to the formation of charge-separated states.

Acknowledgment

W.M. Gnehr, Fraunhofer Institut Elektronenstrahl- und Plasmatechnik, Dresden, Germany, is acknowledged for the generous gift of the SnO_2 substrates. Research in Delft was supported financially by the Delft Research Centre for Sustainable Energy. Research in Karlsruhe was partially supported by the DFG Center for Functional Nanostructures

(CFN) at the University of Karlsruhe through former projects C3.2 and C3.6 and current project C3.5.

References

(1) Alden, R. G.; Lin, S. H.; Blankenship, R. E., *Journal of Luminescence* **1992,** 51, (1-3), 51-66.
(2) Balaban, T. S.; Holzwarth, A. R.; Schaffner, K.; Boender, G. J.; Degroot, H. J. M., *Biochemistry* **1995,** 34, (46), 15259-15266.
(3) Frigaard, N. U.; Chew, A. G. M.; Li, H.; Maresca, J. A.; Bryant, D. A., *Photosynthesis Research* **2003,** 78, (2), 93-117.
(4) Psencik, J.; Ikonen, T. P.; Laurinmaki, P.; Merckel, M. C.; Butcher, S. J.; Serimaa, R. E.; Tuma, R., *Biophysical Journal* **2004,** 87, (2), 1165-1172.
(5) Balaban, T. S.; Bhise, A. D.; Fischer, M.; Linke-Schaetzel, M.; Roussel, C.; Vanthuyne, N., *Angewandte Chemie-International Edition* **2003,** 42, (19), 2140-2144.
(6) Grätzel, M., *Nature* **2001,** 414, 338-344.
(7) Gregg, B. A., *Journal of Physical Chemistry B* **2003,** 107, (20), 4688-4698.
(8) O'Regan, B.; Grätzel, M., *Nature* **1991,** 353, (6346), 737-740.
(9) Schmidt-Mende, L.; Zakeeruddin, S. M.; Grätzel, M., *Applied Physics Letters* **2005,** 86, (1), 013504.
(10) Nelson, J.; Chandler, R. E., *Coordination Chemistry Reviews* **2004,** 248, (13-14), 1181-1194.
(11) Balaban, T. S.; Linke-Schaetzel, M.; Bhise, A. D.; Vanthuyne, N.; Roussel, C.; Anson, C. E.; Buth, G.; Eichhofer, A.; Foster, K.; Garab, G.; Gliemann, H.; Goddard, R.; Javorfi, T.; Powell, A. K.; Rosner, H.; Schimmel, T., *Chemistry-A European Journal* **2005,** 11, (8), 2267-2275.
(12) Balaban, T. S., *Accounts of Chemical Research* **2005,** 38, (8), 612-623.
(13) Haas, M. P. de; Warman, J. M., *Chemical Physics* **1982,** 73, 35-53.
(14) Kroeze, J. E.; Savenije, T. J.; Vermeulen, M. J. W.; Warman, J. M., *Journal of Physical Chemistry B* **2003,** 107, (31), 7696-7705.
(15) Kroeze, J. E.; Savenije, T. J.; Warman, J. M., *Journal of the American Chemical Society* **2004,** 126, 7608.
(16) Huijser, A.; Savenije, T. J.; Kroeze, J. E.; Siebbeles, L. D. A., *Journal of Physical Chemistry B* **2005,** 109, 20166-20173.
(17) Gouterman, M., *The Porphyrins; Volume III.* Academic Press: New York, 1978; Vol. 3.
(18) Balaban, T. S.; Linke-Schaetzel, M.; Bhise, A. D.; Vanthuyne, N.; Roussel, C., *European Journal of Organic Chemistry* **2004**, (18), 3919-3930.
(19) Bak, T.; Nowotny, J.; Rekas, M.; Sorrell, C. C., *Journal of Physics and Chemistry of Solids* **2003,** 64, (7), 1069-1087.
(20) Checcoli, P.; Conte, G.; Salvatori, S.; Paolesse, R.; Bolognesi, A.; Berliocchi, A.; Brunetti, F.; D'Amico, A.; Di Carlo, A.; Lugli, P., *Synthetic Metals* **2003,** 138, (1-2), 261-266.
(21) Kroeze, J. E.; Savenije, T. J.; Warman, J. M., *Journal of Photochemistry and Photobiology A-Chemistry* **2002,** 148, 49-55.

CHAPTER 7

Efficient exciton transport in layers of self-assembled porphyrin derivatives*

The photosynthetic apparatus of green sulfur bacteria, the chlorosome, is generally considered as a highly efficient natural light-harvesting system. The efficient exciton transport through chlorosomes towards the reaction centers originates from self-assembly of the bacteriochlorophyll molecules. The aim of the present work is to realize a long exciton diffusion length in an artificial light-harvesting system using the concept of self-assembled natural chlorosomal chromophores. The ability to transport excitons is studied for porphyrin derivatives with different tendencies to form molecular stacks by self-assembly. A porphyrin derivative denoted as ZnOP, containing methoxymethyl substituents ({*meso*-tetrakis[3,5-bis(methoxymethyl)phenyl]porphyrinato}zinc(II)) is found to form self-assembled stacks, in contrast to a derivative with t-butyl substituents, ZnBuP ({*meso*-tetrakis[3,5-bis(t-butyl)phenyl]porphyrinato}zinc(II)). Exciton transport and dissociation in a bilayer of these porphyrin derivatives and TiO_2 is studied using the time-resolved microwave conductivity (TRMC) method. For ZnOP layers it is found that excitons undergo diffusive motion between the self-assembled stacks, with the exciton diffusion length being as long as 15±1 nm, which is comparable to that in natural chlorosomes. For ZnBuP a considerably shorter exciton diffusion length of 3±1 nm is found. Combining these exciton diffusion lengths with exciton lifetimes of 160 ps for ZnOP and 74 ps for ZnBuP yields exciton diffusion coefficients equal to 1.4×10^{-6} m^2/s and 1×10^{-7} m^2/s, respectively. The larger exciton diffusion coefficient for ZnOP originates from a strong excitonic coupling for interstack energy transfer. The findings show that energy transfer is strongly affected by the molecular organization. The efficient interstack energy transfer shows promising prospects for application of such self-assembled porphyrins in opto-electronics.

---

* This chapter is based on: Annemarie Huijser, Bart M.J.M. Suijkerbuijk, Robertus J.M. Klein Gebbink, Tom J. Savenije and Laurens D.A. Siebbeles, *Journal of the American Chemical Society,* accepted.

7.1. Introduction

The occurrence of photosynthesis is crucial for life on earth. The first essential step in photosynthesis is the capture of sunlight. To absorb sunlight efficiently, photosynthetic organisms are equipped with light-harvesting systems. These light-harvesting systems are typically based on ring-like bacteriochlorophyll-protein complexes. The proteins determine the three-dimensional structure of the light-harvesting complex. The main function of the bacteriochlorophyll molecules involves the absorption of sunlight. Absorption of a photon results in the formation of a strongly bound electron-hole pair, also referred to as an exciton. Due to the specific mutual orientation of adjacent bacteriochlorophyll molecules, excitons are transported efficiently through one or more light-harvesting complexes over distances of typically 10-20 nm towards the reaction center, where exciton dissociation into charged species takes place.[1-8]

An alternative efficient exciton transport pathway can, however, also be present in systems that lack a protein matrix; an example is the chlorosome, the photosynthetic system in green photosynthetic bacteria. The chlorosome is an ellipsoidal shaped organelle with a typical size of 15 nm × 30 nm × 100 nm,[9] based on self-assembled bacteriochlorophyll *c, d* or *e* molecules organized by bacteriochlorophyll-bacteriochlorophyll rather than by bacteriochlorophyll-protein interactions.[10-13] Essential for self-assembly of the bacteriochlorophyll molecules in the chlorosome are (a) the coordinative bonds between electron-donating side groups and the electron-accepting Mg center of the molecule and (b) the π-π interactions between the bacteriochlorophyll macrocycles.[10,11,14,15] Excitons are transferred through the self-assembled stacks over distances of typically 10-15 nm[12] to a bacteriochlorophyll *a* containing base plate, connected to the chlorosomal vesicle, and further towards a reaction center. Energy transfer between adjacent bacteriochlorophyll molecules within one self-assembled stack occurs extremely rapidly; typically on a time scale of 100 fs, corresponding to an energy transfer rate (k_{ET}) equal to 10^{13} s^{-1}.[16-18] If we assume an exciton to be localized on one bacteriochlorophyll molecule, the exciton diffusion coefficient (D_E) follows from

$$D_E = k_{ET} R_{DA}^2 \tag{7.1}$$

where R_{DA} presents the center-to-center distance between adjacent bacteriochlorophyll molecules. Combination of the exciton diffusion coefficient with the exciton lifetime (τ_E) yields the exciton diffusion length (Λ_E), according to

$$\Lambda_E = \sqrt{D_E \tau_E} \tag{7.2}$$

The center-to-center distance of 6.8 Å[19] and the energy transfer rate of typically 10^{13} s^{-1} result in an exciton diffusion coefficient of about 5×10^{-6} m^2/s. Hence, during the lifetime of typically 50 ps[16] an exciton can make on average 5×10^2 hops, and Λ_E is in the order of 15 nm. This length is close to the average distance between the location of exciton formation and the bacteriochlorophyll *a* containing base plate[9], so that almost all photogenerated excitons arrive at the reaction center.

In contrast to natural systems, Λ_E in molecular organic dye layers is typically in the order of only a few nanometers.[20-22] For a few molecular dye systems, exciton diffusion lengths of several tens of nanometers have been realized in vacuum thermal deposited layers.[23-26] The expensive and elaborate deposition method makes these layers, however, less attractive for application in molecular devices. In this context, porphyrin derivatives are of great interest, since thin films of this class of materials can be prepared by spincoating. For several free-base and zinc *meso*-tetrakisphenylporphyrin derivatives, the introduction of appropriate alkyl substituents has been reported to affect the molecular organization and consequently the exciton diffusion length.[27-30] The introduction of octyl side chains has been observed to result in the formation of molecular stacks along which excitons can undergo intrastack diffusion with Λ_E = 9±3 nm.[28] In contrast, exciton diffusion between stacks has been found to be considerably less efficient.[27, 28] The latter is problematic, since for opto-electronic applications efficient exciton transport through the organic layer towards an active (e.g. electron-accepting) interface has to be directed perpendicular to this interface, while the molecular stacks tend to align parallel to a substrate.[27,31] Recently, we have reported a lower limit for Λ_E in the direction perpendicular to a TiO_2 substrate of 12 nm for a system based on nematically organized, homeotropically aligned *meso*-tetrakis(4-*n*-butylphenyl)porphyrin molecules.[32] However, the favorable molecular organization has only been obtained for layers thinner than 35 nm, which can be an important limitation for application in practical devices.

The aim of the current study is to achieve efficient energy transfer towards an active interface using the concept of self-assembled chromophore molecules. Numerous reports deal with the synthesis and structural characterization of self-assembling mimics of bacteriochlorophyll molecules, such as the robust and relatively easily available porphyrin and chlorin derivatives.[33-42] So far, no experimental demonstration of long-range exciton diffusion for such systems has been published. In this work the relationship

between self-assembly and the ability to transport excitons is studied for two porphyrin derivatives, namely {*meso*-tetrakis[3,5-bis(dimethylaminomethyl)phenyl]porphyrinato}zinc(II) (ZnNP) and {*meso*-tetrakis[3,5-bis(methoxymethyl)phenyl]porphyrinato}zinc(II) (ZnOP). The chemical structures of these porphyrin derivatives are shown in Figure 7.1A. Self-assembly is accomplished by the formation of coordinative bonds between the electron-accepting Zn atom and the electron-donating benzylic heteroatoms at the 3- or the 5-position of the *meso*-phenyl rings of an adjacent molecule. A close analogue of ZnOP having Br atoms at the para-positions of the phenyl groups (ZnOPBr) has recently been observed by single crystal X-ray crystallography to self-assemble as shown in Figure 7.1B.[43] Since ZnNP and especially ZnOP possess equivalent electron-donating and electron-accepting groups, comparable self-assembling behavior is expected, as also proposed earlier[43] and validated below. ZnOPBr is not included in the current study on exciton transfer, since the heavy Br atom leads to significant intersystem crossing from singlet to triplet excited states,[44] which will be the topic of another study. To substantiate the impact of self-assembly on the exciton diffusion length, also a porphyrin derivative that is expected not to self-assemble is studied, namely {*meso*-tetrakis[3,5-bis(t-butyl)phenyl]porphyrinato}zinc(II) (ZnBuP). The benzylic substituents of ZnBuP possess a similar steric bulk as the CH_2OCH_3 and $CH_2N(CH_3)_2$ groups, but lack the electron-donating ability.

The molecular organization in spincoated films of the porphyrin derivatives investigated is studied using optical techniques and X-ray diffraction. Exciton transport and dissociation in a bilayer of the porphyrin derivatives and smooth TiO_2 is studied using the time-resolved microwave conductivity (TRMC) method. Excitons are formed by illumination with a nanosecond laser pulse. Those excitons that are able to reach the interface with TiO_2 can undergo interfacial dissociation into separate charge carriers. The electrons injected into the TiO_2 layer are monitored by measuring the microwave conductivity. The exciton diffusion length and the interfacial electron injection yield are determined from fitting an analytical model to the experimental microwave conductivity data. The energy transfer rate between adjacent molecules is strongly affected by molecular self-assembly. This offers promising prospects for use of these materials to convert solar energy into chemical or electrical energy in e.g. photocatalytic applications, sensors and photovoltaics.[45-48]

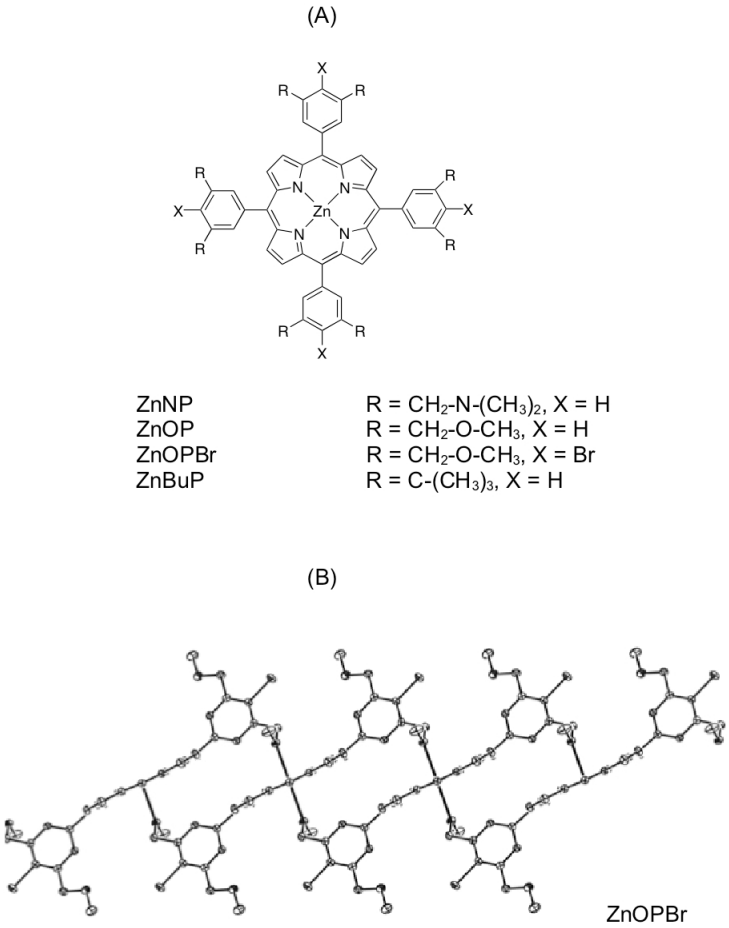

Figure 7.1. Chemical structures of the porphyrin derivatives investigated (A) and a part of the one-dimensional self-assembled stack formed by ZnOPBr molecules (B). Hydrogen atoms and phenyl side groups that are not involved in the self-assembly are omitted for clarity.

7.2. Experimental methods

Synthesis of porphyrin derivatives: The porphyrin derivatives ZnOP, ZnNP and ZnBuP were synthesized as described in ref. 43.

Sample preparation: Thin smooth anatase TiO_2 films with a thickness of ca. 100 nm, prepared by chemical vapor deposition onto 1x12x25 mm^3 quartz substrates, were purchased from Everest Coatings, Delft, The Netherlands. Porphyrin films were prepared by spincoating, either from a solution in $CHCl_3$ (Anhydrous, 99+%, Aldrich, in case of ZnOP, ZnOPBr and ZnBuP) or from a solution in toluene (Anhydrous, 99.8%, Aldrich, used for ZnNP) at 2500 rpm under N_2 atmosphere. The ZnNP solution was filtrated using a 0.45 μm PTFE filter with polypropylene housing. Prior to film deposition, the quartz and TiO_2 substrates were annealed in air at 450 ºC for 1 h. After porphyrin film

deposition, the samples were annealed at 200 ºC under N_2 atmosphere for 15 min. Porphyrin film thicknesses were determined using a Veeco Dektak 8 Stylus Profiler.

Optical characterization: Optical transmission and reflection spectra were recorded using a Perkin Elmer Lambda 900 UV/VIS/NIR spectrometer. The optical density (*OD*), the fraction of absorbed light (F_A) and the extinction coefficient (ε) were determined as described in ref. 49. The wavelength dependent *OD* and F_A are denoted as the absorption spectrum and the optical attenuation spectrum, respectively. Steady state and time-resolved fluorescence spectra were recorded with a Lifespec – ps setup using a 405 nm excitation source (Edinburgh Instruments). Polarized Optical micrographs of the porphyrin films were recorded between crossed polarizers using a Nikon Eclipse E600 Polarizing Optical Microscope.

X-ray diffraction analysis: X-ray diffraction (XRD) measurements were performed in the Bragg-Brentano mode on a Bruker-AXS D8 Advance powder X-ray diffractometer, equipped with automatic divergence slits and a Våntec-1 detector and using a Co anode ($\lambda_{K\alpha}$ = 1.79026 Å) operated at 30 kV and 45 mA. The X-ray diffraction intensity found for a bare substrate was subtracted from the intensity observed for a porphyrin-coated substrate.

Photoconductivity experiments. The TRMC method and experimental setup are described in refs. 22 and 50. The porphyrin/TiO_2 bilayers were mounted in an X-band microwave cavity at a position of maximum electric field strength and illuminated either from the side of the TiO_2 substrate (backside) or from the side of the porphyrin film (front-side). The illumination intensity was varied between 10^{11} and 10^{13} photons/cm^2 per pulse. The data analysis has been described in detail previously.[49] Briefly, formation of mobile charge carriers due to illumination with a nanosecond laser pulse (3 ns FWHM) leads to an increase of the photoconductance (ΔG), followed by an eventual decrease due to decay of charge carriers. The increase in photoconductance is related to the normalized change in reflected microwave power ($\Delta P/P$) according to

$$\frac{\Delta P(t)}{P} = -K\Delta G(t) \tag{7.3}$$

The sensitivity factor K was determined as described in ref. 51 and equals 7×10^4 S^{-1}. From the maximum of ΔG during time, the incident photon to charge separation efficiency (IPCSE) was determined, as described in ref. 29.

7.3. Results and discussion

7.3.1. Structural characterization

In case the formation of a coordinative bond between the electron-accepting central Zn atom and an electron-donating side group of an adjacent molecule leads to a change in optical features, the occurrence of self-assembly can be determined using optical absorption and fluorescence spectroscopy.[36,52,53] Figure 7.2A shows the absorption spectrum of ZnBuP monomers dissolved in pure $CHCl_3$, which is found to be similar to the absorption spectra of ZnOP and ZnNP in pure $CHCl_3$. The transitions from the S_0 to the S_1 level and a higher vibrational mode give rise to the two Q-bands that peak at 589 nm and 550 nm, respectively. The S_0-S_2 transition results in a strong absorption band that peaks at 423 nm.[44] The data in Figure 7.2A show that addition of 25 μl pyridine leads to a red-shift of the absorption bands (peaks at 605 nm, 565 nm and 431 nm) and a more intense lowest Q-band. These changes in optical features are attributed to the formation of one-to-one complexes of pyridine with the ZnBuP molecule, resulting in a penta-coordination of the Zn atom.[54,55] The absorption spectra of ZnOP and ZnNP in $CHCl_3$/pyridine are observed to be similar to that of ZnBuP in $CHCl_3$/pyridine. Hence, the difference in benzylic substituents does not affect the absorption spectra.

Analogous to the changes in monomer absorption due to coordination of the central Zn atom by pyridine, molecular self-assembly in solid films can be monitored by a red-shift in absorption and a more intense lowest Q-band.[54] Figure 7.2B shows the absorption spectra of ZnBuP, ZnOP and ZnNP deposited on quartz. The absorption bands of ZnBuP on quartz are only broadened as compared to ZnBuP dissolved in $CHCl_3$. The absence of a red-shift and a more intense lowest Q-band in the absorption spectrum shows that most likely no coordinative bonds are present in the film, indicative for the absence of self-assembled ZnBuP molecules. In contrast, the absorption spectra of ZnOP and especially ZnNP on quartz show a considerable red-shift and a more intense lowest Q-band as compared to ZnBuP. This is attributed to the presence of coordinative bonds between the electron-accepting Zn atom and the electron-donating oxygen or nitrogen atoms in the side groups. The red-shift in absorption and increase of the intensity of the lowest Q-band are less pronounced for ZnOP than for ZnNP, which might originate from the stronger coordinative bond in case of the latter.[43,56] The Soret absorption band of the ZnOP film is split up more pronounced than for ZnNP. This is attributed to a stronger excitonic coupling between self-assembled ZnOP molecules in a stack, possibly caused by a

smaller center-to-center distance between adjacent molecules[43] leading to a larger excitonic splitting. In terms of the point-dipole approximation for the excitonic coupling,[57] the absence of a significant exciton splitting in the less intense Q-bands can be attributed to the lower transition dipole moments of the corresponding transitions as compared to the S_0-S_2 transition that gives rise to the Soret absorption band.

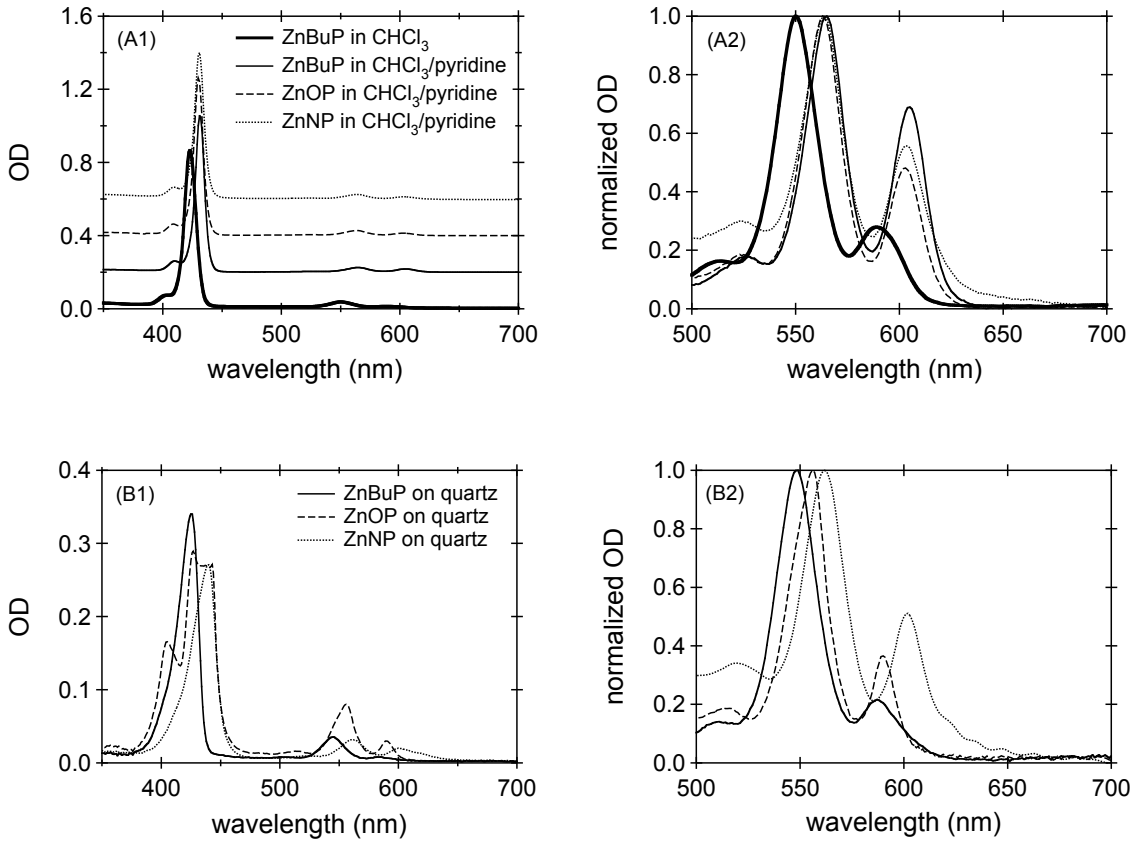

Figure 7.2. Optical density spectra of the porphyrin derivatives in solution (A) and deposited on quartz (B). The data in Figure A1 have different offsets. Left panels show the full OD spectrum; right panels the normalized OD for a limited spectral region.

Figure 7.3A shows the fluorescence spectra for ZnBuP, ZnOP and ZnNP on quartz. In agreement with the results discussed above, ZnOP and especially ZnNP exhibit red-shifted fluorescence bands as compared to ZnBuP, indicative for molecular self-assembly of the first two. Figure 7.3B shows the fluorescence decays of the ZnBuP, ZnOP and ZnNP films on quartz. Fitting a mono-exponential function convoluted with the instrumental response function to the decays yields exciton lifetimes of 74 ps, 160 ps and 400 ps. The fits are included in Figure 7.3B. These lifetimes are significantly lower than

the 1.3 ns lifetime observed for these porphyrin derivatives dissolved in $CHCl_3$/pyridine (data not shown), which is most likely due to enhanced radiationless decay in solid films.

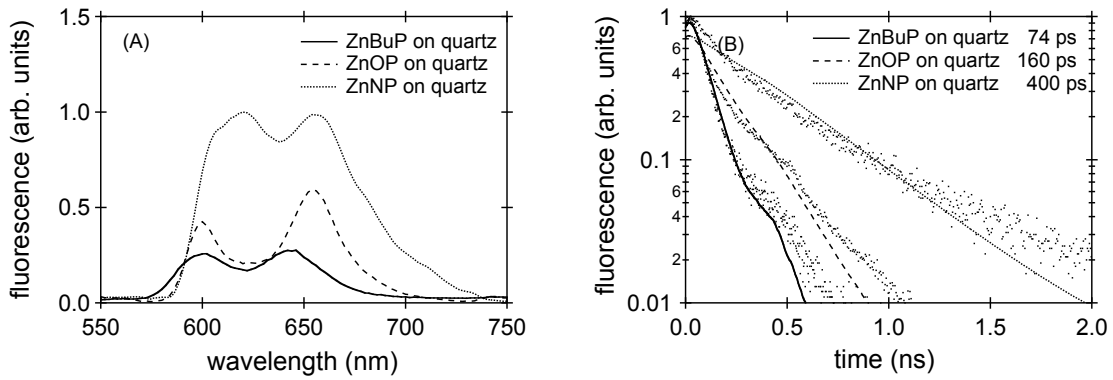

Figure 7.3. Fluorescence spectra (A) and decays (B) of the porphyrin derivatives investigated on quartz, recorded on excitation at 405 nm. The fluorescence decays are detected at the maximum of the lowest fluorescence band. Fits of a mono-exponential function convoluted with the instrumental response function to the fluorescence decays and the resulting lifetimes are included.

The differences in optical features between ZnBuP films on one side and the ZnOP and ZnNP films on the other side are attributed to the presence of coordinative bonds for the latter two, indicative for molecular self-assembly. To obtain further insight in the molecular organization, polarized optical microscopy (POM) and X-ray diffraction (XRD) studies are performed. Figure 7.4A shows the polarized optical micrograph and the X-ray diffraction pattern of ZnBuP on quartz. The ZnBuP film appears dark between crossed polarizer and analyzer and remains dark on rotation of the sample around the axis perpendicular to the plane of the film. This implies that the polarization of the incident light beam does not change upon transmission through the ZnBuP film. As a consequence, the transmitted light cannot pass through the crossed analyzer, resulting in a dark appearance of the film. The observed findings indicate an isotropic film structure with respect to rotation around the axis perpendicular to the plane of the film. This could either be due to an isotropic layer structure or due to a homeotropic molecular alignment (molecular planes aligned parallel to the substrate). The absence of a diffraction peak in the XRD pattern excludes the latter possibility and leads to the conclusion that the ZnBuP film lacks any molecular organization.

The X-ray diffraction pattern of ZnOPBr deposited on quartz, shown in Figure 7.4B, differs significantly from that of ZnBuP on quartz. The pronounced peaks in the XRD pattern observed for ZnOPBr originate from a well-developed periodic structure directed perpendicular to the substrate. The two peaks observed can be explained by first and second order diffraction by parallel planes with an interplanar distance (*d*) equal to 14.8 Å. This distance agrees with the diameter of a self-assembled stack of about 15 Å, or equivalently, with the distance between adjacent self-assembled stacks. Since only a periodic structure directed perpendicular to the substrate can give rise to a diffraction peak, this would imply the alignment of the propagation direction of the self-assembled stacks parallel to the substrate. In previous work on ZnOPBr crystals, the center-to-center distance R_{DA} between ZnOPBr molecules within a self-assembled stack has been found to be 8.75 Å, while the distance between the ZnOPBr macrocycles equals only 3.47 Å.[43] In case the ZnOPBr molecules in a crystal and in a thin film self-assemble in a similar way and the propagation direction of the self-assembled stacks in a film is parallel to the substrate, the angle between the ZnOPBr macrocycles and the substrate equals 23º as shown schematically in Figure 7.4.

The polarized optical micrograph and XRD pattern of ZnOP on quartz, also shown in Figure 7.4B, are observed to be similar to those for ZnOPBr. The first and second order X-ray diffraction peaks are only slightly shifted towards higher angles. These peaks correspond to an interplanar distance equal to 14.01 Å. The slightly smaller interplanar distance as compared to ZnOPBr and less intense diffraction peaks are attributed to the absence of the Br atoms. Both ZnOPBr and ZnOP exhibit similar birefringent domains between crossed polarizer and analyzer. The birefringence is caused by an anisotropy of the index of refraction, leading to a splitting of the linearly polarized incident beam into two components with polarizations perpendicular to each other. As a consequence, part of the transmitted light beam can pass through the crossed analyzer, leading to a bright appearance of the film. The observed birefringence independently confirms the presence of molecular order in the ZnOPBr and ZnOP films. The birefringence is observed to be comparable for layers deposited on TiO_2 and quartz, as also observed previously[32], showing a similar molecular organization on both substrates. The ordered domains have a typical area of 10 μm x 10 μm and a thickness of 50 nm. The comparable X-ray diffraction patterns and polarized optical micrographs suggest similar mutual orientations for the individual molecules in a self-assembled stack and for the alignment of the stacks with respect to the substrate. This implies that the propagation direction of the self-

assembled ZnOP stacks is parallel to the substrate, with the angle between the ZnOP macrocycles and the substrate equal to 23°.

Figure 7.4C shows the polarized optical micrograph and the X-ray diffraction pattern of ZnNP on quartz. The ZnNP film appears to posses both dark and birefringent domains between crossed polarizer and analyzer, corresponding to a combination of disordered and ordered regions, respectively. The X-ray diffraction peak observed for the ZnNP film corresponds in case of first order diffraction to an interplanar distance equal to 16.60 Å, which is attributed to the distance between adjacent self-assembled stacks. The fact that only the ordered domains can contribute to the observed diffraction peak explains the lower intensity of this peak as compared to that observed for the ZnOP film.

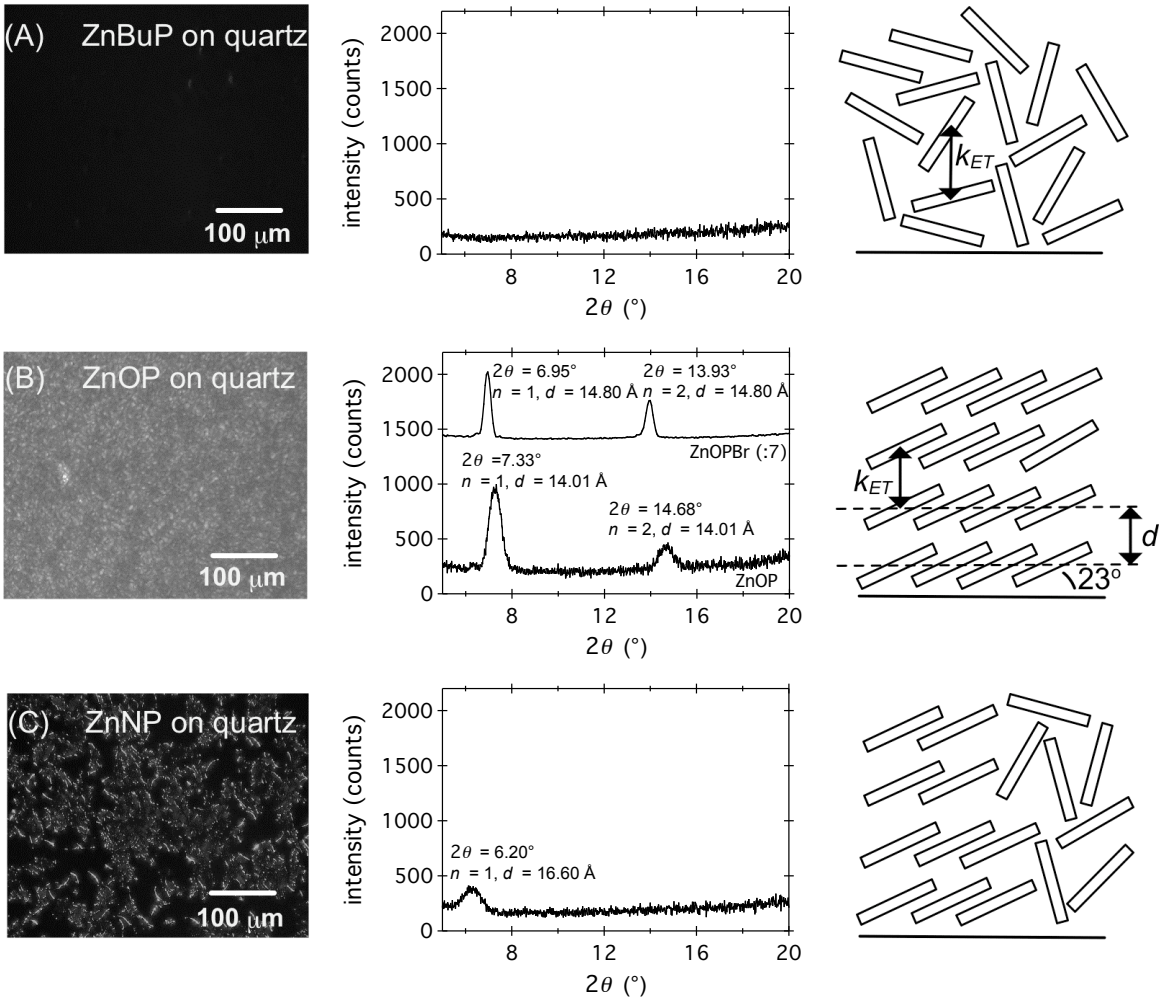

Figure 7.4. Polarized optical micrographs obtained between crossed polarizer and analyzer (left panels), X-ray diffraction patterns (middle panels) and film structures (right panels) of the porphyrin derivatives investigated on quartz. The X-ray diffraction intensities of the porphyrin films on quartz are corrected for the signal obtained for bare quartz.

7.3.2. Determination of the exciton diffusion length

Quantification of the exciton transfer dynamics allows determining the impact of molecular order on the ability to transport excitons efficiently. Exciton diffusion is studied using the time-resolved microwave conductivity (TRMC) technique.[22, 50] Figure 7.5A shows the photoconductance transients obtained on pulsed illumination at the absorption maximum of ZnBuP, ZnOP and ZnNP films on TiO_2. The samples are illuminated through the TiO_2 layer, resulting in a high initial exciton concentration near the TiO_2/porphyrin interface. Those excitons that are able to reach the interface with TiO_2 can dissociate by injection of an electron into the TiO_2 layer. Since the mobility of electrons in TiO_2[58] largely exceeds the mobility of holes in porphyrins[59], the observed change in photoconductance (ΔG) mainly results from an increase of the number of mobile electrons in TiO_2. The initial rise time of ΔG largely exceeds the laser pulse duration and is determined by the 18 ns response time of the microwave cavity. It follows from Figure 7.5A that illumination of a bilayer consisting of the self-assembled porphyrin derivatives ZnOP or ZnNP on TiO_2 results in a larger change in ΔG as compared to a bilayer of non-assembled ZnBuP and TiO_2. This effect is most pronounced for ZnOP on TiO_2, indicative for the most efficient photo-induced charge separation.

The incident photon to charge separation efficiency (IPCSE) is determined from ΔG as described in ref. 29. Figure 7.5B shows the IPCSE as function of wavelength of ZnOP on TiO_2. The IPCSE spectrum follows closely the optical attenuation spectrum, also presented in Figure 7.5B, which demonstrates clearly photosensitization of TiO_2 by the porphyrin derivative. The IPCSE at the absorption maximum equals 16 %, comparably efficient as the system based on nematically organized homeotropically aligned *meso*-tetrakis(4-*n*-butylphenyl)porphyrin molecules on TiO_2 we have studied recently.[32] An important advantage of ZnOP as compared to that system involves the absence of any observed sensitivity of the molecular organization to the thickness of the porphyrin layer, which is highly beneficial for application in molecular opto-electronics. Figure 7.5C shows the IPCSE as function of incident light intensity. At illumination intensities below 2×10^{12} photons/cm^2/pulse no significant influence of the intensity on the IPCSE is observed. This indicates that exciton-exciton annihilation and bimolecular charge recombination processes are insignificant under these illumination conditions.

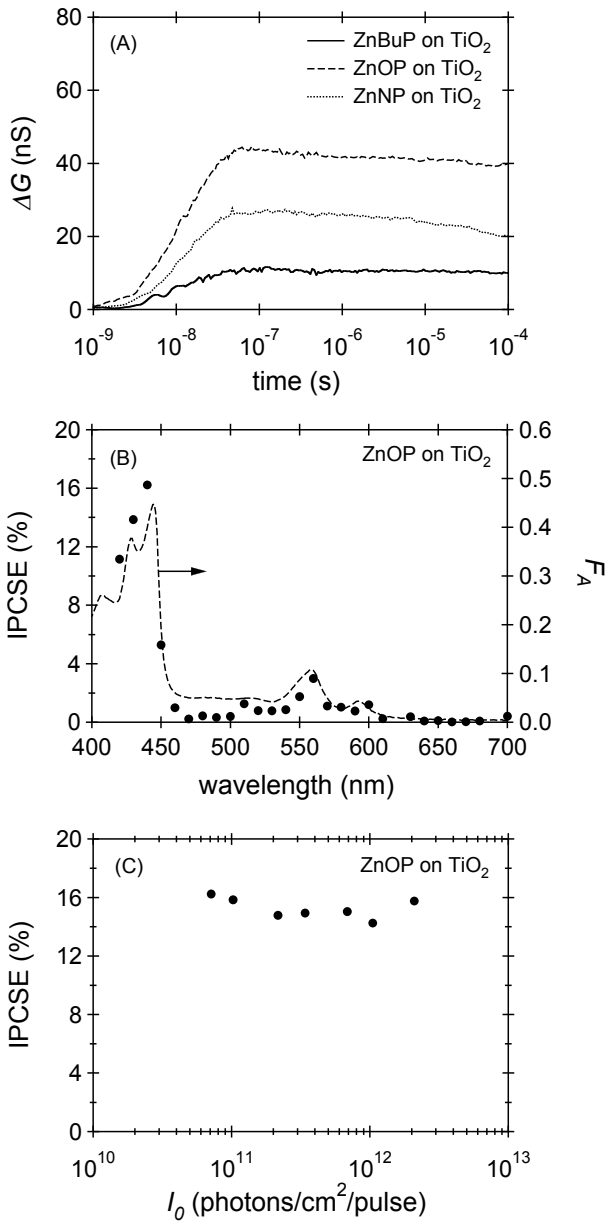

Figure 7.5. Photoconductance transients obtained on pulsed excitation (at 430 nm for ZnBuP, at 440 nm for ZnOP and ZnNP, with 10^{12} photons/cm^2/pulse) of the porphyrin derivatives on TiO_2 (A) and the IPCSE and fraction of absorbed light (F_A) as function of wavelength for ZnOP on TiO_2 (B). Figure (C) shows the IPCSE as function of illumination intensity.

The exciton diffusion length (Λ_E) can be deduced by applying an analytical model for the photo-induced charge separation efficiency to describe the experimental TRMC data, as discussed previously.[60] The IPCSE depends on the fraction of incident photons that is reflected by the bilayer (F_R), the number of excitons that reaches the porphyrin/TiO_2

interface normalized to the number of incident photons (S) and the interfacial electron injection yield relative to all modes of interfacial exciton deactivation (ϕ_{inj}) according to

$$IPCSE = (1 - F_R) \cdot S(\alpha, L, \Lambda_E) \cdot \phi_{inj} \cdot 100\% \tag{7.4}$$

The factor S depends on the exponential absorption coefficient (α), the porphyrin layer thickness (L) and Λ_E. Analytical equations for S on backside (S_{BR}, from the side of the TiO_2 substrate) and front-side (S_{FR}, from the side of the porphyrin film) illumination can be derived by solving the classical diffusion equation for steady-state conditions and are given in Appendix A.[60-62]

Accurate values for both ϕ_{inj} and Λ_E can be obtained by varying the thickness of the porphyrin layer. In case $L<\Lambda_E$ almost all excitons formed are able to reach the exciton-dissociating interface. Since the number of excitons formed is insensitive to the side of illumination, the IPCSE values on backside and front-side illumination are expected to be comparable. Increasing L to values less than Λ_E leads to an increase of the IPCSE, both for backside and for front-side illumination, since more light is absorbed as the porphyrin layer becomes thicker. In case of backside illumination, a further increase of L does not result in an additional increase of the IPCSE, because mainly those excitons formed within a distance Λ_E from the interface can undergo interfacial charge separation. On the contrary, on front-side illumination increasing L results in a lower concentration of excitons near the porphyrin/TiO_2 interface. As a consequence the IPCSE decreases with increasing L and eventually becomes zero.

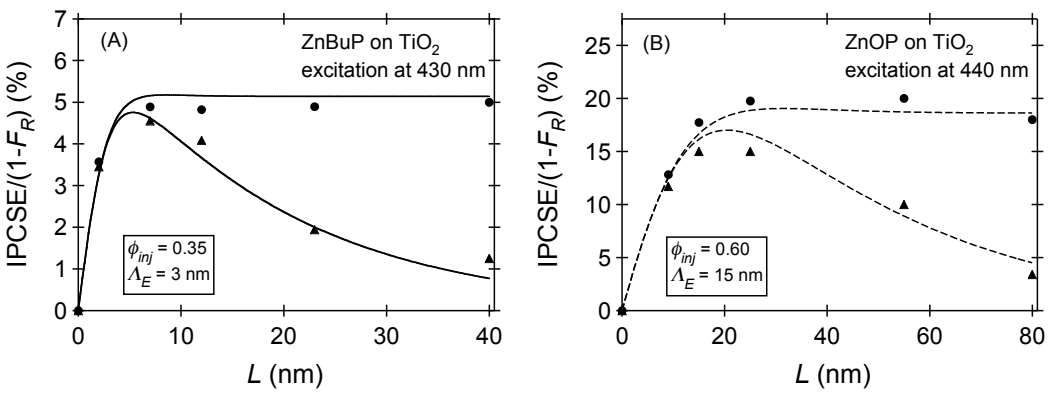

Figure 7.6. IPCSE/(1-F_R) as function of the porphyrin layer thickness (L) for ZnBuP on TiO_2 (A) and ZnOP on TiO_2 (B). Dots represent backside illumination, triangles front-side illumination. The curves through the data points represent the fits of equations 7.4, A3 and A4 to the experimental data; fit parameters are shown in the insets.

Figure 7.6 shows the IPCSE divided by (1-F_R) as function of L on backside and front-side illumination for ZnBuP on TiO_2 (A) and ZnOP on TiO_2 (B). Reason for presenting the IPCSE divided by (1-F_R) involves the difference in F_R between various samples. The experimental data presented in Figure 7.6 exhibit a layer thickness dependence that agrees with the expectations discussed above. Fitting equations 7.4, A3 and A4 to the experimental data obtained for ZnBuP on TiO_2 results in Λ_E = 3±1 nm[63] and ϕ_{inj} = 0.35±0.05. Combining an exciton diffusion length of 3 nm with an exciton lifetime of 74 ps yields an exciton diffusion coefficient of 1×10^{-7} m^2/s, as follows from equation 7.2. Assuming a center-to-center distance R_{DA} between ZnBuP molecules of 15 Å (diameter of a ZnBuP molecule) and using equation 7.1 yields an energy transfer rate equal to 4×10^{10} s^{-1}. Within its lifetime of 74 ps an exciton can hop on average only 3 times between adjacent ZnBuP molecules.

The significantly larger ΔG and higher IPCSE observed for ZnOP and ZnNP on TiO_2 are indicative for more efficient exciton transport through films that consist of self-assembled stacks. The relatively poor solubility of ZnNP in toluene, however, does not allow preparing films thicker than 20 nm. The IPCSE divided by (1-F_R) as function of L on backside and front-side illumination is therefore only determined for ZnOP on TiO_2. Fitting equations 7.4, A3 and A4 to the experimental data shown in Figure 7.6B results in Λ_E = 15±1 nm[63] and ϕ_{inj} = 0.60±0.05. Combining an exciton diffusion length of 15 nm with an exciton lifetime of 160 ps gives an exciton diffusion coefficient equal to 1.4×10^{-6} m^2/s. Since the self-assembled stacks are aligned with their propagation direction parallel to the substrate, exciton motion in a direction perpendicular to the TiO_2 substrate occurs by interstack rather than by intrastack energy transfer, as shown schematically in Figure 7.4. The value of R_{DA} between an exciton-donating and -accepting ZnOP molecule is therefore taken equal to the interstack distance of 14.01 Å, determined by X-ray diffraction. Using equation 7.1, this distance and the found exciton diffusion coefficient yield $k_{ET} = 7.2\times10^{11}$ s^{-1}. Within its lifetime of 160 ps an exciton can on average make 10^2 hops before decay to the ground state occurs.

7.3.3. Origin of the enhanced exciton diffusion length

Table 7.1 summarizes the parameters involved in energy transfer in films of the porphyrin derivatives investigated, together with literature values for natural

chlorosomes. Comparison of the energy transfer parameters for ZnBuP and ZnOP shows that self-assembly of the latter strongly enhances the exciton diffusion length. This is due to a longer exciton lifetime and a larger exciton diffusion coefficient, originating from a higher energy transfer rate, as discussed below. The exciton diffusion length in the self-assembled ZnOP film is comparable to that in natural chlorosomes. It can be seen in Table 7.1 that k_{ET} within a chlorosomal bacteriochlorophyll stack is more than one order of magnitude higher than for ZnOP, as expected on basis of the larger transition dipole moment of the Q-band of bacteriochlorophyll molecules. However, the larger value for R_{DA} and τ_E for ZnOP lead to a value for Λ_E comparable to that for a bacteriochlorophyll stack. In addition, it should be noted that the value for Λ_E determined for ZnOP corresponds to interstack exciton diffusion, while the Λ_E value for bacteriochlorophyll stacks refers to intrastack motion.

Table 7.1. Parameters characterizing the energy transfer in isotropic ZnBuP films, in self-assembled ZnOP films and in natural chlorosomes.

Light-harvesting system	Λ_E (nm)	τ_E (ps)	D_E (m^2/s)	R_{DA} (Å)	k_{ET} (ps^{-1})	τ_{ET} (ps)	$\tau_E \cdot k_{ET}$
ZnBuP	3	74	1×10^{-7}	15	0.04	23	3
ZnOP	15	160	1.4×10^{-6}	14.01	0.72	1.4	10^2
Chlorosome	~15	~50 [16]	5×10^{-6}	6.8 [19]	10	0.1[16-18]	5×10^2

In the limit of weak intermolecular excitonic coupling, motion of excitons can be considered as diffusive with an intermolecular hopping rate k_{ET} given by[64, 65]

$$k_{ET} = \frac{2\pi}{\hbar}\left|V_{DA}\right|^2 J_{DA} \tag{7.5}$$

The factor V_{DA} denotes the excitonic coupling between energy donor and acceptor and J_{DA} represents the spectral overlap integral. The definition and evaluation of the spectral overlap integrals for ZnBuP and ZnOP are specified in Appendix B. The experimental absorption and fluorescence spectra yield comparable values for J_{DA} equal to 1.5×10^{18} J^{-1} for ZnBuP and 1.8×10^{18} J^{-1} for ZnOP. Hence, the much higher k_{ET} found for ZnOP is

mainly due to a larger value of V_{DA}. Using equation 7.5 with the experimentally determined values for k_{ET} and J_{DA} yields excitonic couplings V_{DA} of 36 cm^{-1} for ZnBuP and 1.3×10^2 cm^{-1} for ZnOP. The value of V_{DA} equal to 1.3×10^2 cm^{-1} observed for ZnOP indicates a strong excitonic coupling between adjacent self-assembled stacks, which must originate from a favorable mutual orientation of molecules in adjacent stacks. Quantum-chemical calculations on excitonic couplings are underway in order to establish to which extent the value for interstack excitonic coupling can be understood on basis of the molecular organizations deduced above and whether exciton transfer can be further improved.

7.4. Conclusions

This work involves a study of the relationship between molecular self-assembly of porphyrin derivatives and the ability to transport excitons efficiently to an active interface. ZnBuP films are found to have a disordered structure, in which the exciton diffusion length equals 3±1 nm. In contrast, ZnOP molecules self-assemble via coordinative bonds between adjacent molecules. This leads to the formation of molecular stacks aligned parallel to a TiO_2 substrate. The diffusion length for exciton transport between the stacks is as long as 15±1 nm. The large exciton diffusion length both originates from a long exciton lifetime and a strong excitonic coupling for interstack energy transfer. The difference in exciton diffusion length between ZnBuP and ZnOP demonstrates the importance of molecular self-assembly leading to efficient interstack exciton transport. The efficient interstack energy transfer has promising prospects for application of such self-assembled porphyrins in opto-electronics.

Acknowledgment

The authors thank prof. Stephen J. Picken and Arkadiusz Kotlewski from the Nanostructured Materials Section of TU Delft for helpful discussions and assistance with Polarized Optical Microscopy experiments, respectively. Marjan Versluijs from the Group of Inorganic Chemistry and Catalysis of Utrecht University is acknowledged for performing the XRD measurements. Research in Delft was supported financially by the Delft Research Centre for Sustainable Energy. BMJMS and RJMKG thank the Dutch Organization for Scientific Research NWO for a ‘Jonge Chemici’ scholarship.

Supporting Information

Appendix A

The factor S represents the number of excitons that reaches the porphyrin/TiO_2 interface normalized to $I_0(1\text{-}F_R)$, i.e. the number of photons entering the sample. An analytical expression for S can be derived from solving the classical diffusion equation for steady-state conditions, as described in detail in ref. 63. In brief, in case of backside illumination (from the side of the TiO_2 substrate) the following differential equation applies:

$$\left[\frac{\partial n(z)}{\partial t}\right]_B = \alpha J_0 e^{-\alpha(L-z)} - \frac{n(z)}{\tau_E} + D_E \frac{\partial^2 n(z)}{\partial z^2} \qquad \text{(A1)}$$

The coordinate z corresponds to the distance from the interface between porphyrin and TiO_2. The factor $n(z)$ denotes the concentration of excitons and J_0 is the number of excitons entering the TnBuPP layer ($J_0 = I_0(1\text{-}F_R)$). Analogously, for front-side illumination (from the side of the porphyrin film) the corresponding differential equation is:

$$\left[\frac{\partial n(z)}{\partial t}\right]_F = \alpha J_0 e^{-\alpha z} - \frac{n(z)}{\tau_E} + D_E \frac{\partial^2 n(z)}{\partial z^2} \qquad \text{(A2)}$$

Excitons that reach the porphyrin/TiO_2 interface are assumed to be rapidly deactivated, i.e. $n(L) = 0$. At the surface of the porphyrin layer, excitons are assumed to be reflected, i.e. $D_E \delta n(0)/\delta z^2 = 0$. Solving equations A1 and A2 for steady-state conditions ($\delta n(z)/\delta t = 0$) result in the following equations for S on backside (A3) and front-side illumination (A4), respectively, whereas the square root of $D_E \cdot \tau_E$ has been substituted by the parameter Λ_E:

$$S_{BR} = \left(\frac{\alpha^2 \Lambda_E^2}{\alpha^2 \Lambda_E^2 - 1}\right)\left(1 - e^{-\alpha L} \sec h\left(\frac{L}{\Lambda_E}\right) - \frac{\tanh\left(\frac{L}{\Lambda_E}\right)}{\alpha \Lambda_E}\right) \qquad \text{(A3)}$$

$$S_{FR} = \left(\frac{\alpha^2 \Lambda_E^2}{\alpha^2 \Lambda_E^2 - 1} \right) \left(\sec h \left(\frac{L}{\Lambda_E} \right) - e^{-\alpha L} \left(1 + \frac{\tanh\left(\frac{L}{\Lambda_E} \right)}{\alpha \Lambda_E} \right) \right) \tag{A4}$$

Appendix B

In case of incoherent exciton hopping between molecules, the energy transfer rate k_{ET} between a donor and acceptor depends on the excitonic coupling V_{DA} and the spectral overlap integral J_{DA} according to[64, 65]

$$k_{ET} = \frac{2\pi}{\hbar} |V_{DA}|^2 J_{DA} \tag{B1}$$

The factor J_{DA} corresponds to the Franck-Condon weighted density-of-states and can be obtained from

$$J_{DA} = \int F_D(E) A_A(E) dE \tag{B2}$$

where F_D and A_A denote the emission factor of the energy donor and the absorption factor of the energy acceptor, respectively.[64] The emission factor $F_D(E)$ depends on the fluorescence intensity $I_F(E)$ according to

$$F_D(E) = \frac{E^{-3} I_F(E)}{\int E^{-3} I_F(E) dE} \tag{B3}$$

The absorption factor $A_A(E)$ is related to the extinction coefficient $\varepsilon(E)$ by

$$A_A(E) = \frac{E^{-1} \varepsilon(E)}{\int E^{-1} \varepsilon(E) dE} \tag{B4}$$

Figure 7.7A shows the fluorescence intensity $I_F(E)$ and extinction coefficient $\varepsilon(E)$ for ZnBuP and ZnOP as function of photon energy E. The limits for integration of the functions shown in the denominator of equations B3 and B4 are determined by the energy range of the transitions relevant for energy transfer; i.e. the transitions between the vibrational levels belonging to the S_1 and S_0 electronic states. Application of equations B3 and B4 then yields the emission factor $F_D(E)$ and absorption factor $A_A(E)$, presented in Figure 7.7B. Multiplication of F_D and A_A for the individual compounds results in the

curves presented in Figure 7.7C. Integration of these curves yields values for J_{DA} equal to 1.5×10^{18} J^{-1} for ZnBuP and 1.8×10^{18} J^{-1} for ZnOP.

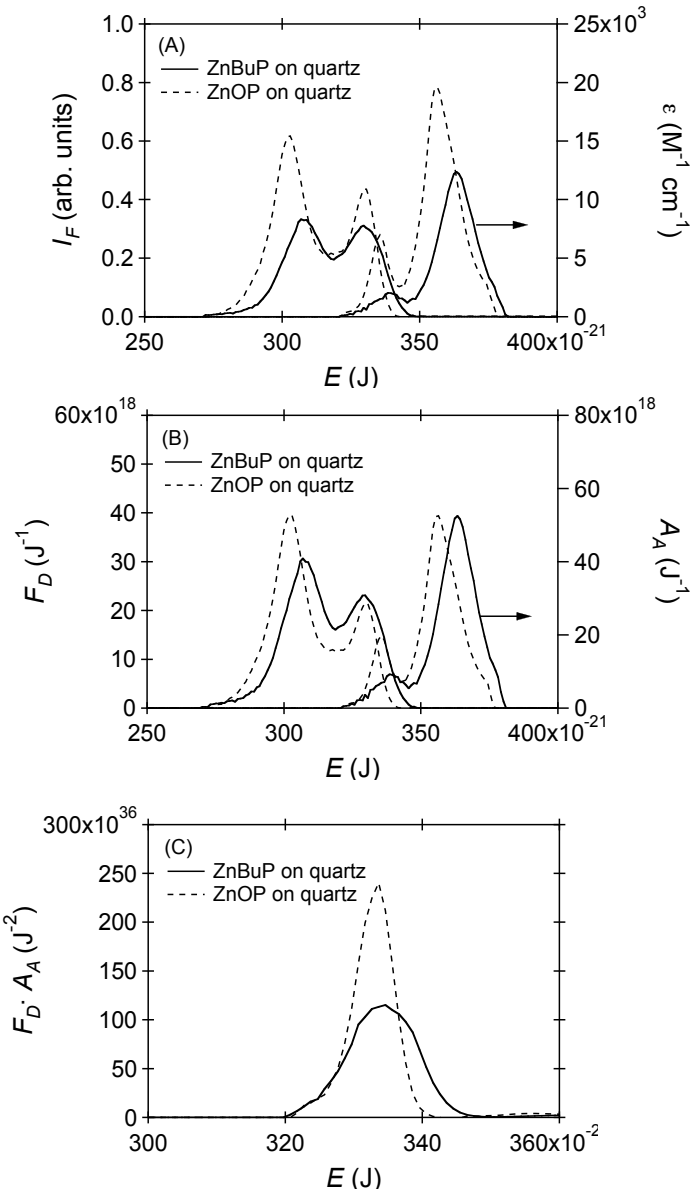

Figure 7.7. Fluorescence and absorption of ZnBuP and ZnOP (A), fluorescence factor F_D and absorption factor A_A (B) and product of F_D and A_A (C) as function of photon energy.

References

(1) Amerongen, H. v.; Valkunas, L.; Grondelle, R. v., *Photosynthetic excitons*. World Scientific: Singapore, 2000.

(2) Kühlbrandt, W.; Wang, D. N., *Nature* **1991,** 350, 130-134.

(3) Krauss, N.; Hinrichs, W.; Witt, I.; Fromme, P.; Pritzkow, W.; Dauter, Z.; Betzel, C.; Wilson, K. S.; Witt, H. T.; Saenger, W., *Nature* **1993,** 361, (6410), 326-331.

(4) Kühlbrandt, W.; Neng Wang, D.; Fujiyoshi, Y., *Nature* **1994,** 367, 614-621.
(5) McDermott, G.; Prince, S. M.; Freer, A. A.; Hawthornthwaitelawless, A.M.; Papiz, M. Z.; Cogdell, R. J.; Isaacs, N. W., *Nature* **1995,** 374, 517-521.
(6) Oijen, A. M. v.; Ketelaars, M.; Köhler, J.; Aartsma, T. J.; Schmidt, J., *Science* **1999,** 285, 400-402.
(7) Roszak, A. W.; Howard, T. D.; Southall, J.; Gardiner, A. T.; Law, C. J.; Isaacs, N. W.; Cogdell, R. W., *Science* **2003,** 302, 1969-1972.
(8) Liu, Z.; Yan, H.; Wang, K.; Kuang, T.; Zhang, J.; Gui, L.; An, X.; Chang, W., *Nature* **2004,** 428, 287-292.
(9) Staehelin, L. A.; Golecki, J. R.; Fuller, R. C.; Drews, G., *Archives of Microbiology* **1978,** 119, (3), 269-277.
(10) Holzwarth, A. R.; Griebenow, K.; Schaffner, K., *Zeitschrift fur Naturforschung* **1990,** 45, (3-4), 203-206.
(11) Hildebrandt, P.; Griebenow, K.; Holzwarth, A. R.; Schaffner, K., *Zeitschrift fur Naturforschung* **1991,** 46, (3-4), 228-232.
(12) Psencik, J.; Ikonen, T. P.; Laurinmaki, P.; Merckel, M. C.; Butcher, S. J.; Serimaa, R. E.; Tuma, R., *Biophysical Journal* **2004,** 87, (2), 1165-1172.
(13) Balaban, T. S.; Holzwarth, A. R.; Schaffner, K.; Boender, G. J.; Degroot, H. J. M., *Biochemistry* **1995,** 34, (46), 15259-15266.
(14) Rossum, B. J. v.; Steengaard, D. B.; Mulder, F. M.; Boender, G. J.; Schaffner, K.; Holzwarth, A. R.; Groot, H. J. M. d., *Biochemistry* **2001,** 40, 1587-1595.
(15) Balaban, T. S.; Linke-Schaetzel, M.; Bhise, A. D.; Vanthuyne, N.; Roussel, C.; Anson, C. E.; Buth, G.; Eichhofer, A.; Foster, K.; Garab, G.; Gliemann, H.; Goddard, R.; Javorfi, T.; Powell, A. K.; Rosner, H.; Schimmel, T., *Chemistry-A European Journal* **2005,** 11, (8), 2267-2275.
(16) Prokhorenko, V. I.; Steensgaard, D. B.; Holzwarth, A. F., *Biophysical Journal* **2000,** 79, (4), 2105-2120.
(17) Psencik, J.; Polivka, T.; Nemec, P.; Dian, J.; Kudrna, J.; Maly, P.; Hala, J., *Journal of Physical Chemistry A* **1998,** 102, (23), 4392-4398.
(18) Savikhin, S.; Zhu, Y. W.; Lin, S.; Blankenship, R. E.; Struve, W. S., *Journal of Physical Chemistry* **1994,** 98, (40), 10322-10334.
(19) Holzwarth, A. R.; Schaffner, K., *Photosynthetic Research* **1994,** 41, 225-233.
(20) Wohrle, D.; Tennigkeit, B.; Elbe, J.; Kreienhoop, L.; Schnurpfeil, G., *Molecular Crystals and Liquid Crystals* **1993,** 230, 221-226.
(21) Kerp, H. R.; Donker, H.; Koehorst, R. B. M.; Schaafsma, T. J.; Faassen, E. E. v., *Chemical Physics Letters* **1998,** 298, (4-6), 302-308.
(22) Kroeze, J. E.; Savenije, T. J.; Warman, J. M., *Journal of Photochemistry and Photobiology A-Chemistry* **2002,** 148, 49-55.
(23) Peumans, P.; Uchida, S.; Forrest, S. R., *Nature* **2003,** 425, (6954), 158-162.
(24) Peumans, P.; Forrest, S. R., *Applied Physics Letters* **2001,** 79, (1), 126-128.
(25) Peumans, P.; Yakimov, A.; Forrest, S. R., *Journal of Applied Physics* **2003,** 93, (7), 3693-3723.
(26) Stubinger, T.; Brutting, W., *Journal of Applied Physics* **2001,** 90, (7), 3632-3641.
(27) Kroeze, J. E.; Koehorst, R. B. M.; Savenije, T. J., *Advanced Functional Materials* **2004,** 14, (10), 992-998.
(28) Donker, H.; van Hoek, A.; van Schaik, W.; Koehorst, R. B. M.; Yatskou, M. M.; Schaafsma, T. J., *Journal of Physical Chemistry B* **2005,** 109, (36), 17038-17046.
(29) Huijser, A.; Savenije, T. J.; Kroeze, J. E.; Siebbeles, L. D. A., *Journal of Physical Chemistry B* **2005,** 109, 20166-20173.

(30) Huijser, A.; Savenije, T. J.; Siebbeles, L. D. A., *Thin Solid Films* **2006,** 511-512, 208-213.
(31) Piris, J.; Debije, M. G.; Stutzmann, N.; van de Craats, A. M.; Watson, M. D.; Mullen, K.; Warman, J. M., *Advanced Materials* **2003,** 15, (20), 1736-1740.
(32) Huijser, A.; Savenije, T. J.; Kotlewski, A.; Picken, S. J.; Siebbeles, L. D. A., *Advanced Materials* **2006,** 18, 2234-2239.
(33) Jesorka, A.; Balaban, T. S.; Holzwarth, A. R.; Schaffner, K., *Angewandte Chemie - International Edition* **1996,** 23-24, 2861-2863.
(34) Tamiaki, H., *Coordination chemistry reviews* **1996,** 148, 183-197.
(35) Miyatake, T.; Tamiaki, H.; Holzwarth, A. R.; Schaffner, K., *Helvetica Chimica Acta* **1999,** 82, (6), 797-810.
(36) Balaban, T. S.; Goddard, R.; Linke-Schaetzel, M.; Lehn, J. M., *Journal of the American Chemical Society* **2003,** 125, (14), 4233-4239.
(37) Balaban, T. S., *Accounts of Chemical Research* **2005,** 38, (8), 612-623.
(38) Kunieda, M.; Tamiaki, H., *Journal of Organic Chemistry* **2005**, (70), 820-828.
(39) Kunieda, M.; Tamiaki, H., *European Journal of Organic Chemistry* **2006,** 10, 2352-2361.
(40) Huber, V.; Lysetska, M.; Wurthner, F., *Small* **2007,** 3, (6), 1007-1014.
(41) Zhou, Y. S.; Wang, B.; Zhu, M. Z.; Hou, J. G., *Chemical Physics Letters* **2005,** 403, (1-3), 140-145.
(42) Elemans, J.; Lensen, M. C.; Gerritsen, J. W.; van Kempen, H.; Speller, S.; Nolte, R. J. M.; Rowan, A. E., *Advanced Materials* **2003,** 15, (24), 2070-2073.
(43) Suijkerbuijk, B. M. J. M.; Tooke, D. M.; Lutz, M.; Spek, A. L.; Koten, G. v.; Klein Gebbink, R. J. M., *Chem. Asian J.* **2007,** 2, 889-903.
(44) Gouterman, M., *The Porphyrins; Volume III*. Academic Press: New York, 1978; Vol. 3.
(45) Gerdes, R.; Wohrle, D.; Spiller, W.; Schneider, G.; Schnurpfeil, G.; Schulz-Ekloff, G., *Journal of Photochemistry And Photobiology A-Chemistry* **1997,** 111, (1-3), 65-74.
(46) Iliev, V.; Mihaylova, A.; Bilyarska, L., *Journal of Molecular Catalysis A-Chemical* **2002,** 184, (1-2), 121-130.
(47) Grätzel, M., *Nature* **2001,** 414, 338-344.
(48) Gust, D.; Moore, T. A.; Moore, A. L., *Accounts of Chemical Research* **2001,** 34, 40-48.
(49) Kroeze, J. E.; Savenije, T. J.; Warman, J. M., *Journal of the American Chemical Society* **2004,** 126, 7608.
(50) Haas, M. P. de; Warman, J. M., *Chemical Physics* **1982,** 73, 35-53.
(51) Savenije, T. J.; Haas, M.P. de; Warman, J. M., *Zeitschrift fur Physikalische Chemie-International Journal of Research in Physical Chemistry & Chemical Physics* **1999,** 212, 201-206.
(52) Chernook, A. V.; Rempel, U.; vonBorczyskowski, C.; Shulga, A. M.; Zenkevich, E. I., *Chemical Physics Letters* **1996,** 254, (3-4), 229-241.
(53) Lee, S. J.; Mulfort, K. L.; O'Donnell, J. L.; Zuo, X. B.; Goshe, A. J.; Wesson, P. J.; Nguyen, S. T.; Hupp, J. T.; Tiede, D. M., *Chemical Communications* **2006**, (44), 4581-4583.
(54) Fleischer, E. B.; Shachter, A. M., *Inorganic Chemistry* **1991,** 30, (19), 3763-3769.
(55) Summers, J. S.; Stolzenberg, A. M., *Journal of the American Chemical Society* **1993,** 115, (23), 10559-10567.
(56) Nardo, J. V.; Dawson, J. H., *Inorganica Chimica Acta-Bioinorganic Chemistry* **1986,** 123, (1), 9-13.

(57) May, V.; Kühn, O., *Charge and Energy Transfer Dynamics in Molecular Systems. A Theoretical Introduction*. Wiley-VCH: Berlin, 2000.
(58) Bak, T.; Nowotny, J.; Rekas, M.; Sorrell, C. C., *Journal of Physics and Chemistry of Solids* **2003,** 64, (7), 1069-1087.
(59) Checcoli, P.; Conte, G.; Salvatori, S.; Paolesse, R.; Bolognesi, A.; Berliocchi, A.; Brunetti, F.; D'Amico, A.; Di Carlo, A.; Lugli, P., *Synthetic Metals* **2003,** 138, (1-2), 261-266.
(60) Kroeze, J. E.; Savenije, T. J.; Vermeulen, M. J. W.; Warman, J. M., *Journal of Physical Chemistry B* **2003,** 107, (31), 7696-7705.
(61) Simpson, O., *Proc. R. Soc. London Ser. A* **1957,** 238, 402-411.
(62) Södergren, S.; Hagfeldt, A.; Olsson, J.; Lindquist, S. E., *Journal of Physical Chemistry* **1994,** 98, (21), 5552-5556.
(63) Note, that the root-mean-square diffusion distance (Λ_D) is related to Λ_E by $\Lambda_D = \sqrt{(2\delta)}\cdot\Lambda_E$ with δ the dimensionality. The one-dimensional Λ_D, in the direction perpendicular to the TiO_2 substrate, hence equals $\sqrt{2}\cdot\Lambda_E$.
(64) Pope, M.; Svenberg, C. E., *Electronic Processes in Organic Crystals and Polymers*. second ed.; Oxford Science Publications: New York, 1999.
(65) Hennebicq, E.; Pourtois, G.; Scholes, G. D.; Herz, L. M.; Russell, D. M.; Silva, C.; Setayesh, S.; Grimsdale, A. C.; Mullen, K.; Bredas, J. L.; Beljonne, D., *Journal of the American Chemical Society* **2005,** 127, (13), 4744-4762.

CHAPTER 8

An experimental study on the molecular organization and exciton diffusion in a bilayer of a porphyrin and poly(3-hexylthiophene)*

The exciton root-mean-square displacement (Λ_D) in regioregular poly(3-hexylthiophene) (P3HT) deposited onto *meso*-tetrakis(n-methyl-4-pyridyl)porphyrin tetrachloride (H_2TMPyP) has been determined from the photovoltaic response of a device based on these materials in a bilayer configuration. Excitons formed on illumination that reach the interface between H_2TMPyP and P3HT can undergo interfacial charge separation by electron injection into the H_2TMPyP and hole injection into the P3HT. The incident photon to current efficiency (IPCE) exceeds 20 % over a broad wavelength regime. Theoretical analysis of the IPCE values gives a value for Λ_D in H_2TMPyP that amounts to 14 nm, while for P3HT a value of 18 nm is obtained. The latter value exceeds literature values reported for P3HT by almost a factor of three. X-ray diffraction analysis shows that in the studied bilayer the P3HT backbones are aligned parallel to the interface with H_2TMPyP. In contrast, in case of P3HT deposited onto TiO_2, for which Λ_D has been reported to equal only 7 nm, hardly any organization of the P3HT backbones is observed. The excitonic coupling between P3HT backbones deposited onto H_2TMPyP is as high as 125 cm^{-1}, a factor of three larger than the excitonic coupling between disordered P3HT backbones that amounts to 47 cm^{-1}. The difference illustrates the importance of controlling the molecular organization for the realization of efficient energy transfer in organic opto-electronics.

---

* This chapter is based on: Annemarie Huijser, Tom J. Savenije, Avi Shalav and Laurens D.A. Siebbeles, *Journal of Applied Physics,* submitted.

8.1. Introduction

Conjugated electron-donating polymers such as substituted poly(phenylene-vinylene) (PPV) and polythiophene derivatives are considered as attractive photoactive materials because of their strong absorption band in the visible and their ease of processing into thin films. The binding energy of an exciton, formed on absorption of a photon, ranges typically from 0.2 eV to 1.0 eV.[1-3] In order to realize an efficient photovoltaic device, excitons have to be dissociated into charges. This can be accomplished at an interface with an electron-accepting material. The driving force for charge separation has to exceed the exciton binding energy to allow exciton dissociation into charges. Electron-accepting materials studied intensively in combination with conjugated polymers include TiO_2[4, 5], perylene derivatives[6] and fullerenes[7]. Initially, bilayers of electron-donor and -acceptor were investigated. An important parameter in such organic-based solar cells is the average distance excitons are able to cover by diffusion before decay to the ground state occurs, referred to as the exciton root-mean-square displacement (Λ_D). In case of one-dimensional exciton diffusion, Λ_D is defined by

$$\Lambda_D = \sqrt{2D_E\tau_E} \tag{8.1}$$

with D_E the exciton diffusion coefficient and τ_E the exciton lifetime. Note, that the degree of exciton diffusion is usually characterized by the exciton diffusion length (Λ_E):

$$\Lambda_E = \sqrt{D_E\tau_E} \tag{8.2}$$

Characterizing the extent of exciton diffusion by Λ_D is however more useful, since equation 8.2 does not take into account the dimensionality of the exciton diffusion process and does not represent the average distance an exciton is able to cover by diffusion. The low efficiencies observed for organic bilayer devices have been attributed to the discrepancy in Λ_D of typically only a few nanometers[8-12] and the optical absorption length in the order of 100 nm. To overcome this limitation, the bulk-heterojunction cell has been developed, which is based on an interpenetrating network of electron-donor and -acceptor.[13,14] To date, a maximum performance of 4.4 % has been realized for a photovoltaic cell based on a blend of poly(3-hexylthiophene) and a fullerene derivative.[15, 16] For a bulk-heterojunction, it is essential to dissociate as much as possible of the excitons formed on light absorption into charge carriers. To achieve this, the size of each phase in a blend should not exceed Λ_D. In addition, the morphology of the interpenetrating network should allow efficient charge transport[17-20]. A particular blend morphology, with specific

domain dimensions, is not necessarily optimal for all these independent processes. However, enhancement of the exciton root-mean-square displacement allows the use of larger domains of electron-donor and -acceptor, which could enhance transport of charge carriers from the exciton dissociating interface through the interpenetrating network towards the electrodes.[21, 22] A value for Λ_D in the same order of magnitude as the optical absorption length would make the application of the electron-donor and -acceptor in a bulk-heterojunction obsolete.

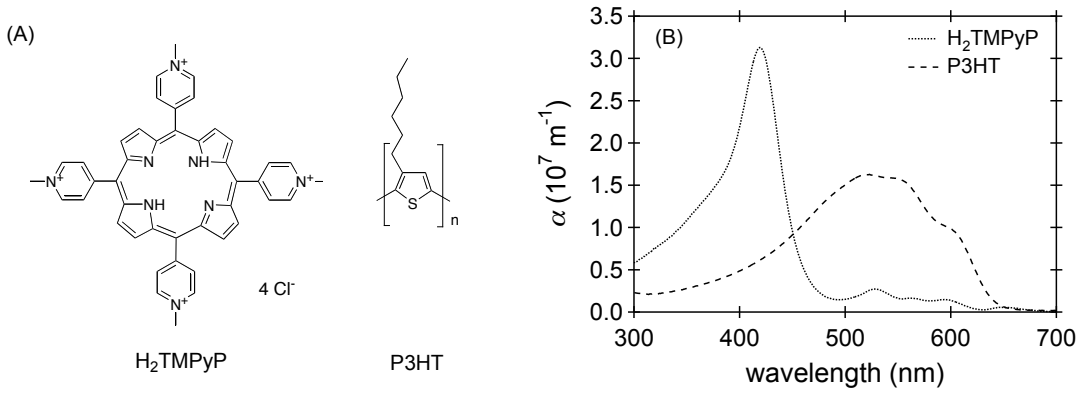

Figure 8.1. Chemical structures (A) and the exponential optical absorption coefficient as function of wavelength (B) of H_2TMPyP and P3HT.

Important advantages of alkyl substituted polythiophenes as compared to PPVs involve the enhanced photostability, the broader absorption band and the ability to self-organize.[23-27] The organization of polyalkylthiophene backbones has been observed to strongly affect charge transport[22,24] and may also influence the extent of exciton diffusion. In this work the photophysical and morphological properties of a novel combination of the visible-light absorbing electron-accepting porphyrin derivative *meso*-tetrakis(n-methyl-4-pyridyl)porphyrin tetrachloride (H_2TMPyP) and regioregular poly(3-hexylthiophene) (P3HT) are presented. The chemical structures of H_2TMPyP and P3HT are shown in Figure 8.1A. The electron-accepting behavior of H_2TMPyP is induced by the presence of quaternized pyridyl side groups, resulting in a reduction potential of -0.2 eV vs. normal hydrogen electrode (*NHE*).[28,29] Bilayers of H_2TMPyP and electron-donating porphyrins have been studied previously, yielding relatively low incident photon to current efficiencies (IPCE's).[29] The excellent solubility of P3HT in a solvent in which H_2TMPyP does not dissolve and vice versa allows spincoating of multiple thin films on top of each other. The possibility for solution processing makes this combination of materials of particular interest over bilayers based on for example a combination of

phthalocyanines and perylene derivatives on C_{60},[30-33] that need to be formed by evaporation. The absorption spectra of P3HT and H_2TMPyP presented in Figure 8.1B show that these compounds exhibit complementary absorption bands, which enhances the spectral overlap with the solar emission spectrum.

The surface morphology of the interface between H_2TMPyP and P3HT is studied using Atomic Force Microscopy (AFM). The photovoltaic properties of a photovoltaic cell based on these materials in a bilayer configuration are investigated by current-voltage and impedance measurements. Fitting an analytical model for the IPCE to the experimental data yields Λ_D in both organic layers. The value for Λ_D in P3HT differs significantly from values reported in the literature. The difference is attributed to the molecular organization of the P3HT chains, which is characterized by X-ray diffraction. The results show that the molecular organization is a key parameter for the realization of efficient energy transfer in organic photovoltaics.

8.2. Experimental methods

Sample preparation: H_2TMPyP and regioregular P3HT (electronic grade) were purchased from Frontier Scientific (Logan, USA) and Rieke Metals, Inc. (Lincoln, USA), respectively. H_2TMPyP films were prepared by spincoating from a solution in CH_3OH (Aldrich, 99.9 %, c = 10 mg/ml) at 2500 rpm onto either a quartz or onto an indium doped SnO_2 (ITO) coated glass substrate. Prior to film deposition these substrates were dried at 250 °C for 1 h. P3HT films were spincoated from a solution in $CHCl_3$ at 2500 rpm (Anhydrous, 99+ %, Aldrich, c = 15 mg/ml). A Hg contact (A = 0.78 mm^2) was used as back contact[34], resulting in the device configuration as presented in the inset of Figure 8.2B. Film thicknesses were determined using a Veeco Dektak 8 Stylus Profiler and equal 25±5 nm and 75±5 nm for H_2TMPyP and P3HT, respectively.

Optical and morphological characterization: Optical transmission and reflection spectra were recorded on a Perkin Elmer Lambda 900 UV/VIS/NIR spectrometer, using an integrating sphere. The optical absorption coefficient (α) was determined from the transmission and reflection spectra as described in ref. 35. Time-resolved fluorescence spectra were recorded with a Lifespec - ps setup using a 405 nm excitation source (Edinburgh Instruments). Atomic force micrographs were recorded using a Nanoscope Atomic Force Microscope, operated in the tapping mode. X-ray diffraction measurements

were performed in the Bragg-Brentano mode on a Bruker D8 Advance X-ray diffractometer, equipped with a Cu anode (λ_{K_α} = 1.5408 Å) operated at 40 kV and 30 mA.

Photovoltaic and Mott-Schottky characterization: Photocurrents were recorded using an Autolab PGSTAT 10 EcoChemie potentiostat controlled by GPES 3 software in combination with a Xe lamp (Eurosep Instruments) equipped with a monochromator (Triax Series 0144B 99/236). The incident power (P_{in}) varied from 6 mW/cm^2 to 8 mW/cm^2 for the wavelength range of 300 nm – 700 nm. Short-circuit currents were measured using a Keithley 2700 Multimeter. The fill factor (FF) was determined using

$$FF = \frac{V_{\max} I_{\max}}{V_{OC} I_{SC}} \tag{8.3}$$

where V_{max} and I_{max} represent the voltage and current at the maximum power point, V_{OC} is the open-circuit voltage and I_{SC} the short-circuit voltage. The incident photon to current efficiency (IPCE) as function of wavelength is determined using

$$IPCE = \frac{I_{SC} hc}{P_{in} e\lambda} 100\% \tag{8.4}$$

where P_{in} represents the power of the incident light.[36]

8.3. Results and discussion

8.3.1. Photovoltaic properties

Figure 8.2A shows the current-voltage characteristics of the photovoltaic device based on H_2TMPyP and P3HT in dark and under monochromatic illumination at 450 nm with an incident power (P_{in}) of 8 mW/cm^2. The configuration of the photovoltaic device is shown in the inset of Figure 8.2B. The forward bias direction corresponds to a negative voltage on the ITO electrode. Under this illumination the open-circuit voltage (V_{OC}) equals 0.65 V, the short-circuit current (I_{SC}) is 0.64 mA/cm^2 and the fill factor (FF) calculated from equation 8.3 is low and amounts to 0.36. Figure 8.2B shows the wavelength dependence of the incident photon to current efficiency (IPCE) determined using equation 8.4. The IPCE value exceeds 20 % over a broad wavelength regime. Comparison of the IPCE spectrum with the absorption spectra of H_2TMPyP and P3HT presented in Figure 8.1B clearly shows that both materials contribute to the photocurrent.

This implies that excitons formed in H_2TMPyP and in P3HT are dissociated into charge carriers. The contribution originating from P3HT to the IPCE considerably exceeds values reported earlier for smooth bilayer devices based on polythiophene derivatives and C_{60}.[37, 38] Possible explanations for the unexpected high IPCE values observed for the photovoltaic cell based on H_2TMPyP and P3HT are discussed in sections 8.3.5 and 8.3.6.

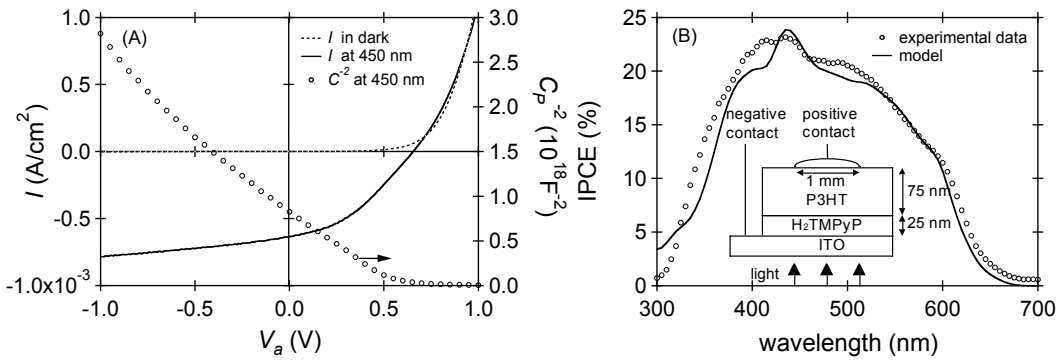

Figure 8.2. Current density (dashed is recorded in dark, solid is recorded under illumination with 8 mW/cm^2 at 450 nm) and C_P^{-2} (8 mW/cm^2 at 450 nm, recorded at 1×10^4 Hz) of the device presented in the inset of Figure B as function of applied voltage (A). Figure B shows the IPCE versus wavelength and a fit of equation 8.9 to the experimental data with Λ_{D,H_2TMPyP} = 14 nm and $\Lambda_{D,P3HT}$ = 18 nm.

8.3.2. Interface morphologies

The average distance an exciton has to travel before it can be dissociated into charge carriers is determined by the smoothness of the interface between H_2TMPyP and P3HT. Figure 8.3 shows the surface morphology of ITO coated glass (A), H_2TMPyP spincoated onto the ITO electrode (B), the sample shown in B spincoated with a P3HT layer (C) and the sample presented in C after dissolving the P3HT layer specifically using $CHCl_3$ (D). The surface morphology of the original H_2TMPyP layer appears to be almost identical to the surface morphology of H_2TMPyP after deposition of P3HT and removal of the P3HT layer. This demonstrates the absence of any significant changes in surface morphology of H_2TMPyP upon deposition of the P3HT layer. Spincoating of P3HT onto H_2TMPyP therefore yields a bilayer configuration as presented schematically in the inset of Figure 8.2B rather than an interpenetrating network of both materials. As a consequence, the high IPCE values observed in this work demonstrate the presence of efficient energy transfer pathways towards the exciton dissociating interface.

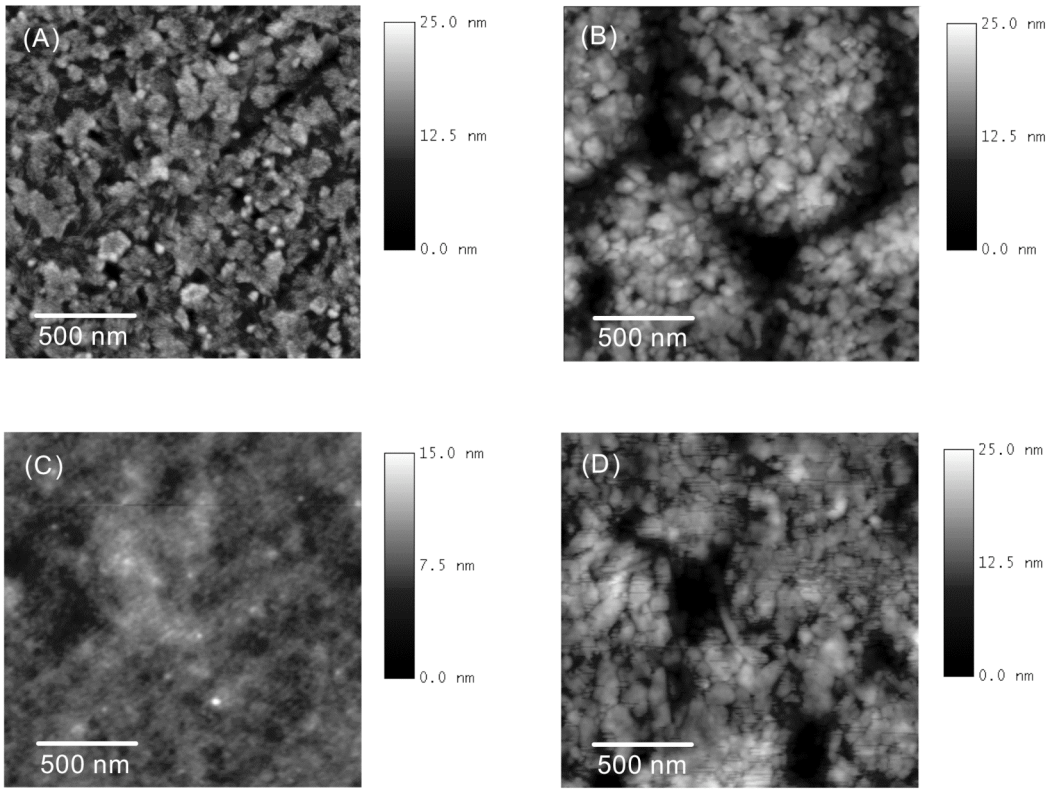

Figure 8.3. Atomic force micrographs of ITO (A), the sample as shown in A spincoated with H_2TMPyP (B), the sample as shown in B spincoated with P3HT (C) and the sample as shown in C after removing the P3HT layer with $CHCl_3$ (D). Note the smaller scale used for C.

8.3.3. Impedance measurements

Apart from efficient exciton diffusion through the H_2TMPyP and P3HT layers and exciton dissociation at the interface, the high IPCE values also indicate efficient collection of charge carriers at the electrodes. Transport of charge carriers from the photoactive interface through the organic layers towards the electrodes can occur by drift induced by the internal electric field and/or by diffusion. The presence and width of a depletion layer near the interface is investigated using impedance measurements. The impedance plots of the device shown in the inset of Figure 8.2B at various applied voltages are presented in Appendix A. A simple equivalent circuit consisting of a capacitor (C_P) parallel to a resistor (R_P) in series with a resistor (R_S) is fitted to the experimental data. The fits and fit parameters are included in Appendix A. The capacitance appears to be a function of the applied voltage (V_a). This indicates a broadening of the width of the depletion layer (w) with stronger reverse bias as follows from

$$w = \frac{\varepsilon_r \varepsilon_0 A}{C_p} \tag{8.5}$$

where A represents the electrode area, ε_r the relative dielectric constant and ε_0 the permittivity of free space. The dependence of the capacitance on the applied voltage is described by[36]

$$\frac{1}{C_P^2} = \left(\frac{2}{e\varepsilon_r \varepsilon_0 N_D A^2}\right)(V_{BI} - V_a) \tag{8.6}$$

where e represents the electronic charge, N_D (or N_A) the concentration of ionized impurities in the depletion layer and V_{BI} the built-in potential present over the depletion layer. A Mott-Schottky plot (C_P^{-2} versus V_a) recorded at 10 kHz under monochromatic illumination at 450 nm with an incident power of 8 mW/cm^2 is included in Figure 8.2A. From the observed capacitance of 1 nF at zero applied voltage and application of equation 8.5 follows a total depletion width of 20 nm. The contact area amounts to 0.78 mm^2 and the values for ε_r of both H_2TMpYP and P3HT are assumed to be equal to 3.[29, 39] From equation 8.6 and the experimental Mott-Schottky data follows a built-in potential of 0.55 V, close to the V_{OC} observed. The presence of only one distinct linear increase in C_P^{-2} rather than two separate regimes with different slopes indicates comparable values for $\varepsilon_{r,P3HT} N_{D,P3HT}$ and $\varepsilon_{r,H_2TMPyP} N_{D,H_2TMPyP}$ amounting to 1.4×10^{18} cm^{-3}. This corresponds to a concentration of ionized impurities in both materials of about 5×10^{17} cm^{-3}, which is close to the value for N_A of 3.5×10^{17} cm^{-3} reported earlier for H_2TMPyP.[28] The origin of the excess of mobile electrons in the H_2TMPyP layer is not clearly established,[40] while the cause of an excess of holes in the P3HT layer is generally attributed to reversible doping with oxygen.[41-44] The negligible difference in $\varepsilon_{r,P3HT} N_{D,P3HT}$ and $\varepsilon_{r,H_2TMPyP} N_{D,H_2TMPyP}$ implies that the depletion layer is located equally through both organic layers. The corresponding internal electric field is expected to reduce the interfacial recombination of electrons and holes formed on exciton dissociation.

8.3.4. Determination of the exciton root-mean-square-displacement

Prime parameters that determine the IPCE of a bilayer device are the value of Λ_D and the fraction of absorbed light (F_A) in the individual layers. The absorption profile within the bilayer device is determined using the optical modeling program SCOUT,[45] assuming the interface between H_2TMPyP and P3HT to be perfectly smooth. More details about the

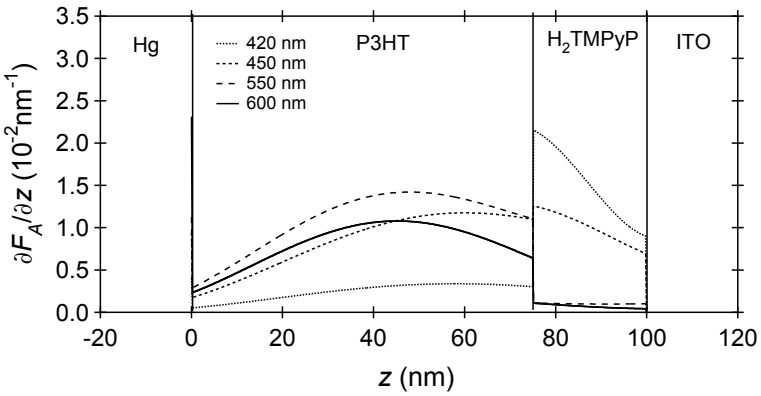

Figure 8.4. First derivative of F_A with respect to z within the bilayer device presented in the inset in Figure 8.2B at selected wavelengths, determined using the optical modeling program SCOUT.

SCOUT modeling are given in Appendix B. Figure 8.4 shows the first derivative of F_A with respect to the distance from the mercury contact (z) for selected wavelengths. Especially within the H_2TMPyP layer the absorption profile turns out to deviate considerably from a Lambert-Beer profile, which mainly originates from the presence of the metal contact. The number of excitons formed that are able to reach the photoactive interface can be deduced from solving the differential equation for exciton diffusion[46]

$$\frac{\partial n_i(z)}{\partial t} = I_0 \frac{\partial F_{A,i}(z)}{\partial z} - \frac{n_i(z)}{\tau_{E,i}} + D_{E,i} \frac{\partial^2 n_i(z)}{\partial z^2} \tag{8.7}$$

where $n_i(z)$ is the exciton concentration at a depth z within layer i and I_0 the incident light intensity. Since a continuous light source is used, the first derivative of $n_i(z)$ with respect to t is zero. In addition, excitons that reach the interface with an electrode are assumed to be rapidly quenched and those that reach the interface between H_2TMPyP and P3HT to be rapidly dissociated into charge carriers, i.e. $n_i = 0$ at these interfaces. Solving equation 8.7 under these conditions and using the absorption profiles determined by SCOUT yields $n_i(z)$. The fraction of I_0 that leads to excitons that reach the photoactive interface (S_i) can be expressed by

$$S_i = -D_{E,i} \frac{\partial n_i(z)}{\partial z} \frac{1}{I_0} \bigg|_{z=L} \tag{8.8}$$

where L is the z coordinate corresponding to the interface between H_2TMPyP and P3HT. More details about the solution of equations 8.7 and 8.8 are presented in Appendix C. The total number of excitons that reaches the photoactive interface is the sum of the number of excitons in each layer that reaches this interface. Hence, the total amount of excitons

reaching the interface divided by I_0 is defined as the sum of the S_i factors of each layer. For expressing the IPCE in terms of S_i, the charge separation yield at the interface into free charge carriers is assumed to be unity. Furthermore, it is assumed that all charge carriers formed on exciton dissociation are collected by the electrodes. Under these conditions, the IPCE of the bilayer device follows from:

$$IPCE = \left(S_{P3HT} + S_{H_2TMPyP}\right)100\% \tag{8.9}$$

Fitting equation 8.9 to the experimental IPCE spectrum, with τ_E is 290 ps for P3HT and 1.28 ns for H_2TMPyP as obtained from fluorescence decay measurements (data not shown), results in the fit included in Figure 8.2B with D_{E,H_2TMPyP} = 8×10^{-8} m^2/s and $D_{E,P3HT}$= 5.9×10^{-7} m^2/s. Combining these values for D_E with the observed exciton lifetimes and using equation 8.1 yields Λ_{D,H_2TMPyP} = 14 nm and $\Lambda_{D,P3HT}$ = 18 nm. This value for $\Lambda_{D,P3HT}$ is significantly larger than previous values for polythiophene derivatives deposited onto C_{60}[37,47] or TiO_2[8], where values close to 7 nm[12] are reported. Possible reasons for the discrepancy in Λ_D between those systems and the bilayer investigated in this study are discussed below.

8.3.5. Determination of the molecular organization

The discrepancy in $\Lambda_{D,P3HT}$ for P3HT deposited onto H_2TMPyP and the previous reported values most likely originates from differences in the molecular organization. The degree of molecular organization in a thin film is elucidated using X-ray diffraction. Figure 8.5A shows the X-ray diffraction patterns of single layers of H_2TMPyP and P3HT deposited on quartz and a bilayer of H_2TMPyP and P3HT on quartz. For reference purposes, the pattern observed for P3HT deposited onto a similar TiO_2/quartz substrate as used in ref. 8 is also illustrated, for which $\Lambda_{D,P3HT}$ has been determined to be 7 nm.[8] The X-ray diffraction intensity observed for a bare TiO_2/quartz substrate is subtracted from the latter pattern, the other patterns are corrected for the diffraction intensity of a bare quartz substrate. The X-ray diffraction pattern of a single layer of P3HT on quartz shows a diffraction peak at 2θ = 5.18°. In case of first order diffraction, this peak reveals the presence of a well-developed structure directed perpendicular to the quartz substrate with an interplanar distance equal to 17.0 Å. This distance most likely corresponds to the spacing between P3HT chains along the hexyl side chains as reported in several earlier works[23, 25-27] and shown schematically in Figure 8.5B. In contrast to a P3HT layer on

quartz, for P3HT deposited on TiO_2/quartz hardly any diffraction peak is observed, indicating a relatively low degree of organization of the P3HT chains for the latter system. The difference in degree of molecular organization could either originate from variations in the roughness of the substrate surface or from the interaction of P3HT with the surface functionalities of the substrate. From AFM analysis follows only a slightly higher surface roughness of TiO_2 as compared to quartz (see Appendix D). This leads to the conclusion that the difference in degree of organization of P3HT chains on TiO_2 and on quartz is most likely due to the interaction of the conjugated polymer with surface functionalities of the substrate.

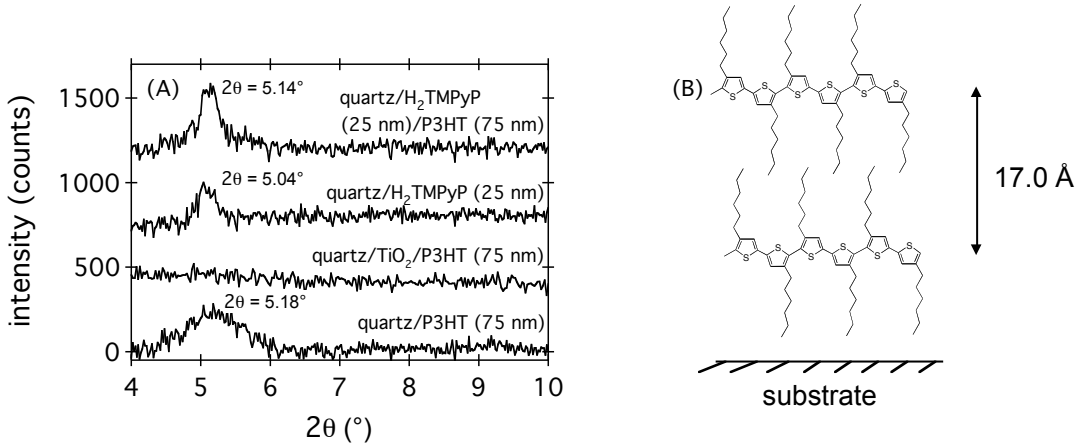

Figure 8.5. X-ray diffraction patterns of quartz/P3HT (75 nm), quartz/ H_2TMPyP (25 nm), quartz/H_2TMPyP (25 nm)/P3HT (75 nm) and quartz/TiO_2/P3HT (75 nm) (A). The X-ray diffraction intensity observed for a bare TiO_2/quartz substrate is subtracted from the latter pattern, the other patterns are corrected for the diffraction intensity of a bare quartz substrate. Note that the data presented have different offsets to improve clarity. Figure B shows the alignment of P3HT backbones parallel with the hexyl side chains perpendicular to a substrate.

Remarkably, a layer of H_2TMPyP deposited on quartz possesses a diffraction peak at almost a similar angle as observed for P3HT on quartz. The maximum diffraction is observed at $2\theta = 5.04°$, corresponding in case of first order diffraction to an interplanar distance equal to 17.5 Å. Since this distance equals the diameter of a H_2TMPyP molecule, the observed peak suggests the alignment of the H_2TMPyP molecular planes perpendicular to the substrate. As compared to a bare H_2TMPyP layer, the bilayer of H_2TMPyP and P3HT deposited on quartz possesses a more intense diffraction peak, which is attributed to a contribution from both organic layers. The degree of molecular order of P3HT chains deposited on H_2TMPyP is hence higher than for P3HT on TiO_2, even though the surface of the latter substrate is smoother (see Appendix D). It should be

noted that quartz and H_2TMPyP possess a stronger hydrophilicity as compared to TiO_2[48-50], which may explain the higher degree of order of P3HT deposited onto the first two materials. The enhanced degree of molecular order of P3HT chains deposited onto H_2TMPyP as compared to TiO_2 can explain the long exciton root-mean-square displacement observed for the first system.

Table 8.1. Parameters characterizing the energy transfer in H_2TMPyP, P3HT deposited on H_2TMPyP and P3HT deposited on TiO_2.

Layer	Λ_D (nm)	τ_E (s)	D_E (m^2/s)	R_{DA} (Å)	k_{ET} (s^{-1})
H_2TMPyP	14	1.28×10^{-9}	8×10^{-8}	17.5	3×10^{10}
P3HT on H_2TMPyP	18	2.90×10^{-10}	5.9×10^{-7}	17.0	2×10^{11}
P3HT on TiO_2	7 (from ref. 8)	2.90×10^{-10}	8×10^{-8}	17.0	3×10^{10}

8.3.6. Origin of the long exciton root-mean-square-displacement

The value for Λ_D depends on the exciton diffusion coefficient (D_E) and the exciton lifetime (τ_E) according to equation 8.1. In case an exciton is localized on a single molecule, D_E depends on the energy transfer rate (k_{ET}) and the center-to-center distance between adjacent molecules (R_{DA}) according to

$$D_E = k_{ET} R_{DA}^2 \tag{8.10}$$

The exciton lifetimes are determined from fluorescence decay measurements (data not shown). The exciton diffusion coefficients in the individual layers are deduced from the experimental IPCE values as described in section 8.3.4. Combining the exciton diffusion coefficient with the interplanar distance determined by X-ray diffraction and using equation 8.10 yields the energy transfer rate. All these parameters characterizing the energy transfer in H_2TMPyP, P3HT deposited on H_2TMPyP and P3HT deposited on TiO_2 are presented in Table 8.1. Note, that the energy transfer rate between disordered P3HT chains on TiO_2 is a factor of seven lower than the value determined for organized P3HT chains deposited onto H_2TMPyP.

In the limit of weak intermolecular excitonic coupling, motion of excitons can be considered as diffusive with an intermolecular hopping rate k_{ET} given by[51, 52]

$$k_{ET} = \frac{2\pi}{\hbar} |V_{DA}|^2 J_{DA} \tag{8.11}$$

where the factor V_{DA} denotes the excitonic coupling between energy donor and acceptor and J_{DA} represents the spectral overlap integral. The definition and evaluation of the spectral overlap integrals for H_2TMPyP and P3HT are specified in Appendix E. The experimental absorption and fluorescence spectra yield values for J_{DA} equal to 4.3×10^{18} J^{-1} for H_2TMPyP and 5.5×10^{17} J^{-1} for P3HT. Combining this with the observed values for k_{ET} yields values for the excitonic coupling V_{DA} of 16 cm^{-1} for H_2TMPyP, 125 cm^{-1} for P3HT deposited on H_2TMPyP and 47 cm^{-1} for P3HT on TiO_2. The stronger excitonic coupling observed for P3HT on H_2TMPyP as compared to P3HT on TiO_2 is most likely due to a higher and more favorable degree of molecular organization of the P3HT chains found for the first system. The value of V_{DA} equal to 125 cm^{-1} found for P3HT deposited on H_2TMPyP indicates a strong excitonic coupling between adjacent P3HT chains that are organized as shown in Figure 8.5B. Quantum-chemical calculations on excitonic couplings are underway in order to establish to which extent the value for the excitonic coupling can be understood on basis of this molecular organization and whether exciton transfer can be further improved.

8.4. Conclusions

This work presents morphological and photophysical properties of a bilayer of the electron-accepting porphyrin derivative H_2TMPyP and P3HT. A photovoltaic cell based on such a bilayer exhibits an incident photon to current efficiency (IPCE) over 20 % over a broad wavelength regime. Fitting a model for one-dimensional exciton diffusion in the direction perpendicular to the interface between H_2TMPyP and P3HT, that includes the absorption profiles in the bilayer to the experimental IPCE values, gives the exciton root-mean-square displacement (Λ_D) in each layer. From X-ray diffraction it is inferred that the H_2TMPyP molecular cores are aligned perpendicular to the interface with P3HT, while the P3HT backbones are aligned parallel to the interface. For the H_2TMPyP layer Λ_D amounts to 14 nm, while a value of 18 nm is found for the P3HT layer. Combining the Λ_D values with the intermolecular distances and the exciton lifetimes observed yields the intermolecular energy transfer rate, which amounts to 3×10^{10} s^{-1} for H_2TMPyP and 2×10^{11} s^{-1} for P3HT. From application of Fermi's golden rule to these energy transfer rates follows an excitonic coupling between H_2TMPyP molecules that amounts to 16 cm^{-1}, while for P3HT a value as high as 125 cm^{-1} is found. The latter value is almost a factor of three higher than the excitonic coupling between disordered P3HT chains determined

to be 47 cm^{-1}. This illustrates the importance of controlling the molecular organization for the realization of efficient energy transfer in organic opto-electronics.

Acknowledgment

Murat Durkut and Menno Poot from the Molecular Electronics and Devices group, Kavli Institute of Nanoscience, TU Delft, are acknowledged for assistance with the AFM measurements. The research was supported financially by the Delft Research Centre for Sustainable Energy. AS gratefully acknowledges Senter Novem for financial support.

Supporting Information

Appendix A

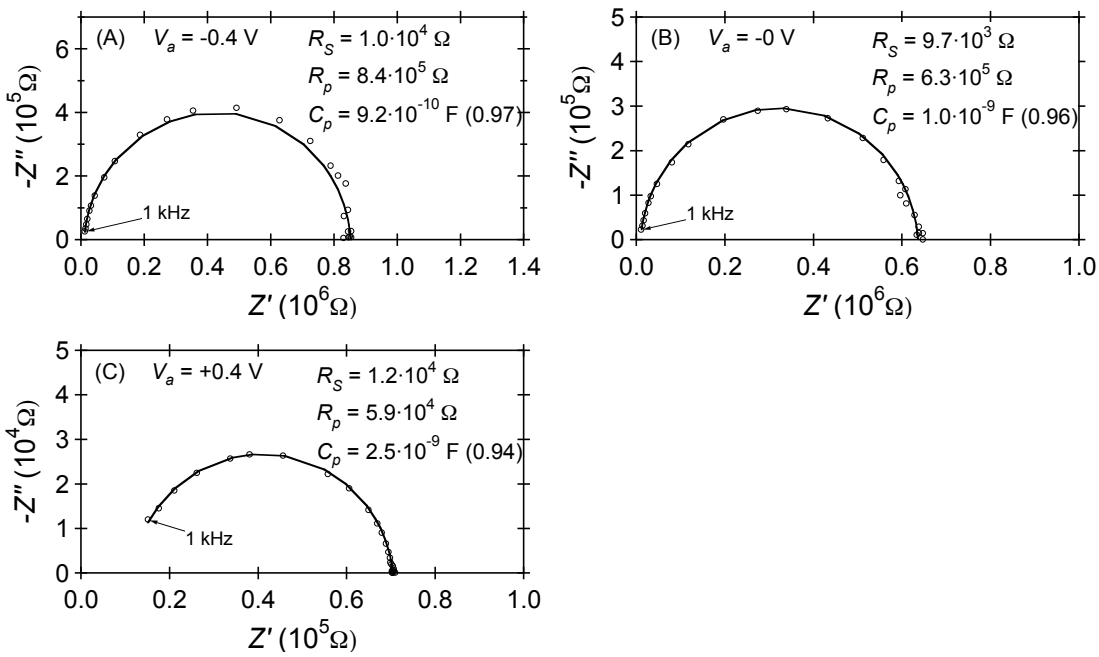

Figure 8.6. Impedance spectra of the device presented in the inset of Figure 8.2B (8 mW/cm^2 at 450 nm) recorded at V_a = -0.4 V (A), V_a = 0 V (B) and V_a = +0.4 V (C) and fits of an equivalent circuit of a capacitor C_P parallel to a resistor R_P in series with a resistor R_S with parameters shown in the insets. The non-idealities of the capacitors are given between brackets.

Appendix B

The real and complex part (n) and (k) of the refractive index of the materials used are determined from the experimental transmission and reflection spectra using the program SCOUT.[45] Figure 8.7A shows the values for n and k as function of wavelength for quartz, H_2TMPyP and P3HT. The fractions of transmitted light (F_T) and reflected light (F_R) of quartz/ H_2TMPyP (25 nm)/P3HT (75 nm), illuminated from the side of the P3HT film, are determined using SCOUT on basis of n and k of the individual materials. The modeled F_T and F_R are shown in Figure 8.7B and agree very well with the experimental data. This validates modeling the absorption profile within the device presented in the inset of Figure 8.2B using SCOUT. The values for n and k of ITO coated glass are determined from the experimental transmission and reflection spectra and n and k of Hg are taken from ref. 53 and shown in Figure 8.7C.

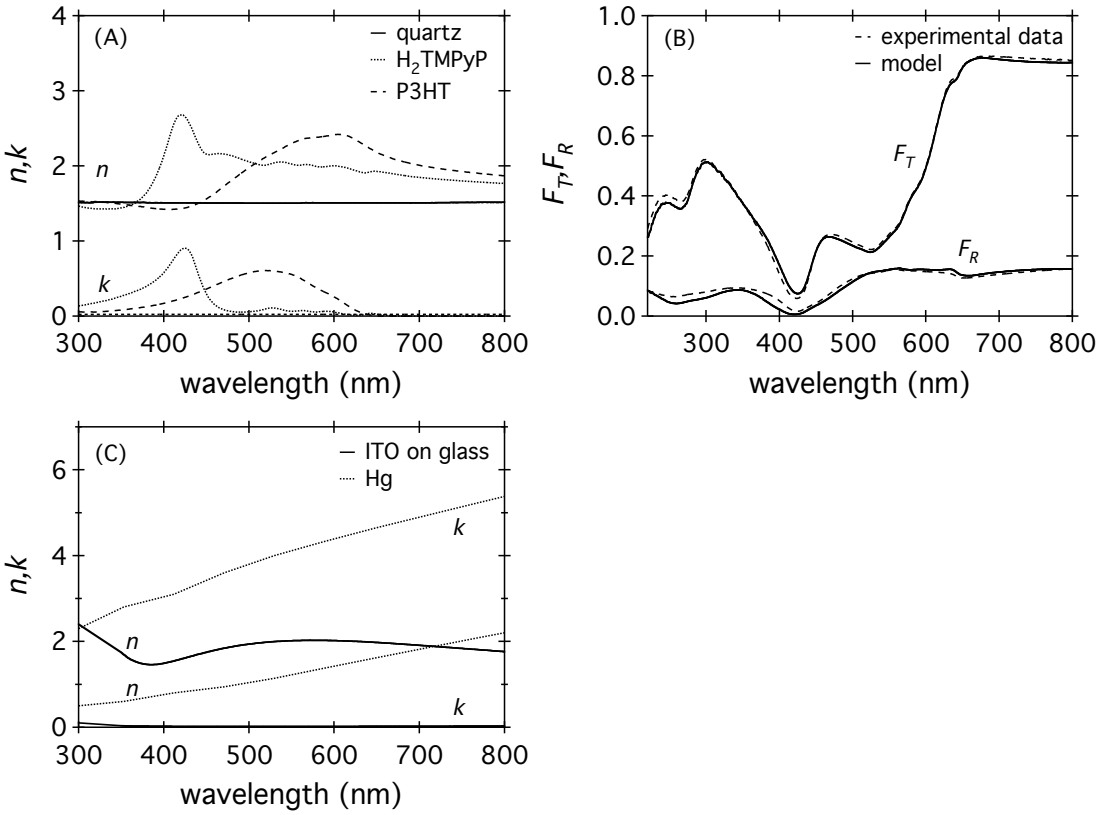

Figure 8.7. Optical constants of quartz, H_2TMPyP and P3HT (A), experimental and modeled fraction of transmitted (F_T) and reflected light (F_R) of quartz/H_2TMPyP (25 nm)/P3HT (75 nm) illuminated from the side of the P3HT film (B) and optical constants of ITO on glass and Hg (from ref. 53) (C).

Appendix C

A. First derivative of F_A with respect to z constant

In the theoretical case the first derivative of F_A with respect to z equals a constant C_i, the steady-state differential equation for exciton diffusion can be expressed as:

$$I_0 C_i - \frac{n_i(z)}{\tau_{E,i}} + D_{E,i} \frac{\partial^2 n_i(z)}{\partial z^2} = 0 \tag{C1}$$

The boundary conditions at the interface between an organic layer and an electrode and at the interface between H_2TMPyP and P3HT have to be defined to solve equation C1. Excitons reaching the interface with an electrode are assumed to be rapidly quenched and those that reach the photoactive interface to be rapidly dissociated into charge carriers. For the P3HT layer this implies that the concentration of excitons is zero at $z = 0$ and $z = L$ (see Figure 8.4). Solving equation C1 under these conditions by using the program MAPLE results in

$$n_i(z) = -\frac{\left(e^{\frac{z}{\sqrt{D_{E,i}\tau_{E,i}}}} + e^{-\frac{z-L}{\sqrt{D_{E,i}\tau_{E,i}}}} - 1 - e^{\frac{L}{\sqrt{D_{E,i}\tau_{E,i}}}} \right) I_0 C_i \tau_{E,i}}{1 + e^{\frac{L}{\sqrt{D_{E,i}\tau_{E,i}}}}} \tag{C2}$$

with i = P3HT. Analogous, for the H_2TMPyP layer the concentration of excitons is equal to zero at $z = L$ and $z = D$, where D is the z coordinate corresponding to the interface between H_2TMPyP and ITO, leading to

$$n_i(z) = -\frac{\left(e^{\frac{z}{\sqrt{D_{E,i}\tau_{E,i}}}} + e^{-\frac{z-D-L}{\sqrt{D_{E,i}\tau_{E,i}}}} - e^{\frac{D}{\sqrt{D_{E,i}\tau_{E,i}}}} - e^{\frac{L}{\sqrt{D_{E,i}\tau_{E,i}}}} \right) I_0 C_i \tau_{E,i}}{e^{\frac{D}{\sqrt{D_{E,i}\tau_{E,i}}}} + e^{\frac{L}{\sqrt{D_{E,i}\tau_{E,i}}}}} \tag{C3}$$

with i = H_2TMPyP. The fraction of incident photons that leads to excitons reaching the photoactive interface by diffusion (S_i) is expressed by:

$$S_i = -D_{E,i} \frac{\partial n_i(z)}{\partial z} \frac{1}{I_0} \bigg|_{z=L} \tag{C4}$$

Application of equation C4 to equations C2 and C3 results in the following analytical expressions for the device, with i = P3HT and H_2TMPyP, respectively:

$$S_i = \frac{C_i\sqrt{D_{E,i}\tau_{E,i}}\left(e^{\frac{L}{\sqrt{D_{E,i}\tau_{E,i}}}} - 1\right)}{1 + e^{\frac{L}{\sqrt{D_{E,i}\tau_{E,i}}}}} \tag{C5}$$

$$S_i = \frac{C_i\sqrt{D_{E,i}\tau_{E,i}}\left(e^{\frac{L}{\sqrt{D_{E,i}\tau_{E,i}}}} - e^{\frac{D}{\sqrt{D_{E,i}\tau_{E,i}}}}\right)}{e^{\frac{D}{\sqrt{D_{E,i}\tau_{E,i}}}} + e^{\frac{L}{\sqrt{D_{E,i}\tau_{E,i}}}}} \tag{C6}$$

To express the IPCE in terms of S_i, the charge separation yield at the photoactive interface into free charge carriers is assumed to be unity. Furthermore, it is assumed that all charge carriers formed on exciton dissociation are collected by the electrodes. The IPCE of the bilayer device then follows from:

$$IPCE = \left(S_{P3HT} + S_{H_2TMPyP}\right)100\% \tag{C7}$$

B. First derivative of F_A with respect to z modeled using SCOUT

The first derivative of F_A with respect to z determined using SCOUT is modeled using a sinus equation, resulting in the following steady-state differential equation for exciton diffusion:

$$I_0\left[A_i \sin\left(f_i z + \phi_i\right)\right] - \frac{n_i(z)}{\tau_{E,i}} + D_{E,i}\frac{\partial^2 n_i(z)}{\partial z^2} = 0 \tag{C8}$$

Solving equation C8 with similar boundary conditions as described in previous section by using the program MAPLE gives the analytical expressions for $n_i(z)$ for i = P3HT and i = H_2TMPyP, respectively:

$$n_i(z) = \frac{\left(\sin\left(f_i L + \phi\right)e^{\frac{z+L}{\sqrt{D_{E,i}\tau_{E,i}}}} - \sin\left(\phi\right)e^{\frac{z}{\sqrt{D_{E,i}\tau_{E,i}}}} + \sin\left(\phi\right)e^{-\frac{z-2L}{\sqrt{D_{E,i}\tau_{E,i}}}}\right)I_0 A_i \tau_{E,i}}{\left(1 + f_i^2 D_{E,i}\tau_{E,i}\right)\left(1 - e^{\frac{2L}{\sqrt{D_{E,i}\tau_{E,i}}}}\right)} + \frac{\left(-\sin\left(f_i L + \phi\right)e^{-\frac{z-L}{\sqrt{D_{E,i}\tau_{E,i}}}} + \sin\left(f_i z + \phi\right) - \sin\left(f_i z + \phi\right)e^{\frac{2L}{\sqrt{D_{E,i}\tau_{E,i}}}}\right)I_0 A_i \tau_{E,i}}{\left(1 + f_i^2 D_{E,i}\tau_{E,i}\right)\left(1 - e^{\frac{2L}{\sqrt{D_{E,i}\tau_{E,i}}}}\right)} \tag{C9}$$

$$n_i(z) = \frac{\left(\sin(f_i L + \phi) e^{\frac{z+L}{\sqrt{D_{E,i}\tau_{E,i}}}} - \sin(f_i D + \phi) e^{\frac{z+D}{\sqrt{D_{E,i}\tau_{E,i}}}} + \sin(f_i D + \phi) e^{-\frac{z-D-2L}{\sqrt{D_{E,i}\tau_{E,i}}}}\right) I_0 A_i \tau_{E,i}}{\left(1 + f_i^2 D_{E,i}\tau_{E,i}\right)\left(e^{\frac{2D}{\sqrt{D_{E,i}\tau_{E,i}}}} - e^{\frac{2L}{\sqrt{D_{E,i}\tau_{E,i}}}}\right)} + \frac{\left(-\sin(f_i L + \phi) e^{-\frac{z-2D-L}{\sqrt{D_{E,i}\tau_{E,i}}}} + \sin(f_i z + \phi) e^{\frac{2D}{\sqrt{D_{E,i}\tau_{E,i}}}} - \sin(f_i z + \phi) e^{\frac{2L}{\sqrt{D_{E,i}\tau_{E,i}}}}\right) I_0 A_i \tau_{E,i}}{\left(1 + f_i^2 D_{E,i}\tau_{E,i}\right)\left(e^{\frac{2D}{\sqrt{D_{E,i}\tau_{E,i}}}} - e^{\frac{2L}{\sqrt{D_{E,i}\tau_{E,i}}}}\right)} \tag{C10}$$

Application of equation C4 to equations C9 and C10 gives the S_i factors, for i = P3HT:

$$S_i = \frac{\left(D_{E,i}\cos(f_i L + \phi) f_i \tau_i e^{\frac{2L}{\sqrt{D_{E,i}\tau_{E,i}}}} - D_{E,i}\cos(f_i L + \phi) f_i \tau_i\right)}{\left(\frac{1 + f_i^2 \tau_i D_{E,i}}{A_i}\right)\left(-e^{\frac{2L}{\sqrt{D_{E,i}\tau_{E,i}}}} + 1\right)} + \frac{\left(2\sqrt{D_{E,i}\tau_{E,i}}\sin(\phi) e^{\frac{L}{\sqrt{D_{E,i}\tau_{E,i}}}} - \sqrt{D_{E,i}\tau_{E,i}}\sin(fL + \phi) e^{\frac{2L}{\sqrt{D_{E,i}\tau_{E,i}}}} - \sqrt{D_{E,i}\tau_{E,i}}\sin(fL + \phi)\right)}{\left(\frac{1 + f_i^2 \tau_i D_{E,i}}{A_i}\right)\left(-e^{\frac{2L}{\sqrt{D_{E,i}\tau_{E,i}}}} + 1\right)} \tag{C11}$$

For i = H_2TMPyP:

$$S_i = \frac{\left(D_{E,i}\cos(f_i L + \phi) f_i \tau_i e^{\frac{2L}{\sqrt{D_{E,i}\tau_{E,i}}}} - D_{E,i}\cos(f_i L + \phi) f_i \tau_i e^{\frac{2D}{\sqrt{D_{E,i}\tau_{E,i}}}}\right)}{\left(\frac{1 + f_i^2 \tau_i D_{E,i}}{A_i}\right)\left(-e^{\frac{2L}{\sqrt{D_{E,i}\tau_{E,i}}}} + e^{\frac{2D}{\sqrt{D_{E,i}\tau_{E,i}}}}\right)} + \frac{\left(2\sqrt{D_{E,i}\tau_{E,i}}\sin(f_i D + \phi) e^{\frac{D+L}{\sqrt{D_{E,i}\tau_{E,i}}}} - \sqrt{D_{E,i}\tau_{E,i}}\sin(fL + \phi) e^{\frac{2L}{\sqrt{D_{E,i}\tau_{E,i}}}} - \sqrt{D_{E,i}\tau_{E,i}}\sin(fL + \phi) e^{\frac{2D}{\sqrt{D_{E,i}\tau_{E,i}}}}\right)}{\left(\frac{1 + f_i^2 \tau_i D_{E,i}}{A_i}\right)\left(-e^{\frac{2L}{\sqrt{D_{E,i}\tau_{E,i}}}} + e^{\frac{2D}{\sqrt{D_{E,i}\tau_{E,i}}}}\right)} \tag{C12}$$

The IPCE of the bilayer device is obtained using equation C7.

Appendix D

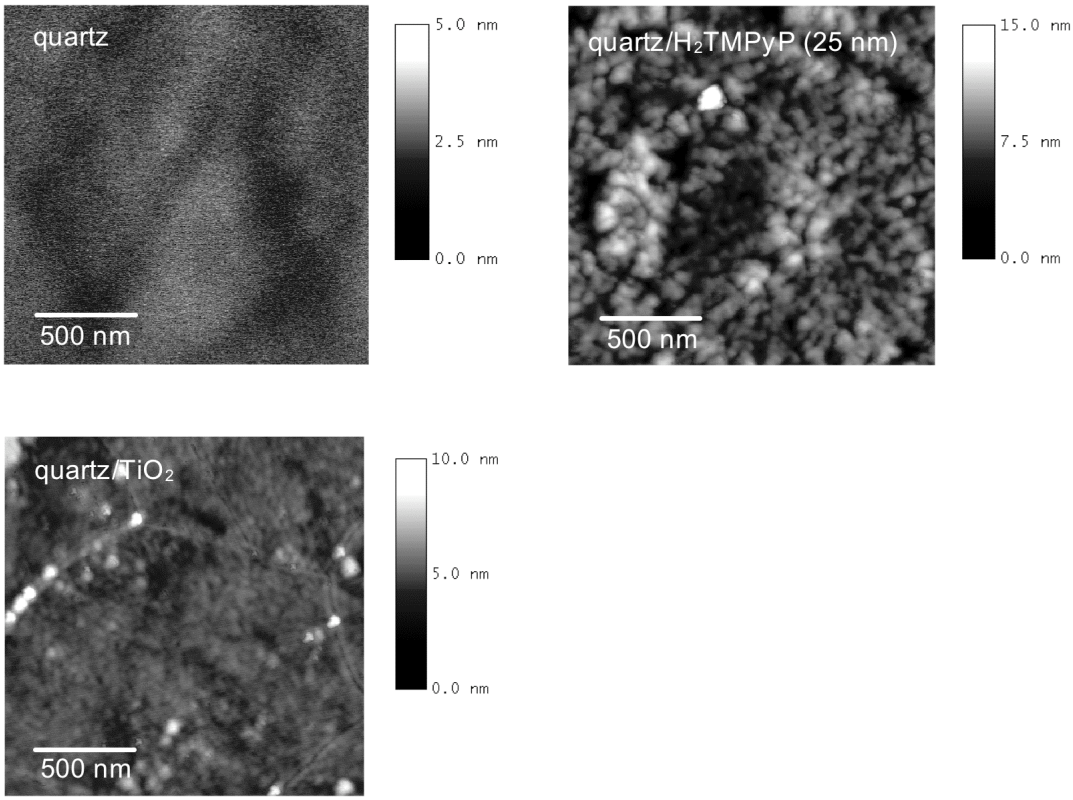

Figure 8.8. Atomic force micrographs of quartz, quartz/H_2TMPyP (25 nm) and quartz/TiO_2. Note the different scales used.

Appendix E

In case of incoherent exciton hopping between molecules, the energy transfer rate k_{ET} between an energy donor and acceptor depends on the excitonic coupling V_{DA} and the spectral overlap integral J_{DA} according to:[51, 52]

$$k_{ET} = \frac{2\pi}{\hbar}|V_{DA}|^2 J_{DA} \tag{E1}$$

The factor J_{DA} corresponds to the Franck-Condon weighted density-of-states and can be obtained from

$$J_{DA} = \int F_D(E) A_A(E) dE \tag{E2}$$

where F_D and A_A denote the emission factor of the energy donor and the absorption factor of the energy acceptor, respectively.[51] The emission factor $F_D(E)$ depends on the fluorescence intensity $I_F(E)$ according to:

$$F_D(E) = \frac{E^{-3} I_F(E)}{\int E^{-3} I_F(E) dE} \tag{E3}$$

The absorption factor $A_A(E)$ is related to the optical absorption coefficient $\alpha(E)$ by:

$$A_A(E) = \frac{E^{-1}\alpha(E)}{\int E^{-1}\alpha(E) dE} \tag{E4}$$

Figure 8.9A shows the fluorescence intensity $I_F(E)$ and optical absorption coefficient $\alpha(E)$ for H_2TMPyP and P3HT as function of photon energy E. The limits for integration of the functions shown in the denominators of equations E3 and E4 are determined by the energy range of the transitions relevant for energy transfer. In case of H_2TMPyP these limits follow from the energy range of the vibrational modes of the lowest S_0 – S_1 electronic transition. For P3HT the functions shown in the denominator of equations E3 and E4 are integrated over the entire S_0 – S_1 absorption band. Application of equations E3 and E4 then yields the emission factor $F_D(E)$ and absorption factor $A_A(E)$, presented in Figure 8.9B. Multiplication of F_D and A_A for the individual compounds results in the curves presented in Figure 8.9C. Integration of these curves yields values for J_{DA} equal to 4.3×10^{18} J^{-1} for H_2TMPyP and 5.5×10^{17} J^{-1} for P3HT.

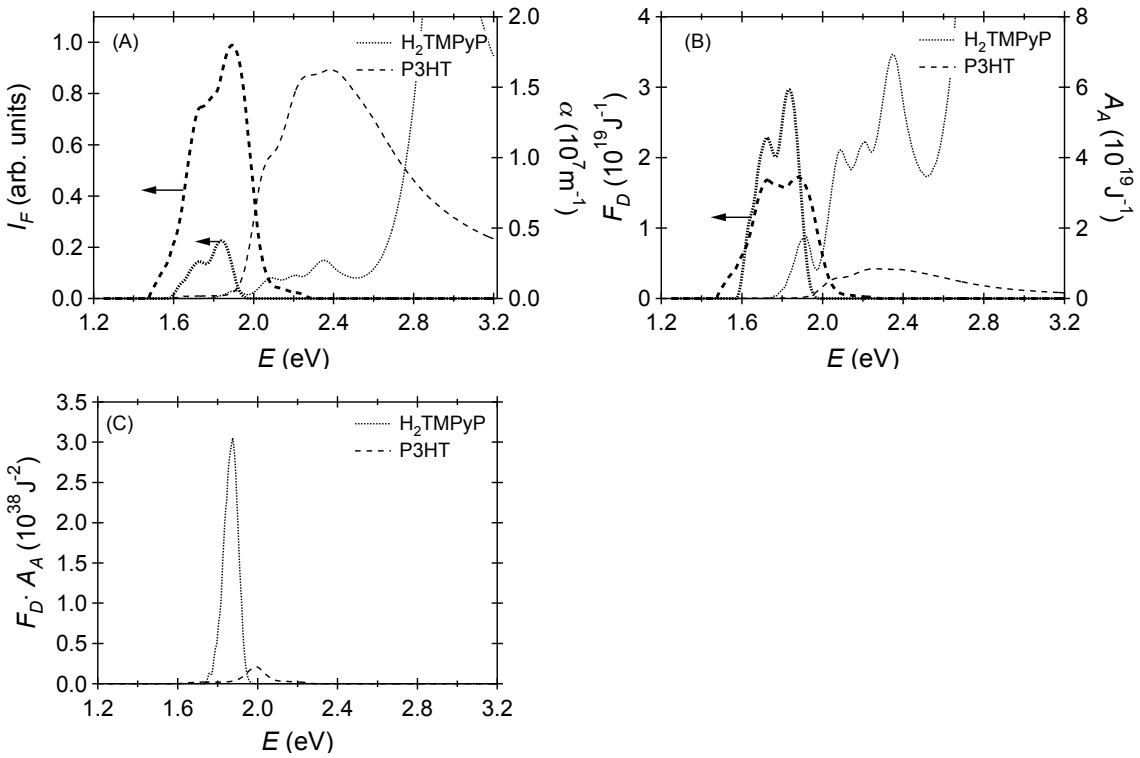

Figure 8.9. Fluorescence and absorption of H_2TMPyP and P3HT as function of photon energy (A), fluorescence factor F_D and absorption factor F_A as function of photon energy (B) and product of F_D and A_A as function of photon energy (C).

References

(1) Knupfer, M., *Applied Physics A-Materials Science & Processing* **2003,** 77, (5), 623-626.

(2) Hill, I. G.; Kahn, A.; Soos, Z. G.; Pascal, R. A., *Chemical Physics Letters* **2000,** 327, 181.

(3) van der Horst, J. W.; Bobbert, P. A.; Michels, M. A. J.; Brocks, G.; Kelly, P. J., *Synthetic Metals* **1999,** 101, (1-3), 333-334.

(4) Kajihara, K.; Tanaka, K.; Hirao, K.; Soga, N., *Jap. J. Appl. Phys.* **1997,** 36, (9A), 5537-5542.

(5) Savenije, T. J.; Warman, J. M.; Goossens, A., *Chemical Physics Letters* **1998,** 287, 148-153.

(6) Horowitz, G.; Kouki, F.; Spearman, P.; Fichou, D.; Nogues, C.; Pan, X.; Garnier, F., *Advanced Materials* **1996,** 8, (3), 242-245.

(7) Halls, J. J. M.; Pichler, K.; Friend, R. H.; Moratti, S. C.; Holmes, A. B., *Applied Physics Letters* **1996,** 68, (22), 3120-3122.

(8) Kroeze, J. E.; Savenije, T. J.; Vermeulen, M. J. W.; Warman, J. M., *Journal of Physical Chemistry B* **2003,** 107, (31), 7696-7705.

(9) Liu, Y. X.; Summers, M. A.; Edder, C.; Frechet, J. M. J.; McGehee, M. D., *Advanced Materials* **2005,** 17, (24), 2960-2964.

(10) Markov, D. E.; Amsterdam, E.; Blom, P. W. M.; Sieval, A. B.; Hummelen, J. C., *Journal of Physical Chemistry A* **2005,** 109, (24), 5266-5274.
(11) Lewis, A. J.; Ruseckas, A.; Gaudin, O. P. M.; Webster, G. R.; Burn, P. L.; Samuel, I. D. W., *Organic Electronics* **2006,** 7, (6), 452-456.
(12) Literature values for Λ_E are multiplied by $\sqrt{2}$ to yield Λ_D.
(13) Yu, G.; Gao, J.; Hummelen, J. C.; Wudl, F.; Heeger, A. J., *Science* **1995,** 270, (5243), 1789-1791.
(14) Halls, J. J. M.; Walsh, C. A.; Greenham, N. C.; Marseglia, E. A.; Friend, R. H.; Moratti, S. C.; Holmes, A. B., *Nature* **1995,** 376, (6540), 498-500.
(15) Li, G.; Shrotriya, V.; Huang, J.; Yao, Y.; Moriarty, T.; Emery, K.; Yang, Y., *Nature Materials* **2005,** 4, 864-868.
(16) Kim, Y.; Cook, S.; Tuladhar, S. M.; Choulis, S. A.; Nelson, J.; Durrant, J. R.; Bradley, D. D. C.; Giles, M.; McCulloch, I.; Ha, C. S.; Ree, M., *Nature Materials* **2006,** 5, (3), 197-203.
(17) Shrotriya, V.; Yao, Y.; Li, G.; Yang, Y., *Applied Physics Letters* **2006,** 89, (6), 063505.
(18) Hoppe, H.; Niggemann, M.; Winder, C.; Kraut, J.; Hiesgen, R.; Hinsch, A.; Meissner, D.; Sariciftci, N. S., *Advanced Functional Materials* **2004,** 14, (10), 1005-1011.
(19) Melzer, C.; Koop, E. J.; Mihailetchi, V. D.; Blom, P. W. M., *Advanced Functional Materials* **2004,** 14, (9), 865-870.
(20) van Duren, J. K. J.; Yang, X. N.; Loos, J.; Bulle-Lieuwma, C. W. T.; Sieval, A. B.; Hummelen, J. C.; Janssen, R. A. J., *Advanced Functional Materials* **2004,** 14, (5), 425-434.
(21) Chirvase, D.; Parisi, J.; Hummelen, J. C.; Dyakonov, V., *Nanotechnology* **2004,** 15, (9), 1317-1323.
(22) Savenije, T. J.; Kroeze, J. E.; Yang, X. N.; Loos, J., *Advanced Functional Materials* **2005,** 15, (8), 1260-1266.
(23) Fell, H. J.; Samuelsen, E. J.; Alsnielsen, J.; Grubel, G.; Mardalen, J., *Solid State Communications* **1995,** 94, (10), 843-846.
(24) Sirringhaus, H.; Brown, P. J.; Friend, R. H.; Nielsen, M. M.; Bechgaard, K.; Langeveld-Voss, B. M. W.; Spiering, A. J. H.; Janssen, R. A. J.; Meijer, E. W.; Herwig, P.; de Leeuw, D. M., *Nature* **1999,** 401, (6754), 685-688.
(25) Aasmundtveit, K. E.; Samuelsen, E. J.; Guldstein, M.; Steinsland, C.; Flornes, O.; Fagermo, C.; Seeberg, T. M.; Pettersson, L. A. A.; Inganas, O.; Feidenhans'l, R.; Ferrer, S., *Macromolecules* **2000,** 33, (8), 3120-3127.
(26) Zen, A.; Saphiannikova, M.; Neher, D.; Grenzer, J.; Grigorian, S.; Pietsch, U.; Asawapirom, U.; Janietz, S.; Scherf, U.; Lieberwirth, I.; Wegner, G., *Macromolecules* **2006,** 39, (6), 2162-2171.
(27) Brinkmann, M.; Rannou, P., *Advanced Functional Materials* **2007,** 17, 101-108.
(28) Moons, E.; Goossens, A.; Savenije, T., *Journal of Physical Chemistry B* **1997,** 101, (42), 8492-8498.
(29) Savenije, T. J.; Moons, E.; Boschloo, G. K.; Goossens, A.; Schaafsma, T. J., *Physical Review B-Condensed Matter* **1997,** 55, (15), 9685-9692.
(30) Tang, C. W., *Applied Physics Letters* **1986,** 48, 183.
(31) Peumans, P.; Forrest, S. R., *Applied Physics Letters* **2001,** 79, (1), 126-128.
(32) Peumans, P.; Yakimov, A.; Forrest, S. R., *Journal of Applied Physics* **2003,** 93, (7), 3693-3723.
(33) Peumans, P.; Uchida, S.; Forrest, S. R., *Nature* **2003,** 425, (6954), 158-162.

(34) Savenije, T. J.; Koehorst, R. B. M.; Schaafsma, T. J., *Chemical Physics Letters* **1995,** 244, (5-6), 363-370.
(35) Kroeze, J. E.; Savenije, T. J.; Warman, J. M., *Journal of the American Chemical Society* **2004,** 126, 7608.
(36) Sze, S. M., *Physics of Semiconductor Devices*. 2 ed.; John Wiley & Sons, Inc.: New York, 1981.
(37) Pettersson, L. A. A.; Roman, L. S.; Inganas, O., *Journal of Applied Physics* **1999,** 86, (1), 487-496.
(38) Drees, M.; Davis, R. M.; Heflin, J. R., *Journal of Applied Physics* **2005,** 97, 036103.
(39) Itoh, E.; Miyairi, K., *Thin Solid Films* **2006,** 499, (1-2), 95-103.
(40) Yamashita, K.; Harima, Y.; Iwashima, H., *Journal of Physical Chemistry* **1987,** 91, 3055.
(41) Horowitz, G.; Peng, X.; Fichou, D.; Garnier, F., *Journal of Applied Physics* **1990,** 67, 528.
(42) Taylor, D. M.; Gomes, H. L.; Underhill, A. E.; Edge, S.; Clemenson, P. I., *Journal of Physics D* **1991,** 24, 2032-2038.
(43) Abdou, M. S. A.; Orfino, F. P.; Son, Y. K.; Holdcroft, S., *Journal of the American Chemical Society* **1997,** 119, 4518.
(44) Hoshino, S.; Yoshida, M.; Uemura, S.; Kodzasa, T.; Takada, N.; Kamata, T.; Yase, K., *Journal of Applied Physics* **2004,** 95, 5088-5092.
(45) Theiss, W. *Hard- and Software*, Dr.-Bernhard-Klein-Str. 110, D-52078 Aachen, Germany.
(46) Simpson, O., *Proc. R. Soc. London Ser. A* **1957,** 238, 402-411.
(47) Theander, M.; Yartsev, A.; Zigmantas, D.; Sundstrom, V.; Mammo, W.; Andersson, M. R.; Inganas, O., *Physical Review B* **2000,** 61, (19), 12957-12963.
(48) Wu, K. R.; Wang, J. J.; Liu, W. C.; Chen, Z. S.; Wu, J. K., *Applied Surface Science* **2006,** 252, (16), 5829-5838.
(49) Mermut, O.; Phillips, D. C.; York, R. L.; McCrea, K. R.; Ward, R. S.; Somorjai, G. A., *Journal of the American Chemical Society* **2006,** 128, (11), 3598-3607.
(50) Vogt, B. D.; Soles, C. L.; Lee, H. J.; Lin, E. K.; Wu, W., *Polymer* **2005,** 46, (5), 1635-1642.
(51) Pope, M.; Svenberg, C. E., *Electronic Processes in Organic Crystals and Polymers*. second ed.; Oxford Science Publications: New York, 1999.
(52) Hennebicq, E.; Pourtois, G.; Scholes, G. D.; Herz, L. M.; Russell, D. M.; Silva, C.; Setayesh, S.; Grimsdale, A. C.; Mullen, K.; Bredas, J. L.; Beljonne, D., *Journal of the American Chemical Society* **2005,** 127, (13), 4744-4762.
(53) Tuminello, P. S.; Arakawa, E. T.; Inagaki, T.; Parks, J. E., *Journal of Chemical Physics* **1991,** 95, (7), 4790-4795.

SUMMARY IN ENGLISH

Current life on earth would not exist without the supply of solar energy. The energy supplied by the sun to the earth is enormous; only one hour of sun irradiation equals the global energy consumption over a full year. The current global energy demand is however mainly fulfilled by the exploitation of fossil fuel reserves, leading to rapid and hardly predictable global environmental changes, declining reserves and increasing economical and political instability. The growing awareness of the huge impact of these aspects on the nowadays civilization drives the demand for renewable alternatives, such as wind turbines, hydroelectric power plants and photovoltaic cells. The prospect of using sunlight is demonstrated by photosynthesis, which involves the light-driven conversion of CO_2 and H_2O into carbohydrates. The energy involved in photosynthesis exceeds the current global energy consumption by a factor of seven, illustrating the enormous potential of utilizing sunlight.

To absorb sunlight efficiently, photosynthetic organisms are equipped with light-harvesting systems. These light-harvesting systems are in general based on chlorophyll derivatives, which strongly absorb the incident sunlight. Absorption of a photon leads to the formation of a strongly bound electron-hole pair, also referred to as an exciton. Due to the specific three-dimensional configuration of the chlorophyll molecules in the light-harvesting complex, excitons are transferred efficiently over a long distance of 10-20 nm towards a reaction center, where the exciton energy is utilized. The concept of a well-organized light-harvesting structure, capable of both light absorption and transport of excitons, could be applied in a solar cell. Such a cell could be realized by applying the light-harvesting dye layer onto a wide bandgap, electron-accepting semiconductor. Excitons formed on light absorption that are capable to diffuse through the dye layer towards the interface with the semiconductor can undergo dissociation into free charge carriers by electron injection into the conduction band of the semiconductor. This type of cell is commonly denoted as the dye-sensitized solar cell. The short exciton diffusion distance in artificial dye layers of typically a few nanometers has led to the development of the Grätzel-cell. This cell is based on a three-dimensional continuous network of semiconductor nanoparticles coated with a monolayer of dye molecules. Such configuration makes exciton diffusion over long distances redundant. However, it requires a more elaborate cell design to compensate for the complicated charge transport.

The long exciton diffusion length in natural light-harvesting systems suggests that long-range energy transfer can be realized by optimizing the specific configuration of the dye molecules. The aim of this thesis is to provide fundamental insights into the relationship between the molecular organization of artificial biomimetic dye molecules and the energy transfer dynamics. A more comprehensive understanding of this relationship could lead to an enhancement of the exciton diffusion length in artificial light-harvesting dye layers, allowing the realization of solar cells based on a simple bilayer design. Such a design is favorable for the transport of charge carriers from the interface towards the electrodes.

Chapter 1 provides a theoretical background describing the energy transfer dynamics in molecular systems. In addition, experimental findings on energy transfer dynamics in natural chlorophyll derivatives and in artificial porphyrin and phthalocyanine derivatives are reviewed and related to the configuration of the dye molecules.

Dye molecules involved in this thesis include several porphyrin derivatives with self-organizing properties. The exciton diffusion length in porphyrin layers deposited onto various semiconductors such as TiO_2 and SnO_2 is determined using the time-resolved microwave conductivity (TRMC) technique. Excitons are formed on pulsed nanosecond excitation of the porphyrin layer. Those excitons that are able to reach the interface between the porphyrin and the semiconductor can undergo interfacial exciton dissociation into separate charge carriers. The electrons injected into the semiconductor are monitored by a change in reflected microwave power, from which the exciton diffusion length is deduced. The morphology of the dye layers is studied using a combination of various techniques such as optical absorption and fluorescence spectroscopy, polarized optical microscopy and X-ray diffraction.

Chapter 2 involves a study on the impact of substituents at the phenyl groups of *meso*-tetraphenylporphyrin derivatives on the incident photon to charge separation efficiency (IPCSE) in a bilayer of the porphyrin derivative with TiO_2. The IPCSE depends on the exciton diffusion length and the yield for charge carrier formation at the interface of the porphyrin with the TiO_2 substrate. The presence of t-butyl substituents at the *para* position and especially the introduction of methyl substituents at the *ortho* position of the phenyl groups is observed to strongly reduce the yield for charge carrier formation. On the other hand, introduction of ethyl substituents at the *para* position of the phenyl groups is observed to strongly enhance the exciton diffusion length. The origin of this phenomenon is discussed in detail in chapter 3. In this chapter it is shown that layers of unsubstituted *meso*-tetraphenylporphyrin molecules consist of both monomers and H-

aggregates. The presence of the latter negatively affects the exciton diffusion length, since H-aggregates act as exciton traps. Ethyl substituents at the *para* position of the phenyl groups suppress the formation of H-aggregates, leading to a more amorphous layer morphology and enhancing the exciton diffusion length from 7 Å to 75 Å.

As discussed in chapter 4, introduction of n-butyl substituents at the *para* position of the phenyl groups enhances the exciton diffusion length even further to a value ≥12 nm. Morphology studies show that the molecules in these layers are aligned with the molecular macrocycles parallel ('homeotropically') to the TiO_2 substrate. As compared to the amorphous layer structure for the ethyl-substituted derivative, such alignment leads to a shorter intermolecular distance and a mutual molecular arrangement that is favorable for energy transfer. This explains the long exciton diffusion length of ≥12 nm. The temperature dependence of the energy transfer dynamics is discussed in chapter 5. Energy transfer is observed to be thermally deactivated; the exciton diffusion length decreases from ≥20 nm at 90 K to ≥12 nm at 300 K. The energy transfer rate decreases by at least a factor of ten from $\geq 3.8\times10^{12}$ s^{-1} at 90 K to $\geq 3.7\times10^{11}$ s^{-1} at 300 K. This decrease is attributed to larger fluctuations in exciton site energies and excitonic couplings at higher temperatures. Exciton motion in this layer hence occurs via a band like mechanism, rather than by thermally activated Förster-like hopping. A reduction of the degree of disorder is promising to further enhance the exciton diffusion length.

Chapters 6 and 7 involve studies on energy transfer in layers of porphyrin derivatives that self-assemble by the formation of coordinative bonds between electron-donating substituents and the electron-accepting central metal atom. The zinc porphyrin derivative discussed in chapter 6 has an electron-donating hydroxyethyl and carbonyl substituent at the 3- and 13-position of the porphyrin macrocycle. Layers of this porphyrin derivative are observed to consist of both self-assembled stacks and non-assembled monomers. Only the monomers are found to contribute to the formation of charge carriers, while no significant contribution from the stacks is observed. This observation is attributed to the presence of a layer of monomers at the interface with the TiO_2 or SnO_2 substrate, while energy transfer from a stack towards a monomer is energetically unfavorable. Chapter 7 involves a study on self-assembling zinc *meso*-tetraphenylporphyrin derivatives, having electron-donating methoxymethyl substituents at the *meta* positions of the phenyl groups. Layers of this porphyrin derivative are observed to consist of stacks oriented with their long axis parallel to the TiO_2 substrate, while the angle between the porphyrin

macrocycles and the TiO_2 substrate amounts to 23°. The energy transfer rate between stacks is observed to be as high as 7.2×10^{11} s^{-1}, leading to an exciton diffusion length as long as 15 nm. For comparison, the exciton diffusion length in a layer of a non-assembling close analogue is found to amount to only 3 nm. This difference illustrates that self-assembly leading to a long-range well-developed molecular organization strongly enhances the exciton diffusion length.

Chapter 8 involves a study on the photophysical properties of a bilayer of regioregular poly(3-hexylthiophene) (P3HT) deposited onto an electron-accepting porphyrin derivative. Both excitons formed in the P3HT and in the porphyrin layer are dissociated into free charge carriers at the interface of both organic layers. The incident photon to current efficiency (IPCE) of a photovoltaic device based on these materials in a bilayer design exceeds 20 % over a broad wavelength regime. The exciton diffusion length in the porphyrin layer is determined to amount to 10 nm, while a value of 13 nm is found for the P3HT layer. The latter value exceeds values reported in literature by almost a factor of three, which is attributed to the alignment of the P3HT backbones parallel to the interface with the porphyrin layer.

In conclusion, this research illustrates the importance of controlling the molecular organization for the realization of efficient energy transfer in organic opto-electronics. Adaptation of the molecular configuration has led to an improvement of the exciton diffusion length from a few nanometers to tens of nanometers, i.e. comparable to the exciton diffusion length in natural photosynthetic systems. An even further improvement of the exciton diffusion length might be realized by a further reduction of disorder and by the prevention of structural defects. This would allow the application of a well-organized dye layer in a bilayer configuration with the semiconductor material, which will lead to more efficient charge transport as compared to the nanostructured cell design.

Annemarie Huijser

SAMENVATTING IN HET NEDERLANDS

Het huidige leven op aarde zou niet bestaan zonder de toevoer van zonne-energie. De toevoer van energie vanaf de zon naar de aarde is gigantisch; slechts één uur zonnestraling is equivalent aan de globale energieconsumptie gedurende een heel jaar. De huidige energievraag wordt echter voornamelijk gerealiseerd door de exploitatie van fossiele brandstoffen, leidend tot snelle en nauwelijks voorspelbare klimaatverandering, afnemende reserves en toenemende politieke en economische instabiliteit. De toenemende bewustwording van de enorme invloed van deze aspecten op de huidige beschaving leidt tot een steeds sterkere vraag naar duurzame alternatieven, zoals windturbines, waterkrachtcentrales en zonnecellen. De mogelijkheden die het gebruik van zonlicht biedt wordt geïllustreerd door fotosynthese, het proces waarbij onder invloed van licht CO_2 en H_2O omgezet worden in koolwaterstoffen. De hoeveelheid energie die betrokken is bij fotosynthetische processen is zeven keer hoger dan de huidige globale energieconsumptie, hetgeen de enorme mogelijkheden van het gebruik van zonne-energie laat zien.

Om zonlicht efficiënt te absorberen zijn fotosynthetische organismes uitgerust met lichtoogstende systemen. Deze systemen zijn in het algemeen gebaseerd op chlorofyl derivaten, die het opvallende zonlicht sterk absorberen. Vrijwel elk geabsorbeerd foton leidt tot de vorming van een sterk gebonden elektron-gat paar, ook wel een exciton genoemd. Door de specifieke driedimensionale configuratie van de chlorofyl moleculen in een lichtoogstend systeem worden excitonen getransporteerd over behoorlijk lange afstanden van 10-20 nm. Hierdoor bereiken de excitonen een reactiecentrum, waar de energie wordt benut. Het concept van een goed georganiseerd lichtoogstend systeem, dat zowel in staat is tot lichtabsorptie als transport van excitonen, kan toegepast worden in een zonnecel. Zo een cel kan gerealiseerd worden door het combineren van de lichtoogstende kleurstoflaag met een halfgeleider materiaal dat een grote bandgap en elektronaccepterende eigenschappen heeft. De excitonen die door de kleurstoflaag naar het grensvlak met de halfgeleider bewegen kunnen uiteenvallen in vrije ladingsdragers, als gevolg van elektroninjectie in de geleidingsband van de halfgeleider. Dit type cel wordt meestal een kleurstofgesensibiliseerde zonnecel genoemd. De in het algemeen korte afstand van een paar nanometers die excitonen kunnen afleggen in kunstmatige kleurstoflagen heeft geleid tot het ontwikkelen van de Grätzelcel. Deze cel is gebaseerd

op een driedimensionaal continu netwerk van halfgeleider nanodeeltjes bedekt met een dun laagje kleurstofmoleculen. Zo een configuratie maakt diffusie van excitonen overbodig, maar vereist echter ook een complex celontwerp om te compenseren voor het gecompliceerde ladingstransport. De efficiënt functionerende natuurlijke lichtoogstende systemen, aan de andere kant, laten zien dat energieoverdracht over behoorlijk lange afstanden gerealiseerd kan worden door de configuratie van kleurstofmoleculen te optimaliseren. Het doel van het onderzoek dat beschreven wordt in dit proefschrift is het verschaffen van inzicht in de relatie tussen de moleculaire organisatie en de eigenschappen van energieoverdracht. Een beter begrip van deze relatie kan leiden tot een vergroting van de exciton diffusielengte in kunstmatige lichtoogstende kleurstoflagen. Dit kan leiden tot toepassingsmogelijkheden van kleurstof en halfgeleiders in een tweelagensysteem. Zo een configuratie leidt tot beter transport van ladingsdragers van het grensvlak tussen de twee materialen naar de elektrodes.

In hoofdstuk 1 wordt een theoretische achtergrond gegeven voor de energieoverdracht processen in moleculaire systemen. Ook worden experimentele waarnemingen aan energieoverdrachtsparameters in natuurlijke chlorofyl derivaten en kunstmatige porfyrine en ftalocyanine derivaten samengevat en gerelateerd aan de moleculaire organisatie.

Dit proefschrift behandelt voornamelijk energieoverdracht in verschillende porfyrine derivaten met zelforganiserende eigenschappen. De exciton diffusielengte in porfyrine lagen aangebracht op verschillende halfgeleiders zoals TiO_2 en SnO_2 is bepaald met behulp van de tijdsopgeloste microgolf geleidingstechniek (TRMC). Excitonen in de porfyrine lagen zijn gevormd door belichting met een korte laserpuls die een tijdsduur heeft van enkele nanoseconden. Die excitonen die in staat zijn het grensvlak tussen de kleurstof en de halfgeleider te bereiken kunnen gedissocieerd worden in ladingsdragers. De resulterende elektronen, geïnjecteerd in de geleidingsband van de halfgeleider, worden gedetecteerd door een verandering in gereflecteerd microgolfvermogen, aan de hand waarvan de exciton diffusielengte is bepaald. De morfologie van de kleurstoflagen is bestudeerd door een combinatie van verschillende technieken te gebruiken zoals optische absorptie en fluorescentie spectroscopie, gepolariseerde optische microscopie en röntgendiffractie.

In hoofdstuk 2 wordt de invloed van diverse zijgroepen aan de fenylgroepen van *meso*-tetrafenylporfyrine derivaten op de lichtgeïnduceerde ladingsscheidingsefficiëntie (IPCSE) in een tweelagensysteem van een porfyrine met TiO_2 besproken. De IPCSE is afhankelijk van de exciton diffusielengte en de exciton dissociatie efficiëntie aan het

grensvlak van de porfyrine en het TiO_2. De aanwezigheid van t-butyl zijgroepen op de *para* positie van de fenylgroepen en in het bijzonder de introductie van methyl zijgroepen op de *ortho* positie van de fenylgroepen leidt tot een sterke afname van de exciton dissociatie efficiëntie. Aan de andere kant leidt introductie van ethyl zijgroepen op de *para* positie van de fenylgroepen tot een behoorlijke toename van de exciton diffusielengte. De oorzaak van dit fenomeen wordt bediscussieerd in hoofdstuk 3. In dit hoofdstuk wordt besproken dat lagen van porfyrine moleculen zonder zijgroepen (*meso*-tetrafenylporfyrine) bestaan uit zowel monomeren als H-aggregaten. Dit laatste beïnvloedt de exciton diffusielengte negatief, omdat H-aggregaten zich gedragen als exciton traps. De ethyl zijgroepen op de *para* positie van de fenylgroepen voorkomen de vorming van H-aggregaten, hetgeen leidt tot een meer amorfe laagstructuur en een toename van de exciton diffusielengte van 7 Å naar 75 Å.

De introductie van n-butyl zijgroepen op de *para* positie van de fenylgroepen, besproken in hoofdstuk 4, leidt tot een verdere toename van de exciton diffusielengte tot ≥12 nm. Morfologiestudies laten zien dat de moleculen in deze lagen georiënteerd zijn met het molecuulvlak evenwijdig aan het TiO_2 substraat. Vergeleken met de amorfe structuur van de porfyrine met de ethyl zijgroepen leidt deze structuur tot een kortere intermoleculaire afstand en een voor energieoverdracht gunstigere configuratie van moleculen ten opzichte van elkaar. Dit verklaart de lange exciton diffusie lengte van ≥12 nm. Om het proces van energieoverdracht in deze porfyrine lagen in meer detail te bestuderen, werd de temperatuursafhankelijkheid van de energieoverdrachtsparameters bepaald, zoals is besproken in hoofdstuk 5. Energieoverdracht blijkt thermisch gedeactiveerd te zijn; de exciton diffusielengte neemt af van ≥20 nm bij 90 K naar ≥12 nm bij 300 K. De energieoverdrachtsconstante neemt met minstens een factor tien af van $\geq 3.8\times10^{12}$ s^{-1} bij 90 K naar $\geq 3.7\times10^{11}$ s^{-1} bij 300 K. Deze afname is toegeschreven aan sterkere fluctuaties in exciton site energieën en exciton koppelingen bij hogere temperaturen. Hieruit is geconcludeerd dat energieoverdracht plaatsvindt via een bandmechanisme en niet via een thermisch-geactiveerd Förster-achtig hopping proces. Een verdere afname van wanorde is daarom een zeer veelbelovend perspectief om een verdere toename van de exciton diffusielengte te realiseren.

In hoofdstuk 6 en 7 wordt ingegaan op energieoverdracht in lagen van porfyrines die zelfassembleren door het vormen van een coördinatieve binding tussen elektrondonerende

zijgroepen en het elektronaccepterende centrale metaal atoom. De zink porfyrine die besproken wordt in hoofdstuk 6 heeft elektrondonerende hydroxyethyl en carbonyl zijgroepen op de 3- en de 13-positie van het porfyrine molecuul. Dunne lagen van zulke moleculen bestaan uit zowel zelfgeassembleerde kolommen en niet-geassembleerde monomeren. Alleen de monomeren dragen bij aan de vorming van ladingsdragers, terwijl de bijdrage van de kolommen verwaarloosbaar is. Dit is toegeschreven aan de aanwezigheid van een laag van monomeren aan het grensvlak met het TiO_2 of SnO_2 substraat, terwijl energieoverdracht van een monomeer naar een kolom energetisch gezien onaantrekkelijk is. In hoofdstuk 7 worden zelfassemblerende zink *meso*-tetrafenylporfyrines met elektrondonerende methoxymethyl zijgroepen op de *meta* posities van de fenylgroepen behandeld. Dunne lagen van deze porfyrine moleculen bestaan uit kolommen georiënteerd met de as parallel aan het TiO_2 substraat, met een hoek van 23° tussen de molecuulvlakken en het TiO_2. De energieoverdrachtsconstante tussen kolommen heeft een behoorlijk hoge waarde van 7.2×10^{11} s^{-1}, resulterend in een exciton diffusielengte van 15 nm. Ter vergelijking, de exciton diffusielengte in een laag van sterk gerelateerde niet-assemblerende moleculen is slechts 3 nm. Het verschil laat zien dat zelfassemblage leidend tot moleculaire organisatie op relatief grote schaal de exciton diffusielengte sterk verbetert.

In hoofdstuk 8 worden de fotofysische processen besproken in een tweelagensysteem van regioregulair poly(3-hexylthiofeen) (P3HT) aangebracht op een elektronaccepterende porfyine. Zowel excitonen gevormd in het P3HT als in de porfyrine laag worden gedissocieerd in vrije ladingsdragers aan het grensvlak tussen beide organische lagen. De monochromatische efficiëntie IPCE (incident photon to current efficiency) van een zonnecel gebaseerd op deze materialen in een tweelagensysteem is ruim 20 % over een breed golflengte gebied. De exciton diffusielengte in de porfyrine laag is 10 nm, terwijl een diffusielengte van 13 nm bepaald is voor de P3HT laag. De laatste waarde is bijna een factor drie hoger dan literatuurwaarden, hetgeen toegeschreven is aan de oriëntatie van de P3HT ketens parallel aan het grensvlak met de porfyrine.

Concluderend kan gesteld worden dat dit onderzoek het belang aangeeft van het kunnen manipuleren van de moleculaire organisatie voor het realiseren van efficiënte energieoverdracht in organische opto-elektronica. Het aanpassen van de moleculaire organisatie heeft geleid tot een toename van de exciton diffusielengte van een paar nanometers naar tientallen nanometers, hetgeen vergelijkbaar is met de exciton diffusielengte in natuurlijke lichtoogstende systemen. Een verdere verbetering van de

exciton diffusielengte kan mogelijk gerealiseerd worden door een verdere reductie van wanorde en het vermijden van structurele defecten. Dit biedt het perspectief om een goed gestructureerde kleurstoflaag in een tweelagensysteem met het halfgeleidermateriaal toe te passen, hetgeen zal leiden tot efficiëntere ladingstransport vergelegen met een nanogestructureerd systeem.

Annemarie Huijser

DANKWOORD

Dit proefschrift beschrijft de resultaten van vier jaar promotieonderzoek bij de vakgroep Opto-Electronische Materialen binnen de afdeling DCT van de Technische Universiteit Delft. Nu alles eindelijk helemaal op papier staat en gereed is om naar de drukker te worden verstuurd, wil ik graag hieronder iedereen bedanken zonder wie dit proefschrift zeker niet tot stand zou zijn gekomen.

Allereerst wil ik mijn dagelijkse begeleider, dr. ir. Tom Savenije, heel erg bedanken voor de buitengewoon goede begeleiding van mijn promotieonderzoek. In het eerste jaar maakte jij mij grondig wegwijs met de verschillende experimentele technieken. Het feit dat jij toen al het schrijven van publicaties stimuleerde, heeft volgens mij in belangrijke mate bijgedragen aan het binnen vier jaar afronden van dit onderzoek. Ook de vrijheid die jij mij gaf wat betreft het wel of niet doen van bepaalde experimenten en het zelf een richting geven aan mijn promotieonderzoek waardeer ik bijzonder. Kortom, wat mij betreft was dit de perfecte manier van samenwerken!

Ook mijn promotor, prof. dr. Laurens Siebbeles, wil ik bedanken voor zijn belangrijke bijdrage aan dit proefschrift. Ik heb het altijd klaar staan van jou voor promovendi altijd erg gewaardeerd. Ook bedankt voor jouw theoretische inbreng, alle uren die je hebt besteed aan besprekingen en het altijd snelle commentaar op manuscripten. Verder is mij ook altijd de iets andere kijk die jij op resultaten hebt opgevallen, hetgeen volgens mij een belangrijke bijdrage heeft geleverd aan de kwaliteit van dit onderzoek. Heel erg bedankt hiervoor!

Verder wil ik ook alle andere collega's van de groep bedanken voor alle samenwerking, de gezellige sfeer en de goede adviezen tijdens werkbesprekingen en pauzes. De oud-promovendi die inmiddels de groep al hebben verlaten, dr. ir. Pieter Quist, dr. ir. Paulette Prins en dr. Silvia Fratiloiu, wil ik bedanken voor de prettige tijd samen op het IRI en later bij DCT. The other PhD students, Wojtek, Tuan, Elise, Joris, Ruben, Sameer en Aleksey, I am definitely going to miss the breaks with interesting conversations with you. All the best to you and good luck with finishing your PhD thesis! De technici Paul Rijkers, ing. Martien Vermeulen, ir. Ruben Abellon en ing. John Suijkerbuijk wil ik bij deze van harte bedanken voor alle technische ondersteuning. Mijn voorgangster, dr. Jessica Kroeze, bedankt voor je hulp vanuit Londen in het begin van mijn promotieonderzoek. Former colleague dr. Avi Shalav, thanks for

introducing me to the optical modelling software, which was very useful! Ook dr. Ferdinand Grozema wil ik bedanken voor de altijd nuttige adviezen en onze recente samenwerking wat betreft berekeningen aan porfyrines. Cecilia Quick, heel erg bedankt voor het altijd afhandelen van alle papierwerk. Verder wil ik ook prof. dr. Joop Schoonman, dr. Harry Donker en de gepensioneerde oud-collega's van het IRI, dr. John Warman, dr. Thijs de Haas en dr. Lee Luthjens, bedanken voor hun interesse in mijn onderzoek en alle goede adviezen.

Prof. dr. Stephen Picken en Arek Kotlewski, heel erg bedankt voor jullie bereidheid altijd te willen helpen met POM metingen en mee te denken hoe de XRD en POM resultaten te verklaren. Ook wil ik Ben Norder bedanken voor het uitvoeren van DSC experimenten, ir. Edward Maloney voor de TiO_2 samples, Niek van der Pers voor de XRD metingen beschreven in hoofdstuk 4 en dr. Stefan Meskers voor zijn hulp bij de optische metingen beschreven in hoofdstuk 5. I also would like to thank dr. Ryuzi Katoh for the collaboration. I really appreciated your enthusiasm and the fact that you prepared the experiments very well in advance, so we could do a lot of experiments during your stay of only a few weeks.

Prof. dr. habil. Silviu Balaban and Peter Marek, I would like to thank you very much for collaborating and your hospitality when we visited Karlsruhe. Silviu, I also really appreciate your willingness to spend quite some time on travelling to be a member of my PhD committee. Hierbij wil ik ook dr. Bart Suijkerbuijk en prof. dr. Bert Klein Gebbink bedanken voor de succesvolle samenwerking en jullie enthousiasme voor onderzoek dat toch net iets minder binnen jullie vakgebied ligt. Bart, wat ik bijzonder heb gewaardeerd is jouw flexibiliteit aangaande de synthese van materialen; de bereidheid om deze in flinke hoeveelheden te maken en speciaal voor de experimenten in Delft ook andere materialen te synthetiseren, zelfs tijdens de drukke periode rond het afronden van je eigen proefschrift.

Als laatste, maar zeker niet in de laatste plaats, wil ik mijn familie en vrienden heel erg bedanken voor hun interesse in mijn onderzoek dat voor buitenstaanders niet altijd even duidelijk moet zijn geweest. In het bijzonder wil ik mijn ouders, broers, zus en zwager (en neefje Bart natuurlijk...) bedanken voor alles...

Annemarie Huijser

Delft, februari 2008

CURRICULUM VITAE

Annemarie Huijser was born on the 19th of November 1979 in Sint Philipsland, The Netherlands. She received her atheneum diploma in June 1998 from the Prins Maurits Scholengemeenschap in Middelharnis. In August of the same year she started her studies in Chemical Engineering at the Delft University of Technology. During the fourth year of her study she worked for three months at the Risø National Laboratory in Denmark on proton diffusion in electrolytes. She completed her studies with a Master of Science thesis on charge transport in polythiophene films (with honours), in the Inorganic Chemistry group of prof. dr. Joop Schoonman. In April 2004 she started her PhD studies in the Radiation Chemistry group at the Interfaculty Reactor Institute, under the supervision of prof. dr. Laurens D.A. Siebbeles and dr. Tom J. Savenije. In this group, since January 2005 the Opto-Electronic Materials section at the DelftChemTech department, she performed an experimental study on the impact of the molecular organization on energy transfer dynamics in molecular thin films. The results of this research are presented in this PhD thesis and in a number of publications. As of May 2008, the author of this thesis will be working as a post-doctoral researcher in the Department of Chemical Physics at Lund University, Sweden, under the supervision of prof. dr. Villy Sundström.

PUBLICATIONS

Carolien L. Huisman, Annemarie Huijser, Harry Donker, Joop Schoonman and Albert Goossens, UV polymerization of oligothiophenes and their application in nanostructured heterojunction solar cells, *Macromolecules* **2004**, *37*, 5557-5564.

Annemarie Huijser and Joop Schoonman, Materials for intermediate-temperature solid oxide fuel cells and for proton exchange membrane fuel cells, *Environmental Engineering and Management Journal* **2005**, *4*, 293-305.

Annemarie Huijser, Tom J. Savenije, Jessica E. Kroeze and Laurens D.A. Siebbeles, Exciton diffusion and interfacial charge separation in meso-tetraphenylporphyrin/TiO_2 bilayers: effect of ethyl substituents, *Journal of Physical Chemistry B* **2005**, *109*, 20166-20173.

Annemarie Huijser, Tom J. Savenije and Laurens D.A. Siebbeles, Effect of the structure of substituents on charge separation in meso-tetraphenylporphyrin/TiO_2 bilayers, *Thin Solid Films* **2006**, *511-512*, 208-213.

Annemarie Huijser, Tom J. Savenije, Arkadiusz Kotlewski, Stephen J. Picken and Laurens D.A. Siebbeles, Efficient light-harvesting layers of homeotropically aligned porphyrin derivatives, *Advanced Materials* **2006**, *18*, 2234-2239.

Ryuzi Katoh, Annemarie Huijser, Hohjiro Hara, Tom J. Savenije and Laurens D.A. Siebbeles, Effect of the particle size on the electron injection efficiency in dye-sensitized nanocrystalline TiO_2 films studied by time-resolved microwave conductivity (TRMC) measurements, *Journal of Physical Chemistry C* **2007**, *111*, 10741-10746.

Annemarie Huijser, Peter Marek, Tom J. Savenije, Laurens D.A. Siebbeles, Torsten Scherer, Robert Hauschild, Jedrzej Szmytkowski, Heinz Kalt, Horst Hahn and Teodor Silviu Balaban, Photosensitization of TiO_2 and SnO_2 by artificial self-assembling mimics of the natural chlorosomal bacteriochlorophylls, *Journal of Physical Chemistry C* **2007**, *111*, 11726-11733.

Annemarie Huijser, Bart M.J.M. Suijkerbuijk, Robertus J.M. Klein Gebbink, Tom J. Savenije and Laurens D.A. Siebbeles, Efficient exciton transport in layers of self-assembled porphyrin derivatives, *Journal of the American Chemical Society* **2008**, in press.

Annemarie Huijser, Tom J. Savenije, Avi Shalav and Laurens D.A. Siebbeles, An experimental study on the molecular organization and exciton diffusion in a bilayer of a porphyrin and poly(3-hexylthiophene), submitted to *Journal of Applied Physics*.

Tom J. Savenije, Annemarie Huijser, Martien J.W. Vermeulen and Ryuzi Katoh, Charge carrier dynamics in TiO_2 nanoparticles at various temperatures, submitted to *Chemical Physics Letters*.

Annemarie Huijser, Tom J. Savenije, Stefan C.J. Meskers, Martien J.W. Vermeulen and Laurens D.A. Siebbeles, Thermally deactivated exciton diffusion in a nematic layer of homeotropically aligned tetraphenylporphyrin derivatives, manuscript in preparation.

Annemarie Huijser, Tom J. Savenije, and Laurens D.A. Siebbeles, Effect of molecular organization on energy transfer dynamics in natural and biomimetic light-harvesting systems, manuscript in preparation.